Active Target Location Using Crossed-Dipole Based Circular Array FMCW Radar

Shashi Halai

A thesis submitted for the degree of

Doctor of Philosophy

of

University College London

Sensors, Systems and Circuits Group

Department of Electronic and Electrical Engineering

University College London

December 2014

I, Shashi Halai, confirm that the work presented in this thesis is my own. Where information has been derived from other sources, I confirm that this has been indicated in the thesis.

Signature _____

Date _____

.

Abstract

Active target location systems capable of measuring both range and bearing have niche applications, including maritime navigation where a seafaring vessel is manoeuvring in the vicinity of a harbour or an oil rig. Such systems can also be used to determine the location of other vessels for vessel-to-vessel personnel or material transfer. The usual approach is to combine FMCW radar with a mechanically or electrically steered beam, establishing both range and bearing to a target, respectively. The radar system described in this thesis is an innovative alternative approach, one that combines FMCW radar with a crossed-dipole antenna, which conveniently functions as a circular array, thereby simultaneously determining the range and bearing of an active target. By using phase mode excitation, neither mechanical nor electrical beam steering is required to locate the active target, as the receive antenna is able to monitor 360° in azimuth continually. However, due to the use of $+1^{st}$ and -1^{st} order phase modes, the radar can only operate in an 180° sector unambiguously. The usual inherent problems with circular arrays being affected by multipath are also easily mitigated by the range resolution of the radar.

This thesis describes in detail the development of a 2.44 GHz crossed-dipole antenna structure and its associated feed network. It also describes the first prototypes that led to its current form and goes on to discuss in detail the design and construction of the radar system and frequency shifted active target. Frequency shifting was implemented within the target to overcome the increased clutter power due to the omnidirectional receive antenna. However, firstly this thesis lays the foundation of radar theory, active targets, phase modes and basic antenna theory. Some of the literature associated with radars currently used in this type of scenario is also discussed.

Appropriate analysis, modelling and experimental validation is conducted to assess system performance in relation to the predicted behaviour. The radar system was then tested in an open field, with the active target detected to a range of 125 m.

Acknowledgements

Firstly, I would like to thank my supervisor Prof. Paul Brennan whose support and direction allowed this project to develop and produce the results it has. Secondly, my second supervisor Dr. Kenneth Tong was also there to help with antenna related questions and helped with using certain equipment. Both Dave Patrick and Ian Weller, from Guidance Microwave chose me over other candidates and allowed me to pursue this PhD, for that I am eternally grateful. Their quarterly visits ensured this project was relevant to their work and gave me milestones to aim for. I would also like to thank them for their support when testing the radar at their office. My family have provided tremendous support for my studies, both my parents and my sisters, Reena and Sheetal were even kind enough to proof read this document, providing much needed spelling and grammar corrections.

Throughout my PhD I met some interesting people, who were always there to bounce ideas off, namely Samiur, Arvind, Ajmal, Lai Bun, Matt Ash, Matt Ritchie, Jian Ling, Allann and others. Many thanks go to the latter five individuals especially Lai Bun, Matt Ash and Allann who helped me during the Shenley trials, taking time out of their busy schedules to help set up and collect the data. This close knit UCL radar group are always on hand to support with kind words and advice whenever it was required, allowing me to enjoy my time here.

Without the support staff at UCL, actually making parts of this radar system especially the antennas and support structure would have been virtually impossible. Their valuable input with design and innovative solutions, as well as use of their lab, tools and parts allowed this project to succeed. For these reasons I would like to thank the following people Gerald, Andy, Tom, Scott and Trevor.

Publications

The following publication was produced during this PhD:

Conference Paper

- S. Halai, P. V. Brennan, D. Patrick and I. Weller, “Frequency shifted active target for use in FMCW radar systems,” in *2014 IEEE Radar Conference*, Cincinnati, Ohio, United States, 19-23 May 2014

Contents

List of Figures

List of Tables

Symbols

β	Propagation Constant (= $2\pi/\lambda$)
$\delta(t)$	Dirac Delta Function
ε_{eff}	Effective Dielectric Constant
ε_r	Dielectric Constant
$\theta_{-3dB,az}$	Azimuth Beamwidth
$\theta_{-3dB,el}$	Elevation Beamwidth
λ_o	Operating Wavelength
σ	Radar Cross Section
σ^o	Backscatter Coefficient
τ	Time Delay for Transmitted Signal
Γ	Reflection coefficient
$\Delta\phi_{RMS}$	Phase Jitter
Δr	Range Resolution
Ω_A	Beam Solid Angle
A_e	Antenna Aperture
$AF(\phi)$	Array Factor
B	Bandwidth
B_n	Noise Bandwidth
c	Speed of Light in a vacuum (= $3\text{x}10^8$ ms^{-1})
$E(\phi)$	Farfield Radiation Pattern
$EL(\phi)$	Element Pattern Factor
$E_m(\theta,\phi)$	m^{th} Phase Mode Farfield Radiation Pattern

d	Spacing Between Elements
D	Antenna Directivity
F	Pattern Propagation Factor
f_0	Initial Frequency
f_{beat}	Beat Frequency
f_c	Centre Frequency
f_{clk}	Clock Frequency
f_D	Doppler Frequency
$f_{d,LSB}$	Deramped Frequency Lower Sideband
$f_{d,USB}$	Deramped Frequency Upper Sideband
f_o	Transmitted Frequency
F_n	Noise Figure
F_{nf}	Noise Factor
$F_{n,ADC}$	ADC Noise Figure
f_o	Transmitted Frequency
f_{shift}	Shift Frequency
G_{amp}	Gain of Amplifier
G_r	Gain of Receive Antenna
G_{rec}	Gain of Receiver
G_t	Gain of Transmit Antenna
G_{tar}	Gain of Target Antenna
k	Boltzmann's constant (= 3.18×10^{-23} W/K/Hz)
L	Losses
P_{+1}	$+1^{st}$ Order Phase Mode
P_{-1}	-1^{st} Order Phase Mode
P_{inc}	Intercepted Power
$P_{max,ADC}$	Noise Power
$P_{min,ADC}$	Received Power

P_n	Noise Power
P_r	Received Power
$P_{r,clutter}$	Received Clutter Power
$P_{r,tar}$	Received Power for Active Target
P_t	Transmitted Power
$P_{t,tar}$	Transmitted Power for Active Target
r	Range
R_e	Edge Impedance
R_i	Input Impedance
r_u	Unambiguous Range
T_0	Noise Reference Temperature (= 290 K)
T_s	Receiver Noise Temperature (K)
v_{fs}	Full Scale Voltage
V_n	Excitation Amplitude
v_r	Radial Velocity
$v_{ADC,noise}$	ADC Noise Voltage

Abbreviations

AC	Alternating Current
ADC	Analogue to Digital Converter
BPF	Bandpass Filter
BT	Bandwidth Time
CFAR	Constant False Alarm Rate
CST MWS	Computer Simulation Technology Microwave Studio
CW	Continuous Wave
DAC	Digital to Analogue Converter
DAQ	Digital Acquisition
DC	Direct Current
DDS	Direct Digital Synthesiser
DSB	Double Sideband
ENOB	Effective Number Of Bits
EM	Electromagnetic Wave
ESM	Electronic Support Measure
FFT	Fast Fourier Transform
FM	Frequency Modulated
FMCW	Frequency Modulated Continuous Wave
FOV	Field Of View
HFBW	Half-Power Beamwidth
IF	Intermediate Frequency
IFF	Identification Friend or Foe

LED Light Emitting Diode

LFM Linear Frequency Modulated

LO Local Oscillator

ML Mismatch Loss

PCB Printed Circuit Board

PD Pulsed Doppler

PLL Phased Locked Loop

PRF Pulse Repetition Frequency

PSU Power Supply Unit

RCS Radar Cross Section

RL Return Loss

RIB Rigid Inflatable Boat

RF Radio Frequency

RMS Root Mean Square

RWR Radar Warning Receiver

SART Search And Rescue Transponder

SAW Surface Acoustic Wave

SCR Signal to Clutter Ratio

SNR Signal to Noise Ratio

SSB Single Sideband

STD Standard Deviation

UCA Uniform Circular Array

ULA Uniform Linear Array

USB Universal Serial Bus

VNA Vector Network Analyser

VCO Voltage Controlled Oscillator

VSWR Voltage Standing Wave Ratio

Chapter 1

Introduction

1.1 Overview

Target detection is the primary aim of a radar. Radar systems transmit their own generated electromagnetic radiation usually in the form of a pulse toward aforementioned target. The target reflects back a proportion of this transmitted radiation which is detected by the receiving radar antenna. The received signal can be processed to determine some target features, such as range and direction. Targets can be anything that can reflect or scatter the radio wave, both desired and undesired, as is the case with clutter. Radar systems operate in the radio and microwave region of the electromagnetic spectrum, they can be used in 'all-weather' scenarios, such as fog and at any time of the day or night, something an optical sensor such as a camera is unable to do, making radars ideal for marine navigation.

Radar systems have been aiding marine navigation for almost 80 years. Around the time of the Second World War, many nations, including UK and USA had their own radar systems. The use of transponders with radars has a history almost as long as radar itself. Initially, in the 1940's they were used as Identification Friend or Foe (IFF) beacons [1]. Approximately a decade later they were introduced as harbour navigation aids [2]. Current marine radar systems are used in both military and commercial applications, with many companies developing radar systems for navigation [3] and other at sea applications requiring close control, such as transferring materials and personnel between vessels [4]. The two cited systems are of differing radar types, the first a Pulsed Doppler (PD) and the second a Frequency Modulated Continuous Wave (FMCW).

FMCW radar systems allow the measurement of range whereas Continuous Wave (CW) do not. FMCW radars operate at a much lower peak output power when compared to PD radar systems, usually at $\approx$10%, due to the substantial processing gain. The use of FMCW radars in marine applications are fairly recent, but is gaining momentum. Their simple construction

and widely available components make them ideal for research. There are many systems on the market that are able to offer both range and bearing measurements, but are usually for large vessels [4]. Hence, there remains a gap in the market for a smaller radar system, which could be mounted to smaller ships, one which is also able to detect active targets placed around harbours on obstacles to avoid them.

This is where this project enters a somewhat niche market, it discusses the development of a crossed-dipole receiving radar antenna with no electronic or mechanical beam steering, however is able to measure both range and bearing to a frequency shifted active target. The use of such a target was vital in the operation of this system, due to the omnidirectional antenna, the clutter covers an annular ring area. Whereas, for conventional radar systems this clutter region is limited by the antenna beamwidth and dwell time (for a mechanically scanned radar).

1.2 Aims

The key aim of this PhD is to develop a FMCW radar system using existing circular array theory for the detection, in both range and bearing of an active target. The use of circular array theory, focusing on phase mode theory removes the need for neither electronic nor mechanical steered beams to establish the targets bearing.

The aim when constructing the radar is to design and construct it in sections, testing and verifying each part before the whole system is put together. With respect to the antennas and associated feed networks used for the radar system, all of them were to be simulated and constructed. Once the radar is ready for trials, the signal processing will hopefully show, in real-time, the bearing and range of the target. When trialling the system, determining the bearing accuracy and maximum operating range will be vital features, for comparison to existing systems. Operating the radar with the similar characteristics with existing systems will give it similar features, such as range resolution. How the bearing deviates from the expected value could indicate systematic error, the aim here would be to remove any systematic error, hence, establishing that any range and/or bearing errors are due to environmental factors.

Aiming to design the parts of the system such that they can be easily assembled is essential on trials, ensuring the maximum amount of data collection. Whilst planning trials, designing experiments and any supporting structures which allow repeatable measurements are vital for the comparisons between different data sets. It is hoped that if this radar system operates well, then it could be retro-fitted to existing small and medium sized vessels. This project was funded by Guidance Microwave Ltd. in the hope that if the prototype was successful, then it could be carried forward into a production item and be part of their portfolio.

1.3 Novel Contributions

The main novel contributions this research has included the following:

- Development of a single-sided crossed-dipole antenna, this type of antenna has been discussed in literature previously, however for this project it was combined with a quadriphase feed network (see Chapter 5). The combination of antenna and feed were able to approximate a circular array and produce phase difference measurements, which were directly proportional to target bearing. The measured results helped to validate the antennas theorised behaviour.

- Clutter suppression using a frequency shifted active target, without the use of frequency shifting, the target would be undetectable at a range of 15 m for a backscatter co-efficient of 0.1 (see Chapter 5). By modulating the RF frequency within the target with a 6 kHz sinusoid, it was detected by the radar to a range of 125 m.

- Generation of range and bearing measurements, plotting them on a Cartesian coordinate system using an FMCW radar and crossed-dipole antenna. This antenna allowed the target bearing to be determined with no beam steering neither electronic nor mechanical. This was the main aim of the research and it was achieved with measurements in an open field and an urban office car park (see Chapter 6).

- Real-time signal acquisition and processing using a sound card. The card was used to acquire both analogue baseband signals from its line-in input. With little calibration and the use of MATLAB, both acquiring and processing the time-domain signal was implemented in real-time.

1.4 Thesis Organisation

The content in this thesis is broken down into seven chapters, firstly the introduction. The next chapter discusses the relevant theory required for this PhD, with the inclusion of radar theory mainly focusing on FMCW radar. This chapter also discusses antenna theory, initially a general overview and then in greater detail circular array antenna, finishing off with some methods of feeding such antenna.

Chapter 3 reviews the relevant literature for this project. It begins with how navigation at sea currently occurs, it goes on to discuss the role of transponders in marine and other applications. Then FMCW radar literature is analysed with how current systems are designed. This radar system measures both range and bearing. How other radar systems are able to measure

the same two target features are considered, this chapter ends with a small overview of how sea clutter can affect the received signal and the evolution of circular arrays.

The fourth chapter analyses the receive antenna, the outline of the project had as one of its requirements, a circular array. It discusses the arrays design based on simulation of different types of antenna and feed networks which required careful consideration. With the use of relevant equations and practical constraints, this chapter shows why the crossed-dipole antenna was the correct choice.

The majority of the time spent on this work went into designing and constructing the radar system, the steps taken to build this radar are discussed in Chapter 5. It begins with the radar antenna, both the receive based on the crossed-dipole with differing feeds both balun and quadriphase. Then the transmit, initially, a small ground plane monopole then the conical ground plane monopole antenna. The radar construction itself is broken down into two parts, firstly, the transmit chain including the super-Nyquist mode signal generation from the DDS. Secondly, the receive chain, which includes the link budget and receiver noise figure. This chapter goes on to detail the design and construction of the active target, comprising of the antennas developed for the final target and clutter considerations. The frequency shift within the target caused an update to the baseband filter which is also discussed. The chapter ends with an overview of the other hardware constructed, such as power supplies.

Chapter 6 analyses the data obtained with the radar, beginning with pre-processing the acquired raw time domain data. The radar was taken to two trial sites, an open field in Shenley, Watford and Guidance Microwave office in Hitchin. The collected data at both of these locations is discussed and analysed in this chapter.

The final chapter, Chapter 7 discussed the conclusions of this project and the relevance of the data obtained with the radar system. It goes on to convey the next steps needed to be taken to realise the full potential of this system. The implementation of some of these upgrades on subsequent versions, such as target coding are discussed.

There are four appendices after the conclusion. These show: proof of continual circular array far-field radiation pattern in terms of the pattern function. The simulated feed network for the 9.25 GHz circular array. An attempt to clutter suppression/removal at low frequencies, such that an unmodulated target could be detected in the lab. Finally, some results obtained in Hitchin, with an elevated target and the effect of absorber on bearing accuracy.

Chapter 2

Background Theory

This chapter forms the theoretical knowledge needed for the rest of the thesis. It introduces the relevant radar theory tailored towards the use of active targets within radar systems and emphasising FMCW radar. Antenna theory although extensive will be narrowed to focus on theory that was valid for this project, particularly radiation patterns, feed networks and antenna gain. Finally, it will also cover antennas arranged in circular array configuration, and the method of appropriately phasing the elements. The vast amount of radar theory is quite well established going back as early as 1904, however, the design of FMCW systems are tailored for their own particular application. The backbones of typical systems are quite similar and better understood by reading peer reviewed papers, which are covered in Chapter 3. The majority of the theory in this chapter is based on [5], [6], [7] and [8], with [8] having a particularly good chapter for the understanding of circular arrays.

2.1 Radar Theory

Radar systems operate by using the transmission from a radar sensor to emit and direct electromagnetic radiation, in the form of a radio wave. The transmitted signal, usually in pulse form propagates through a medium (usually air) and the reflected radiation is collected by a receiving antenna, containing information regarding some of the target's properties. This information includes the targets distance from the radar, by determining the time taken for the transmitted signal to be reflected off the target and intercepted by the receiver. The target's velocity is calculated by measuring the Doppler shift of the echo. Finally, by using the directivity of the antenna beam, the direction of arrival, i.e. the bearing of the target can also be indicated.

2.1.1 Range Resolution and Maximum Unambiguous Range

The range resolution of a radar system is the minimum distance that two targets are separated in order to be individually identified. However, the radar range must first be established. This can be determined by a two way propagation delay that an EM wave experiences, from when it

is expelled from the radar transmitter, reflected from a target and received by the radar:

$$\tau = \frac{2r}{c} \tag{2.1}$$

Which can be rearranged to calculate, r, range (m), the term c, is the speed of light in a vacuum and is given by the value, 3 x 10^8 ms^{-1}, (this will be true for where c is used through thesis unless otherwise stated). In terms of a pulsed radar system, the radars range resolution, is the minimum separation two targets at the same bearing can be independently verified as two targets. The separation in time for the echoes from two independent targets would have to be:

$$T = \frac{2(r + \Delta r)}{c} - \frac{2r}{c} = \frac{2\Delta r}{c} \tag{2.2}$$

Due to the pulse travelling two ways, Δr, the minimum range resolution, is proportional to one half of the pulse length, T, measured in seconds. The range resolution can also be thought of in terms of the pulse bandwidth, B. One definition for B, with regards to a non-modulated signal, is the smallest positive frequency at which the power spectral density is zero. By considering a rectangular pulse in the time domain, the first positive zero value in the frequency domain would be at $1/T$ and the -3 dB bandwidth is $1/T$, at an magnitude of $2T/\pi$ (V/Hz), both are shown in Figure 2.1. Also shown is the normalised energy spectral density, this illustrates how the energy is distributed across the frequency band and is obtained by squaring the magnitude spectrum. The range resolution can then be written in terms of the pulse bandwidth, B, which can be exploited in FM radar systems (see section 2.3) to improve the range resolution:

$$\Delta r = \frac{c}{2B} \tag{2.3}$$

For a simple pulsed radar system, pulses are transmitted at a regular rate, the *Pulse Repetition Frequency* (PRF), is vital for determining the maximum unambiguous range, r_u. Target ambiguities occur when a pulse is transmitted and a targets echo arrives after the transmission of the next pulse. Hence, the target cannot be unambiguously associated with the original pulse, causing a range ambiguity. The maximum unambiguous range can be expressed as:

$$r_u = \frac{c}{2PRF} \tag{2.4}$$

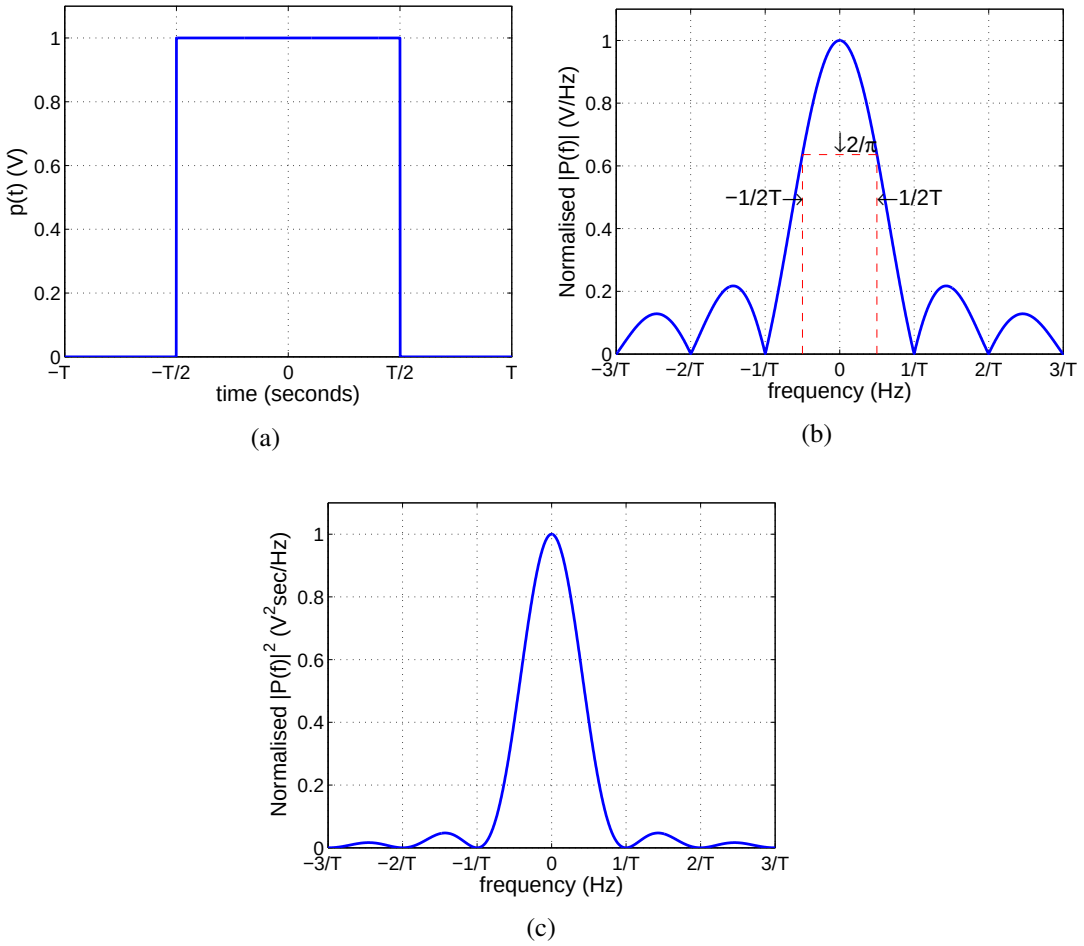

(a) (b)

(c)

Figure 2.1: (a) Time (b) frequency domain representation of a rectangular pulse (c) normalised energy spectral density of a single rectangular pulse

2.1.2 Radar Equation

The radar equation takes into account the range, the operating frequency of the radar and combines them along with the hardware parameters associated with the antennas, amplifiers and other RF hardware components. This leads to the specific applications that can be carried out with any given radar, the basic theory will remain the same. However, a single radar system will only be optimised for any one application. As mentioned previously, the signal travels to the target and back to the receiver so there is a two-way propagation. The propagation is through a lossy medium and the signal spreads in a spherical manner, to and from the target. By setting the maximum range required for the system, the minimum signal needed to be detected can be calculated, the general relationship between the signal power to a point target and range is now shown [5]:

$$P_r = \frac{P_t G_t G_r \lambda_o^2 \sigma}{(4\pi)^3 r^4} \tag{2.5}$$

where P_t, is the transmit power (W) (for pulsed radar systems, the average transmitted power rather than the peak transmitted power would be used), G_t, is the gain of the transmit antenna, G_r, is the gain of the receive antenna, λ_o, is the operating wavelength of the radar (m), σ, is the Radar Cross Section (RCS) of the target (m^2) and r, is the distance (range) between the radar antennas and the target (m).

Equation (2.5) holds when both transmit and receive antennas are co-located (monostatic radar configuration), or separated by a very small distance when in relation to maximum operating distance of the radar. The majority of parameters in equation (2.5) are set and optimised by the radar engineer, with the exception of the RCS of the target, but even this is only restricted to passive targets. If the target was active they too could be designed and optimised. Although the engineer can choose the gain of the antenna, restrictions such as maximum range, operating frequency and intensity of transmitted power are set by regulatory committees, some of the boundaries are highlighted in [9]. In some radars, the transmitted and received radar signals go via a single antenna, the antenna is cycled in turn by a duplexer whether it is receiving or transmitting. However, in most cases for a FMCW radar the transmitter and receiver will have two separate antennas.

Generally for most radar systems, equation (2.5) is sufficient to calculate the power received from a point target at range, r. For systems used in conjunction with active targets as in this project, modifications to equation (2.5) are required. Firstly, by taking a step back and considering the Friis transmission equation, which is usually used to measure the power received by an antenna some distance away from a transmitting antenna. This equation is used in communication links and in Radar Warning Receiver (RWR) systems. The range measuring the distance to a point target in equation (2.5) now measures the distance between the transmit and receive antennas. The Friis transmission equation is now shown [10]:

$$P_r = \frac{P_t G_t G_r \lambda_o^2}{(4\pi r)^2} \tag{2.6}$$

where the parameters of the radar are the same as those in equation (2.5), except for, r, as described previously.

In a radar system where an active target is employed as point target, the power received, $P_{r,tar}$, by the active targets receiving antenna aperture A_e, is:

$$P_{r,tar} = \frac{P_t G_t}{(4\pi) r^2} \cdot A_e \tag{2.7}$$

where, A_e, the antenna aperture is related to the antennas gain by the following:

$$A_e = \frac{G_{tar}\lambda_o^2}{(4\pi)} \tag{2.8}$$

substituting equation (2.8) into (2.7) the following can be written:

$$P_{r,tar} = \frac{P_t G_t G_{tar} \lambda_o^2}{(4\pi r)^2} \tag{2.9}$$

(*note. equations (2.9) and (2.6) are identical)

The active targets amplifier, G_{amp}, amplifies the signal before the targets transmit antenna re-radiates the signal, the power received by the radars receive antenna, is:

$$\begin{aligned} P_{t,tar} &= P_{r,tar} \cdot G_{amp} \\ P_r &= \frac{P_{t,tar} G_{tar}}{(4\pi) r^2} \cdot A_e \\ &= \frac{P_t G_t G_r G_{tar}^2 G_{amp} \lambda_o^4}{(4\pi r)^4} \end{aligned} \tag{2.10}$$

At first glance equations (2.10) and (2.5) appear identical, but, in an active target radar systems there are extra $1/4\pi$ and λ_o^2 (for S and X band radars $\lambda \ll 1$) terms in equation (2.10) and no σ (σ values can vary from 10^{-5} for insects to 5000 for 1000 ton frigates). Hence, the power received from an active target system could be less than from an equivalent point target system. However, as the target has amplification, with the correct level of amplification, the received power, for the same range can be greater than a point target system.

When considering the power received from a target, be it point or active, the ability of the radar to detect a low power from great distances must too be considered. The limitation of a radar system is the noise energy contained within the detection bandwidth, B_n. The noise bandwidth is usually approximated as the half-power bandwidth, which is defined as the bandwidth at which the power is reduced to 0.5 of the maximum (-3 dB in power) [5]. Noise can be acquired externally via the receive antenna or generated internally by the receiving hardware, the total noise power is the summation between the environmental noise and the receiver noise:

$$P_n = kT_o B_n + kT_s B_n \tag{2.11}$$

where, k, is Boltzmann's constant, T_o, is the noise reference temperature, B_n, is the operating bandwidth and T_s is the receiver noise temperature. Equation (2.11) can be simplified by using

the term, 'noise figure' F_n, which is defined as:

$$F_n = \frac{SNR|_{input}}{SNR|_{output}} = \frac{\frac{P_s}{kT_0B_n}}{\frac{P_s}{kT_0B_n+kT_sB_n}} = 1 + \frac{T_s}{T_0} \tag{2.12}$$

$\therefore$

$$P_n = kT_0B_nF_n \tag{2.13}$$

The ratio between the received power, P_r (equation (2.10)), and the noise power, P_n (equation (2.13)), can now be taken, thus calculating the minimum signal-to-noise ratio (SNR) at maximum range:

$$SNR|_{min} = \frac{P_r}{P_n} = \frac{P_tG_tG_rG_{tar}^2G_{amp}\lambda_o^4LF^4}{(4\pi r_{max})^4kT_0B_nF_n} \tag{2.14}$$

The term, L, is the amalgamation of the various losses, including, beamshape losses, atmospheric losses etc... (as L is in the numerator in equation (2.14) it is assumed that $L \leq 1$). The other new term is F^4, this is the pattern propagation factor. This is used to take into account the path loss, multipath, ground reflections etc... experienced by the pulse. By altering the phases of the measured signal, which can cause extra gain or attenuation depending on the type of interference, constructive or destructive and incorrect measured distances. Usually for the more simpler link budget calculations it can be assumed that both $L = 1$ and $F^4 = 1$.

2.2 Doppler Radar

Doppler radar can be broken down into two sections, Continuous Wave (CW) and Pulsed Doppler (PD), the main distinction as the name suggests is how long the radar pulse is on the 'on' state. With current navigation at sea applications focusing on PD systems, unmodulated CW has had less involvement in maritime navigation, but as section 2.3 shows there are navigation applications where modulated CW can be of great benefit, hence follows a brief overview of unmodulated CW. Doppler radars can be used in Moving Target Indication (MTI) applications detecting moving targets in clutter situations.

2.2.1 CW Doppler Radar

Where the theory in 2.1 focuses on pulsed systems. This section describes a simpler system, one which has no modulation nor pulsing, but that is continually on will now be discussed. The Continuous Wave (CW) radar system is as the name suggests continually transmitting and receiving. The transmitted signal will be very strong in relation to the received echo, therefore

to minimise the transmitted energy coupling directly into the receiver separate antennas may be employed for the transmitter and receiver. If their spatial separation is sufficient it will provide enough isolation to minimise the coupling between the antennas. There are many advantages of such a system, firstly, the cost of manufacturing and operating, secondly there is no minimum or maximum range. However, practically the transmitted energy will be limited, restricting the maximum detectable range.

CW radar uses the Doppler effect to separate the transmitted and the Doppler shifted echo, this however does restrict it to the detection of moving targets and not of stationary and slow moving objects. The Doppler shift can be created by a moving target, stationary radar or vice versa and also by both radar and target movements. As a target approaches a Doppler radar, the transmitted signal travels a shorter distance, hence, the received phase of the signal varies with time. As the targets velocity increases, the rate of change phase increases, therefore the rate of change of received phase can give an indication to the relative velocity of the target to the radar.

Due to the relationship between the Doppler shift and the target velocity, consider a target at range, r, from a co-located transmitter and receiver, the received signal travels a distance of $2r$. The wavelength of a transmitted signal is, λ_o. The ratio of covered distance and the wavelength, multiplied by the number of full phase cycles, 2π, indicates the phase of the received signal relative to the transmitted:

$$\phi = \frac{2r \cdot 2\pi}{\lambda_o} \tag{2.15}$$

the moving targets radial velocity is given by:

$$v_r = \frac{\mathrm{d}r}{\mathrm{d}t} \tag{2.16}$$

As the target approaches the radar, its distance decreases and the rate of change of phase of the received signal increases, as discussed previously. Thus requiring a negative sign in the relationship, this has the effect of also conforming to standard radar convention, therefore the following can be written:

$$\frac{\mathrm{d}\phi}{\mathrm{d}t} = -\frac{4\pi}{\lambda_o}\frac{\mathrm{d}r}{\mathrm{d}t} \tag{2.17}$$

substituting equation (2.16) into equation (2.17), the angular Doppler shift can be written be-

cause rate of change of phase is the definition of frequency:

$$\frac{\mathrm{d}\phi}{\mathrm{d}t} = \omega_D = -\frac{4\pi v_r}{\lambda_o} \tag{2.18}$$

the Doppler frequency shift, f_D (Hz), can now be written in terms of the transmitted frequency, f_o:

$$f_D = \frac{\omega_D}{2\pi} = -\frac{2v_r}{\lambda_o} = -\frac{2v_r f_o}{c} \tag{2.19}$$

A simple unmodulated CW radar system can be made from a few components. A signal generator operating at the desired frequency would be an ideal signal source and quick implementation. This signal is transmitted via the transmitting antenna and if a moving target is detected, a Doppler shifted echo would be superimposed on the transmitted signal. If the target was moving toward the radar then a positive Doppler shift, or if it was moving away, then a negative Doppler shift. A frequency mixer would then take the received signal and mix it with a portion of the transmitted signal, f_o, outputting just the Doppler frequency, f_D. This is then passed to a Doppler filter, in its most simplest form, a bandpass pass filter rejecting all higher frequencies beyond the maximum Doppler frequency. Also removing the DC component and some of the lower frequency components, where all the stationary and slow moving objects (clutter) would be spectrally located. Although not shown in Figure 2.2 a Doppler amplifier may also be used to amplify the weak returned signal in order for it to be detected by the signal processing hardware. The only unknown in equation (2.19) is the targets' velocity, which can be determined by evaluating this equation, as the rest of the terms are constants or measurable quantities.

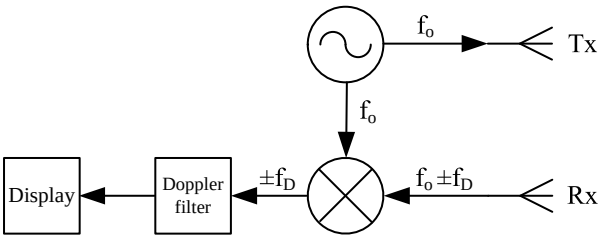

Figure 2.2: Simple CW radar system block diagram

2.2.2 Pulsed Doppler Radar

Although Pulsed Doppler (PD) radar system was not implemented for this project, many other navigation at sea radar systems are PD, therefore their use and implementation will be discussed in brief. The use of PD systems in navigation at sea applications is to remove the sea clutter that can affect the target detection ability of a radar system. Using the PD technique also allows the measurement of target range, something that is not possible with its CW counterpart. PD radars require more hardware than CW radars, but as the transmitter and receiver are not being operated continually, a single antenna can be used for both transmit and receive. CW radars can too operate with a single antenna but usual operation is with two antennas as stated previously. Another hardware difference is the inclusion of a high power amplifier for the generation of a high power transmission, in the order of 100's of watts of peak power a large klystron or magnetron is needed.

PD radar systems also differ from pulsed radars in terms of hardware, where a simple pulsed radar would not have a need for any portion or version of the transmitted waveform. The PD radar requires a version of the transmitted waveform that has not been modulated i.e a 'coherent reference' [5]. This is so that the transmitted signals phase is preserved in the reference signal, and with the use of Doppler filters the Doppler frequency can be detected. Doppler filters banks are usually implemented, containing a set of bandpass filters where a detected target can be separated in frequency from the surrounding clutter. Delay line filters could also be used to remove clutter, both are possible implementations for MTI applications.

Blind speeds are also a problem for MTI radars as they could mask moving targets as clutter. Blind speeds occur if the targets Doppler shift is equal to the PRF of the waveform. Hence, the Doppler sampling occurs at the same point and could be cancelled in the Doppler filters as zero Doppler clutter. Methods to resolve the blind speed problem include operating with more than one PRF, or constantly changing the transmitting frequency.

The equations derived for the CW radar require slight modification for a PD radar. Where previously the transmitted frequency was, f_o, it is now represented as $A_t \sin(2\pi f_o t)$. Where A_t is the transmitted signals' amplitude, the received signal is now $A_r \sin[2\pi f_o(t-\tau)]$ where A_r is the received signals amplitude, τ is as described in equation (2.1). A target moving toward the radar, r, can be re-written as $r(t) = r_0 - v_r t$ (the sign inverts for targets moving away from the radar). Where v_r is again the radial velocity but assumed constant, hence, the received signal, V_r can be expressed as:

$$V_r = A_r \sin\left[2\pi f_o\left(1 + \frac{2v_r}{c}\right)t - \frac{4\pi f_o r_0}{c}\right] \tag{2.20}$$

The received signal varies with the Doppler frequency, f_D, as ($f_D = 2f_o v_r/c$) as shown in equation (2.19), mixing (hetrodyning) the received signal with a portion of the transmitted, reveals the difference frequency and can be written as:

$$V_d = A_d \cos\left(2\pi f_D t - \frac{4\pi f_o r_0}{c}\right) \tag{2.21}$$

The hetrodyning process causes the sin to be replaced by cos, stationary targets are located at $f_D = 0$ and the output signal is constant. The clutter amplitude can be $+/-$ due to the cosine varying from $+1$ to -1. Moving targets will have a Doppler shift which can then be passed through to the display or for further signal processing whilst the zero Doppler clutter will be rejected.

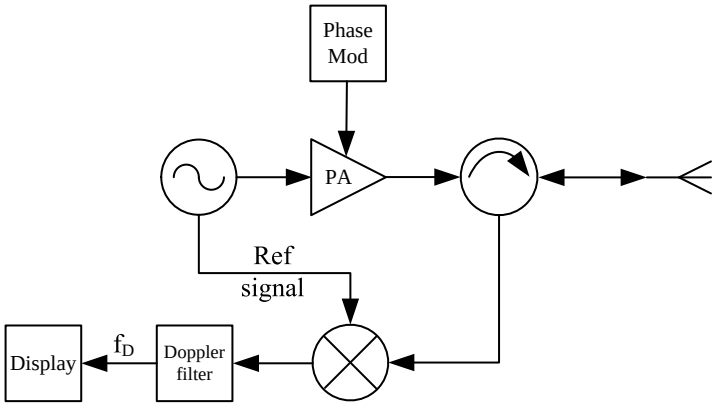

Figure 2.3: Simple PD radar system block diagram

2.3 FMCW Radar

Previously CW radars have been discussed in section 2.2.1. One glaring disadvantage of CW radars is the inability to measure range. This is due to the lack of timing mark indicating the start of pulse, the round trip time of the signal cannot be determined. It is possible with PD radars, however, the high peak power can cause strains on the rest of the radar hardware. Modulating the continuous wave in terms of frequency or phase would allow for the presence of a timing mark and the ability to measure the range. Frequency Modulated Continuous Wave (FMCW) radars, allow for low transmit power and the measurement of range. However, the key benefit of FMCW, or indeed any pulse compression radar, is that it breaks the compromise between operating range and resolution. The range detection is achieved by modulating a frequency sweep also known as a frequency 'chirp', to a continuous transmitting signal. When the echo

from the target is received, it can be compared to the transmitted signal, and the difference between the two signals indicates the range. In essence, the FMCW radar provides the features to a continuous wave i.e. a wave with a 100% duty cycle as PD system provides to a pulsed radar system.

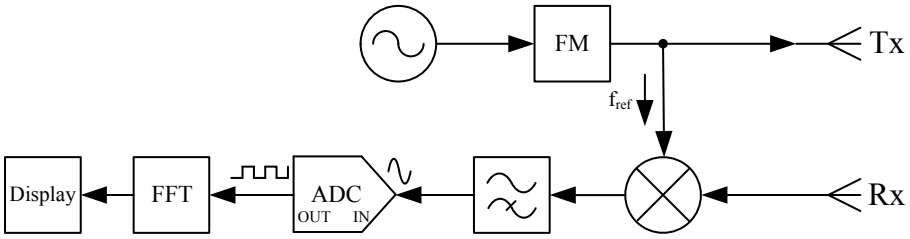

Figure 2.4: Simple FMCW radar system block diagram

2.3.1 FM Signal Analysis

Chirps signals are widely used in FMCW they are simply a linear variation in frequency over a sweep bandwidth, B, over a pulse duration, T [11]. The mathematical representation of a chirp is given by the equation:

$$f(t) = f_0 + \alpha t, \qquad 0 \leq t \leq T \tag{2.22}$$

where, f_0, is the initial frequency ($f_0 = f_o - \frac{B}{2}$), is the operating frequency minus half the bandwidth, B and α is the increase of frequency rate i.e the 'chirp rate' and is defined as $\alpha = \frac{B}{T}$. The phase of the linear chirp is the integral of the frequency:

$$\phi(t) = \phi_0 + 2\pi \int_0^t f(t)\,\mathrm{d}t = \phi_0 + 2\pi \int_0^t (f_0 + \alpha t)\,\mathrm{d}t = \phi_0 + 2\pi \left(f_0 t + \frac{\alpha t^2}{2} \right) \tag{2.23}$$

where, ϕ_0, is the initial phase at time, $t = 0$, assuming that $\phi_0 = 0$, equation (2.23) simplifies to:

$$\phi(t) = 2\pi \left(f_0 t + \frac{\alpha t^2}{2} \right) \tag{2.24}$$

The complex linear frequency modulated signal, with constant amplitude, s_o over time [12], can then be expressed as:

$$s(t) = s_o e^{j\phi(t)} = s_o e^{2\pi j \left(f_0 t + \frac{\alpha t^2}{2} \right)} \tag{2.25}$$

An FMCW radar pulse in its most simplest form is a constant amplitude signal, where a continuous generated frequency has frequency modulated upon it. The modulated frequency is a linear sawtooth variation in frequency with time, as seen in Figure 2.5. The returned echo contains a version of the transmitted signal delayed by a time, τ. The mathematical analysis is described in [13] and will be reproduced here. Firstly, the instantaneous amplitude of the transmitted linear chirp signal is:

$$x(t) = x_o \sin 2\pi \left(f_0 t + \frac{\alpha t^2}{2} \right) \tag{2.26}$$

The received echo as described before and has the form:

$$y(t) = y_o \sin 2\pi \left(f_0 (t - \tau) + \frac{\alpha (t - \tau)^2}{2} \right) \tag{2.27}$$

Usually, $y_o \leq x_o$, because the signal will be attenuated as it travels through the medium. As seen in Figure 2.4, the received signal is again multiplied with a replica of the transmitted signal, producing the Intermediate Frequency (IF) signal, in a process known as deramping:

$$z(t) = x(t).y(t) = z_o \cos 2\pi \left(f_0 \tau + \alpha \tau t - \frac{\alpha \tau^2}{2} \right) \tag{2.28}$$

The above result is from using the trigonometric product-to-sum identities and filtering the two frequency products (sum and difference) produced in the mixing process and rejecting the former and allowing through the latter (low pass filtering) [14]. The $\alpha \tau t$ term in equation (2.28), is the instantaneous frequency difference which is known as the beat frequency and can be thought of as converting the time delay into the frequency domain [15]. With the use of spectral processing, such as a Fast Fourier Transform (FFT), the beat frequency can be recovered.

$$f_{beat} = \alpha \tau = \frac{2Br}{Tc} \tag{2.29}$$

In Figure 2.5 the lower beat frequency, f_{b0}, can be measured and equation (2.29) rearranged to determine the target range, r. The upper, f_{b1}, is due to the overlap between the transmitted and received signals. Usually the time overlap is quite small as the chirp duration is much longer than the time of flight, $T \gg \tau$.

The derivation for a stationary target has been previously shown, but with some modifications a moving target scenario can be envisaged. If the target is moving as previously discussed for PD and CW radar systems, there will be a Doppler shift associated with the received sig-

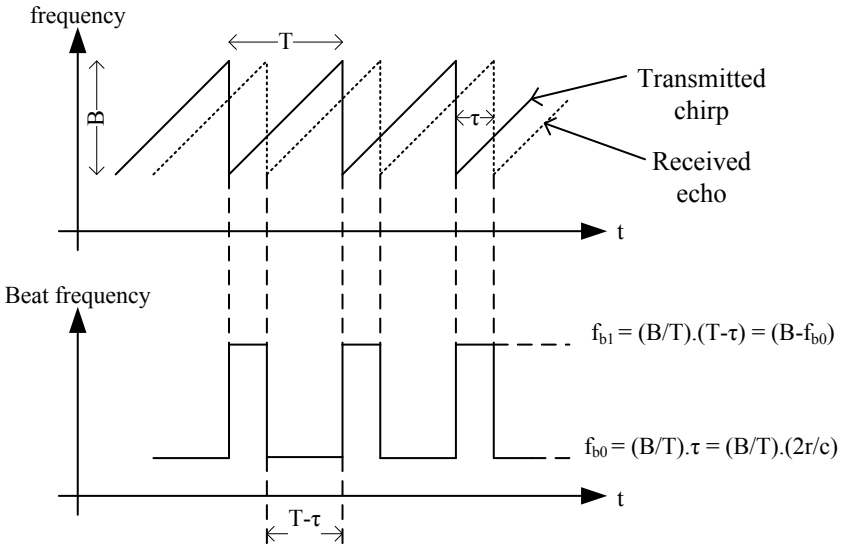

Figure 2.5: A sawtooth frequency variation FMCW signal with time and its time delayed echo (top), the resulting beat frequencies after deramping (bottom).

nal causing erroneous range measurements. Chapter 5 will provide more details as to why for this project the static target scenario was the correct interpretation and the sawtooth waveform was implemented. Should this system be adapted for a moving target scenario, then triangular modulation over sawtooth would be an option to resolve the introduced Doppler shift.

The method in which the Doppler shift is resolved, for a single moving target, with triangular modulation will now be mathematically discussed. A moving target, with radial velocity, v_r, will have a range which varies with time and can be expressed as:

$$r(t) = r_0 + v_r t \tag{2.30}$$

hence, the time taken for the retuned echo is:

$$\tau = \frac{2r(t)}{c} = \frac{2(r_0 + v_r t)}{c} \tag{2.31}$$

Substituting equation (2.31) into equation (2.28) the following IF signal can be obtained:

$$z(t) = z_0 \cos 2\pi \left[\frac{2\alpha r_0 t}{c}\left(1 - \frac{2v_r}{c}\right) + \frac{2f_0 v_r t}{c} + \frac{2\alpha v_r t^2}{c}\left(1 - \frac{v_r}{c}\right) + \frac{2r_0}{c}\left(f_0 - \frac{\alpha r_0}{c}\right)\right] \tag{2.32}$$

The first term in equation (2.32) is proportional to the range of the target, also known as the range beat, the second term is the Doppler shift, which can be measured. The third term is the

cross-term which can be interpreted in two ways, either the chirp on the range beat because of the changing range or the chirp on the Doppler frequency due to the varying transmitted signal's frequency. The fourth term is non-time varying component of constant phase.

Equation (2.32) shows that the frequency of the echo sweep will be offset by the Doppler shift, which corresponds to a time delay error:

$$t_{err} = \frac{f_D}{\alpha} = \frac{T f_D}{B} \tag{2.33}$$

This can be interpreted as a range error using equation (2.3):

$$r_{err} = \frac{c t_{err}}{2} = \frac{cT f_D}{2B} \tag{2.34}$$

By using triangular modulation the errors shown in equations (2.33) and (2.34) can be resolved. Figure 2.6b shows the effects of a moving target on the beat frequency. The two resulting beat frequencies can be measured and the errors removed. The sum and difference of f_{b0} and f_{b1},

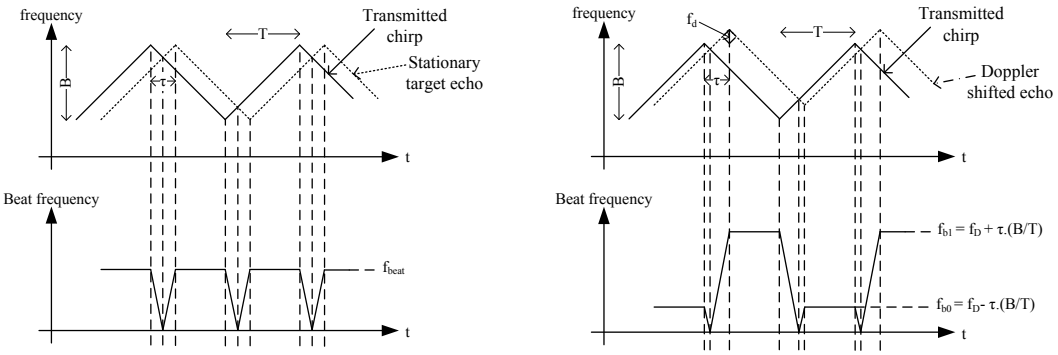

(a) (b)

Figure 2.6: The transmitted triangular waveform and received echo from (a) stationary target (b) moving target, both showing the sweep and beat frequency varying with time

shown in Figure 2.6b contains both the Doppler frequency and the beat frequency. Hence, the target range can be determined by rearranging equation (2.36):

$$\frac{f_{b1} + f_{b0}}{2} = f_D \tag{2.35}$$

$$\frac{f_{b1} - f_{b0}}{2} = f_{beat} = \frac{2Br}{Tc} \tag{2.36}$$

The various radar equations mentioned have limits on the maximum range and have many parameters that govern the said range. However, the IF signal will have to be sampled in order

for processing. Hence, the acquisition hardware too sets a maximum range that can be detected, not in terms of amplitude, although this can also limit the performance, but in sampling frequency. The Nyquist criterion must be met to avoid aliasing of the signal and in terms of FMCW signal processing, it states that the maximum beat frequency must be equal or less than half the sampling frequency of the acquisition unit [16].

$$f_{beat}|_{max} = \frac{f_s}{2} = \frac{2Br_{max}}{Tc} \tag{2.37}$$

The choice of sampling frequency, hence, maximum range, r_{max}, does put a constraint on the chirp duration, T. It must also satisfy the requirement that it is longer than the time of flight, τ. Such that the range resolution after deramping is conserved. This therefore allows equation (2.3) to be rewritten to include this requirement:

$$\Delta r = \frac{c}{2B} \cdot \frac{T}{T - \tau} \tag{2.38}$$

The denominator, $T - \tau$, is the overlapped transmitted and received signals, depicted in Figure 2.5.

To generate the beat frequency, a replica of the transmitted signal is multiplied by the received signal, in Figure 2.4 depicted as f_{ref}. As this type of radar is continually transmitting and receiving, a similar problem exists as with unmodulated CW radar systems. The transmitted signal can couple directly into the receiver, processing the IF signal would show a strong target response equivalent to the distance between the transmitter and receiver. If the transmitter noise is quite high, this too could couple into the receiver increasing the receivers noise figure, hence, affecting the receiver sensitivity. The coupling could also damage the receiver hardware, even at modest power levels, the sidebands of the signal could result in hardware problems. Modelling the coupling as a high power target at close range is one option. However, this approach could mask potential targets at close range, usually FMCW radar systems for this reason have a minimum operating range. The easiest method to the minimise the coupling problem is to ensure that there is sufficient separation between the transmitter and receiver. Another, depending on the target specification, is to have different polarisations for the receive and transmit antenna.

2.3.2 Advantages of FMCW radar

Much focus thus far has been on FMCW radar, the benefits it has for this project will be continually emphasised as this thesis progresses. However, compared to other types of radar some

of the fundamental advantages will be discussed now.

As CW radar, FMCW has a 100 % duty cycle, therefore its energy is spread across the whole bandwidth and duration of the chirp. The beat frequency however is over smaller bandwidth, $1/T$, this gives rise to additional processing gain referred to the time-bandwidth product, BT [11]. The extra gain allows for a lower transmit power compared to unmodulated radar systems for the same range. Applying this additional gain to the SNR equation for an active target equation (2.14) and can now be written as:

$$SNR|_{min} = \frac{P_t G_t G_r G_{tar}^2 G_{amp} \lambda_o^4}{(4\pi r_{max})^4 k T_0 B_n F_n} \cdot BT = \frac{P_t G_t G_r G_{tar}^2 G_{amp} \lambda_o^4 T}{(4\pi r_{max})^4 k T_0 F_n} \tag{2.39}$$

with the assumption that the noise bandwidth, B_n, is approximately equal to the chirp bandwidth, B. Equation (2.39) also reveals a potential problem. If the chirp length, T, is too long it could cause high receiver power resulting in damage to hardware, although unlikely, it is worth bearing in mind.

Equation (2.38) shows that the range resolution is dependant not only on the chirp duration and time of flight but also the chirps bandwidth, B. Some FMCW radar systems have the ability to vary the chirp bandwidth from chirp to chirp, having the effect of varying the range resolution. Thus, the range resolution can be improved with little or no hardware modifications.

If the radar designer was to implement chirp to chirp bandwidth alterations for range resolution purposes, it would also have the added effect of making the radar resistant to Electronic Support Measure (ESM) systems. This is due to the impracticalities in matching the ESM receiver to the radar's sweep pattern [13]. Even without chirp to chirp bandwidth adjustments it would be quite difficult for a ESM receiver to match the chirps bandwidth and duration.

In Figure 2.4, the receiver chain has a high pass filter, but its purpose is to linearly increment the receiver gain with frequency. This allows the received signal amplitude roll off with range (frequency) to be managed in terms of the dynamic range of the ADC, which is considerably lower than without the filter. The gain for low frequencies would be minimal and usually unity, allowing no additional gain for direct coupled signals between the transmit and receive antenna. The linear relationship between the frequency and range is unique to FMCW radar systems over other modulated CW radar systems. It allows the reduction of the ADC's dynamic range, with just a simple high pass filter.

Generally FMCW systems cost less than its pulsed equivalent, usually the high power transmitter needed for pulsed systems is the most expensive component. The lack of which for FMCW radar makes it a cost effective solution. However, this does limit the maximum range

as there is a lower transmit power in FMCW radar, hence their use in short and medium range applications.

2.4 Antenna Theory

The previous discussion has all been focused on the different radar systems and their hardware, signal analysis and design equations. Recalling equation (2.39), the gain of the antennas involved with the radar systems are vital as are their radiation patterns and efficiency. The rest of the hardware could be perfect, but if the antennas are not designed carefully then the maximum range and/or bearing accuracy required will be severely degraded.

Antennas are defined as 'metallic device for radiating or receiving radio waves' [6]. They can be thought of as the structure that connects free space to the guiding device. They can take many forms, early (pre World War II) examples were in wire form. A major revolution in the early 1970's with the discovery of microstrip (patch) antennas have allowed lightweight, simple, cost-effective and conformal solutions. Single radiating elements have wide radiation patterns and low directivity, in order to tailor the radiation pattern and have highly directive antenna, the electrical length of the antenna needs to increase. The increase in size will have the desired effect but the consequential mechanical structure will be large and heavy, one solution is to use *arrays*. An array of single antenna elements can be thought of as a sampled large single antenna element, increasing directivity without the large single element. However, this comes at a cost as an electrical problem has replaced the mechanical, as the array requires a feed network, nevertheless, with current technology these complex feed structures are quite achievable. Arrays can be made up of a replicas of single antenna element for simplicity, but this is not a requirement. Arrays also have the added advantage of allowing the generation of virtually any type of radiation pattern, with the main radiation lobe controlled by the relative phase between the elements. The array beamwidth is also adjustable by controlling the amplitude excitation between elements, but a trade off must be made between the power in the main lobe and the side lobes, by windowing.

2.4.1 Angular Resolution

The range resolution of a radar system has been discussed in section 2.1.1 and does not depend on the antenna parameters, however, the angular resolution does. The angular resolution of the radar antenna is defined as the minimum angular separation that two equal targets at the same range can be uniquely identified. The point at which the antennas main lobe is above half power (or -3 dB point) defines the antennas angular resolution and can be applied in both azimuth ($\phi = 0°$) and elevation ($\phi = 90°$). The main lobe for an antenna is defined as the angular

beamwidth for which the power density is at its highest. For a single element the beamwidth of the antenna is largely dependent on its electrical dimensions, as previously discussed. The beamwidth can be determined by observing the power density across all angles azimuth and elevation. The azimuth and elevation beamwidths are dependent on the physical horizontal length, W, and vertical length, H, of the antenna respectively [17]:

$$\theta_{-3dB,az} \approx \frac{\lambda}{W} \tag{2.40}$$

$$\theta_{-3dB,el} \approx \frac{\lambda}{H} \tag{2.41}$$

From equations (2.40) and (2.41), the angular resolution at slant range, $\Delta r|_{az}$, can be determined and is shown for azimuth resolution in equation (2.42) and is also shown in Figure 2.7. This approximation is possible due to a narrow beamwidth being constant with range:

$$\Delta r|_{az} = r.\theta_{-3dB,az} \approx r \cdot \frac{\lambda}{W} \tag{2.42}$$

The same analysis can be applied to the angular resolution for the elevation beamwidth.

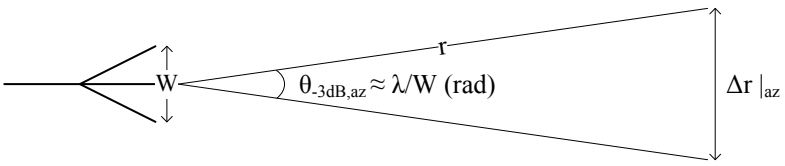

Figure 2.7: Azimuth angular resolution of an antenna

2.4.2 Far field Region

The far field region is where most antennas typically operate and determines its radiation pattern. In this region the radiation pattern does not vary with distance. The electric and magnetic fields in this region are orthogonal to one another and to the propagation direction. To safely be in the far field, three criteria must be met [18]:

- $r > 2W^2/\lambda$, where, W, is the principle largest dimension of the antenna
- $r \gg W$
- $r \gg \lambda$

The first two points are to ensure that the fields in the far field region act as plane waves, the third is to ensure that the reactive near field is cleared. In the reactive near field region, the E and H fields have a $1/r^2$ and $1/r^3$ decay with distance respectively, whereas in the far field the decay rate is $1/r$. The two closer regions, the reactive near field and the radiating near field still exist in the far field, but decay much more rapidly and have less influence in the far field. The majority of radar applications the reactive and radiating near field regions are very close, with respect to the maximum range and are usually ignored.

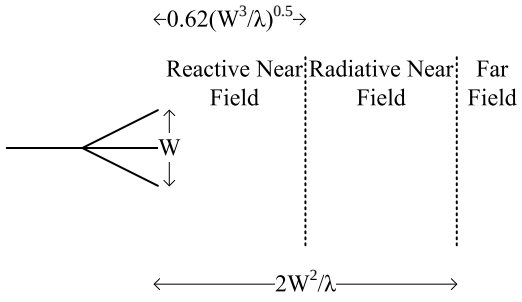

Figure 2.8: The field regions for antennas

2.4.3 Radiation Pattern and Directivity

The term radiation pattern is discussed frequently among antenna designers. It defines how the radiated power by the antenna variates, with distance, at different arrival angles in the far field, from the antenna. There are three main types of radiation pattern that are associated with antennas: isotropic, omnidirectional and directional. Isotropic antennas in the real world do not exist but are used as a reference point of other types of antenna, having an equal radiation pattern in all directions. The omnidirectional radiation pattern is realisable, it has an equal (isotropic) radiation pattern in one plane. Some examples include the dipole antenna and electrically small loop antenna. Finally is the directional antenna, with no symmetry in radiation pattern, they focus their radiation in a single peak and the majority of the radiated power travels in this direction. This gives rise to the term directivity which is the measure of the peak direction of the radiation pattern i.e. the main lobe. These are probably the most common type of antenna and can be found in dish antenna for satellite television.

The term directivity when applied to an antenna is the ratio of the radiation intensity to the average radiation intensity in all directions. The radiation intensity is the power radiated per

unit solid angle in the direction of peak power, mathematically can be written as:

$$D = \frac{1}{\frac{1}{4\pi}\int_0^{2\pi}\int_0^{\pi} |F(\theta,\phi)|^2 \sin\theta \mathrm{d}\theta\mathrm{d}\phi} \tag{2.43}$$

where, $F(\theta,\phi)$, is the antenna's normalised antenna pattern, in spherical coordinates.

This can be then be further simplified if the directivity is related to the antenna beamwidth. Firstly, if the beam solid angle, Ω_A, which is defined as the solid angle through which all power would flow if the antennas radiation efficiency is maximal and constant, was known, the directivity can be re-written as:

$$D = \frac{4\pi}{\Omega_A} \tag{2.44}$$

An approximation can be made for the beam solid angle in terms of its half power beamwidth for azimuth and elevation ($\theta_{-3dB,az}, \theta_{-3dB,el}$), provided the main lobe is narrow and with negligible side lobes:

$$D \approx \frac{4\pi}{\theta_{-3dB,az} \cdot \theta_{-3dB,el}} \tag{2.45}$$

2.4.4 Antenna Efficiency and Gain

The efficiency of an antenna is the total power radiated relative to the power delivered to the antenna. Not all the power delivered is radiated as some is absorbed within the antenna. The higher the efficiency the more power that is radiated away. Low efficiency antenna losses consist of conduction losses due to a finite conducting plane and dielectric losses due to conduction within the substrate as is the case with printed antenna. The other losses are due to the mismatch between the antenna and the feed, as some of the radiation is reflected back.

The gain of an antenna is relative to the gain of an isotropic antenna. Recalling that an isotropic antenna has an equal radiation pattern in all directions, the gain is measured in dBi. The gain, efficiency and the directivity are all related by the following equation:

$$G = \eta D \approx \frac{4\pi\eta}{\theta_{-3dB,az} \cdot \theta_{-3dB,el}} \tag{2.46}$$

where, G, is the gain in dBi, η, is the efficiency with values from 0 to 1 and, D, is the directivity as defined in equation 2.44.

2.4.5 Patch Antenna

Some of the most versatile antennas are patch antennas, sometimes referred to as the rectangular microstrip antenna. A patch can be designed on a Printed Circuit Board (PCB) and has number of different options that could be implemented for the feed such as insert feed or probe feed, with both having their own merits. For the latter arrangement, the removal of the feed line from the radiating surface allows for better isolation between the patch antenna and the feed line [19].

A single patch antenna has a gain of approximately 8 dBi [20], Figure 2.9 shows simulated gain of a single patch antenna with $\phi = 0°$ (Figure 2.9a) and $\phi = 90°$ (Figure 2.9b) of 8.7 dBi in both planes and beamwidths of 70° and 72.5° respectively. The ideal 8 dBi can be determined from the properties of a patch antenna. Firstly, as there is a ground plane the assumption is that all the radiation is in one hemisphere, thus introducing 3 dBs of directivity, whose efficiency depends on the size of the ground plane. The estimate for the size of the ground plane is that it should be approximately six times the thickness of the substrate added to the width and length of the patch [20]. Another 3 dB is introduced by visualising the radiating edges as two radiating slots above a ground plane. The final approximately 3 dBs of gain is from the gain of a typical slot which is between 2 and 3 dBs. Its simple construction method allows for different iterations with minute modifications to be fabricated and tested in a cost and time effective manner.

The patch antenna in its most basic form is a metallic 2-d shape over a ground plane, between these two pieces of metal, is a air cavity or substrate, which is why it can be designed on a PCB. The reason for the patch having the ability to radiate is from the fringing fields that are generated at the periphery of the patch, depicted in Figure 2.10.

The equations realising the dimensions of the patch antenna depend on the frequency of operation and the dielectric constant of the materials substrate. They are now shown using the proof as in [21] and [22]. Firstly, defining the width, W, of the patch, this is not as critical as the length, but for efficient radiation is given as:

$$W = \frac{c}{2f_c\sqrt{\frac{\varepsilon_r+1}{2}}} \tag{2.47}$$

where, c, is the speed of light in free space, f_c, is centre (resonant) frequency of the antenna and ε_r, is the dielectric constant of the material.

The fringing fields needed for the patch to resonate have the effect of increasing the length of the patch electrically. Thus, electrically it appears to be longer than it physically is, the extra

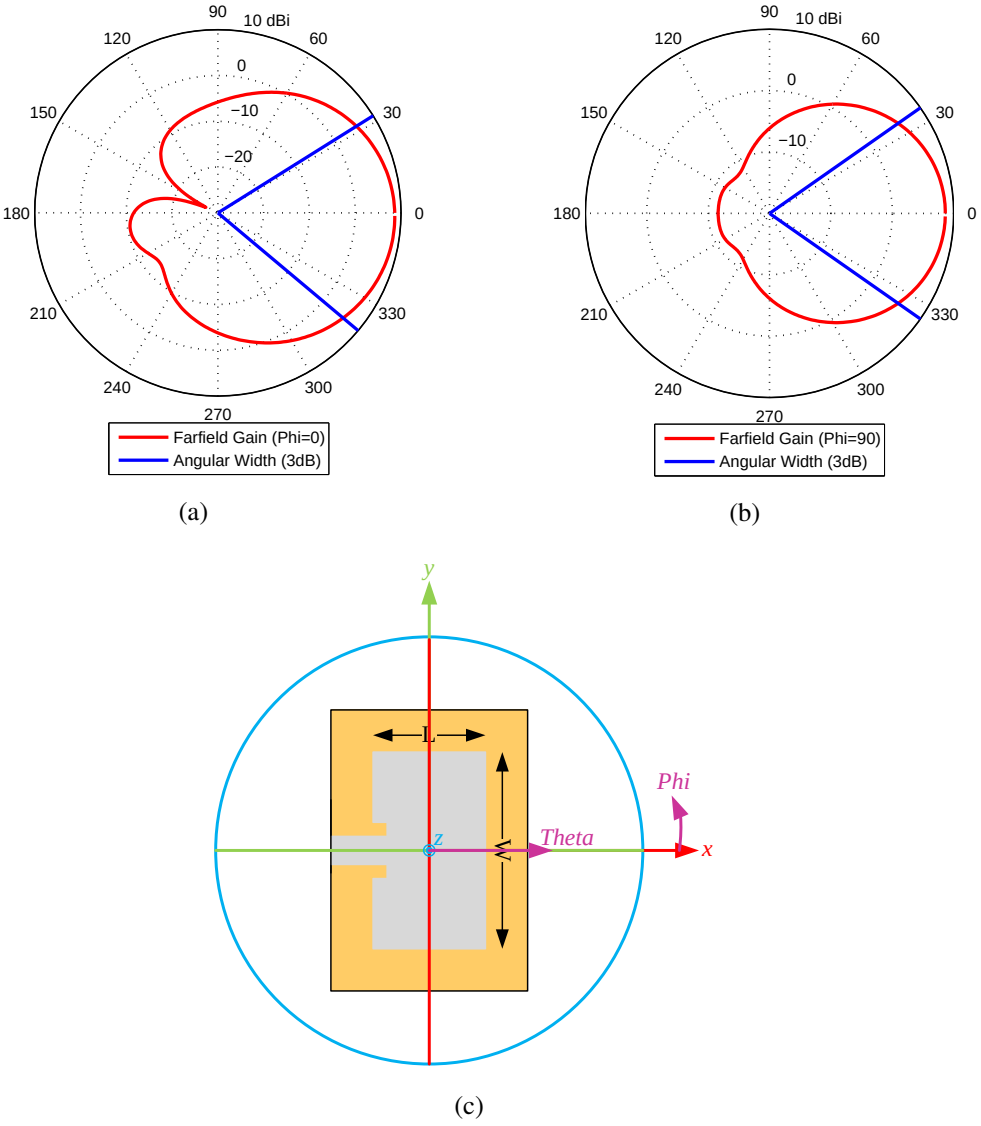

Figure 2.9: Simulated (a) $\phi = 0°$ and (b) $\phi = 90°$ (using the coordinate system defined in Figure 2.15) far field radiation pattern from a single inset fed patch antenna designed to operate at 9.25 GHz (c) orientation of the patch antenna that produced the far field patterns in (a) and (b), where L=7.11 mm and W=9.96 mm for an FR-4 substrate PCB (ε_r=4.3, h=1.6 mm)

length ΔL, is now shown:

$$\Delta L = 0.412h\left(\frac{(\varepsilon_{eff}+0.3)}{(\varepsilon_{eff}-0.258)}\cdot\frac{\left(\frac{W}{h}\right)+0.264}{\left(\frac{W}{h}\right)+0.8}\right) \tag{2.48}$$

where, h, is the height of the substrate (i.e. the substrate thickness) and, ε_{eff}, is the effective dielectric constant. This is required because the electric field line exist in both the air and the substrate, accounting for the fringing electric field and the electric field in the patch. The

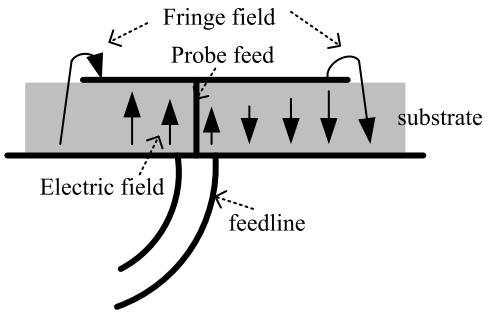

Figure 2.10: Probe fed patch antenna, with the fringing fields depicted [20]

calculation for which is shown below:

$$\varepsilon_{eff} = \frac{\varepsilon_r + 1}{2} \cdot \frac{\varepsilon_r - 1}{2} \cdot \left[1 + \frac{12h}{W}\right]^{-0.5} \tag{2.49}$$

From which the effective length of the patch can be determined:

$$L_{eff} = \frac{c}{2f_c\sqrt{\varepsilon_{eff}}} \tag{2.50}$$

Using equations (2.48) and (2.50) the actual length of the patch can be obtained by the following subtraction:

$$L = L_{eff} - 2\Delta L \tag{2.51}$$

The radiation of the patch antenna occurs due to the fringing fields as discussed previously. The field effectively extends the electrical length in both directions equally. Hence, the reason for a subtraction of twice the extra length, ΔL, from the effective length, L_{eff}.

The point at which the patch antenna is fed for a probe feed also varies according to the impedance required for the feed network. At the edge of the patch the impedance is approximately 200 Ω and at the centre it is 0 Ω. The equation for determining the location of the probe feed along the length of the patch is now shown [7]:

$$x = \frac{L}{\pi}\sin^{-1}\left(\frac{R_i}{R_e}\right)^{\frac{1}{2}} \tag{2.52}$$

where R_i, is the required input impedance and R_e, is the edge impedance of the patch.

For an inset feed the equation alters as the feed disturbs the transmission line model of the

antenna and increases the impedance variation with distance when compared to a probe feed. Again a formula is shown for the extent of the inset of the transmission line into the patch along the length of the patch [7]:

$$x = \frac{L}{\pi} \sin^{-1} \left(\frac{R_i}{R_e} \right)^{\frac{1}{4}} \tag{2.53}$$

Other points of note for the patch antennas are that they can have both vertical and horizontal polarisations. Where the polarisation refers to the direction of the electric field, which is dependent on the orientation of the antenna. Also circular polarisation is possible from a patch antenna, it can be achieved by feeding a single patch with two separate feeds, one with a 90° phase delay with respect to the other. This causes a rotation of the electric field along the propagation path, both clockwise and anticlockwise (right and left hand) polarisations are possible. The circular polarisation can be achieved with a single feed, if the patch is fed from the corner.

2.4.6 Dipole Antenna

Dipole antennas are one of the simplest antenna types [23] and their use as "rabbit antenna" for television makes them one of the most common. Consisting of two conductors, with wire or rods ideal conductors with each arm connected to a feed network.

Dipole antennas can be analysed in terms of a transmission line model. Consider a transmission line as depicted in Figure 2.11. Points **'a'** and **'b'** on the diagram are both open circuits, therefore the magnitude of the current is zero at that point. The current peak is at $\lambda/4$ and there is a null at $\lambda/2$, the sign of the current is in opposite directions in each half of the transmission line.

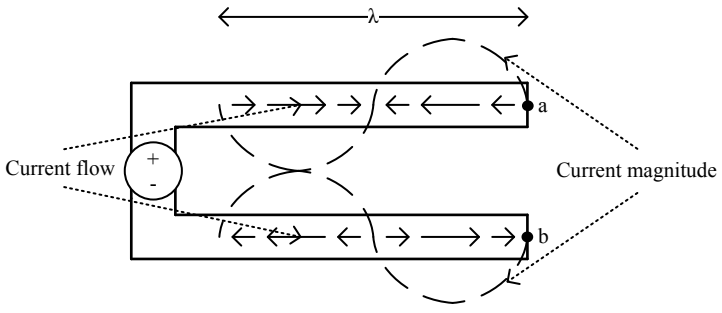

Figure 2.11: Current distribution along a transmission line

If the ends of the transmission line are bent as shown in Figure 2.12, such that the total

length of the transmission line is $\lambda/2$. The maximum current is at the centre of the half wave

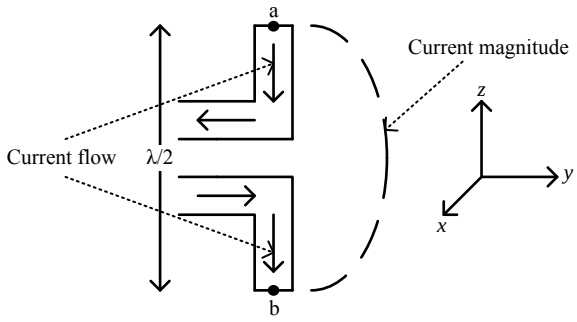

Figure 2.12: Dipole antenna depicted as bent transmission line, $\frac{\lambda}{2}$ in length, also known as the half wave dipole

dipole with points **'a'** and **'b'** still both open circuits. The maximum current occurs at the centre due to the flow of the current. In the conductors, the flow of current is in opposite directions. However, spatially the current is in the same direction, as both of these currents add in phase, the sum of currents results in a maximum at the centre of the two.

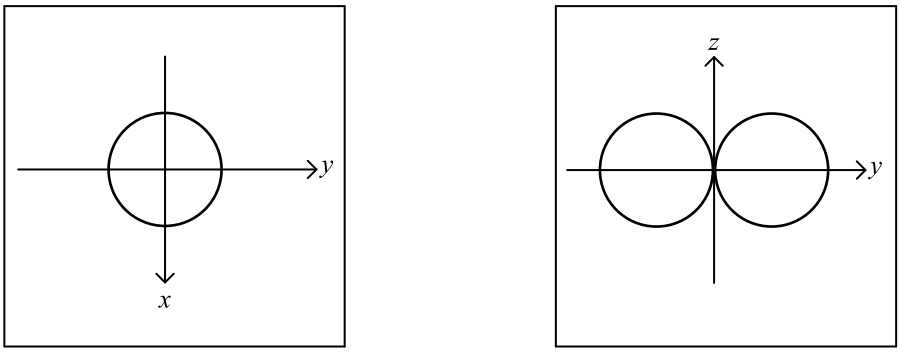

(a) (b)

Figure 2.13: Dipole antenna far field radiation pattern for (a) $\phi = 0°$ and (b) $\phi = 90°$

A single half-wave dipole antenna has a directivity of 1.64 and an isotropic gain of 2.15 dBi [24]. The radiation resistance of a centre fed half wave dipole is given by the well-known value Z=73+j42.5 Ω [24]. For the antenna to resonate the reactance needs to equal zero and this can be achieved by decreasing the length of the conductor, for a dipole length of 0.48 λ, the resistance drops to about 70 Ω. The bandwidth for this antenna is approximately 7%, slightly higher than a single standard patch antenna. For a short dipole (where $L \approx \lambda/10$), the half power beamwidth is 90° and the dipole has a gain of approximately 1.76 dBi. The half-wave dipole

has a reduced beamwidth of 78°, hence a more directive pattern and a slightly higher gain. Also note that the azimuth radiation pattern is omnidirectional, very different to the pattern generated by a single patch antenna, ideal for full 360° monitoring in a single plane.

The dipole has a feed network where the conductors are fed with balun. A *balun* is a device to connect a *bal*anced transmission line to an *un*balanced transmission line. The dipole is a balanced transmission line, the coax cable it connects to, is not. Therefore, a balun is needed between these two transmission lines. There are many different types baluns, the simplest to analyse is the sleeve (bazooka) balun. Essentially it is a short circuited sleeve that surrounds a $\lambda/4$ length section of coax that is connected to dipole.

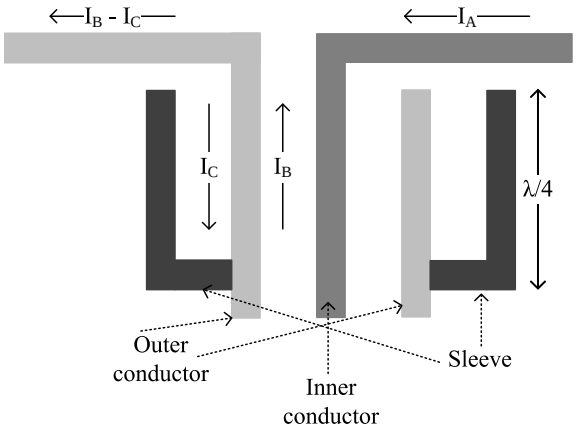

Figure 2.14: Current flow from a dipole antenna connected to a coax cable, surrounded by a sleeve balun

The sleeve is electrically short circuited to the outer conductor, thus eliminating the current, I_c, and makes the coax feed the dipole correctly. This can be explained using Gauss's law, current in the bazooka is flowing in the opposite direction to the current flowing on the outside of the coax. As the length of the balun is $\lambda/4$ the impedance that the current, I_c, sees is infinite. The impedance downward outside of the coax is infinite, thus the current flowing out of the inner conductor has to equal the current flowing out of the outer conductor. As a result the transmission line appears balanced [6] [7], if there is no balun between the coax line and the antenna, then the coax line would also radiate.

Another type of balun is a transformer balun, a balun as its name suggests, a transformer, which can readily be bought off the shelf. A PCB can be designed and the balun directly soldered to the dipole, it has no transmission like equivalent. The output impedance of the balanced line is rated in terms of the input unbalanced impedance, with each output line having the same ground through the transformer. No transmission line effects are seen at the windings

or the core of the transformer. Hence, is suitable for mainly low frequency operations [7].

2.5 Circular Array Theory

Circular array antenna networks have been investigated since the 1930s [25], being used as a starting point for many conformal antenna designers. The circular arrays being discussed in this report are of the ring type and should not be confused with the circular planar array. Ring based circular arrays consist of uniformly distributed radiating antenna elements, their amplitudes and relative phases are exploited for creating omnidirectional patterns in the horizontal plane of the array. One of the earliest pieces of work describing pattern synthesis and the behaviour of circular arrays can be found in [26]. Circular array performance with design characteristics such as amplitude ripple for omnidirectional patterns, number of array elements, their spacing and directivity have been covered in [27]. These aspects of circular arrays will be investigated as this section progresses.

The fundamentals of a circular array all stem from those applicable to linear arrays, as they are both forms of planar array. The most generic circular array is the Uniform Circular Array (UCA). The elements are placed equidistant apart along the circumference of a circle, as seen in Figure 2.15 with the elements excited equally both in amplitude and phase. Figure 2.15 also shows the coordinate system used in the local coordinates and in the far field, not in a continual form, but the more practical and realisable discretised form. The geometry described in Figure 2.15, considers a two dimensional (x, y) problem in azimuth and neglects the effects of mutual coupling and elevation.

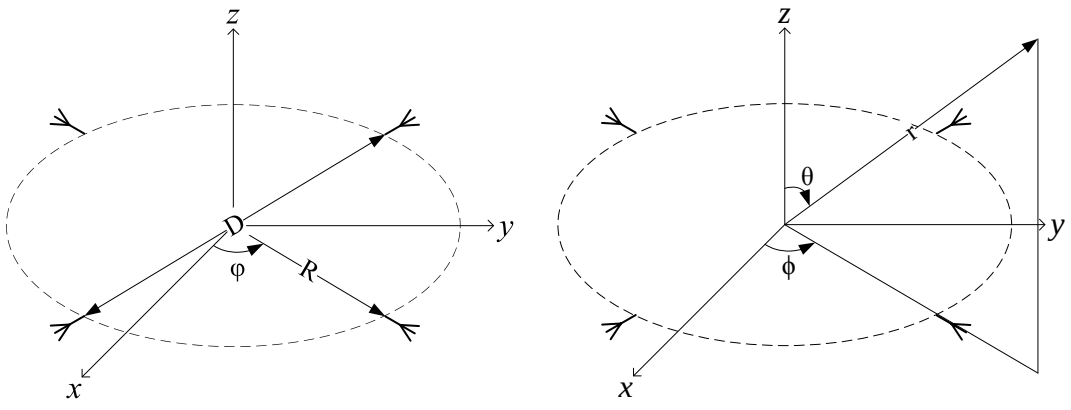

(a) (b)

Figure 2.15: (a) Local and (b) far field coordinates for a discrete circular array

The analysis for the far field radiation pattern for a UCA is analogous to the Uniform

Linear Array (ULA) when using phase mode analysis (Figure 2.16a), hence the same principles can be applied. The equation for the far field radiation pattern in the azimuth plane for a ULA, can be found in [8] and is reproduced here:

$$E(\phi) = EL(\phi)AF(\phi) = EL(\phi)\sum_{n} V_n e^{j\beta nd\sin(\phi)} \tag{2.54}$$

where, $EL(\phi)$, the element pattern factor and $AF(\phi)$, the array factor. If all the elements are the same then the element factor can and has been taken out of equation (2.54). The propagation constant, $\beta = 2\pi/\lambda$, V_n is the excitation amplitude of element n and d, is the inter-element spacing. For the UCA, equation (2.54) has to be slightly modified to take into account the phase centre of the elements phase (centre of the circle). The phase centre is the point at which the radiation seems to originate. Depicted in Figure 2.16b and the equation for the UCA is:

$$E(\phi) = \sum_{n} V_n EL(\phi - n\Delta\varphi)e^{j\beta R\cos(\phi - n\Delta\varphi)} \tag{2.55}$$

The elements are all identical along the circumference of the circle with a spacing between

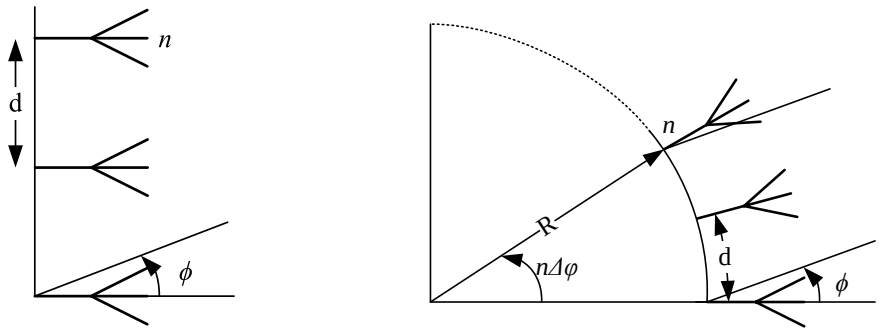

(a) (b)

Figure 2.16: Part of (a) linear array and (b) circular array

elements of $R\Delta\phi$, and all pointing outward in a radial direction. This is what differentiates the UCA to the ULA as the element factor is a function of the radial direction of the elements which are all different. Hence, the element factor is within the summation in equation (2.55) and not for equation (2.54).

Obtaining an omnidirectional radiation pattern in the azimuth plane can be achieved quite effectively from a UCA, due to the circular symmetry of the array. In an omnidirectional application all the elements would need to be fed in equal phase and amplitude. The term βR in equation (2.55) can be rewritten as Nd/λ, which is given in [8] and also can be determined

from simple geometry. N, is the number of elements and d, is the arc length of the inter-element spacing along the periphery of the circle.

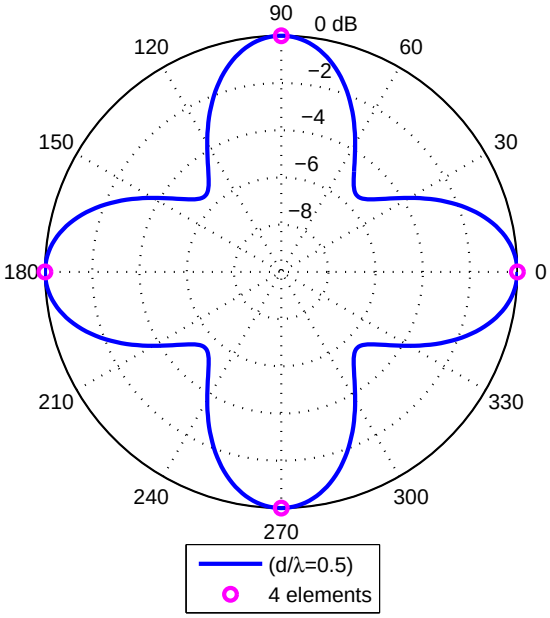

Figure 2.17: Normalised radiation pattern for a UCA with 4 omnidirectional elements spaced at 0.5 wavelengths ($d = 0.5\lambda$), where, d, is the arc length, with equal phase and amplitude for all elements

The radius for the array shown in Figure 2.17 is ($R = dN/2\pi = \lambda/\pi = 0.318\lambda$ (m)), the normalised amplitude ripple for this array size is apparent ($\sim$ 5.5 dB) and can minimised by reducing the radius of the array or by increasing the number of elements. Examples of both cases are shown in Figures 2.18a and 2.18b, with the amplitude ripple reduced by $\sim$4 and $\sim$5 dB respectively. The equal amplitude and phase was achieved by setting the element factor and the excitation amplitude to unity. Similarities remain between ULAs and UCAs with regards to their ability to focus a radiation beam in the direction ϕ_0. For a linear array, a linear phase shift $\psi(n)$, would be applied to elements along the array [8]:

$$\psi(n) = -\beta n d \sin \phi_0 \tag{2.56}$$

The same can be applied to the circular array by imposing different phases for the elements within the array, such that all the phases sum coherently in the direction of ϕ_0, shown in Figure 2.19, where, $\phi_0 = 45°$, for correct phase (beam cophasal) excitation for every element, n:

$$\psi(n) = -\beta R \cos(\phi_0 - n\Delta\varphi) \tag{2.57}$$

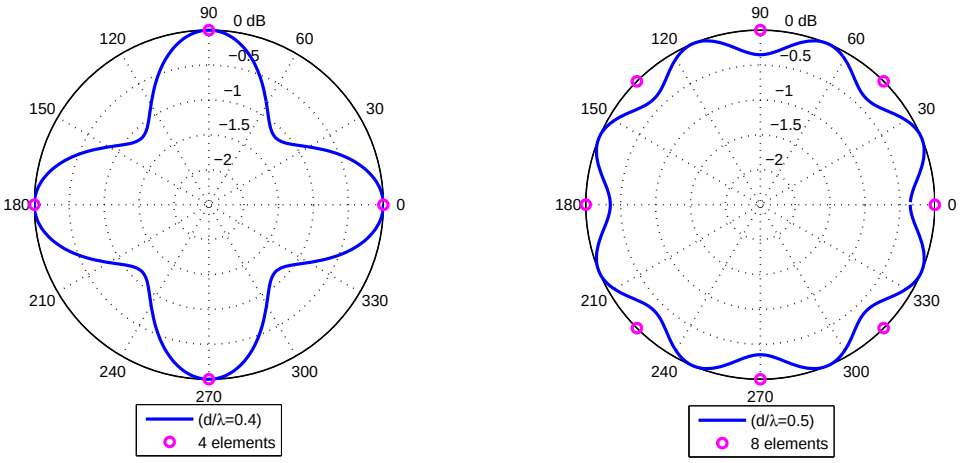

(a) (b)

Figure 2.18: The radiation pattern for a UCA (a) with 4 omnidirectional elements spaced $d = 0.4\lambda$, (b) with 8 omnidirectional elements spaced at $d = 0.5\lambda$

Therefore, equation (2.55) can be rewritten for a focused circular array:

$$E(\phi) = \sum_{n} V_n EL(\phi - n\Delta\varphi) e^{j\beta R[\cos(\phi - n\Delta\varphi) - \cos(\phi_0 - n\Delta\varphi)]} \tag{2.58}$$

Evaluating equation (2.57) for Figure 2.19, $\psi(0) = -\sqrt{2}$, $\psi(1) = -\sqrt{2}$, $\psi(2) = \sqrt{2}$ and $\psi(3) = \sqrt{2}$.

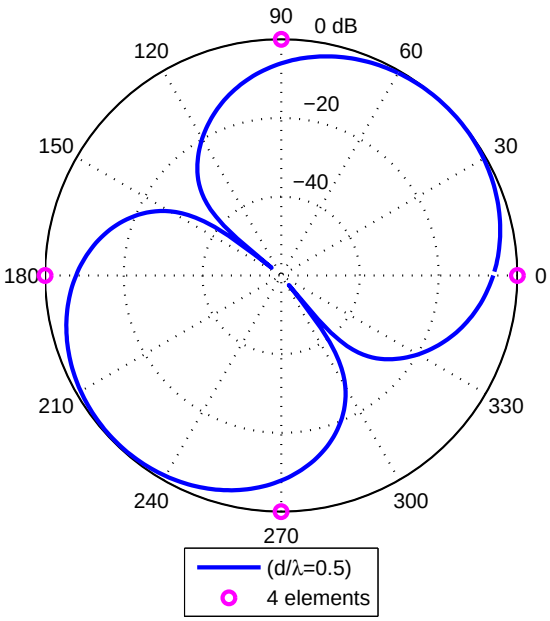

Figure 2.19: Normalised radiation pattern for a steered (where $\phi_0 = +45°$) UCA with 4 omnidirectional elements spaced at 0.5 wavelengths ($d = 0.5\lambda$), where, d, is the arc length

The number of elements and the size of the array could depend on the availability of the parts, but most probably constrained by the frequency as the radius clearly shrinks with

frequency. For very high frequencies this could create a problem with constructing such an array. This may not necessarily be an issue with the antenna construction, but could be with the feed network associated with the array. Consider the placement of the feed network for all the outward facing elements, its location is the in the centre of the antenna array. This space could potentially be tiny for high frequencies and render the feed inadequate.

2.5.1 Phase Mode Excitation

Phase Mode Excitation Introduction

The excitation of the circular array can be analysed in terms of their spatial components, known as phase modes [28][29]. If the continuous excitation function is written as $V(\varphi)$, the far field radiation in the azimuth plane is:

$$E(\phi) = \frac{1}{2\pi} \int_{-\pi}^{\pi} V(\varphi) EL(\phi - \varphi) e^{j\beta R \cos(\phi - \varphi)} \mathrm{d}\varphi \tag{2.59}$$

the total radiated far field can be written as the summation over all m pattern functions (see [8] for the full proof, also reproduced in Appendix A). The pattern function from the m^{th} excitation mode is:

$$E_m(\phi) = j^m C_m J_m(\beta R) e^{jm\phi} \tag{2.60}$$

The term $J_m(\beta R)$, is a Bessel function of the first kind in its integral form. Hence, for the corresponding m^{th} excitation mode the Bessel function can be thought of as scaling factor. Where its value for a single phase mode determines how much that phase mode contributes to the total pattern. Figure 2.20 shows that the higher order modes radiate poorly, to a point where their contribution is negligible. The general rule of thumb for the number of phase orders needed for pattern synthesis is as follows, m should be equal to at least βR [30]. When the Bessel function J_m is close to zero, which often occurs as the Bessel function oscillates with several zero crossings (see Figure 2.20). The far field component, E_m, will not be excited, with pattern synthesis and stability versus frequency affected [8]. The other phase modes which make up the total radiation pattern will continue to radiate, with the lower order phase modes contributing with the most influence.

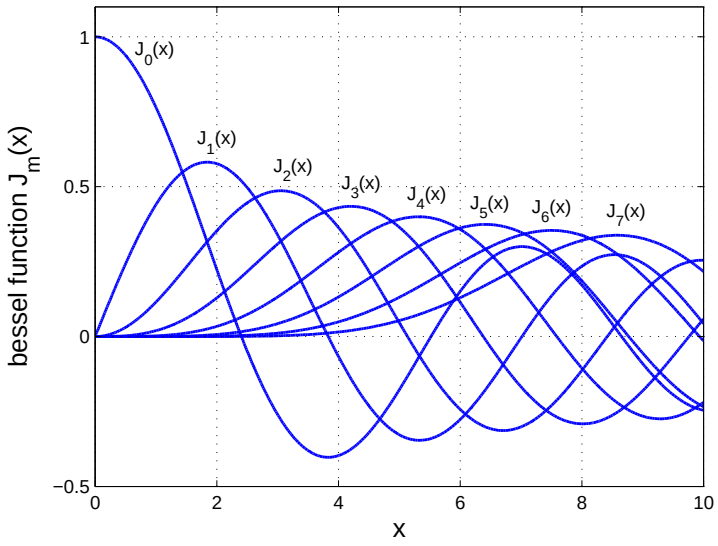

Figure 2.20: Bessel functions of the first kind for orders from $m = 0$ to 7 [31]

Discrete Elements

In general, the discrete excitation is a sampled version of the continuous excitation. One method of generating the required phase mode is to linearly increase the phase of the feed network to the array elements. This however gives rise to harmonics of the fundamental phase mode, which could cause pattern distortion [30].

The continuous function has a Fourier expansion with a single spectral component at C_0, corresponding to the DC component of the signal. By sampling at discrete equidistant elements, N, results in a line spectrum. The lines are separated by N/T, where, $T = 2\pi$, the periodic extent of the source. Using the complex Fourier series conversion (see equation (A.3)) the following can be written:

$$X\left(\frac{q}{T}\right) = X_q = \frac{1}{T}\int_{-\frac{T}{2}}^{\frac{T}{2}} \sum_{n=1}^{N} \delta(t - t_n) e^{-j2\pi q\left(\frac{t}{T}\right)} \mathrm{d}t \tag{2.61}$$

where t_n is the position of element n and $\delta(t)$ is the Dirac delta function and q represents the spectral line number (where previously in (A.3) 'm' was used, however 'm' is used to denote the phase mode order hence, the use of 'q'), equation (2.61) can be rewritten as:

$$X_q = \frac{1}{T} e^{-j2\pi q\left(1+\frac{1}{N}\right)} \sum_{n=1}^{N} e^{-j2\pi q\left(\frac{n}{N}\right)} = \begin{cases} \pm\frac{1}{T}, & \text{where } q = 0, \pm N, \pm 2N, \ldots \\ 0, & \text{otherwise} \end{cases} \tag{2.62}$$

The exponential term outside of the summation dictates the phase. Matrix feed systems such as

the one described in section 2.6.2 can be used to excite multiple phase modes simultaneously. The pattern generated would have an omnidirectional pattern in amplitude, but each with different phase progressions in azimuth. This can be exploited to determine the bearing to a target by taking the difference in the phases between phase modes.

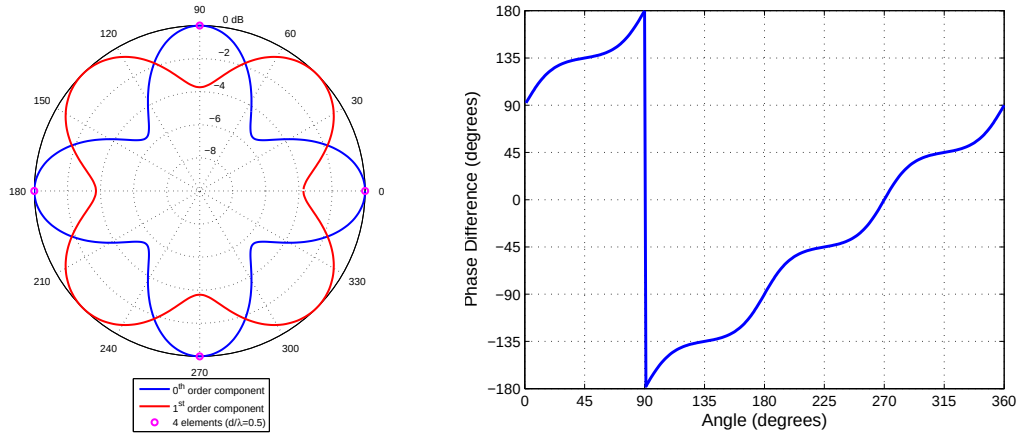

(a) (b)

Figure 2.21: (a) The radiation pattern for a UCA with 4 isotropic elements, where ($p = 0$), spaced at $d = 0.5\lambda$ for the 0^{th} and 1^{st} order phase modes, (b) the phase difference between the 0^{th} and 1^{st} order phase modes

The approximations that are made by the discrete element array to approximate a continuous array have the following general rules: the highest order phase mode that can be supported, without aliasing by an N-element array is $N/2$. Another constraint is that the inter-element spacing must not be greater than 0.5λ, this is for suitable phase distribution sampling [32].

Directive Elements

The previous have all described an isotropic antenna element, using directive elements can improve the bandwidth and pattern stability when compared to this isotropic element [31]. From the general expression for a circular array radiation pattern, given in equation (2.59), the element radiation function $EL(\phi - \varphi)$ is also periodic over 2π and can be expanded in a Fourier series:

$$EL(\phi - \varphi) = \sum_{p=-\infty}^{\infty} D_p e^{jp(\phi-\varphi)} \tag{2.63}$$

where, p, is the spatial Fourier component of the elements radiation pattern. Inserting this form of the element radiation function into equation (2.59), the radiated far field can be written as:

$$E(\phi) = \frac{1}{2\pi} \int_{-\pi}^{\pi} V(\varphi) \sum_{p=-\infty}^{\infty} D_p e^{jp(\phi-\varphi)} e^{j\beta R\cos(\phi-\varphi)} \mathrm{d}\varphi \tag{2.64}$$

After changing the order of the summation and integration and by expanding the excitation in terms of phase modes $V(\varphi) = \sum C_m e^{jm\varphi}$, the m^{th} phase mode result can be obtained:

$$E_m(\phi) = C_m e^{jm\phi} \sum_{p=-\infty}^{\infty} D_p \frac{1}{2\pi} \int_{-\pi}^{\pi} e^{j(m-p)(\phi-\varphi)} e^{j\beta R\cos(\phi-\varphi)} \mathrm{d}\varphi \tag{2.65}$$

which can be rewritten, using the definition of A_m, as in equation (A.9):

$$E_m(\phi) = \left[C_m \sum_{p=-\infty}^{\infty} D_p j^m J_{(m-p)}(\beta R) \right] e^{jm\phi} = A_m e^{jm\phi} \tag{2.66}$$

This is the product of the spectral form of the excitation function and the element radiation function. It is essentially a convolution between the excitation and the radiation, again summation of all phase modes would result in total radiation, in practice the value of p is finite. In most practical applications, an element pattern is a slowly varying function with mainly low spectral orders, some examples are an element with a $(\cos\phi)$ or $(1 + \cos\phi)$ type radiation pattern (see Figures 2.22a and 2.23a respectively). The use of the directive elements can have a great improvement with the stability of the radiation function over large range of values of βR allowing for broadband array performance [31]. Figures 2.22 and 2.23 are both generated by evaluating a modified version of equation (2.55) for the 0^{th} (equation 2.67) and 1^{st} (equation 2.68) order phase modes, rather than determining the p coefficients:

$$E_0(\phi) = \sum_{n=0}^{N} EL(\phi - n\Delta\varphi) e^{j\beta R\cos(\phi-n\Delta\varphi)} \tag{2.67}$$

$$E_1(\phi) = \sum_{n=0}^{N} EL(\phi - n\Delta\varphi) e^{j\beta R\cos(\phi-n\Delta\varphi)} . e^{jn\Delta\varphi} \tag{2.68}$$

2.5.2 Elevation Pattern

Thus far, the theory described has neglecting the antennas elevation pattern. The radiation function given in equation (2.59) which considers isotropic elements in the azimuth plane can be rewritten to take into account the elevation angle θ:

$$E(\theta, \phi) = \frac{1}{2\pi} \int_{-\pi}^{\pi} V(\varphi) EL(\phi - \varphi) e^{j\beta R\sin\theta\cos(\phi-\varphi)} \mathrm{d}\varphi \tag{2.69}$$

where, R, in equation (2.59) is replaced with $R\sin\theta$. The m^{th} phase mode with isotropic elements can also be rewritten using this substitution:

$$E_m(\theta, \phi) = j^m C_m J_m(\beta R\sin\theta) e^{jm\phi} \tag{2.70}$$

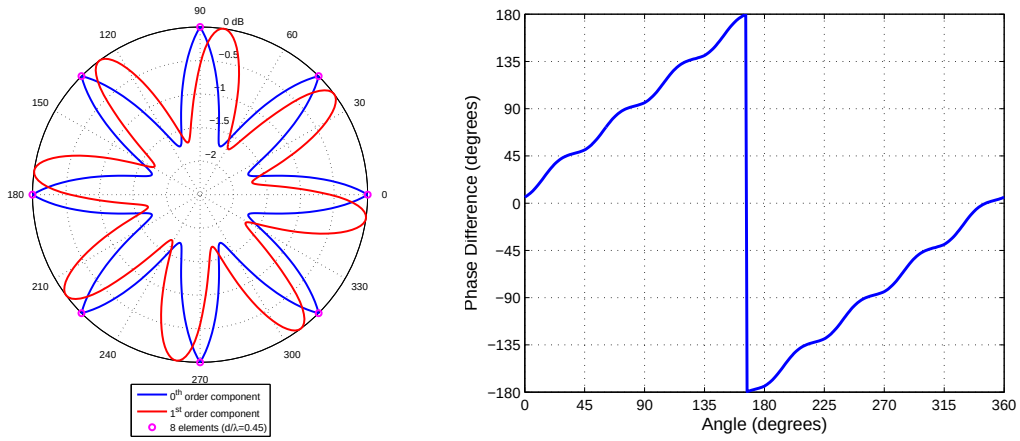

(a) (b)

Figure 2.22: (a) The radiation pattern for a UCA with 8 directive elements, with an $(\cos\phi)$ element pattern spaced at $d = 0.45\lambda$ for the 0^{th} and 1^{st} order phase modes, (b) the phase difference between the 0^{th} and 1^{st} order phase modes

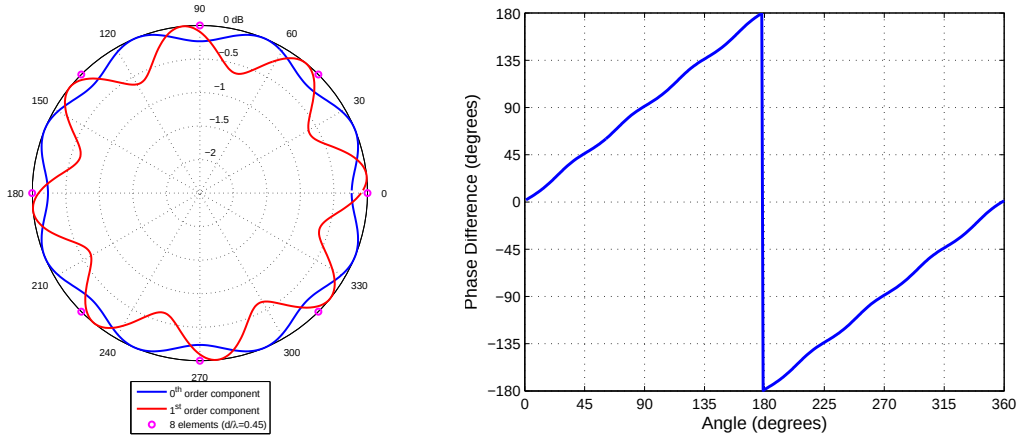

(a) (b)

Figure 2.23: (a) The radiation pattern for a UCA with 8 directive elements, with a $(1+\cos\phi)$ element pattern spaced at $d = 0.45\lambda$ for the 0^{th} and 1^{st} order phase modes, (b) the phase difference between the 0^{th} and 1^{st} order phase modes

For the 0^{th} phase mode where all the elements radiate in phase have the maximum radiation when $\theta = 0$. It has been shown in [31] that directive elements improve the performance in the elevation plane, as the phase mode amplitude is dependant on the elevation angle. This implies that the use of directive elements would be highly beneficial to any practically implemented circular array. Referring back to Section 2.4.5, the $(1 + \cos\phi)$ element radiation pattern is directional and realisable from a single patch antenna.

2.6 Analogue Feed Network

The feed system is vital for connecting the antenna elements to the rest of the system, for transmission its purpose is to transmit power to the elements. On receiving, a feed system collects the signals from the elements. The feed system must be able to carry this out whilst also maintaining the phase and amplitude excitations, and can also contain various switches for beam steering or integrated amplifiers. This section showcases two such analogue feed systems. Firstly, the Vector Transfer Matrix System [33] and in more detail the Butler Matrix Feed System [34], there are other analogue feed systems and digital feed systems, but which require more complex designs. The two mentioned allow for modularisation, separate construction and independent testing of subsystems.

2.6.1 Vector Transfer Matrix System

This is a basic feed network system that has all the radiators fed via attenuators, phase shifters and power dividers. The sectoral active regions are maintained with appropriate attenuation to the channel that is not in use, hence, making it ideal for beam steering. This feed system has all the functions that are required from feed systems of this type such as: switching between active sectors (commutating), amplitude tapering and phase steering. However, this feed network is rarely used due to its complexities and large transmission line losses, other losses also arise from the attenuators. Figure 2.24 shows an example of a vector transfer matrix being used to feed a circular array.

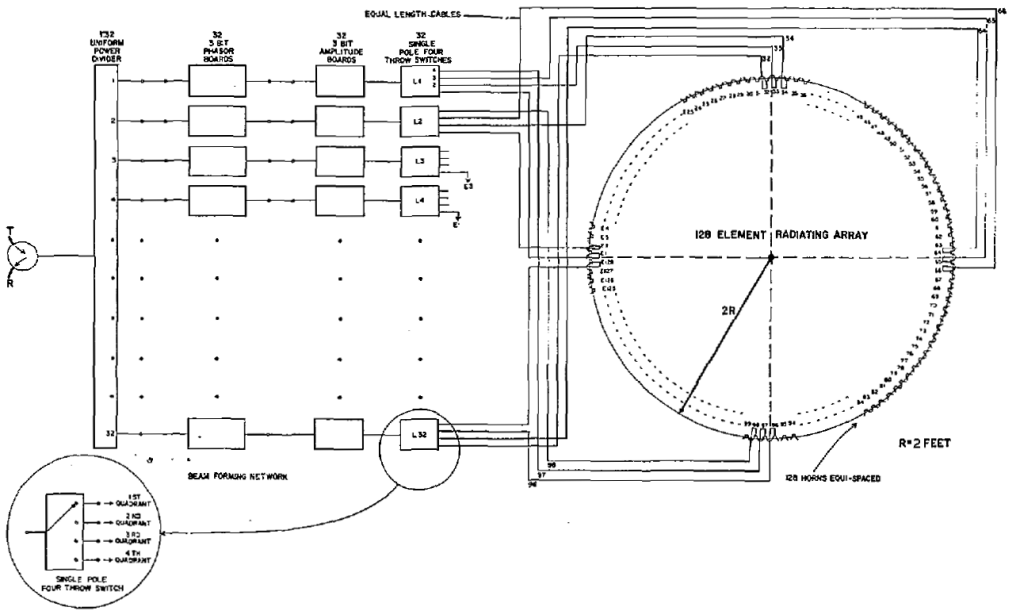

Figure 2.24: Vector transfer fed circular array, image taken from [33]

2.6.2 Butler Matrix

In section 2.5.1, a matrix feed network was suggested as method of generating the required phase modes simultaneously. One such feed network is a Butler Matrix [34], more information about Butler matrices can be found in [35] and [36]. However, their operation will be discussed in brief now along with some design suggestions. A Butler Matrix is described as a lossless N input N output device, when it is feeding a circular array antenna network, it generates linear phase variations of the elements within the array. A Butler Matrix can be used to excite N independent phase modes, each element radiating its pattern, but each with a different phase variations with angle.

Consider equation (A.8) which describes the far field radiation in terms of phase modes with amplitude A_m. The radiating phase modes and their respective excitation phase mode amplitudes, C_m, are proportional to one another, as seen in equation (A.9). By adding phase increments to the corresponding phase mode number linearly, allows for the mathematical representation of a Butler Matrix. So, $A_m^{new} = A_m^{old} e^{m\Delta\phi}$ results in a modified radiation pattern which is expressed below as a Fourier series:

$$E^{new}(\phi) = \sum_{-\infty}^{\infty} A_m^{old} e^{jm(\phi+\Delta\phi)} = E(\phi + \Delta\phi) \tag{2.71}$$

A simple four port Butler Matrix with four inputs and four outputs can be designed from a combination of 90° and 180° hybrids and a crossover. Figure 2.25 shows a Butler Matrix that would produce four phase modes, the 0^{th}, $\pm 1^{st}$ and $+2^{nd}$. The phase difference described previously that can be used to determine the target bearing, can be achieved by terminating the -1^{st} and the $+2^{nd}$ order phase modes with matched loads and taking the difference of the 0^{th} and $+1^{th}$ order phase modes.

The use of these two phase modes allows unambiguous azimuth coverage through all angles, using the 0^{th} and -1^{st} order phase modes or the $+1^{st}$ and $+2^{nd}$ modes, would also equally provide the same unambiguous azimuth coverage. However, if the 0^{th} and $+2^{nd}$ or the $+1^{st}$ and -1^{st} order phase modes were used to determine the target bearing then an ambiguity could occur this is because for every measured angle there could be two possible target locations which are 180 degrees apart, further discussion of this can be found in Section 4.2.

The Butler Matrix can be thought of as a hardware equivalent version of a FFT which have been thoroughly compared in [37] and [38]. One of the main reasons for this analogy is that as the output of a Butler Matrix is a Fourier transform of the input. The signal processing that the Butler Matrix carries out is exactly the same as the “computational operations depicted by the

FFT tree graph" [37].

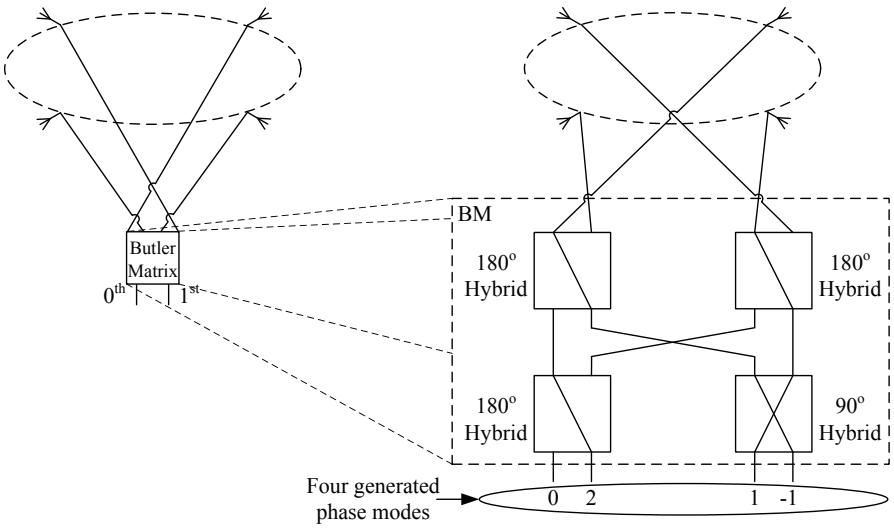

Figure 2.25: An implementation of the four element circular array fed with a Butler Matrix feed network

Chapter 3

Current Technologies

The chapter forms a review of current technologies that make up a modern active target FMCW radar system, analysing the relevant literature needed throughout this project. It begins with a review of current navigation at sea radar systems, however, there are also other navigation technologies such as laser ranging systems, which are also discussed. Another aspect of this project is the use of transponders and are shown as useful aids for marine navigation. Continuing on from Section 2.3 modern FMCW design techniques will be reviewed. As this prototype system is for measuring range and bearing for use in harbours, methods of measuring range and bearing and sea clutter are described. Circular array theory was also discussed in Section 2.5, now they will be reviewed as developed systems with their typical uses.

3.1 Navigation at Sea

Navigation at sea is a multi billion pound industry with the majority of income from shipping. To keep these ships safe and away from obstacles is essential. Many companies exist to provide systems that can be used for safe navigation based on various technologies, largely based on different types of radar systems. Previously these were PD radar systems and more frequently the emergence of FMCW radar systems for this safety role. Some of which will be highlighted now, as well as other technologies for safe navigation.

3.1.1 SharpEye

The SharpEye radar system has been designed by Kelvin Hughes Surveillance in 2006, a radar that is used to aid navigation of seafaring vessels. A company that in 1948 had produced the first radar system that adhered to the UK's national performance standard for merchant ships, the Kelvin Hughes Type 1 [3]. The SharpEye radar is a Pulsed Doppler radar which can be bought as a S-band or X-band radar system. The S-band variant radar has the specifications laid out in Table 3.1 [39].

In [3] the specifications for typical radar systems operating at S- and X-band circa 2006

Table 3.1: SharpEye S-band radar specification [3]

RF Frequency	2.93-3.07 GHz
Peak Power	170 W
RF Power Source	Power Amplifier
RF Duty Cycle	10%
Pulse Repetition Frequency	2.3 kHz
Pulse Width	0.1-100μs
Antenna Rotation Rate	24 RPM
Horizontal Beamwidth	1.9°
Vertical Beamwidth	26°
Transmitter/Receiver	Upmast
Display	Colour Flat Panel LCD

are also discussed, as is shown in Table 3.2. Comparing the specification for SharpEye with the systems that were typically used, shows that it operates at approximately 0.57% of the peak power. This is possible due to the use of longer pulse lengths than the general systems described in 3.2, such that the energy remains equal between the two radar systems. Previously discussed is the use of Doppler filter banks, typically narrow band filters that have a width of 3 ms^{-1} (~333 Hz) [3], thus allowing the detection of targets close to slow moving clutter. The SharpEye radar uses a Direct Digital Synthesiser (DDS) for ease of generating pulses with repeatability, flexibility and reliability, see Section 3.3.1 for further analysis of DDS. Although the maximum operating range is not stated, by modifying equation (2.4) slightly to take into account the ability of this PD radar to have different pulse widths (0.1 to 100 μs):

$$r_u = \frac{c}{2} \cdot \left(\frac{1}{PRF} - P_w \right) \tag{3.1}$$

where P_w is the pulse width, the maximum unambiguous range at $P_w = 0.1$ μs is 65 km and at $P_w = 100$ μs is 50 km. Usually if the pulse width, P_w, is quite small, equation (2.4) would be adequate. Other deductions based on the parameters in Table 3.1 reveals the range resolution using equation (2.3) is 1.07 m.

To conclude the use of this radar as an aid for sea navigation is valid, the range resolution and low power operation are all in keeping with the expectations of the prototype systems built for this thesis. The use of clutter cancellation is very rightly implemented as sea conditions would vary the sea clutter characteristics greatly, causing many false positive results. [3] also discusses challenges faced by 'New Technology radar' (radars with a PA as its power source) in existing marine target detection, where targets can be of two types. Firstly, objects such as surface vessels, coastlines, off shore structures etc... and secondly radar beacons (Racons) and Search And Rescue Transponders (SARTs). The energy requirements discussed matches typ-

Table 3.2: Marine radar parameters for X- and S-band radar systems [3]

	X-band	**S-band**
RF Frequency	9.410 GHz	3.05 GHz
Peak Power	25 kW	30 kW
RF Power Source	Magnetron	Magnetron
Pulse Repetition Frequency	1.5 kHz	1.5 kHz
Pulse Width	0.055μs	0.055μs
Antenna Rotation Rate	24 RPM	24 RPM
Horizontal Beamwidth	1.2°	1.9°
Vertical Beamwidth	25°	26°
Transmitter/Receiver	Upmast or Downmast	Upmast or Downmast
Display	Colour Flat Panel LCD	Colour Flat Panel LCD

ical systems, however, the pulse length is significantly longer and may not trigger a response from Racons or SARTs. It also describes navigational aids operating on the transponder principle, where the transponder is located buoys or off shore platforms, two such locations for the active target designed in this project. Finally, [3] suggests that FMCW radars will struggle with the commercial marine market. However, since [3] was written, some FMCW radars have been brought to the marketplace and are discussed as this section progresses. FMCW radars' emergence is largely due to their low radiated power and cost effectiveness, two main reasons for an FMCW based radar system for this project.

3.1.2 RadaScan

RadaScan is an FMCW X-band radar system developed by Guidance Microwave Ltd. In [4] a system is described that is comparable to the one that is proposed in this report. RadaScan uses active targets as part of its radar system and for this reason it is being discussed here. Using the data from RadaScan i.e. maximum range, power limits, operating frequency use set some of the initial specifications for the proposed radar system discussed in this thesis.

The RadaScan system is used in 'Vessel Underway Replenishment at Sea Applications'. This is where one vessel is transferring personnel and/or materials to another. RadaScan is used for accurate control of the two vessels using the radar system and transponders. This arrangement allows for very accurate measurement of range and bearing. The control system allows one vessel to track and follow the other, it can also be used for tracking sea floor pipes. Before this system, ship to ship tracking was achieved with laser ranging systems and following sea floor pipes with the aid of acoustic sea floor techniques or taut wire systems. The ship tracking manoeuvre had the laser system as its only option, but was dependent on the weather conditions, as with many laser based ranging systems. So, RadaScan was produced to be a viable solution for all weather scenarios. The system involves microwave radar that interrogates a radar retro-

reflective Van-Atta transponder [40] an example of which is shown in Figure 3.1. A Van-Atta array redirects the incoming signal back towards where it originated, hence, providing signal enhancement without amplification. Some of the radar parameters are as follows: an operating centre frequency of 9.25 GHz with a 100 MHz bandwidth, as this is one operating band for maritime radiolocation systems. The transponder discussed comes in two varieties: one that it passive, in terms of RF signal, with a battery to provide modulation for an identification tag. The other is a portable RF amplified version. The quoted range in this paper for finding and tracking a transponder is 750 m, but it does indicate that it can work beyond this range.

RadaScan uses a triangular FM waveform, generated by a combination of DDS/PLL/VCO, to determine the range of the transponder with an output power of approximately 32 dBm. It uses a vertically polarised horn illuminating a parabolic antenna, both of which are rotating whilst encased within a radome. At the receiver end, the signal received from the transponder is mixed with a portion of the transmitted signal for deramping, with filtering where appropriate. A method which is quite typical of most FMCW radar systems, as discussed in Section 2.3.

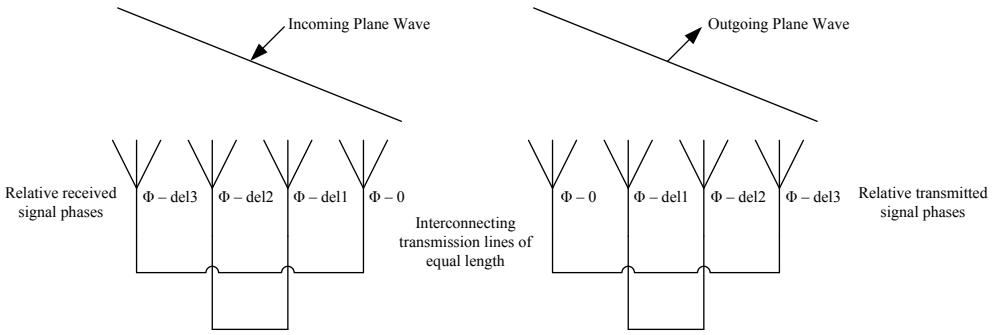

Figure 3.1: Example layout of an unmodulated passive retro-reflector Van-Atta array [40]

The retro-reflector transponders as mentioned previously use Van-Atta array principle, as shown in Figure 3.1 [40], the transmitted signal is directed to where it originated. The RadaScan transponder transmit and receive antennas have different polarisations and has its RF signal modulated with an identifier code. The coding also allows for better clutter rejection by coherent detection of the transponder's identification code. Correct location of the transponder is vital to minimise sources of clutter from structures on the vessel as well as other vessels. Multipath is still an issue, but has been minimised and largely negated with transponder location. The transponders horizontal and vertical viewing angle is 170° and up to 70° respectively. With both mains and battery power options, the battery life is 1 and 12 months for rechargeable and fixed cells respectively [41].

Measurements from RadaScan have shown that for static measurements the position of a target can be resolved with a standard deviation of a few inches. When the standard deviation is compared to guidelines for laser systems, where the standard deviation is within 3 feet for resolved and motion correct positions. It also states that if the standard deviation is greater than 9 feet, the sensor is deemed unworthy regardless of sea conditions.

To conclude, this system has shown that using an FMCW radar to find and track active targets in marine applications is feasible, it can be compared to other technologies such as laser-based systems for similar if not better accuracy. The range is significantly less than the PD radar discussed in Section 3.1.1, but more than sufficient for short/medium (250 - 500 m) range applications. The transmitted power of RadaScan is significantly less than the SharpEye PD radar system described in Section 3.1.1 (32 dBm (1.6 W) vs. 170 W peak power).

3.1.3 INDRA

INDRA [42] is *ra*dar developed by the *Ind*onesian government which is used for maritime surveillance with two versions: INDRA I a ship mounted radar and INDRA II a coastal radar. This radar is being reviewed in this section as it raises valid arguments for antenna beamwidths of ship mounted radar and has a full radar specification.

INDRA, is a 1 W FMCW based radar, that is used for safeguarding the vast coastline of Indonesia from illegal activities such as illegal fishing and piracy. It was built as a collaboration between the Indonesian government and Delft University (Netherlands). The INDRA specifications are summarised in Table 3.3. It shows a similar specification, with regards to the centre frequency and output power to the RadaScan system discussed previously.

It is interesting to note that [42] discusses the importance of the vertical beamwidth being quite large; this is to account for the movements (rolling and pitching) of the ship. For any ship-based radar system this would be an important parameter, which they have established to be 20°, comparing this to the fixed coastal radar INDRA II which has a vertical beamwidth of only 10°. The maximum range of this system is quoted at 40 NM (~ 74 km). This maximum range is very high in comparison to other FMCW radar systems, achieved with a sweep time of almost 0.5 seconds. Hence, the time bandwidth product discussed in Section 2.3.2 adds quite significant processing gain which is utilised to achieve this maximum range. This does however reduce the range resolution significantly from 2.9 m at the shortest maximum range to 144.7 m at the longest, because the number of range cells is fixed at 512. Also, the use of a sawtooth waveform means that for a moving ship, fixed target scenario, there is a limit on how much the ship can move before a Doppler shift is introduced and the target position is incorrect, for the INDRA system the maximum unambiguous Doppler speed is ±15.58 ms^{-1}.

Table 3.3: INDRA technical specification [42]

Radar Type	FMCW
Output Power	1 W
Centre Frequency	9.4 GHz
Modulation	Sawtooth
Frequency Sweep	50 MHz (max)
Sweep Time	0.4939 ms
Sweep PRF	2.047 kHz
Beat Frequency	1 MHz
Sampling Frequency	2 MHz
Range Scales	0.8, 1, 2, 4, 8, 16, 32, 40 NM
Range Resolution	2.9 m max, 144.7 m min
Range FFT size	1024
Maximum unambiguous Doppler speed	15.58 ms^{-1} (56.1 kmh^{-1})
Horizontal Beamwidth	2.5° (INDRA I), 1.25° (INDRA II)
Vertical Beamwidth	20° (INDRA I), 10° (INDRA II)
Antenna Rotation Speed	Variable (24 RPM max)
ADC Resolution	12 bits
Tracking system	ARPA compliant (INDRA I)

The antenna array is designed to be modular, comprising of a group of four, 8 element patch antennas for the INDRA I radar and a group of eight, 8 element patches for the INDRA II radar. Each group of 8 patches is the same for both radar systems, as INDRA II has twice as many patches as INDRA I, indicating that the beamwidth is naturally smaller for INDRA II and happens to be exactly half in the H-plane. The use of parabolic reflectors has also reduced the beamwidth in the E-plane by half compared to the INDRA II radar. Modularising the patch arrays means that the system can be quickly altered if improvement and enhancements are required and only the design of one such array is required the rest are copies, decreasing complexity. A simple power divider/combiner with phase matched coaxial cable are used as the feed network for the patches.

To conclude, [42] raises some issues that must be considered when designing a ship mounted radar, such as the minimum acceptable vertical beamwidth to account for the ship movements. The regulatory committee will set the operating frequency and the transmitted power. If a sawtooth waveform is used then the maximum unambiguous Doppler shift must be calculated and if it is not within acceptable limits, then the triangular modulation could be an option. The use of modularised parts will significantly reduce the time taken to develop a prototype. For a proof of concept design and increasing simplicity, the use of modular components should be implemented in the initial stages. Finally, it discusses how increasing the maximum range with longer chirps will affect the range resolution provided that the number of range cells

stays constant.

3.1.4 Scanter 6000

The SCANTER 6000 developed by Terma [43] [44] is an X-band PD radar system operating at 9.0 to 9.5 GHz with long range and medium range varieties with either a peak power of 200 W or 50 W Solid State Power Amplifier (SSPA), running at 20% duty cycle. SSPAs have also been used in [3], the use of which does increase the cost compared to a magnetron based amplifier. However, with a longer lifetime and improved signal-to-noise ratio from pulse compression, it counteracts the reduced peak power when compared to magnetron based PD radar systems.

One advantage of this system over others is the use of frequency diversity on a pulse to pulse basis, with a selection of up to six frequencies. The application of differing pulse lengths has the effect of separating the ranges into three regions depending on the length of these pulses, with range resolutions from 1.5 to 6 m [44]. Their tests have shown that a Rigid Inflatable Boat (RIB) with an RCS of 1.5 m^2 was detected with a 100% probability at 9.1 NM [43]. Other tests have shown a small target measuring 0.1-0.2 m^2 was detected at a range of 1.5 km [44].

In [44] the advantages of implementing pulses of varying length allows the simultaneous reception from both short and long ranges. However, between pulses sufficient isolation is required such that targets appear at the correct range, with their calculations showing 80 dB isolation requirement between adjacent pulses.

To summarise, this system introduces valuable concepts that could be implemented such as diverse chirp lengths to segment the range into regions. The use of an SSPA and signal-to-noise improvements, gives this system an equivalent peak power of 200 kW. Allowing the use of lower peak power, with less strain on the rest of the hardware components within the radar, for similar performance to magnetron based radar systems.

3.1.5 Navigation at Sea: Radar Overview

Preceding this Section, four radar systems were discussed, all operating on board ships for either navigating applications or target detection whilst at sea. All the highlighted systems have a rotating antenna; other systems too use the rotating antenna approach such as the FMCW BR24 radar sensor developed by SIMRAD discussed in [45]. The advantages of a rotating antenna are the increased gain due to narrow beamwidths and clutter reduction by only illuminating a small area at any given time. Mechanical or electronic beam steering can achieve this rotation, but there could be scope for a smaller scale system, which has no electronic or mechanical steering to locate targets for navigation and collision avoidance systems.

The radars discussed have quite similar hardware characteristics, with regards to their oper-

ating frequency. The International Maritime Organization (IMO) would require a certain sized vessel to have an S-band system to cope with rain clutter and for higher precision implemented a X-band system, and also systems that can detect SART type beacons or Racons. However, the software they have developed for their respective radar systems would be very different, with some optimised for sea clutter rejection [44], which for maritime radar systems would be a definite requirement. The software implemented in these radars is heavily restricted due to competition between companies, hence, is not being reviewed here.

The current maritime radars fall into two types either PD or FMCW, with FMCW increasingly attractive for short to medium ranges due to cheaper hardware components. PD systems are still required for longer range systems, but the specifications presented have shown that FMCW could also be used up to 40 NM (74 km) [42]. Modern PD radars within the last 10 years have increasingly used SSPAs whereas previously magnetrons where used. The price of magnetrons are considerably lower than SSPAs, hence, are still being used in some modern systems. The advantages of SSPAs are significantly lower peak power and can operate at a longer duty cycle giving the same average power as a magnetron based radar. The reduced peak power has the added affect of improving the lifespan of the radar.

3.1.6 Other Technologies

Up to this point, only radar systems have been discussed for navigation type applications. Other technologies have begun to make more of an impact in this field for shorter ranges, up to 300 m. Two that are currently being explored are laser based ranging systems and night vision based optical systems.

One such LAser Detection And Ranging (LADAR) system has been developed by Instituto de Automática Industrial (IAI) in Spain [46] [47]. This is a laser based range measuring device and has an output peak power of 1 kW, with a pulse repetition rate of 15 kHz, the average power being 22.5 mW. The maximum quoted range based on the some assumptions and using the *laser radar equation* [46], shows that it will work up to 1 km, 600 m or 300 m depending on visibility from high (15 km), medium (2 km) and low (300 m) respectively. Actual tests have shown high visibility range of 500 m and low visibility of 250 m. The range resolution with 95% confidence level at 500 m was 11 cm. The systems have a horizontal scan range of 80° taking 200 ms and a vertical scan range of 340° at a rate of 15 deg/s. They have rotated the sensor in their trials to cover angles similar to that of conventional rotating antenna radar systems, which offer lower scan range vertically than horizontally. Their tests have yielded good inland results where the vessel (a cargo freighter length/breadth (100/11 m)) is manoeuvring in canals, with the canal sensor requirements requiring less maximum range than open sea navigation (500 m vs. 1 km).

One test in a lock chamber of length/breadth (250/15 m) was successfully navigated and height of a bridge was accurately measured within 13 cm of the actual height.

The main points from this type of system are that accuracy is very good for short/medium range applications, but fundamentally heavily dependant on the weather conditions. So, this type of system probably would not replace a conventional radar system, merely supplementing it, for short range applications. The same area of coverage is possible with both types of systems, but the radar system antenna would usually rotate at 24 RPM, whereas the laser based system is much slower 15 deg/s, for 340° coverage.

Another emerging technology for navigation and target detection at sea is an electro-optical imaging system described in [48], produced by Diehl BGT Defence GmbH & Co. KG (Germany). They have designed and implemented close range surveillance systems for detection of threats to the platform. Using multiple electro-optical sensors (infrared) located around the ship, connected by Ethernet to a central processing unit, a single crew member can monitor the ship against threats day and night. These systems are modular, hence, the number of sensors can be altered to accommodate any size of ship, 14 infrared sensor heads arranged in six sensor modules can give full 360° coverage for a frigate class warship. An electro-optical tracking unit containing infrared, daylight channels and laser range finder cover a smaller angular domain but at an increased resolution.

This type of system can be deployed rapidly with modularisation key for full ship coverage. The developed software accompanying this system can trigger alarms based on track left in the water near the ship by targets. Using microbolometer infrared detectors allows the system to be passively cooled (cooling required for accurate temperature measurement) and reduces cost, deployment time and lifespan. These types of detectors are also used in the automotive industry to add night vision capability and better vision in bad weather. The final result is a panoramic real time image of the vicinity around the ship, displayed to a crew member to take appropriate action. They have tested algorithms or different targets, the generation of stable panoramic images and had it successfully connected to combat defence systems.

To conclude, these types of systems could be employed for navigation in narrow waters, additional sensors at the harbour could beam images to the ship for harbour manoeuvres. Unlike a usual radar, multiple sensors would be needed for full azimuth coverage. However, many ships have multiple radar systems that all feed into a central terminal which overlays all the information obtained by the individual radars. Large cargo ships or ships with large central bridges would too need multiple radars for full azimuth coverage. These types of systems can be used to supplement a radar system providing higher resolution for short ranges, but will not

be able to replace current radar systems for long range navigation.

Finally, two different approaches have been discussed in terms of their ability and potential as a navigation aid for ships. They both present good arguments for close vicinity targets, but do not possess the long range ability and all weather features of conventional radar systems. This does give some scope for a short/medium all weather radar for navigation, target detection and for use around harbours and other structures natural or man made.

3.2 Transponders

Previously, current navigation at sea and marine target detection radars and other non radar technologies were discussed. In this section, the transponder based radar systems will be discussed mainly focusing on marine applications. However, not all transponder systems are for marine applications, they are also useful as encoded targets which can be unambiguously identified in SAR images [49]. This is one application where coded targets can be used. In Section 3.1.2 active targets together with a FMCW radar system were used to measure the distance between two ships [4]. There is also scope for unmodulated passive targets, which would simply re-radiate the signal to where it originated, such as Van-Atta arrays [40] described previously. A natural extension would be the use of active transponders, a simple example can be constructed using two antenna connected via an amplifier, with some form of signal conditioning, which could comprise of a mixer and some sort of modulation or some sort of limiter to limit self RF coupling. The separation between the two antenna should be sufficient for the same reason, as it could damage the amplifier. An example of an active target is shown in Figure 3.2. Different types of target detection by marine radar are extensively covered in [50], however, as this section progresses the design and applications of transponders along with some relevant history will be discussed.

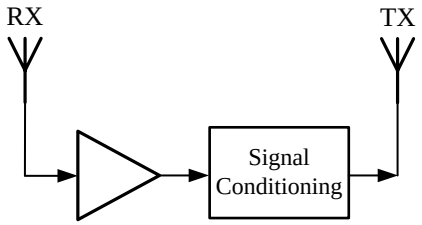

Figure 3.2: A simple active transponder

Transponders have been used with radar systems for almost as long as radar itself. Initially employed as Identification Friend or Foe (IFF) beacon for military aircraft [1] and in one form or

another still used as air traffic control beacons. In the 1940s, [51] discussed universal beacons, which could be used with any airborne or ground based radar systems regardless of frequency. This would increase the radar range or for ground based air traffic control systems to be able to detect the aircraft's transponder for identification. The universal aspect was proposed to be implemented by the using three bands X, S and L antennas for receive and the L band antenna would also be used to transmit.

Not too long after universal beacons were proposed, they were discussed as harbour navigation aids in 1955 [2]. Then considered in high traffic harbours as a possible solution as aid for the captain to manoeuvre the vessel around fixed points and other vessels. Also being discussed in the same meeting in 1955, was the detection of target vessels in a harbour setting, using radar and radio telephones [52] and the use of radar during peacetime for navigation in poor visibility.

In 1958, [53] different options of beacons were considered, lightvessels where discussed which had 'racons' (*ra*dar bea*cons*) fitted. These operated in the marine band between 9.32-9.50 GHz and were intended to be fitted to lightvessels and around the shores of Britain as navigational tools. Also considered was the use of buoys as radar targets and if they were to be successful, then clusters of corner reflectors could be mounted to them making them bright radar targets. The advantages of harbour surveillance radar over standard marine radar were discussed, some advantages are as follows:

- Fixed echoes produced by a stationary radar, hence easier to interpret radar data by a veteran navigator.
- Larger antenna, therefore increased bearing resolution
- Moving object echoes do not require tidal drift correction.
- Shorter pulses and wider receiver bandwidths, hence increased range resolution.
- Location of the surveillance radar can be strategically placed to offer the greatest view of the harbour.

As [53] is a survey of which were current harbour approach aids in 1958, it shows the validity of beacon use around harbours, with different beacons having different primary roles such as identification and course beacons. It was shown that they have been implemented in various harbours and ports around the world and had a future.

From 1960 onwards, having already been established as aids for marine navigation, more focus has revolved around coding and various design aspects of transponders. In 1969 [54] discussed a target design that is largely similar to the final target design discussed in this thesis,

it showed that if the target was frequency modulated then the clutter could be significantly reduced. It was successfully tested using a CW radar system operating between 8.2-8.3 GHz, at ranges of 10 and 20 m.

Much work was carried out in passive target design [55] [56], which involved both uncoded and coded transponders. Although the uncoded has the obvious advantage of no power source requirement for the target, the identification of the target will be unknown. [56] describes a method of identity coding for a passive target using tapped delay lines, for n delay lines 2^n could be generated, for short (6 m) range applications. This approach was however prone to both the transmit and receive antennas replying to interrogation, a method suggested to overcome this problem was the use of different polarisations for the two antenna, using isolators could also work for this problem. During this time, coded targets with battery powered coding schemes were discussed [57], as a viable solution for up to one year of operation as the target only responds to interrogation. Thus extending battery life, as the target has no form of powered amplifier imparting additional gain. These targets would be considered as passive with a battery only required for the coding scheme, something still being implemented today [4].

Previously discussed were targets designed to operate in X-band, S-band *racons* continued to be designed. One step further than passive targets with delay line coding discussed in [56] is to have active targets providing additional RF gain to the signal [58]. Using the marine S-band required no additional radar systems on board the vessel, but would provide a significant navigational aid.

In poor visibility conditions, vessels manoeuvring with one another to avoid collisions relied on communication between the vessels captains. The radar display shows multiple targets, how would one captain know that a certain blip corresponds to the other vessel he is communicating with? [59] describes a 'Marine Radar Interrogator-Transponder' (MRIT), a beacon that would be carried by vessels that could be used for a variety of different manoeuvring applications such as target course, speed etc... as well as identification. The MRIT system would operate in X-band and a comparative analysis was carried alongside an omnidirectional interrogator-transponder system. The former having better interference protection due to directional antenna and increased maximum range capability due to a better SNR. The proposed use for this system would be used in conjunction with radar systems already on board. The same authors discuss in [60] technical optimisation of the location transponder, concluding that it depends heavily on user requirements, over technical optimisation would probably define the location of the transponder. This should be kept in mind when designing the transponders antenna in terms beamwidth.

Modern transponder systems continue to build on the older technology such as a passive radar transponder designed from a modulated retro-reflector [61], which includes additional features to the Van-Atta array. Further improvements have been made to increase the detectable range and improve accuracy [62], by using elements in an array configuration.

Current marine transponders have evolved from navigational aids (racons) to include Search and Rescue Transponder (SART) which operate in the marine X-band. They are primarily used in emergencies by locating survival crafts. Any vessel with a X-band radar will see a SART in their radar display provided that it is within 8 nautical miles. Other forms of racons also exist called ramark (*ra*dar *mark*ers) they differ slightly from usual racons as they do not require interrogation and are continually transmitting their Morse characters.

Other example uses of coded transponders are in personnel and vehicle detection, useful in short range applications. Cost effective transponders can be designed to identify or log movement [63] [64].

3.3 FMCW Technology

Many short range radar systems are FMCW based as they have significant advantages over their pulsed equivalent. In Section 2.3 some of the fundamental design and signal processing techniques for FMCW radar were discussed. Now some of the more modern FMCW techniques with regards to design, construction, signal processing and some new uses for FMCW radar systems will be discussed. Some of the ideas that follow have been implemented for the radar system built for this PhD.

FMCW radar systems originate from ionosphere research dating back to the 1920s. In 1928 the first practical applications of FMCW radar were patented by J. O. Bentley on an "airplane altitude indicating system" [65]. Since then FMCW radar systems have been employed in various applications from avalanche detection [66] to automotive cruise control [67]. The use of FMCW radar for short range marine navigation has still remained a core application and is continually researched. Some of the radar systems described in Section 3.1 are FMCW based and are commercially available today.

3.3.1 Modern FMCW System Design

FMCW radar systems can vary in design significantly and are usually tailored for specific applications. However, an FMCW signal must be generated for all, with past radar systems using Surface Acoustic Wave (SAW) for the generation of the Linear Frequency Modulated signal (LFM). Modern radar systems favour the use of linear voltage ramp fed Voltage Controlled Oscillators (VCOs) and more recently with large reduction in costs, Direct Digital Synthesiser

(DDS) chips and DDS evaluation boards.

VCO-based radar systems tend to be used more with higher bandwidth applications [68], of the order of GHz. For lower bandwidths either a VCO or DDS can be used [69]. VCOs are inherently non-linear, hence a complementary voltage ramp is applied, with the voltage corrections stored in look up tables. DDSs have a clear advantage due to their linear sweep and for an FMCW radar system designer with a low bandwidth applications (several hundreds of MHz), the DDS option quite is attractive.

Another reason for using DDSs to generate the FMCW signal and further importance of linearity is discussed in [70]. It describes phase and amplitude errors in the FMCW signal and how they degrade the radar performance with respect to the time/range sidelobe level and the range resolution. It also considers taper/window functions to decrease sidelobe levels. Window functions are applied to real data obtained for this PhD and is further discussed in Section 6.1.2.

Generally, the FMCW radar system receive architecture is of two types, either homodyne or heterodyne. The former is simpler with less components with at least one less mixer stage than the latter, as seen in Figure 3.3. The hetrodyne downconverter is preferred in some applications as the first downconversion stage can be close to the RF hardware with the rest of the receiver components elsewhere. This is beneficial for high RF frequencies as the cable losses can be high by having two downconversion stages the cable losses will be minimised.

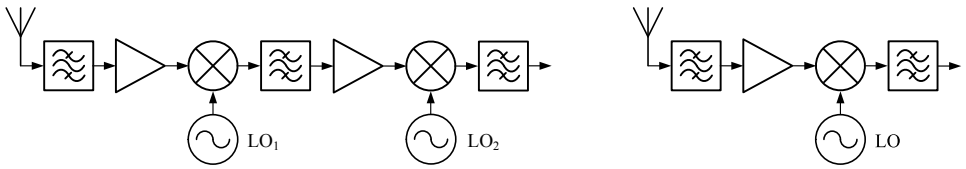

(a) (b)

Figure 3.3: (a) Heterodyne (b) Homodyne downconverters for an FMCW radar system

With regards to signal processing, the fundamental range information is in the same format, contained within the deramped frequency. Where previously banks of bandpass filters would be used each centred on different frequencies [71], hence different ranges. Modern systems have fast processors and the FFT processing is done on computers, making use of all of the deramped frequency spectrum.

3.4 Range and Bearing Estimation

To determine the range from an FMCW radar system, a simple FFT will suffice. Bearing estimation depends on various factors and is mainly solved in hardware. One obvious method

is to use highly directive antenna, and mechanically or electronically steering the mainlobe. The direction at which the antenna is pointing when the signal is received, the elevation and azimuth angles of the target can be determined. The true bearing of the target can be relative to the true north position determined by compasses or with modern radars using GPS receivers. The bearing to the target can also be measured relative to a centreline of a vessel, hence determining the relative bearing.

Electronic beam steering is achieved using phased array antennas. However, they have one slight disadvantage over mechanical antenna in that the radiation pattern is not the same across the array (near end-fire). For a mechanically steered antenna the same mainlobe pattern can be steered in all directions in the hemisphere [72]. However, the advantages of phased arrays such as less weight and scan rates far outweigh its disadvantages.

Traditionally, triangulation has also been used to determine the location of targets. In [73] the data from three FMCW radars is combined. Each one calculates the range (time difference) to the target and using their relative positions to one another, the bearing of the target can be determined. By separating the antenna in two planes, the elevation angle of the target can also be calculated. Other triangulation schemes could use multiple feed networks for the receive antenna and using either amplitude or phase comparison between the feeds to determine the bearing of the target. In this configuration the radar would be known as a monopulse radar, the name is due to its ability to determine the range and bearing with a single pulse [74].

Monopulse antennas are needed for a monopulse radar. Its arrangement can be such that range, velocity, azimuth and elevation of the target can be determined. This type of radar is mainly used for single target tracking. Tracking is achieved as mentioned before by determining the error in azimuth and elevation, then mechanically steering the antenna to correct the error. It is also possible for both phase and amplitude comparison to determine the target location and examples of which are shown in Figures 3.4 and 3.5, respectively. In phase comparison monopulse a minimum of two antenna are required and are separated ideally by $\lambda/2$, for an unambiguous result. It may not necessarily have to be two antennas it could be a single antenna with multiple lobes generated by the feed network along the length of the antenna. The phase difference ($\Delta\phi$) between the two antennas can be used to calculate the signals direction of arrival.

$$\theta = \sin^{-1}\left(\frac{\lambda\Delta\phi}{2\pi d}\right) \tag{3.2}$$

For amplitude comparison, the antennas main lobes would need to be overlapped, the

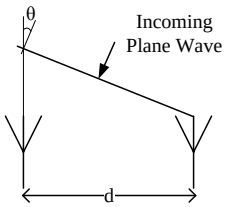

Figure 3.4: Determining the target bearing using phase comparison monopulse

centre of the two main lobes would indicate zero error. If the amplitude is not equal for both antennas, the antenna array would be steered to equate the amplitudes, thus, indicating the direction of arrival of the signal, as a function of the steered angle.

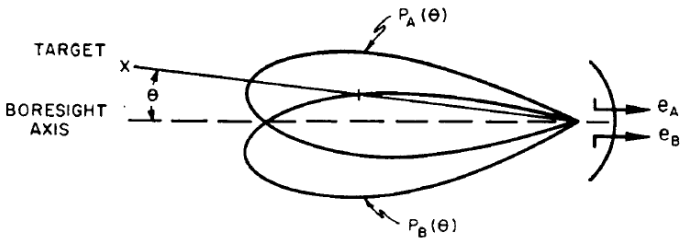

Figure 3.5: Determining the target bearing using amplitude comparison monopulse, image taken from [75]

It is also possible to measure both the error in elevation and azimuth by feeding an antenna with a four feed feed network. Although only three channels are needed, as seen in Figure 3.6 [76]. The feed network can be very simple and constructed with only four 180° hybrids. The antenna could also be used as a transceiver, this would require the sum channel to be bi-directional. Additional RF hardware such as a circulator, to cycle between transmitting and receiving. The sum channel on receive can be used to measure range, as could any channel. The two difference channels are used to determine the azimuth and elevation errors and could be configured for either phase or amplitude comparison, to determine the bearing to the target. The unused channel is the diagonal measurement between the four mainlobes and is usually terminated with a matched load.

3.5 Sea Clutter

The topic of sea clutter is broad and diverse with many factors and has been an area of research that has been studied for many years [77] [78]. Clutter is defined as the unwanted signals that the radar receives from the environment such as ground returns, weather, buildings etc... [5]. Sea clutter is the returns of a radar signal from the sea surface. Its properties change greatly

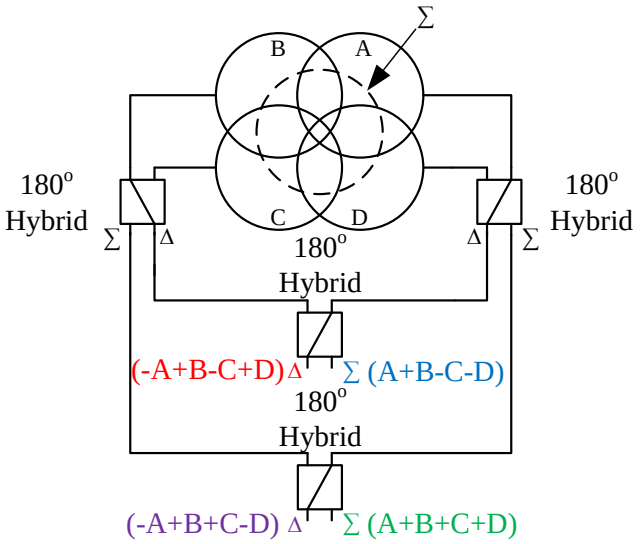

Figure 3.6: Phase-Amplitude monopulse antenna and feed network, image from [76]

with sea state, weather conditions, operating frequency, range resolution, antenna polarisation and other variables. Multiple mathematical models exist to represent the statistics and average reflectivity of sea clutter [79] [80].

The ability for a target to be seen is dependant on the received power from the target not only being greater than the noise floor of the radar, the noise limited case, however, also being greater than the clutter power, the clutter limited case.

In Section 3.1 many of the radar discussed use clutter cancellation techniques, such as Doppler filters to ensure that slow moving or stationary clutter is removed. The use of transponders as discussed in Section 3.2 can be used to enhance the target signal to overcome clutter power. Highly directive antennas also limit the area in which the clutter can affect the target signal, as can the grazing angle produced by the radar antennas and the sea surface.

When evaluating whether a target can be detected against the background clutter, the backscatter coefficient (σ^0), can be used to calculate the clutter NRCS (Normalised RCS). With clutter NRCS dependant on the factors mentioned previously. In terms of how the clutter is considered in this thesis, a backscatter coefficient is set to a constant value and how the RCS varies with range is determined, with further discussions in Section 5.2.3

3.6 Circular Array

Previously, in Section 2.5, the theory behind circular arrays was discussed; here practical applications will be reviewed. The circular array has been investigated for many years mainly in the

area of direction finding, using the phase difference between antenna elements similar to that of phase comparison monopulse [81] [82]. One of the most famous circular arrays is the Wullenwever array, a circular array of 40 dipole antennas measuring 120 m in diameter. Its purpose during the second world war was direction finding, after World War II many countries around the world had their own [8]. Although the original array used dipole antennas, to increase the directivity a reflective screen was place behind the antennas, such that the antennas radiation pattern was outwardly facing from the centre of the array.

Previously discussed in Section 2.5 was the generation of omnidirectional radiation patterns and steerable mainlobes using circular arrays for direction finding applications. Modern day uses of circular arrays still follow this main application [83]. Other variations of the uniform circular array is the sparse circular array. This is when fewer elements are used and using various algorithms are strategically placed to approximate the continual array [84] with the inter-element spacing greater than 0.5λ. Some advantages of sparse arrays are reduced sidelobe levels, less mutual coupling between elements as the elements are spaced further apart and reduced costs due to less number of elements in the array [85].

Uniform semi-circular arrays also can be used for direction finding and have been reported recently. [86], discusses a higher angular resolution of a semi-circular arrays over fully circular arrays due to an increased radius, with both having the same number of elements equally spaced at 0.5λ. Some uses of such arrays are wall mounted WLAN base stations or short range automotive radar sensor [87]. The conformal array reported on in [87] has a 64 % increase in beamwidth over a planar array, however, with a 2 dB decrease in mean directivity.

3.7 Summary

This chapter has discussed various types of navigation-at-sea systems, focusing on radars with both Pulsed Doppler and FMCW varieties commercially available today. Radars are not the only tool for marine navigation applications; optical and laser based systems with their advantages and disadvantages have also been discussed. The history of navigational aids for marine vessels were considered, with some modern day uses of short range transponder based radar systems such as personnel or vehicle identification.

For short range applications, FMCW radar systems offer significant advantages over Pulsed Doppler radars. Some of the modern hardware implementations were discussed with DDSs proving to be an ideal source for the FMCW signal. The primary purpose of a radar is the location of targets. Range is fairly easy to establish, by taking an FFT. The direction of arrival of the target can be determined using different methods, such as antenna beam direction

in a mechanically-scanned system. Monopulse systems with a single pulse can determine the bearing and range to a target, by comparing the amplitude, phase or both on more than one receive antenna.

Clutter is always present and in marine applications can be substantial. All practical radar systems will employ some method of clutter cancellation techniques. By assuming a value for the backscatter coefficient, the clutter area and clutter power variation with range is going to be considered for this thesis. Using a transponder-based radar increases the target RCS making it more visible to the radar in high clutter environments. Finally, discussed were circular arrays and how their modern day uses have not differed from when they were first developed for direction finding applications.

The background theory and literature that have been discussed thus far have led to development of a prototype radar system. As this thesis progresses it will show a system with no electronic- nor mechanical-steering, yet is able to measure both range and bearing to a cooperative target.

Chapter 4

Receive Antenna Design and Analysis

The systems shown in Chapter 3, are all physically big in size and require a large area for mounting them to vessels, hence suitable for fairly large vessels. There remains a niche market for pleasure vessels that could benefit from a low cost, lightweight and small profile system, which can be easily mounted on the ship to aid navigation in the harbour environment. With price and size being the main concern, components that make up an FMCW radar, should both be cost and size effective. If the FMCW hardware is then combined with a circular array additional mechanical or electronic steering would not be required to determine the range and bearing to a target. combining these two aspects and targets which are transponders, will further enhance the target RCS. Thus, would enable the target to be detected in high clutter environments. A technique implemented in some of the radar systems, namely RadaScan, discussed in Chapter 3.

This chapter discusses the design and analysis of the circular array antenna that can meet the prior requirements. It begins with a design of a single antenna element that approximates a cardioid pattern ensuring the phase difference between phase modes is monotonic. It is discussed alongside its potential feed network. This is then followed by the development of a printed crossed-dipole antenna, which is designed to estimate a circular array. The analysis regarding this antennas performance with respect to its gain, target bearing vs. angle monotonicity and how the bearing accuracy responds to increasing elevation angles is also considered.

4.1 9.25 GHz Circular Array

In Chapter 3, the current marine navigation radars systems fall into two bands (S (2-4 GHz) and X (8-12 GHz)). The advantage of operating in X band is that the antenna profile is significantly smaller than an S band antenna, making it ideal for smaller vessels.

Chapter 2 has already shown that the use of directive elements is a better alternative than a single omnidirectional antenna. Placing these directional antenna elements around the periph-

ery of a circle whose inter-element spacing is 0.45λ and each element with cardioid radiation pattern, will generate the required phase difference vs. angle relationship. This is essential in determining the bearing to the target and the required omnidirectional radiation pattern by the combined antenna elements, see Figure 2.23. Also, discussed in Chapter 2 was the simple patch antenna, referring back to Figure 2.9, which shows that this type of antenna very conveniently has the exact pattern required for each element. The receive circular antenna array total gain will comprise of the individual gains of each element and the array factor. The array factor is determined by scaling the array gain by the individual elements. Figure 4.1 shows the normalised array response for different element patterns, each with an 8 element array and an inter-element spacing of 0.45λ (diameter of 1.146λ for the entire array).

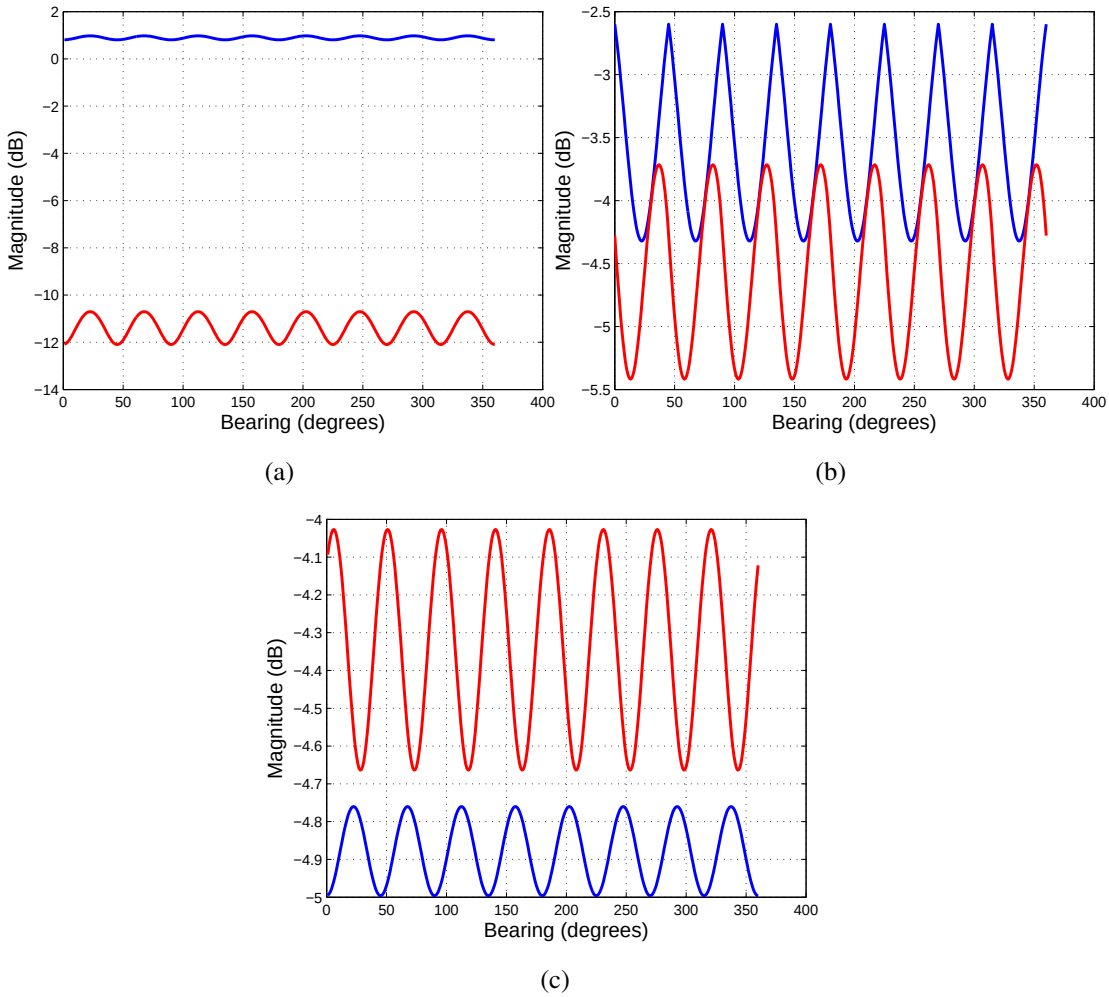

Figure 4.1: Normalised array response of an 8 element circular array with d = 0.45λ element spacing, 0^{th} order mode (blue), 1^{st} order mode (red) with (a) omnidirectional (b) $\cos(\theta)$ and (c) $1 + \cos(\theta)$ element patterns

There is a key difference between Figures 4.1b and 4.1c where the 0^{th} and 1^{st} order modes seem to switch, with the average magnitude (dB) of the 0^{th} lower than the 1^{st} for the latter figure.

This can be explained by the firstly considering a circular array with omnidirectional antenna, the array response for which is shown in Figure 4.1a. The 0^{th} order phase mode all the elements if placed fairly closer together then this should give constructive summation for all angles. For the 1^{st} order mode, the elements have a phase shift equal to their angular position. Hence, the signals cannot possibly be constructively combined and so a lower mean amplitude would be expected which is shown in Figures 4.1b and 4.1c. If the elements are directional then things are different as, typically, only one or two elements will receive a significant signal and, in this case, there should be less variation in the amplitudes of the modes.

The array responses can be used as a starting point to determine the total receiver gain, usually the array factor is positive and increases the overall gain. However, in the case of Butler Matrix type feed (shown in Figure 4.2) the array factor is negative, which can be explained in a qualitative manner. Consider a weighted element with a perfect 45° mainlobe with no sidelobes or radiation in any other direction, if there was a reflection from a target, then it would only be seen by one of the elements. However, the output power would be averaged across all the input ports, hence reducing total antenna and feed network gain. Figure 4.1c shows a minimum magnitude of -5 dB. This value must be overcome by the antenna to ensure that there is an overall gain at the receiver array.

A single patch antenna described previously has a gain of approximately 8 dBi with a cardioid radiation pattern, in the azimuth plane. This suits its application in the proposed system. However, taking into account feed losses and other losses, such as cable and connector the overall receiver gain could be entirely eroded. This led to the development of a single antenna element consisting of multiple patches all fed in phase with equal power to increase the gain of the antenna element, thereby increasing the overall receiver gain. The arrangement of the other patches has to be such that it leaves the azimuth pattern relatively intact. The specification for the antenna beamwidths was as follows, full 360° coverage in azimuth, with an approximate elevation beamwidth of 20°. This gives some scope to stack multiple patches in vertical direction to increase each elements gain. However, as the number of patches increases vertically the elevation beamwidth decreases. Using 20° as the limit [42], simulations were carried out to see how the far field radiation pattern changed with the increased number of patches and also to ensure the microstrip inset feed network combining the singular patches is performing as desired.

The arrangement of the patches can be realised either by a conformal array or an eight sided polygon. The former would be practically impossible to construct, however, the latter is much more realisable. When simulating the patches, it became apparent that the size of

the antenna element and its feed were larger than the space available to maintain a circular diameter of 1.146 λ. Therefore, a decision was made to split the array up into two sections each comprising of four antenna elements, with one section having a 45° azimuth rotation to the other. The splitting of the receive array allowed for a greater separation between adjacent elements, thereby allowing a diameter to 1.146 λ.

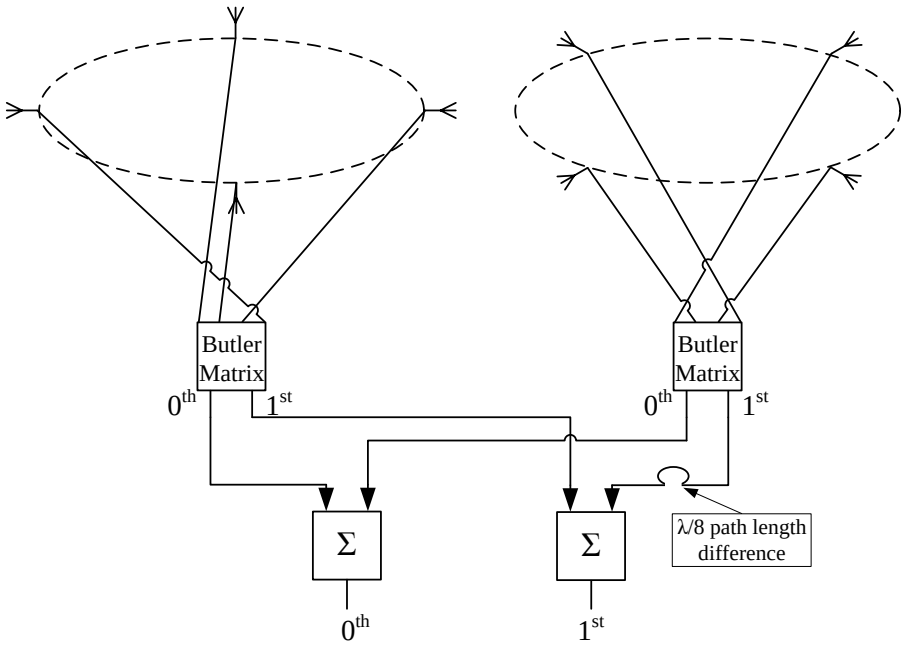

Figure 4.2: Splitting the 8 element array into two 4 elements arrays, with the associated feed network, all coaxial cables/ microstrip lines from the array to the feed network are of equal length, except for the labelled 1^{st} order mode

.

The Butler Matrix in Figure 4.2 would be of the type as shown in Figure 2.25. Where the two unused ports which have the -1^{st} and $+2^{nd}$ phase modes would be terminated with matched loads. Also shown in Figure 4.2 is an increase in transmission line by $\lambda/8$. Which is required to shift the phase of half the array by 45° from the other half for the $+1^{st}$ order phase mode. The combiners shown in Figure 4.2 would both be the same as one another with equal phase and amplitude weightings.

By splitting the array, also impacts the complexity of the Butler Matrix, from an 8 input, 8 output to a 4 input, 4 output, which is much simpler to implement, as it does not require 45° hybrids. This substitution can be made because not all the phase modes are needed in this radar system to determine the target range and bearing. As previously mentioned only the 0^{th} and 1^{st} order modes are needed, with the phase difference indicating the bearing of the target. One

final note to make is that by splitting the array in elevation every adjacent element is now further apart. Hence, intrinsically reducing the effects of mutual coupling between the elements. The intended arrangement of the antenna elements is shown in Figure 4.3.

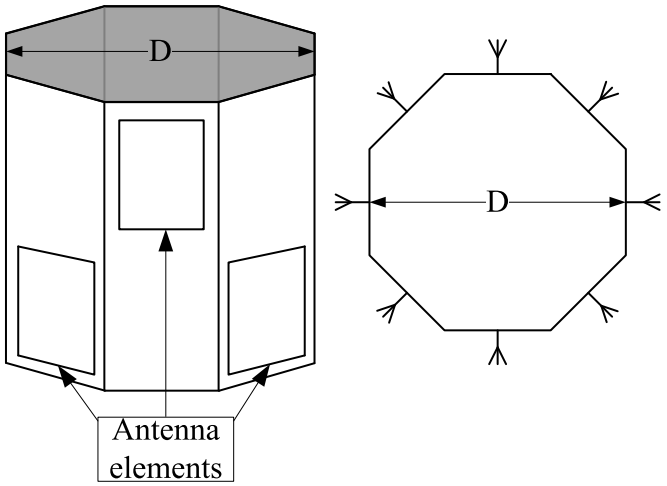

Figure 4.3: Splitting the array in elevation, with the elements arranged around the perimeter of an octagon

The antenna element design was carried out in stages; firstly a single patch antenna was designed using the equations in Section 2.4.5. Its resonance was calculated and then a second was vertically stacked, this process was repeated twice, to finally realise the design in Figure 4.4. At every stage the azimuth and elevation radiation pattern was checked to ensure it continued to stay within initial beamwidth specification. Another aspect to consider was the actual size of the PCB that the antennas were designed on, the height was set at about $5\lambda_g$ (0.109 m). This design was optimised for Rogers Duriod 5880 with a substrate thickness of 0.787 mm, a copper thickness on both sides of 35 μm and a dielectric constant of 2.2. This PCB was chosen due to its low dielectric constant, hence lower losses. However, the physical size of the patches and the feed network were large enough enabling it to be machined.

The single patch was designed to resonate at 9.25 GHz with a 50 Ω input impedance, initially with an inset feed such that multiple patches could be connected together to form single antenna element. The inset was calculated again using the equations in Section 2.4.5, but then optimised for each doubling of the number of patches. Every increase in the number of patches required minor adjustments to the size of the patches and the spacing in between the antenna, ensuring correct a resonant frequency.

By having the feed network on the same side as the antenna, its size is comparable to

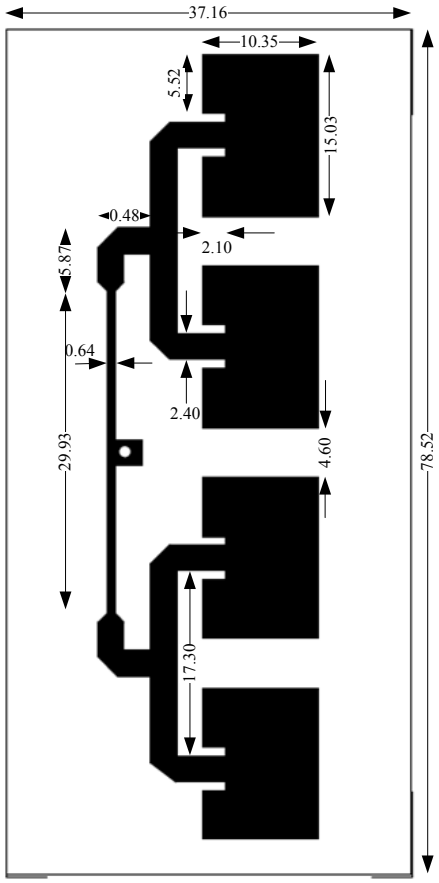

Figure 4.4: The four vertically stacked patch antennas with associated power splitter feed network (mm)

the antennas, hence it too resonates. This is the reason for the antenna main lobe not being at 0° azimuth, as shown in Figure 4.6a. The feed network ensures that each patch is in phase and has equal amplitude with one another. It is fairly similar, however with a few differences, to a microstrip Wilkinson power divider [88] and the impedances of the microstriplines are as follows: Each patch is matched to 50 Ω, connected to a 50 Ω microstrip transmission line, which calculated to be 2.40 mm wide, given by equation (4.1) [89]. The variables are the same as in equations (2.49) and (2.48), also note as there is no variable for the thickness of the copper this formula, hence will only apply for thin layers. Where two patches first connect, the impedance is 25 Ω, as two 50 Ω combine in parallel, which is connected to a quarter-wave transformer. Thus, transforming the impedance to 100 Ω. The two 100 Ω transmission lines again combine in parallel at the centre to transform the impedance back to 50 Ω. This is then probe fed with a

SMA connector or similar, soldered on the reverse.

$$Z_o = \begin{cases} \frac{60}{\sqrt{\varepsilon_{eff}}} \ln\left(\frac{8h}{W} + \frac{W}{4h}\right), & \text{when } \left(\frac{W}{h} < 1\right) \\ \frac{120\pi}{\sqrt{\varepsilon_{eff}} \cdot \left[\frac{W}{h} + 1.393 + \frac{2}{3}\ln\left(\frac{W}{h} + 1.444\right)\right]}, & \text{when } \left(\frac{W}{h} \geq 1\right) \end{cases} \tag{4.1}$$

The 3D radiation pattern of the simulated patch antenna is shown in Figure 4.5. Simulations were carried out using CST MWS, as it is able to carry out full 3D analysis of the antenna, both in near and far field. Figure 4.5 also shows the arrangement of the adjacent antenna elements, this however is not the final arrangement for the antenna elements as it does not include half of the array. This would be offset by 45°, the full array can be seen in Figure 4.8. The array was simulated in parts to reduce simulation time (~ 15 hours) and system resources. The main result from Figure 4.5 is the gain of this array for a single antenna elements in the presence of three others arranged in a cuboid structure is approximately 12.5 dBi. This result however, does not include the mutual coupling between elements, which will cause the maximum gain to reduce and may even cause the resonant frequency to shift. Assuming that the gain of a single antenna element is true for all the elements and the effects of mutual coupling are negligible. Then finally recalling the array factor for the feed network, which indicates an average gain of -4.6 dB, the entire receive arrays overall gain would be approximately 7.9 dBi. Accounting for feed losses and mutual coupling this value will probably reduce to around 7 dBi.

The -3 dB beamwidth for the antenna are 85.6° and 20.9° for azimuth (ϕ = 0°) and elevation (ϕ = 90°) respectively (see Figure 4.6). The elevation is within the specification that was initially put forward, the azimuth beamwidth may seem a bit low, but there are going to be eight of these antenna elements around the periphery of a octagon. Provided that an azimuth beamwidth is greater than 45° for each antenna element, the full omnidirectional pattern should still be maintained.

The simulation for the return loss (S_{11} S_{22} S_{33} S_{44}) looks very promising as they all have troughs below -20 dB, indicating good resonance at 9.25 GHz. The antenna has a -10 dB bandwidth of approximately 400 MHz, the approximate required bandwidth for this design was only 100 MHz. From the configuration of the antenna in Figure 4.5, there will be three distinct S-parameter couplings: the return loss of the antenna under test, the coupling between the antenna under test and the antenna geometrically opposite and the mutual coupling between an antenna and its adjacent two antenna. All S-parameter couplings are shown in Figures 4.7a, 4.7b and 4.7c respectively.

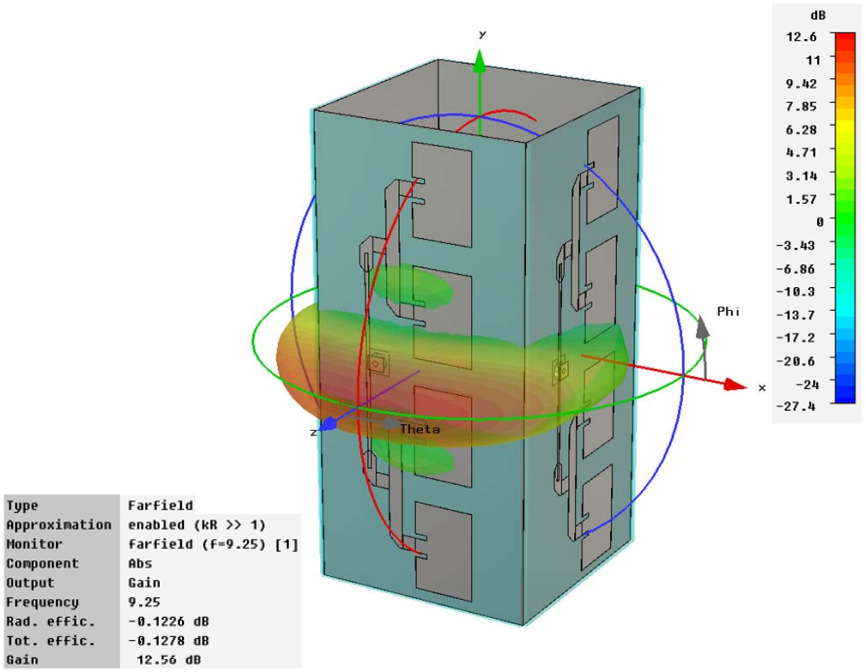

Figure 4.5: 3D radiation pattern of 4 antenna elements arranged around the perimeter of a cuboid

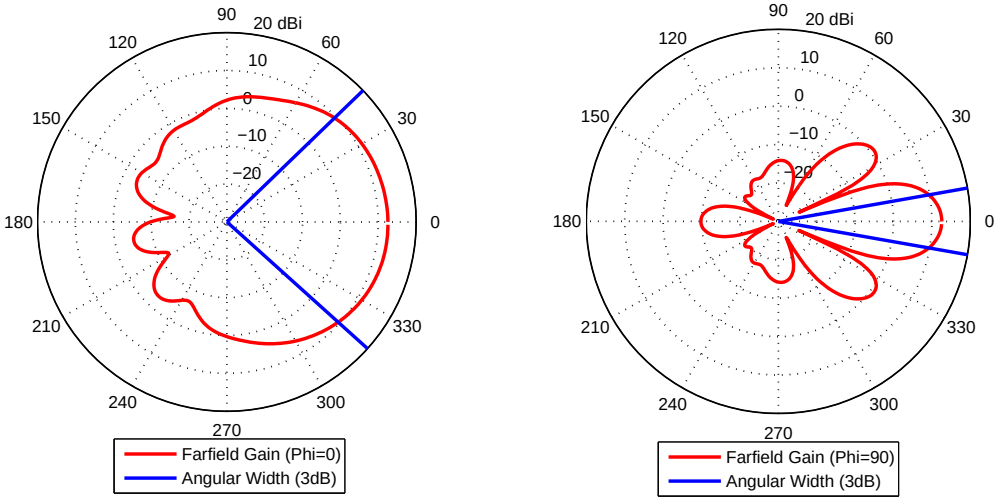

(a) (b)

Figure 4.6: Simulated far field gain at (a) $\phi = 0°$ (b) $\phi = 90°$ of the antenna depicted in Figure 4.4

4.1.1 9.25 GHz Circular Array - Feed network

Using a Butler Matrix to correctly feed the entire array may be problematic due to the various components needed to construct the four port Butler Matrix (three 180° hybrids, a 90° hybrid and a crossover). It has already been established that only two out of four outputs will be needed to determine the bearing of the target. As the feed network would have to be in the centre of the

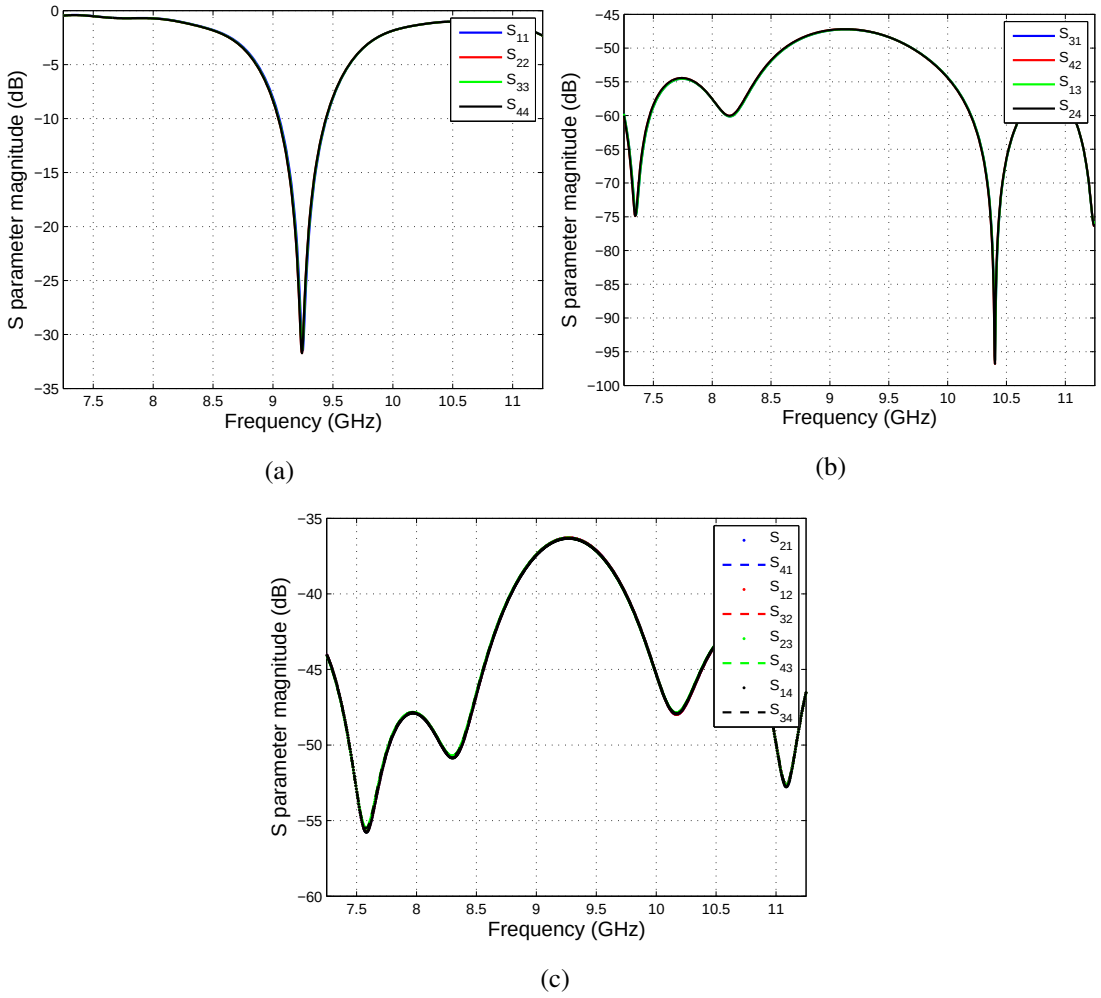

Figure 4.7: S-parameters for the array configuration as shown in Figure 4.5

array with the elements around it, the amount of space would be quite limited. It was therefore decided that a system of equal line lengths would be employed for the 0^{th} order, as there is no phase deviation between the elements. For the 1^{st} order a system of increasing line lengths is used, such that the phase of the element corresponds to its position relative to the first element. For the 1^{st} order there would also have to be an additional phase shift of 45° degrees between the top and bottom halves of the array, a phase shift not required for the 0^{th} order feed.

Note that the probe feed for the antenna is not in the geometric centre and that this 50 Ω probe feed point would have to be accessed by two separate feed networks (0^{th} and 1^{st}). It imposes an initial line impedance of each feed to 100 Ω. When all eight feeds combine in parallel they would have to be matched to a 50 Ω input impedance, such that the antenna could be connected via a coaxial cable to the radars receiver port. Taking the 0^{th} order as an example, the impedance of the microstrip lines are matched as follows: The four lines of the 0^{th} order feed network of 100 Ω each combine in the centre to give 25 Ω, which then is transformed using

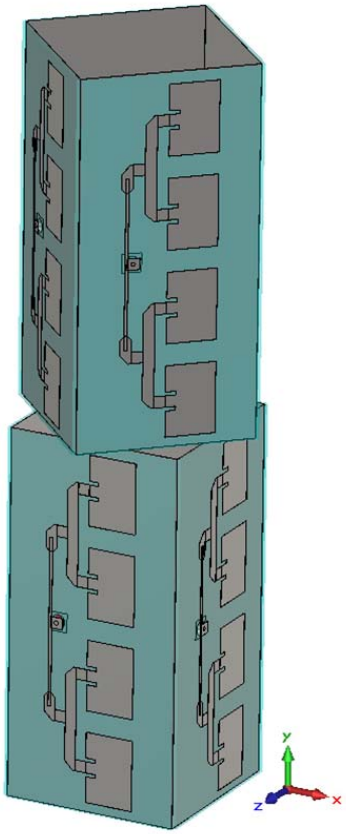

Figure 4.8: Intended arrangement of the antenna elements

a quarter wave transformer to 100 Ω. Finally, the top and bottom half of the 0^{th} feed network combine to a 50 Ω transmission line with a single coaxial connector per feed network.

There are four different PCBs that make up the total feed network described above. Their individual designs are shown in greater detail in Appendix B.

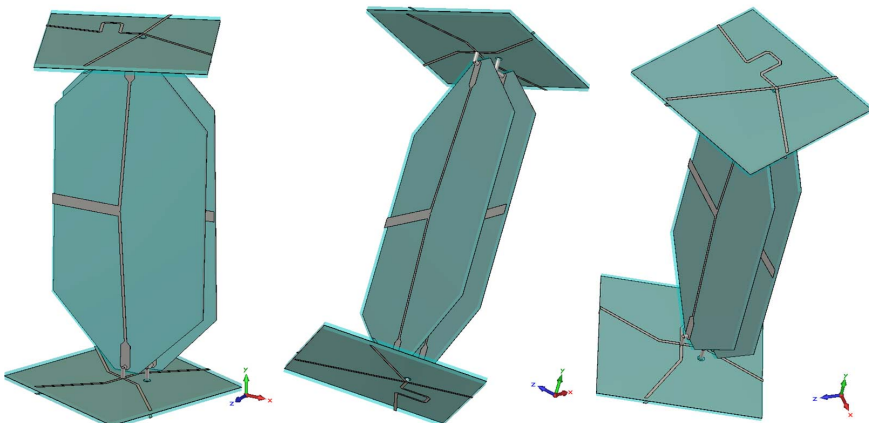

Figure 4.9: The entire feed network from three different perspectives

To conclude Section 4.1, the complexities involved with the feed network resulted in the development for this antenna to stop at the simulation stage. The only PCBs to be constructed

were two 9.25 GHz patch antenna element, with their return losses shown in Figure 4.10. The first example was tested using a network analyser and S_{11} of the antenna was -12 dB at 9.44 GHz, a deviation of 0.19 GHz (2.1%) from the desired centre frequency. Each of the patches widths were reduced in an attempt to shift the measured resonant frequency lower to the desired 9.25 GHz. A new constructed altered antenna was tested and was resonating at 9.12 GHz with an S_{11} at approximately -15 dB, the frequency was shifted in the correct direction, but slightly more than desired.

This is where the construction ended and this approach to the circular abandoned. The main reasons for stopping the development revolved around the feed network, its design meant that it was likely to be very lossy. The spacing between the vertical PCBs of the 0^{th} and 1^{st} order feed networks was optimised to be approximately 2 mm apart, making it virtually impossible for a coaxial cable or connector to fit in this space. The position of the pin to connect the horizontal and vertical parts of the 1^{st} order feed network results in the board being slightly twisted, thus its mounting would be fairly difficult.

The focus was then shifted to a crossed-dipole antenna, which is where this thesis now progresses.

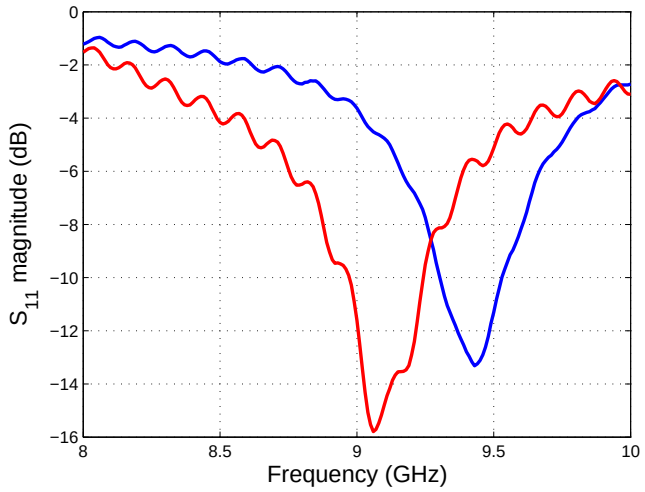

Figure 4.10: Measured S_{11} from the two constructed prototype patch antenna

4.2 Crossed-dipole Antenna

This type of antenna, as discussed in Section 2.4.6 has an omnidirectional pattern about its centre, orthogonal to the plane of the antenna. A crossed-dipole comprises of two dipoles in quadrature with one another, the far field radiation pattern of each dipole in the plane of the antenna as that of Figure 2.13b. Crossed-dipoles have been explored for use with DF since the 1940s, with further information regarding operational characteristics discussed in [90]. When considering both dipoles with one dipole having an elevation radiation pattern similar to that of a *cosine*. The other dipole, a geometrically rotated dipole by 90°, hence, has a *sine* pattern. If the dipoles patterns were exactly cosine and sine, the in phase addition of the two would result in an perfect omnidirectional pattern ($|\cos\alpha + j\sin\alpha| = 1$). The -3 dB elevation beamwidth for a electrically short dipole is 90°, but for the practical half-wave dipole, this elevation beamwidth value reduces to 78°, as previously discussed. The imperfect omnidirectional pattern can be thought of as introducing an amplitude ripple in the combined elevation radiation pattern. However, the bearing indication relies on comparing the target phase received at these two antennas and provided that the phase varies monotonically, the amplitude ripple should not be too significant. This type of approach for bearing estimation can be considered similar to a phase comparison monopulse system, which was previously discussed in Section 3.4.

To understand the operation of the crossed-dipole antenna, it is easier to first analyse it in terms of an electrically short dipole, whose radiation pattern tends to $\cos\alpha$. Where, α is the angle to the normal of the dipole, as shown in Figure 4.11. This figure also shows how the $+1^{st}$ and -1^{st} phase modes can be extracted, using a crossed-dipole antenna feeding into a 90° hybrid. The output of the two phase modes can be expressed as:

$$P_{+1} = V(\cos\alpha + j\sin\alpha) = Ve^{j\alpha} \tag{4.2}$$

$$P_{-1} = V(j\cos\alpha + \sin\alpha) = Ve^{j(-\alpha+\frac{\pi}{2})} \tag{4.3}$$

Referring back to Section 2.5.1 it is clear that these are perfect phase modes. However, the -1^{st} order mode does have a $\pi/2$ offset. The phase difference between these two phase modes is:

$$\angle P_{+1} - \angle P_{-1} = 2\alpha - \frac{\pi}{2} \tag{4.4}$$

This result shows that the phase difference between the phase modes will vary linearly at twice the rate of the angular bearing albeit with a 45° angular offset. As mentioned previously,

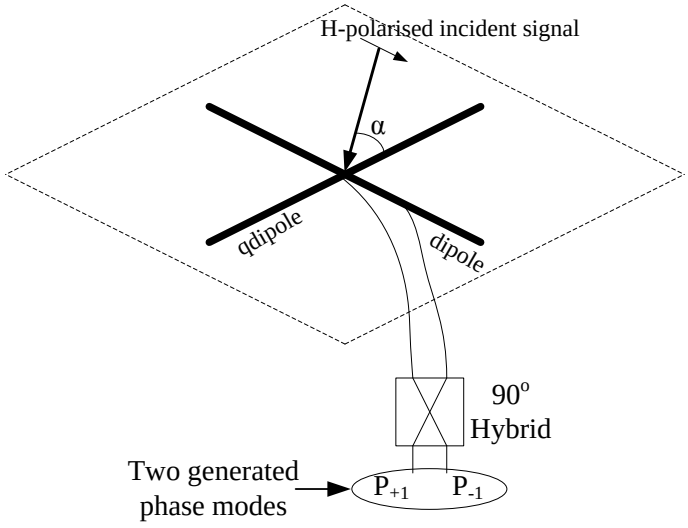

Figure 4.11: Crossed-dipole antenna receiving an incident horizontally polarised signal in the plane of the antenna

the half-wave dipole is the more practically reliable, hence, the phase modes of equations (4.2) and (4.3) need to be modified for the radiation pattern of the half-wave dipole. The equation for the electric field for a half-wave dipole is given as [6]:

$$E(R,\alpha) = j\eta\frac{I_0 e^{-j\beta R}}{2\pi R}\left[\frac{\cos\left(\frac{\pi}{2}\cos\alpha\right)}{\sin\alpha}\right] \tag{4.5}$$

where, η, in this equation is the intrinsic impedance (377 Ω). For a half-wave dipole, the component in equation (4.5) which is 'α' dependant is proportional to the radiation pattern of the dipole and is not too dissimilar to a '$\cos\alpha$' pattern. The phase modes can then be written in terms of the +1st and -1st order phase modes:

$$P_{+1} = V\left(\left[\frac{\cos\left(\frac{\pi}{2}\sin\alpha\right)}{\cos\alpha}\right] + j\left[\frac{\cos\left(\frac{\pi}{2}\cos\alpha\right)}{\sin\alpha}\right]\right) \tag{4.6}$$

$$P_{-1} = V\left(j\left[\frac{\cos\left(\frac{\pi}{2}\sin\alpha\right)}{\cos\alpha}\right] + \left[\frac{\cos\left(\frac{\pi}{2}\cos\alpha\right)}{\sin\alpha}\right]\right) \tag{4.7}$$

As discussed previously, the half-wave dipole radiation pattern is approximately equal to a $\cos\alpha$ pattern. Hence, both the phase and amplitude differ from the perfect phase mode and both have reduced linearity. An amplitude ripple of 1.03 dB is shown in Figure 4.14b for the crossed-dipoles azimuth plane. However, the phase deviation from linearity in the phase difference between the +1st and -1st order phase modes is more evident, which is shown in

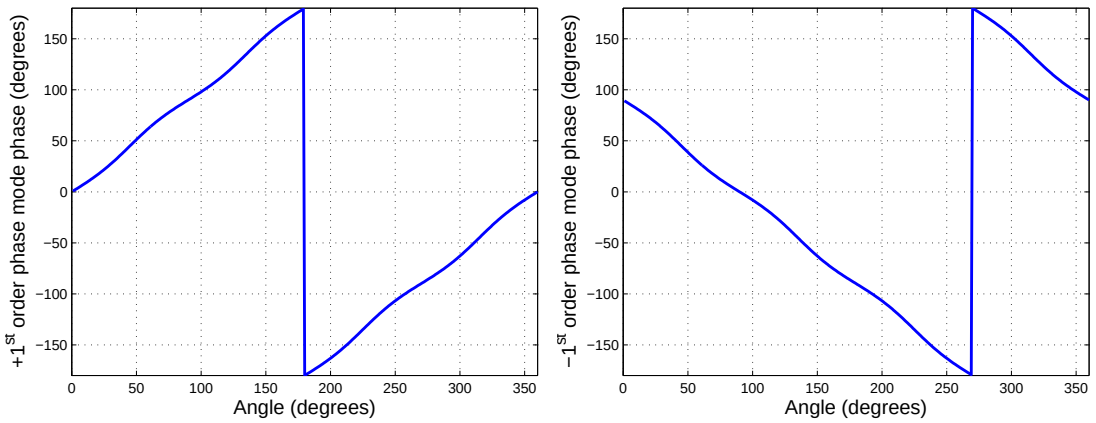

(a) (b)

Figure 4.12: Simulated phase of (a) +1st (b) -1st order phase modes from a half-wave crossed-dipole antenna

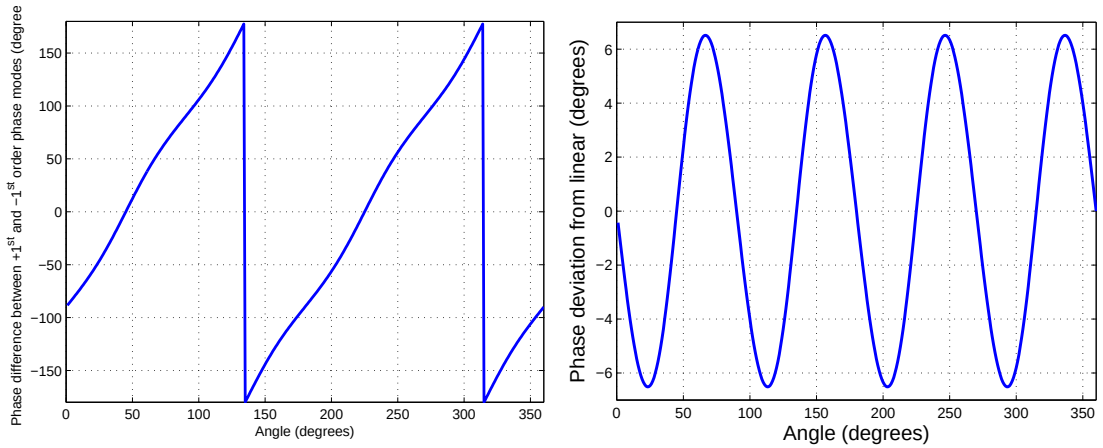

(a) (b)

Figure 4.13: (a) Simulated phased difference between the +1st and -1st order phase modes (b) phase deviation from linear of the simulated phased difference between the +1st and -1st order phase modes

Figure 4.13. With a phase ripple of ±6.51° (4.61° RMS) and as discussed previously, this relates to an angular bearing ripple to one half of the phase ripple. Hence, the bearing ripple is ±3.26° (2.30° RMS). Referring back to Figure 2.23b, both the amplitude and phase ripples are slightly higher for this crossed-dipole antenna, than implementing a 0th and +1st order phase mode antenna system. However, the feed required is significantly simpler to implement than that described in Section 4.1.1.

The fundamental disadvantage of the crossed-dipole arrangement presented here is that it is unable to provide a 0th order phase mode, only the +1st and -1st order phase modes. Whereas, the circular patch antenna array described in Section 4.1 generates 0th and +1st phase modes. Due to the lack of the 0th phase mode in a crossed-dipole antenna, the bearing suffers from a

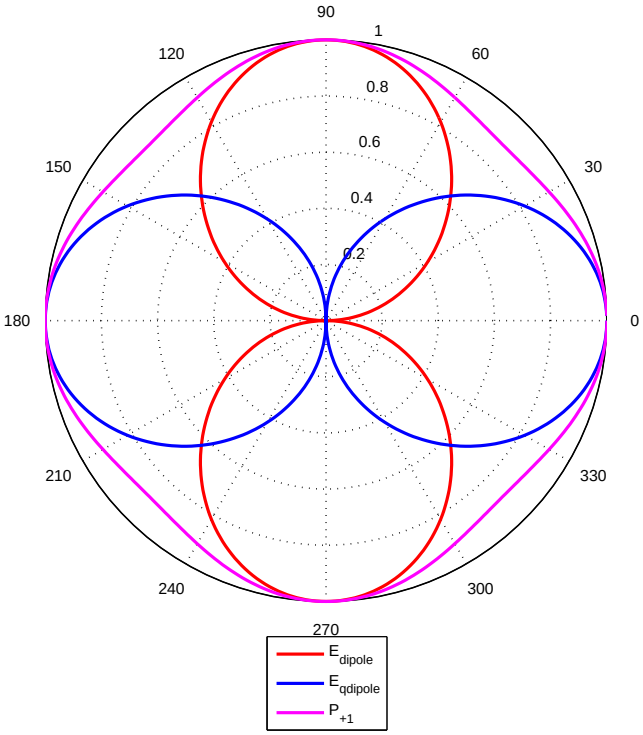

(a)

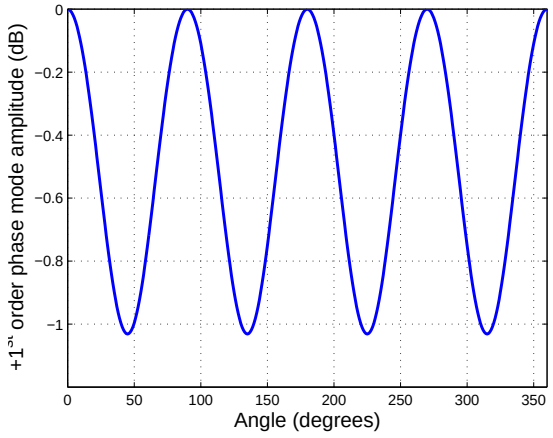

(b)

Figure 4.14: (a) Simulated normalised radiation pattern magnitude of two dipoles in quadrature and the $+1^{st}$ order phase mode magnitude (b) $+1^{st}$ order phase mode amplitude ripple (dB) from a half-wave crossed-dipole antenna

180° ambiguity. This is due to the difference between the $+1^{st}$ and the -1^{st} phase modes having a 720° change of phase for every 360° of azimuth rotation. Hence, the target bearing is mapped to two possible difference angles 180° apart. In terms of performance this constraint would restrict the use of the system to an angular sector of 180°. With other large structures on the top surface of ships, it is likely that the field of view will be restricted to less than 180°. In the typical application, the ambiguity may not be a significant problem, also with the use of historic information the ambiguity may be resolved. However, its no longer a fully omnidirectional

radar system.

As discussed in Section 3.1 there is great importance in receive antennas elevation beamwidth due to the vertical motion of the ship. Hence, it is vital to understand how the crossed-dipole behaves when the target bearing is measured in azimuth at unknown elevation angles. Using the antenna geometry, as shown in Figure 4.15. On reception of a signal from an azimuth angle, γ, and elevation, ϕ. α from equations (4.6) and (4.7), which is the angle of incidence to the antenna, can be expressed as a function of both azimuth, γ, and elevation, ϕ, as follows:

$$\alpha = \tan^{-1}\left(\frac{\cos\phi\sin\gamma}{\sqrt{\sin^2\phi + \cos^2\phi\cos^2\gamma}}\right) \tag{4.8}$$

The increased elevation has the affect of introducing a polarisation mismatch resulting in a

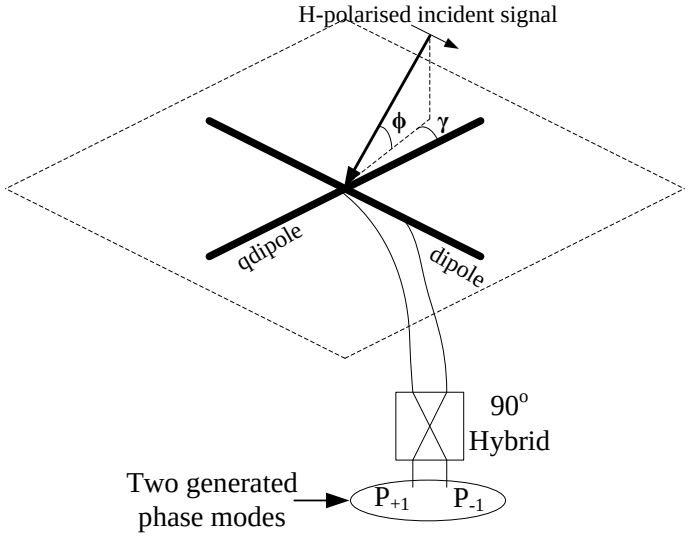

Figure 4.15: Crossed-dipole antenna receiving an incident horizontally polarised signal at an azimuth angle, γ and elevation, ϕ

reduction in the signal amplitude by a factor:

$$polfactor = \mathrm{sgn}(\cos\gamma)\cos(\tan^{-1}|\sin\phi\tan\gamma|) \tag{4.9}$$

Equations (4.8) and (4.9) can be used to extend equations (4.6) and (4.7). Figure 4.16 shows how the amplitude and phase ripple vary for incident angles at elevations from 0° to 30°.

It is clear from Figure 4.16 and Table 4.1 that with increased elevation the phase modes

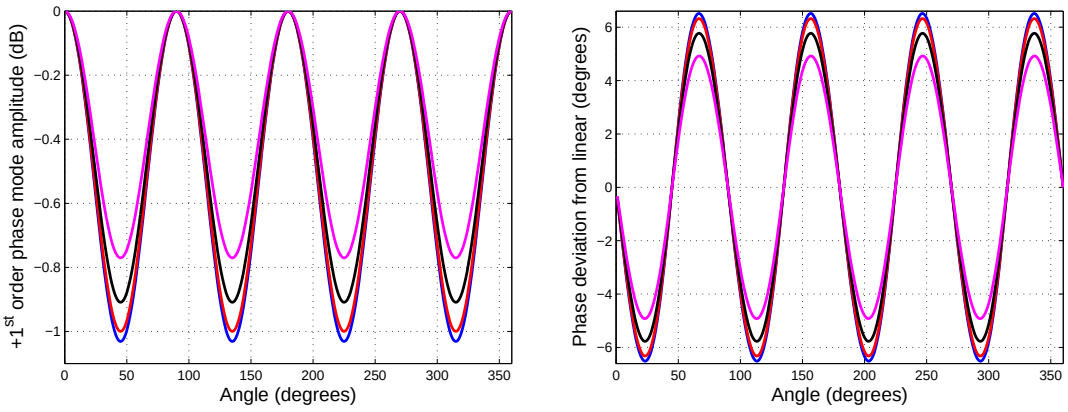

(a) (b)

Figure 4.16: Simulated (a) amplitude ripple of the +1st order phase mode (b) phase deviation from linear of the phase difference between +1st and -1st order phase modes, for incident signals of increasing elevation 0° (blue), 10° (red), 20° (black) and 30° (magenta)

Table 4.1: Affects from increasing elevation angles on the amplitude ripple from the +1st order phase mode and phase difference ripple from the phase difference between the +1st and -1st order phase modes

Elevation Angle (degrees)	**Amplitude Ripple +1st Phase Mode (dB)**	**Phase Difference Ripple (degrees)**	
		Pk-Pk	**RMS**
0	1.03	± 6.51	4.61
10	1.00	± 6.32	4.47
20	0.91	± 5.77	4.08
30	0.77	± 4.92	3.48
40	0.62	± 3.86	2.73
50	0.42	± 2.74	1.93
60	0.25	± 1.66	1.18
70	0.12	± 0.78	0.55
80	0.03	± 0.20	0.14
90	0.00	0.00	0.00

become more perfect i.e. more linear. The worst case in terms of ripple is when the incident received signal is in the same plane as the antenna. This can also be interpreted from equation (4.9), when the elevation angle is 90° the dipoles radiation patterns would be $\cos\gamma$ and $\sin\gamma$. This shows that the crossed-dipole is very tolerant to variations in highly elevated received signals, hence, ideal for marine radar applications.

4.3 Summary

This chapter has revealed that a conventional circular array system will present some issues with development at high (X-band) frequencies, due to the position and size of its feed network. The orientation especially has some issues because of the vertical 1st order feed network PCB, which meant that mounting attaching a coaxial cable to the feed network would be physically

impossible, due to the small gap (~2 mm) between the vertical feed network boards. If a more realisable feed network could be designed, perhaps using a different technology, then this antenna could be used as part of the radar system. The advantage of such a system would its size with the whole antenna and feed fitting into the size of ~150 x ~37 mm. At this present time there is no continuation of developing this antenna and feed.

An alternative was suggested based on a crossed-dipole antenna, the phase mode theory associated with circular array antenna also applies to the crossed-dipole. The feed network for a simple dipole consists of balun. The transformer balun discussed in Section 2.4.6 is conveniently small and can be integrated easily. The other required component is the 90° hybrid can be bought as an off the shelf component and connected via a coax cable to the feed network. One disadvantage of the crossed-dipole is the 180° ambiguity as the antenna can only generate the $+1^{st}$ and -1^{st} order phase modes. Hence, lacks the required 0^{th} order phase mode for unambiguous 360° azimuth coverage, which could have been achieved with the 9.25 GHz array. Finally, it has been shown that the crossed-dipole antenna is very tolerant to elevation angle and the phase difference between the phase modes have no phase ripple when the arriving signal is normal to the plane of the antenna.

Chapter 5

Radar System Development

Crossed-dipole performance has been analysed in Section 4.2. This chapter begins with the development of two different printed crossed-dipole antenna. For most FMCW radar systems the transmitter is a separate antenna and its development is also discussed. This chapter then proceeds to discuss the development of the prototype radar, including all of the internal components and relevant designed PCBs. When a prototype radar system is being designed a watchful eye must be kept on the link budget to ensure that correct components are chosen and that the noise figure of the system is kept low to maximise the SNR. Hence, the link budget is shown as well as the estimated and actual noise figure for this radar.

The active target is a vital component of this radar system, it is therefore analysed to determine how it can be improved to reduce the clutter and enhance the SNR. The various active target designs are also shown, with first concepts to the final working prototype, which was eventually used to generate the results in Chapter 6. The final component before the deramped signal can be analysed, is the final active bandpass filter which is used to compensate for the low powered signal arriving from long ranges. This bandpass filter relies on the minimum and maximum deramped frequency as well as the dynamic range of the ADC.

5.1 Antenna Development

A simple dipole antenna can be constructed using two pieces of wire, where each one is $\lambda/4$ long or simpler still a piece of stripped coax cable. A more sturdy approach would be to design the dipole on a Printed Circuit Board (PCB). Hence, allowing a transformer balun to be mounted as close to the antenna as possible, thereby minimising losses. To accommodate the balun, the crossed-dipole antenna was first designed over both sides of a double sided FR-4 PCB. This is where this section begins and later leads to the quadriphase-fed crossed-dipole antenna.

5.1.1 Balun-fed Crossed-dipole

Initial simulations of the crossed-dipole antenna began with modelling it using CST MWS. Firstly, the operating frequency was lowered to S-band ISM band (2.400-2.4835 GHz). Previously discussed were navigation at sea radar systems operating in the S-band with the majority of them closer to 3 GHz rather than the ISM band. The choice of using the ISM band for the prototype is ideal as it allows using many off the shelf Wi-fi components. Another obvious feature is the increase in size of the antenna, from 9.25 to 2.44 GHz centre frequency, the size of the antenna will increase by approximately 400%. This size increase is vital for prototyping when considering the size of each dipole's conductor at X-band would be approximately 8.1 mm whereas the S-band would be 31.25 mm. Finally, this increase in size allowed for further rigidity of the antenna. For a compact radar system, the higher frequency would allow for smaller antenna, but an increased frequency has a higher propagation loss over the same distance. Hence, another advantage of using the lower frequency band.

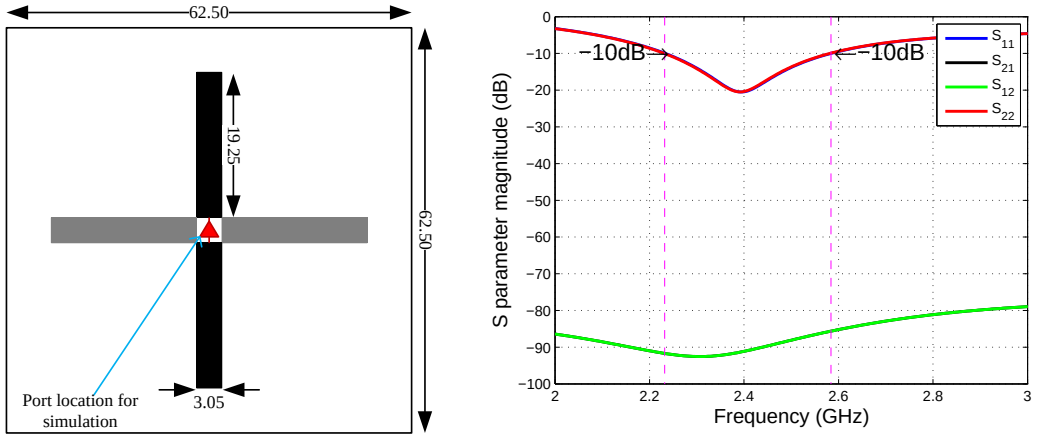

(a) (b)

Figure 5.1: (a) Dimensions (mm) of the balun-fed crossed-dipole designed on lossy FR-4 substrate (substrate thickness of 1.6 mm) and a copper clad thickness of 35 μm (grey dipole is on the reverse side of substrate) (b) Simulated S parameters (magnitude (dB)) for the balun-fed crossed-dipole as shown in (a)

The simulation results from an ideal dipole operating at 2.4 GHz are shown in Figures 5.1 and 5.2. A 50 Ω port was placed between opposite arms arm of the dipole, providing a perfect 180° phase difference between the conductors, representing a perfect balun. The S_{11} and S_{22} magnitudes show that the ideal dipole has a bandwidth of 352 MHz (≈15%) across -10 dB. Figures 5.2a and 5.2b show that the -3dB elevation and azimuth beamwidths are approximately 84° and 360° respectively, both agreeing well with theory. The other dipole that makes up the crossed-dipole has the same azimuth radiation pattern, but has a rotated azimuth far field by 90°. The important aspect of the proposed system is how the amplitude ripple varies in the plane of

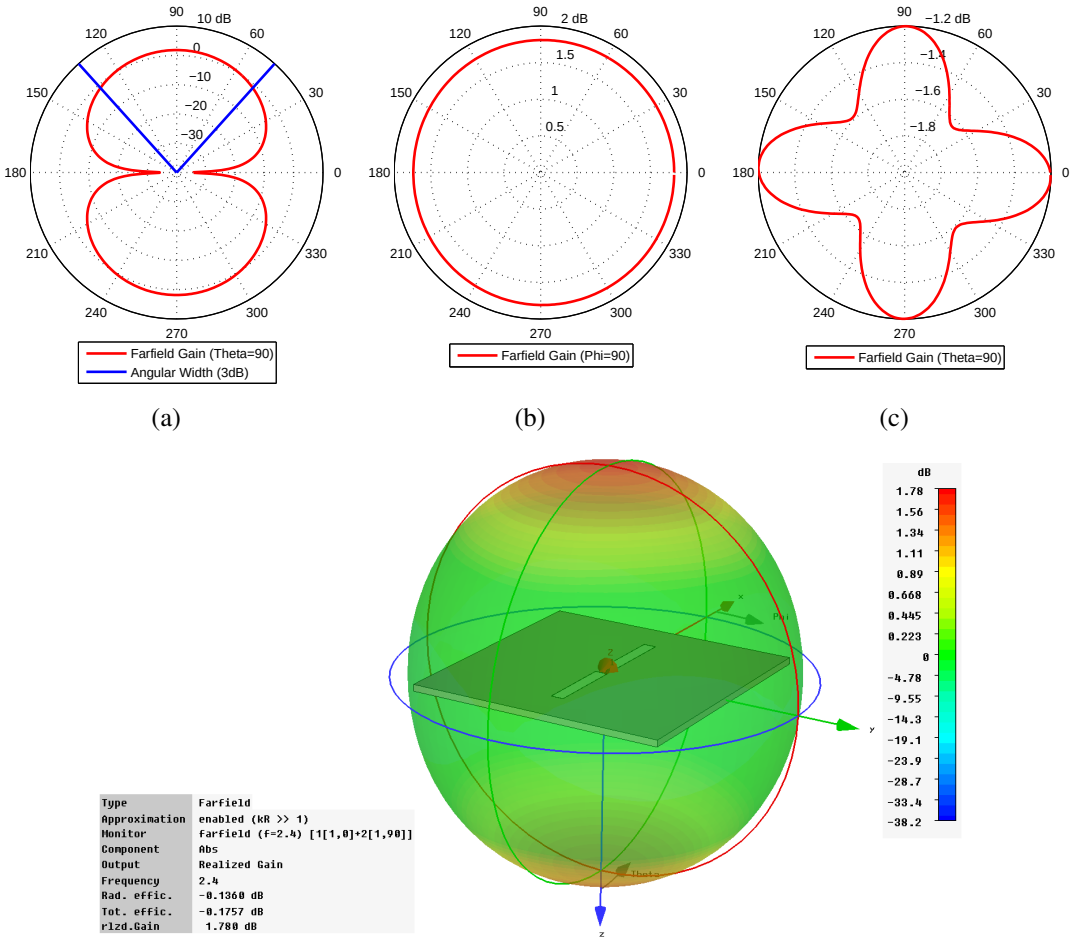

Figure 5.2: Simulated (a) Elevation ($\theta = 90°$) (b) Azimuth ($\phi = 90°$) 2D far field radiation pattern for one of the dipoles that make up the crossed-dipole, as depicted in Figure 5.1a (c) 2D far field radiation pattern for the crossed-dipole antenna in the plane of the antenna (d) 3D far field radiation pattern, when both dipoles are stimulated simultaneously with one dipole having a 90° phase shift (the coordinate system for the simulation is as shown in the far field (d) and as Figure 2.15)

the antenna, hence its depiction in Figure 5.2c. For this simulated antenna there is a 0.5 dB ripple in the realised gain of the antenna. The realised gain includes the fact that an antenna has some mismatching loss and loss in efficiency. Whereas, if the simulation showed just the gain or directivity these losses would be excluded respectively, hence, why the simulation data is depicted in this format. When the crossed-dipole is simulated, the combination of far fields causes the maximum antenna gain to be perpendicular to both dipoles as shown in Figure 5.2d.

By simulating the antenna, the exact gap between each arm of the dipole could be optimised and verified that this gap is sufficiently large enough to accommodate the physical size of the balun. Also, the dielectric properties of the PCB would alter the length of the dipole. Hence, the length as well as the width could both be optimised at the simulation stage. Section 2.4.6

discussed how the dipole is a balanced antenna, the coax cable connecting it to the rest of the radar is unbalanced, hence the requirement of a balun. As the gap between the antenna would be fairly small it would be ideal for a 1:1 transformer balun. The one chosen for this antenna was the NCS1-292+ (available from www.minicircuits.com, 2011), whose circuit is shown in Figure 5.3, its small profile, pin locations and operating frequency (1.650 - 2.850 GHz) were all ideal for this application. As this is a 1:1 balun and the assuming the antenna is a resonant dipole, hence, has a real impedance of 70 Ω, the reflection coefficient, $|\Gamma|$, can be calculated:

$$|\Gamma| = \left|\frac{Z_L - Z_0}{Z_L + Z_0}\right| \tag{5.1}$$

which equals 0.167, then the return loss (RL) and VSWR can be calculated using:

$$RL = -20 \log_{10} |\Gamma| \tag{5.2}$$

$$VSWR = \frac{1 + |\Gamma|}{1 - |\Gamma|} \tag{5.3}$$

which are 15.55 dB and 1.40 respectively, this suggests although the match is not prefect it should be sufficient.

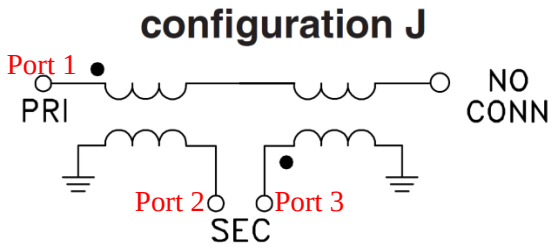

Figure 5.3: NCS1-292+ balun circuit diagram, image obtained from manufactures data sheet [91], labelled ports are for the benefit of Figure 5.4

Figure 5.4 shows that the balun is not quite ideal, the amplitude and phase imbalance between the output ports (ports 2 and 3) relative to the input port (port 1), across the 83.5 MHz bandwidth is from 0.93 to 1.01 dB and -170 to -169° respectively. Ideally, the amplitude imbalance between the outputs should be 0 dB and the phase 180°. This result was obtained with the use of the S parameter file provided by the manufacturer of the balun, with the assumption that the balun is operated at room temperature.

Some optimisation techniques were required for the actual antenna. Firstly, by altering the length and width of the dipole, would make the antenna resonate at the centre frequency.

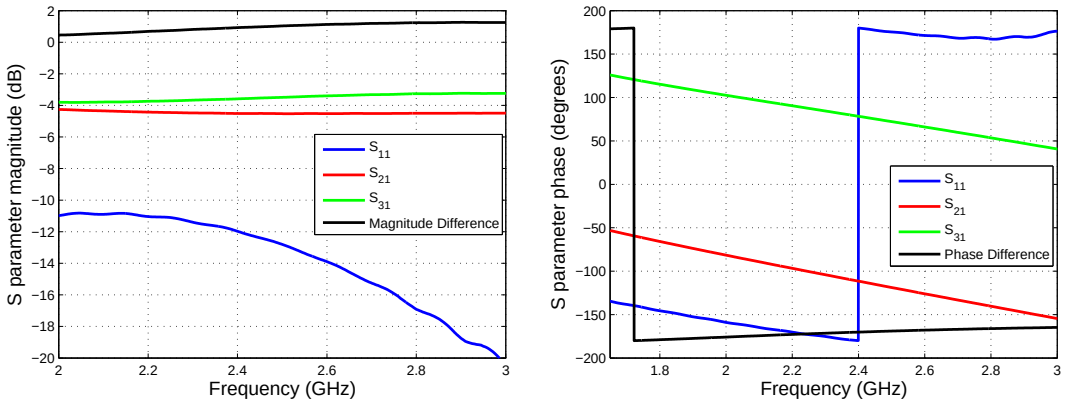

(a) (b)

Figure 5.4: S parameters for the NCS1-292+ balun (a) magnitude (dB) (b) phase (degrees), generated using the .s3p file available from the manufacturer

Secondly, the gap between the dipole arms could be altered slightly, however a minimum size was required to accommodate the balun. Also, to ensure that the balun circuit board had as little interference as possible it was mounted vertically, such that both balun PCBs were perpendicular to the crossed-dipole antenna. In addition, a small acrylic wedge was glued behind the balun PCB and to the antenna substrate to increase the integrity of the solder joint between the balun and the dipole. This was not ideal as the wedge was over one arm of the adjacent dipole as shown in Figure 5.5, but definitely required when testing this antenna.

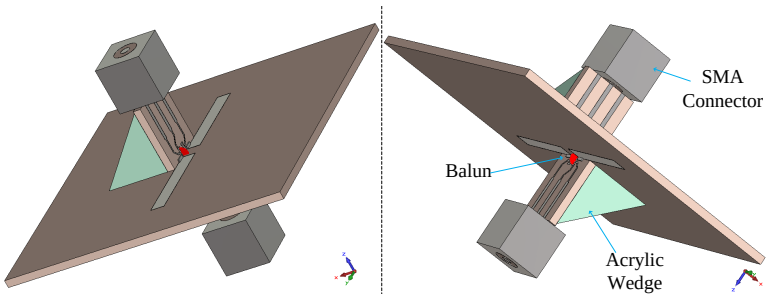

Figure 5.5: Crossed-dipole antenna with supporting acrylic wedge and balun PCB, shown in two perspectives

With the introduction of the additional components and the acrylic wedge, the antenna bandwidth suffered, which can be seen by comparing Figures 5.1b and 5.6a, which both are simulation results with a perfect balun, it should also be noted the additions have slightly detuned the antenna.

In Figure 5.6 the S_{12} and S_{21} parameters should be the same as one another, across all frequencies, however not the case for these simulations. This is most likely due to the meshing employed by the simulation software, as the structure is not symmetrical, but the mesh is uni-

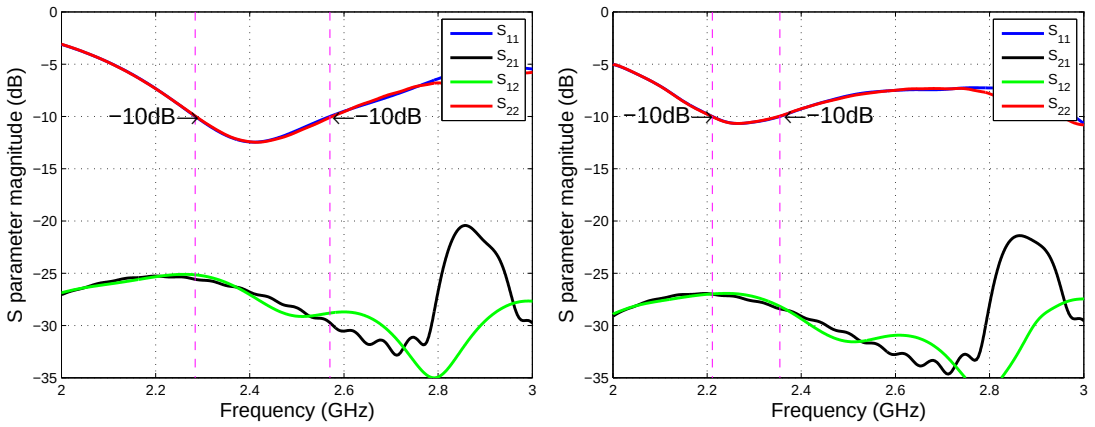

(a) (b)

Figure 5.6: Simulated S parameter magnitude (dB) for antenna as shown in Figure 5.5 (a) with ideal 1:1 balun (b) actual balun

form. Hence, resulting in increased meshing in certain areas causing the S_{12} and S_{21} to differ. Figure 5.6b shows the antenna simulated response with the NCS1-292+ balun, the .s3p files was obtained from the manufacturer and imported into CST to add the response of the actual balun to the antennas S parameters. Its imperfections have caused the centre frequency to shift from 2.41 to 2.27 GHz and the -10 dB bandwidth which was 286 MHz (2.28-2.57 GHz) and now is 144 MHz (2.21-2.35 GHz).

Using a Vector Network Analyser (VNA) the S_{11} of each dipole was measured and are shown in Figure 5.7 and the main results highlighted in Table 5.1. These measured responses show how slight differences in the construction can cause the antenna characteristics to differ significantly. The features coincide with the simulation results, with the measured antenna having a lower centre frequency when the additions of the balun PCB and the wedge are present, however not as low as expected from the simulation. The -10 dB bandwidth of the simulated antenna fairly similar to the measurement for dipole 1, with dipole 2 having a measured -10 dB bandwidth approximately 60 MHz greater than the simulation. Figure 5.7c shows the measured S_{21} result, which has a mean value of -19.47 dB across the 1 GHz bandwidth, thus indicating good separation between the two dipoles.

Table 5.1: Significant results from S_{11} measurements of Figure 5.7

	Dipole 1	**Dipole 2**
Centre Frequency (GHz)	2.33	2.38
-10 dB bandwidth (MHz)	159	201

Figure 5.8 presents the same data representation as Figure 5.2, however with the inclusion of the supporting acrylic wedge and balun PCB. The simulation uses the S parameter file (s3p

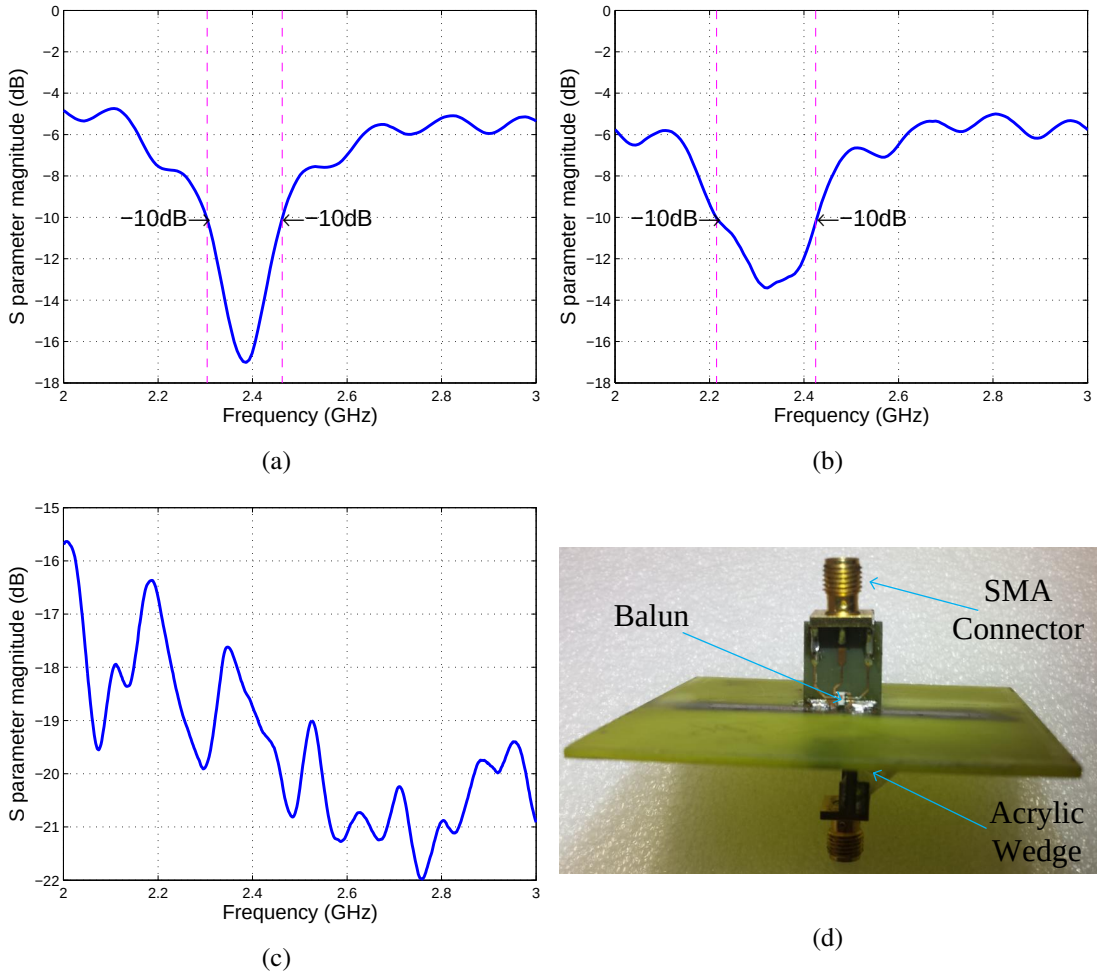

Figure 5.7: Measured S_{11} return loss magnitude (dB) for (a) dipole 1 and (b) dipole 2 (c) S_{21} measurement between the two dipoles (d) Photo of the antenna under test

format) for the balun, provided by the manufacturer and the acrylic wedge, for simulation purposes, has a dielectric constant of 2.1. In the CST library of materials, acrylic has a wide range of dielectric constants varying from 2.1 to 3.9. Simulations of the different dielectric constants had very similar results and was therefore left at the default value of 2.1. The effect of using the balun, its PCB, the supporting acrylic wedge and the SMA connector have altered the azimuth far field radiation pattern of the antenna. The elevation beamwidth remains unchanged at 84°, where previously the azimuth beamwidth for a single dipole was perfectly omnidirectional, a 0.23 dB ripple has now been introduced. However, the biggest difference is the radiation pattern in the plane of the crossed-dipole. The realised gain ripple is 1.3 dB, which is higher than the ideal dipole shown in Figure 5.2c, but as shown in Table 4.1, slightly higher than the maximum expected amplitude ripple of 1.03 dB. The maximum gain is also not exactly perpendicular to the crossed-dipole antenna, but slightly off centre, which is depicted in Figure 5.8d.

A simple S_{21} measurement, which is depicted in Figure 5.9a, was carried out using the

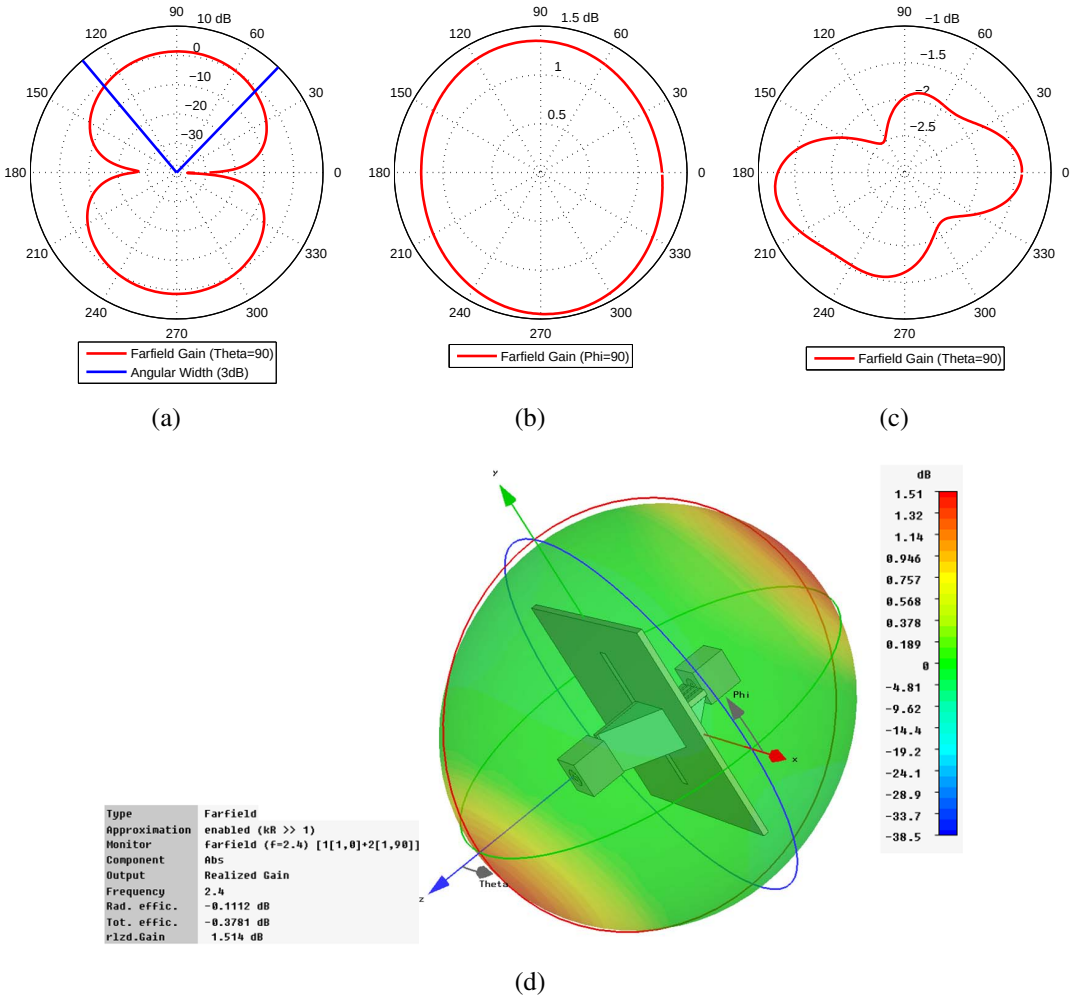

(a) (b) (c)

(d)

Figure 5.8: Simulated (a) Elevation ($\theta = 90°$) (b) Azimuth ($\phi = 90°$) 2D far field radiation pattern for one of the dipoles that make up the crossed-dipole with inclusions of the wedge and upright balun PCB (c) 2D far field radiation pattern for the crossed-dipole antenna in the plane of the antenna (d) 3D far field radiation pattern, when both dipoles are stimulated simultaneously with one dipole having a 90° phase shift

balun-fed crossed-dipole antenna as a receiver and a separate dipole antenna acting as a transmitter. The return loss of the transmitter dipole can be seen in Figure 5.9b, with both antennas orientated for horizontal polarisation. This experiment involved keeping the transmitter and receiver at the same height and rotating the receive antenna from 45° to 225° in 5° steps. Where, 45° refers to mid point between the two dipoles, i.e. the corner of the antenna PCB. The experiment consisted of one port of the 90° hybrid terminated with a matched load and the phase of the S_{21} measurement was recorded. Then repeated for the other port and the phase noted once again. The S_{21} phase was measured at 2.33 GHz slightly lower than the wanted frequency for this radar system, but this frequency corresponded to all antennas having a better return loss at 2.33 GHz rather than 2.44 GHz. Hence, the initial experiments using these antenna were all

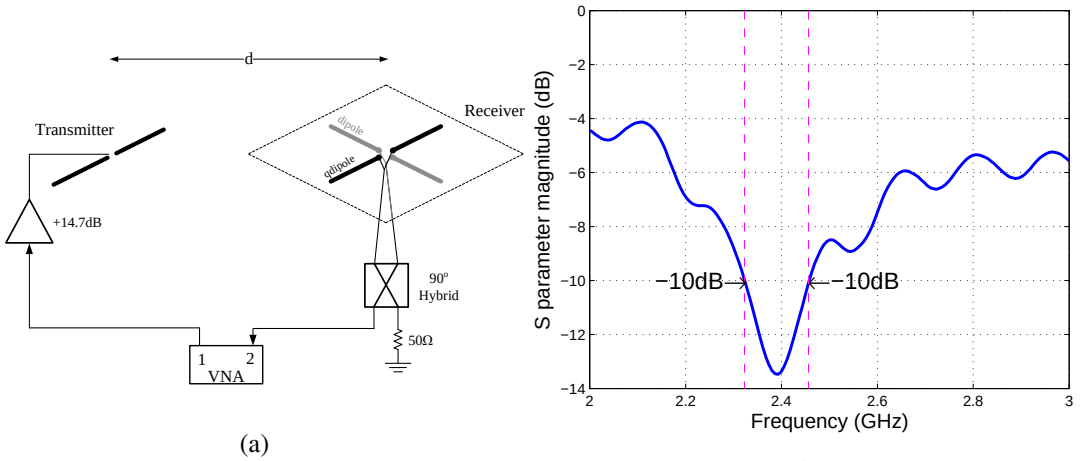

(a) (b)

Figure 5.9: (a) Experimental set up to test the balun-fed crossed-dipole antenna (b) S_{11} return loss from the transmitter dipole

at this lower frequency. Also the distance, *d*, between the transmit and receive antenna was set at 300 mm, allowing the experiment to be carried out in the receive antennas far field. The purpose of this S_{21} measurement was to determine how well the phase difference related to the actual bearing. The experiment was carried out in an anechoic chamber.

Figure 5.9a shows the use of a connectorised amplifier (ZX60-6013E-S+), with the datasheet stating a gain at 2.5 GHz of 14.7 dB. Two other connectorised components were required for this experiment a 90° hybrid (ZX10Q-2-27-S+) and 50 Ω matched load (ANNE-50L+) all three were purchased from www.minicircuits.com. The amplifier was required to amplify the transmitted signal, ensuring that the received signal was above the noise floor of the VNA. The measured phase difference was determined by the difference in the recorded S_{21} phases. The bearing as discussed previously is obtained by halving the phase difference and is shown in Figure 5.10.

Table 5.2: Significant outcomes from the experimental results in Figure 5.10 (*note that this is slightly lower than 2.30°, as the ideal crossed-dipole response is determined every 5° rather than the simulated 1° precision)

	Mean Bearing Error (degrees)	**RMS Bearing Deviation (degrees)**
Linear - Ideal	0.00	2.27*
Linear - Measured	-0.55	3.91

In summary these results show that the theory and the practical measurements agree fairly well. There is an increased RMS bearing deviation and an introduced mean error, which could be explained by the fact that the crossed-dipole antenna was far from ideal. Simulations have shown that the placement of the balun and the wedge has affected the far field radiation pattern,

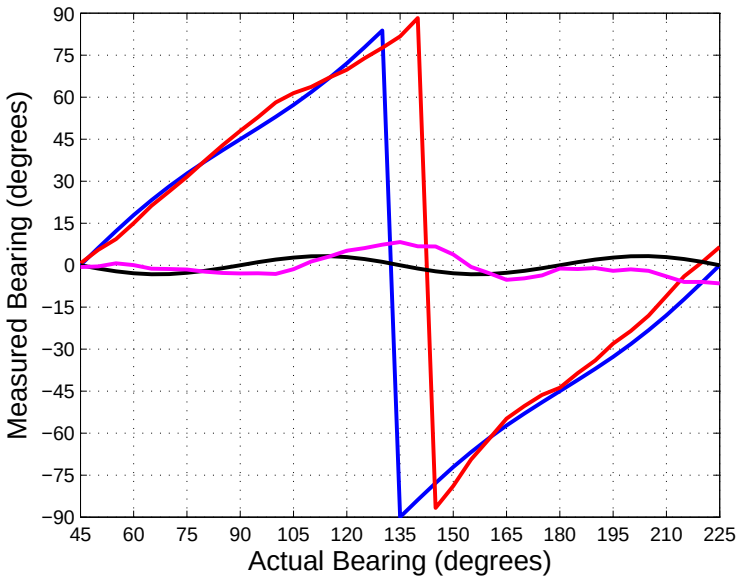

Figure 5.10: Ideal crossed-dipole bearing response (blue), measured bearing response from the prototype (red), difference between linear variation and ideal crossed-dipole bearing (black) and difference between linear variation and measured crossed-dipole bearing (magenta)

which could have influenced the phase measurement obtained for this experiment. Also, this experiment revealed some practical problems with the design of the crossed-dipole antenna, which mainly consisted of the cable positioning and weak solder joint between balun PCB and crossed-dipole antenna. The cable position was due to the orientation of the antenna and with one cable connected to the top side of the antenna and the other to the bottom. As this was a phase sensitive measurement, the RF cables for both antennas were required to be equal length and have bends of the same radius in approximately the same place, which proved difficult to maintain. The acrylic wedge was used to ensure the integrity of the solder joint. However, this was not entirely sufficient and the join required repairs on a few occasions. These practical problems coupled with the balun placement led to the development of the quadriphase-fed crossed-dipole antenna, which follows this section.

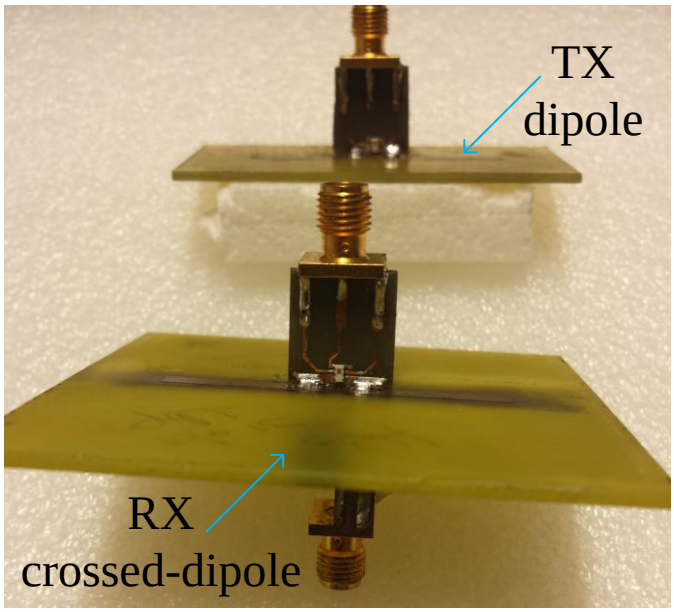

(a)

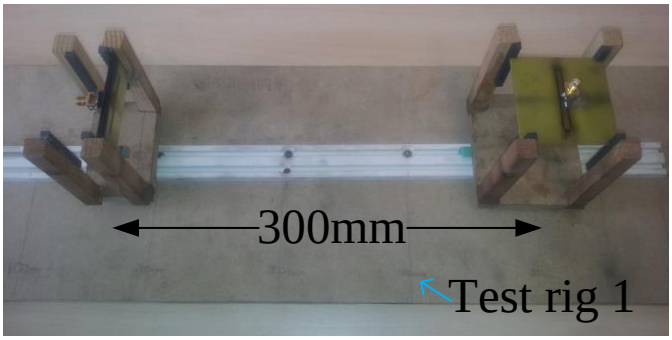

(b)

Figure 5.11: Photo of the (a) transmit dipole (background) and receive crossed-dipole antenna (foreground) (b) test rig 1 used for the experiment in this section

5.1.2 Quadriphase-fed Crossed-dipole

From the issues that have been discussed for the balun-fed crossed-dipole antenna it was decided that it could be advantageous to develop a quadriphase-fed crossed-dipole version. This would involve both dipoles on the same side of the PCB and coaxial cables directly to the antenna. This would allow the feed network to be moved further away from the antenna, hence, with less influence on the radiation pattern. The coaxial cables could be bought off the shelf to ensure exactly the same length, thus keeping the phase along the cable constant from each conductor. Bends in the cable can also be managed by cable tying them together. Therefore, any bends in

one cable would be replicated in the other three. The outer conductor of the coaxial cable can be soldered together as they all have a common ground, the inner conductor would be soldered to each arm of the crossed-dipole.

An important difference between the quadriphase-fed and balun-fed crossed-dipole antennas involves the impedance between the conductor of the antenna. For the balun fed, the simulation port impedances were set at 50 Ω, this is so 1:1 balun is well matched to the single coaxial cable. The quadriphase-fed crossed-dipole has each arm directly soldered to a 50 Ω coaxial cable. Hence, using equations (5.1), (5.2) and (5.3) the reflection coefficient, return loss and VSWR can be calculated and are 0.177, 15.06 dB and 1.43 respectively. Also, using equation (5.4) the mismatch loss can be calculated which is 0.137 dB. These values are using the assumption that each arm is equivalent to a monopole, hence has half the impedance of a resonant dipole, approximately 35 Ω single ended.

$$ML = -10\log_{10}(1 - \Gamma^2) \tag{5.4}$$

The mismatch loss and VSWR revealed that improving the match was not essential. However, some steps were taken to increase the impedance which were to decrease the width of each arm of the dipole and to change the substrate type and thickness, with a lower dielectric constant, ε_r. The substrate chosen was Rogers Duriod 5580 with thickness of 0.787 mm and a ε_r of 2.2, from the 1.6 mm FR-4 substrate with a ε_r of 4.3.

Another option of increasing the impedance was to use loaded dipoles and has been discussed in literature [92] [93]. This involves adding lumped elements, a combination of resistors, capacitors and inductors to the dipole. A slight variation of the loaded dipole is to use a stub at the end of the dipole, this is to decrease the impedance at the end of the dipole. In doing so, the dipole effectively becomes a quarter-wave transformer. Hence, close to the feed point of the antenna the impedance would naturally increase. Using the design characteristics described above, the antenna shown in Figure 5.12a was simulated, constructed and tested.

This antenna was simulated using CST MWS and its S_{11} return loss and the far field radiation pattern was calculated, with the port located between opposing arms, as shown in Figure 5.12a. This was to ensure that the important characteristics of the crossed-dipole remained, such as the omnidirectional pattern and the -3 dB elevation angular beamwidth of the antenna. Comparing the two simulations, the quadriphase-fed is slightly less tuned, with a higher S_{11} return loss (-12.7 dB vs. -20 dB). The simulated -10 dB S_{11} bandwidth is shown to be 256 MHz (≈10%) slightly lower than the balun fed. However, still more than sufficient than is re-

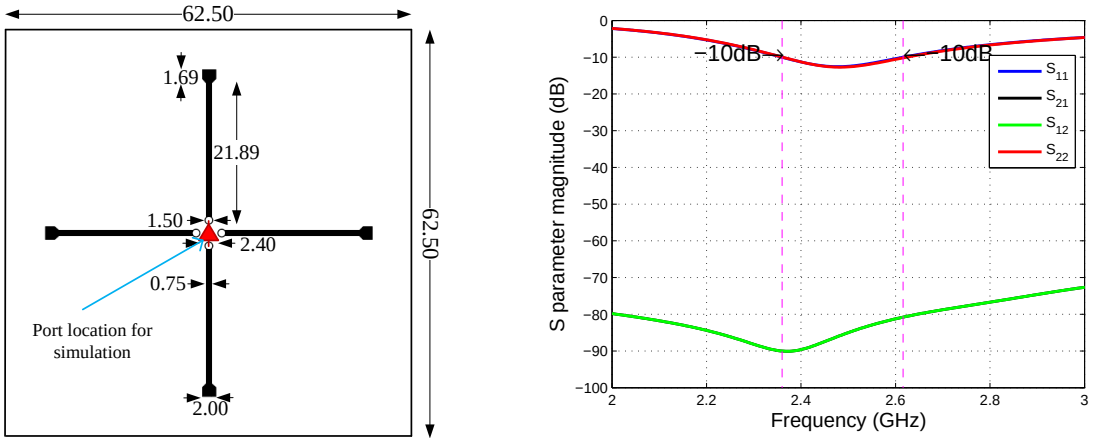

Figure 5.12: (a) Constructed quadriphase-fed loaded crossed-dipole antenna (all dimensions in mm) (b) Simulated S parameters (magnitude (dB)) for the quadriphase-fed crossed-dipole as shown in (a) (results for S_{11} and S_{22} overlap, as do S_{21} and S_{12})

quired from this radar operation and has a centre frequency of 2.48 GHz. Not included in this simulation is the effect of the cable (rg-174 coaxial cable) that was eventually soldered to the constructed antenna. The simulated S_{21} and S_{12} shown in Figure 5.12b, reveal the coupling between the two dipoles, if they were excited by two ports, where in Figure 5.12a the placement of a single port is shown.

The measured S_{11} of the antenna can be seen in Figure 5.14 which shows multiple curves in each figure. This is due to the soldered coaxial cable to the antenna and the rat race coupler, the coupler was purely construed for measuring the S_{11} of each dipole. The couplers dimensions were determined using the parameters as shown in Figure 5.16a. The photo of the how the antenna and coupler were connected to determine the S_{11} of each dipole, is shown in Figure 5.13, the unused ports (labelled 'C' and 'D' in this figure) were terminated with matched loads.

The blue curves in Figures 5.14a and 5.14b show a 'ringing' type response, this was determined to be an effect of the length of the coaxial cable, at 1 m in physical length, cutting off one of the ends leaves it approximately 0.97 m long. The datasheet quoted velocity factor for the coaxial cable is 0.66, hence, an electrical length of approximately 1.47 m (0.97/0.66). For a return loss measurement the electrical length of the cable is 2.94 m. Therefore, a frequency in free space of 102 MHz, which is approximately the repetition of the spikes. The in phase, out of phase nature of the measurement due to the length of cable can be removed by using a feature of the of the VNA. By using the time domain analysis feature called 'gating' the time domain response due to the antenna and cable can be separated. Using a 'bandpass' gate whose width is very much in the perspective of the user, the reflections due the cable can be zeroed and the response just due to the antenna can be seen (red and green curves in Figure 5.14). As

this feature is user dependant, two different time length gates were used, to illustrate just how different length gates can result in differing S_{11} response of the antenna.

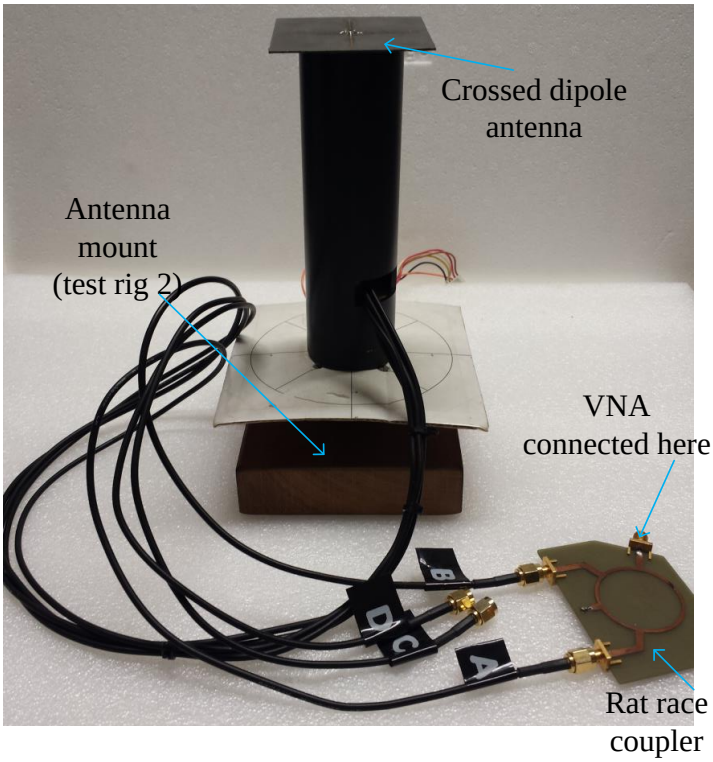

Figure 5.13: Photo of quadriphase-fed crossed-dipole and rat race coupler, used to generate the results in Figure 5.14

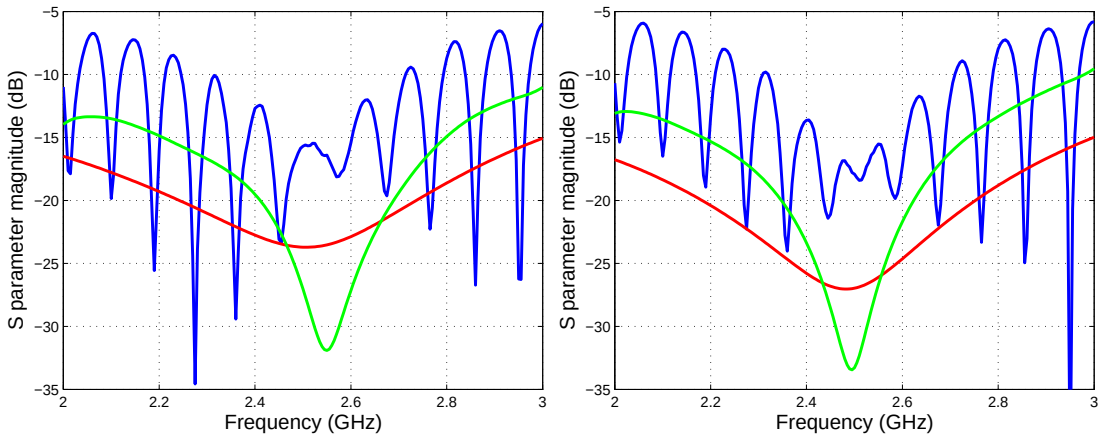

(a) (b)

Figure 5.14: Measured S_{11} of the quadriphase-fed crossed-dipole antenna, no gating (blue), short time gating (red) longer time gating (green) for (a) Dipole 1 (b) Dipole 2

The simulation results in Figure 5.15 shows a very similar performance to that of the balun fed crossed-dipole characteristics shown in Figure 5.2. Where, Figure 5.2 shows the crossed-dipole with a -3 dB elevation beamwidth of 84°, the quadriphase-fed version has a

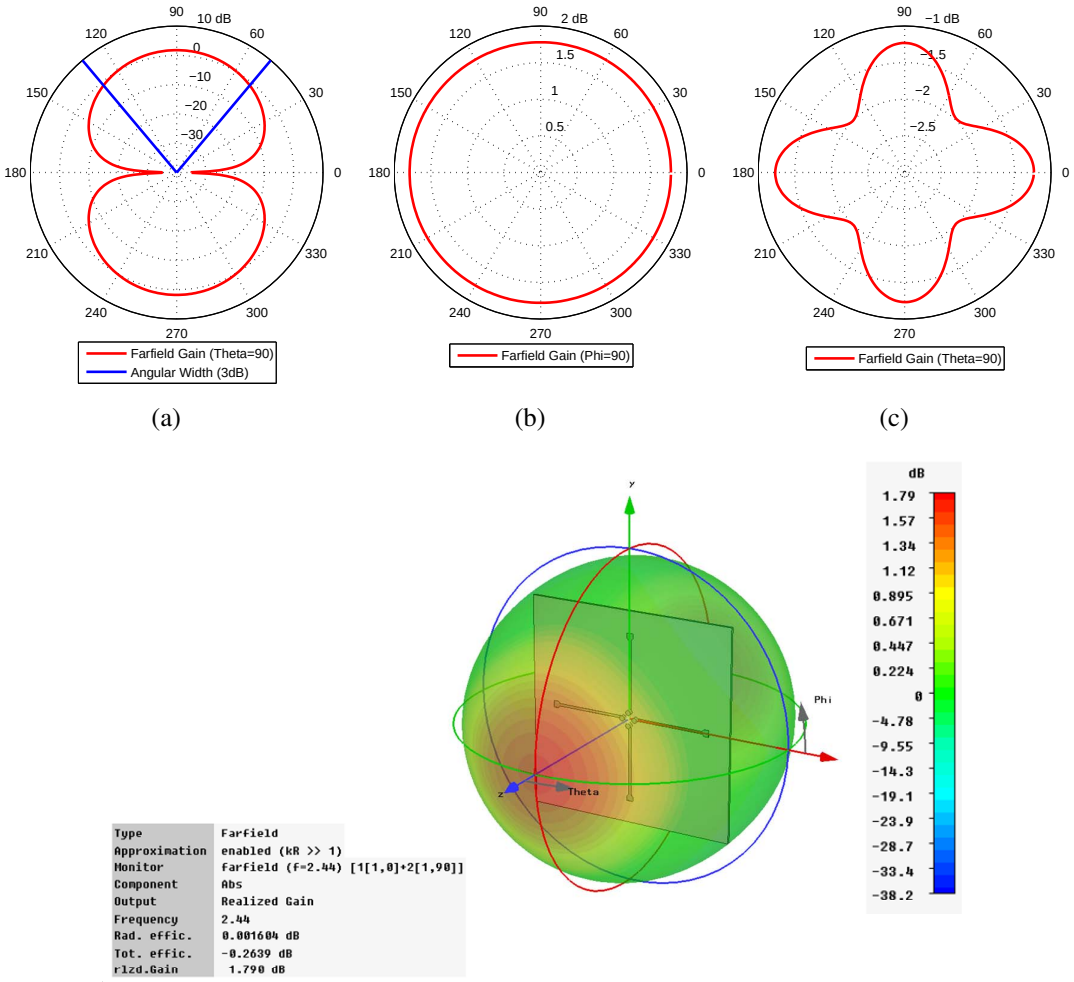

(a) (b) (c)

(d)

Figure 5.15: Simulated (a) Elevation ($\theta = 90°$) (b) Azimuth ($\phi = 90°$) 2D far field radiation pattern for one of the dipoles that make up the constructed quadriphase-fed crossed-dipole (c) 2D far field radiation pattern in the plane of the crossed-dipole antenna (d) 3D far field radiation pattern, when both dipoles are stimulated simultaneously with one dipole having a 90° phase shift

slightly reduced beamwidth of 80°. This has the effect of increasing the ripple magnitude in the antennas combined azimuth far field and is shown in Figure 5.15c. The combined far field gain is identical to the ideal dipole shown in Figure 5.2d, with the maximum gain perpendicular to the plane of the antenna. This arrangement of the crossed-dipole antenna was required for symmetry and it also allowed for a more customised feed network which will now be discussed.

Quadriphase Feed Network

Essentially the aim was to keep same basic layout as that of the balun fed crossed-dipole. The balun which was used previously was unusable due to the increased input impedance of the antenna. Also, the unavailability of an off the shelf component with the correct specification led to the development of a 180° rat-race coupler [94] [95] as a viable substitute. The rat-

race coupler has two outputs of equal amplitude with a 180° phase shift between them, hence, ideal for this antenna. The total circumference of this type of coupler is 1.5λ, whose width is determined by the impedance which equals $\sqrt{2}Z_\circ$ (70.71 Ω), for a $Z_\circ$ of 50 Ω.

The 90° splitter/combiner across the required bandwidth was widely available, such as the connectorised part (ZX10Q-2-27-S+) used for the balun fed crossed-dipole antenna test. However, as one part of the feed network i.e. rat race coupler was required to be fabricated, it was logical to implement the 90° combiner too on the same PCB. Hence, for this combiner a branchline coupler was the chosen methodology. The 180° coupler too can be made using a combination of quarter-wave transformers and a branchline couplers, but lacks symmetry and has less bandwidth, so it was not investigated for this purpose.

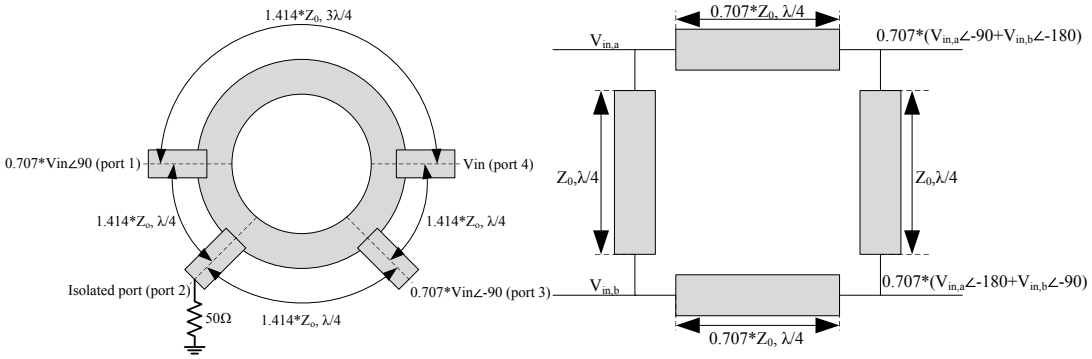

Figure 5.16: Dimensions of a equal power split (a) Rat race [94] (b) Branchline coupler [95]

The rat-race and branchline couplers were simulated individually on a 1.6 mm FR-4 substrate using CST MWS. This was to verify the correct phase and magnitude for the output ports relative to the input. These two couplers were then combined to produce the final four-phase feed network board whose dimensions can be seen in Figure 5.17b and the simulation results are shown in Figure 5.18.

The main conclusions from Figure 5.18, are shown in Table 5.3 which highlights key phase differences between the ports. Also, the magnitude plots Figures 5.18a and 5.18b, both show the coupling between the input and output ports. The expectation is if one of the input ports is under test and the rest are terminated by matched loads as is one of the output ports, then ideally there should be a 6 dB reduction in magnitude, 3 dB from each coupler. When all the antenna elements are connected the loss would only be 3 dB for the loss due to the rat-race coupler, with no loss from the branchline coupler. Figures 5.18c and 5.18d show the phase difference between input and output ports which are shown in Table 5.4, these are vital for a monotonic measured and actual bearing response. The simulation agrees quite well with the ideal phase difference

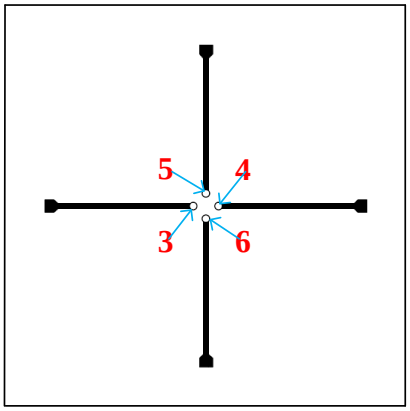

(a)

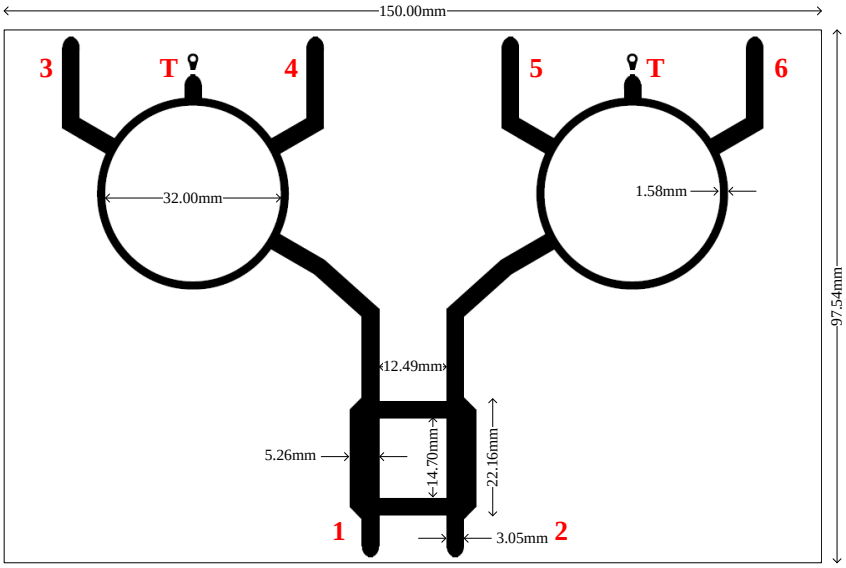

(b)

Figure 5.17: (a) Intended connection from antenna to feed network (b) Feed network for the quadriphase-fed crossed-dipole antenna, dimensions in mm (ports are labelled in red, port 'T' is the isolated port of the rat-race coupler terminated with a matched 50 Ω load)

required, as does the S parameter magnitudes. There is a approximate 7 dB magnitude reduction between the input and output, 1 dB greater than expected. This could be due to the choice of lossy FR-4 in the simulation to emulate the real scenario. The S parameters both magnitude and phase were measured of the constructed feed network using a VNA. These are shown in Tables 5.5 and 5.6.

The measured results are very similar to the simulated feed network. The maximum measured phase difference deviation from the ideal is 5.13°, this would correspond to a bearing error at half this value of 2.57°. The measured result shows that this offset is not equal across the whole bandwidth. By establishing whether or not this offset is repeatable, provided it is not

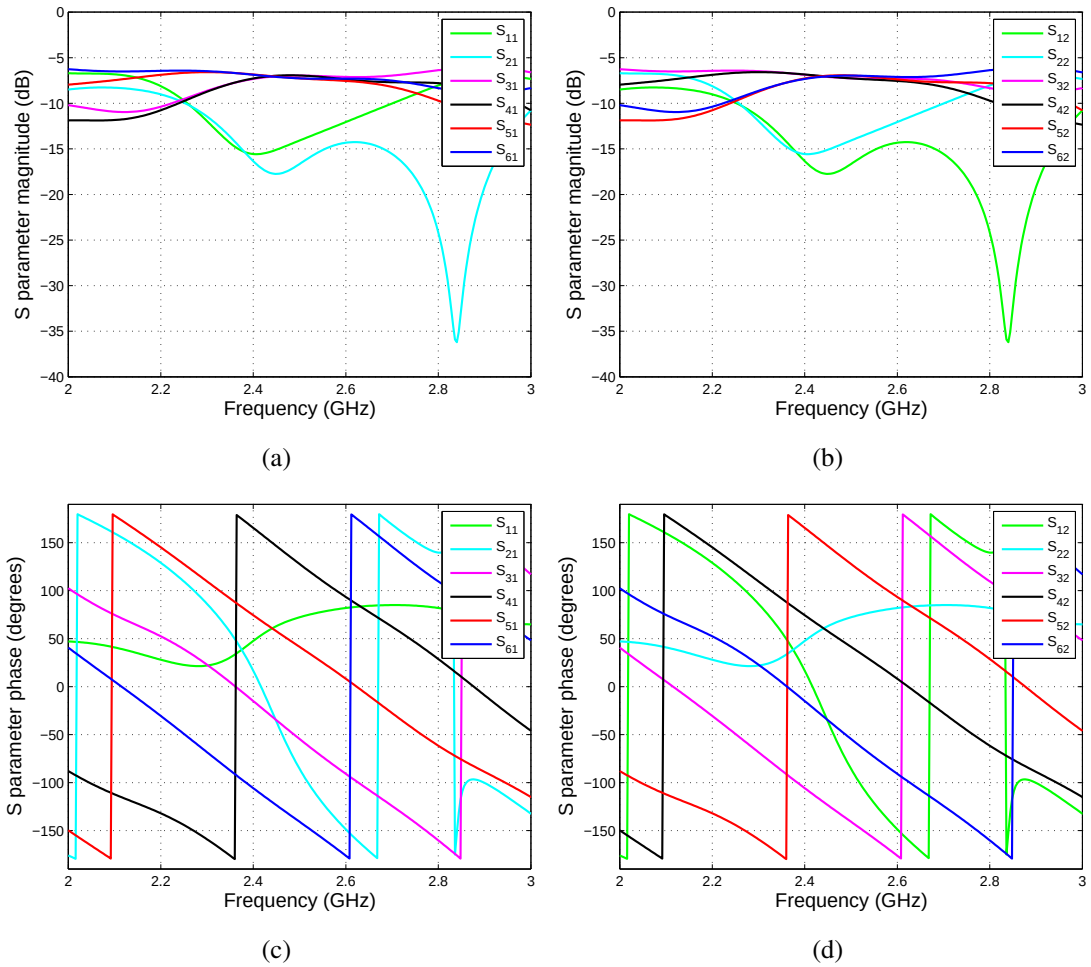

Figure 5.18: Simulated S parameters for the quadriphase-fed crossed-dipole antenna (a) S_{n1} (magnitude (dB)) (b) S_{n2} (magnitude (dB)) (c) S_{n1} (phase (degrees)) and (d) S_{n2} (phase (degrees)) (note: n=1, 2, ..., 6)

Table 5.3: Significant results from S parameter magnitude simulation of Figure 5.18

Frequency	**2.400 GHz**		**2.484 GHz**	
	Magnitude (dB)	**Phase (degrees)**	**Magnitude (dB)**	**Phase (degrees)**
$\mathbf{S_{11}}$	-15.57	47.62	-14.41	69.84
$\mathbf{S_{21}}$	-16.34	16.60	-17.16	-71.41
$\mathbf{S_{31}}$	-7.32	-15.05	-6.97	-48.37
$\mathbf{S_{41}}$	-7.27	165.40	-6.93	133.69
$\mathbf{S_{51}}$	-6.84	74.39	-7.21	46.64
$\mathbf{S_{61}}$	-6.87	-105.82	-7.22	-135.30
$\mathbf{S_{12}}$	-16.34	16.60	-17.16	-71.41
$\mathbf{S_{22}}$	-15.56	47.62	-14.41	69.83
$\mathbf{S_{32}}$	-6.87	-105.82	-7.22	-135.30
$\mathbf{S_{42}}$	-6.84	74.39	-7.21	46.64
$\mathbf{S_{52}}$	-7.27	165.40	-6.93	133.68
$\mathbf{S_{62}}$	-7.33	-15.05	-6.97	-48.37

Table 5.4: Simulated phase difference between the S parameters for the quadriphase-fed crossed-dipole feed network from Figure 5.18

Frequency	**Ideal**	**2.400 GHz**	**2.484 GHz**
	Phase difference (degrees)	**Phase difference (degrees)**	**Phase difference (degrees)**
$\angle S_{31}$ - $\angle S_{41}$	±180.00	-180.45	-182.05
$\angle S_{31}$ - $\angle S_{51}$	-90.00, 270.00	-89.43	-95.00
$\angle S_{31}$ - $\angle S_{61}$	90.00, -270.00	90.77	86.94
$\angle S_{41}$ - $\angle S_{51}$	90.00, -270.00	91.01	87.05
$\angle S_{41}$ - $\angle S_{61}$	-90.00, 270.00	271.22	268.99
$\angle S_{51}$ - $\angle S_{61}$	±180.00	180.21	181.94
$\angle S_{32}$ - $\angle S_{42}$	±180.00	-180.20	-181.94
$\angle S_{32}$ - $\angle S_{52}$	90.00, -270.00	-271.22	-268.99
$\angle S_{32}$ - $\angle S_{62}$	-90.00, 270.00	-90.77	-86.94
$\angle S_{42}$ - $\angle S_{52}$	-90.00, 270.00	-91.01	-87.05
$\angle S_{42}$ - $\angle S_{62}$	90.00, -270.00	89.43	95.00
$\angle S_{52}$ - $\angle S_{62}$	±180.00	180.45	182.05

Table 5.5: Measured S parameters from the prototype quadriphase-fed crossed-dipole feed network

Frequency	**2.401 GHz**		**2.486 GHz**	
	Magnitude (dB)	**Phase (degrees)**	**Magnitude (dB)**	**Phase (degrees)**
S_{11}	-12.34	0.00	-14.61	0.00
S_{31}	-8.83	-53.65	-7.89	-87.39
S_{41}	-8.91	124.29	-7.76	92.52
S_{51}	-7.09	31.22	-7.37	0.01
S_{61}	-6.99	-148.06	-7.42	178.97
S_{22}	-12.34	0.00	-15.17	0.00
S_{32}	-7.03	-144.74	-7.45	-177.60
S_{42}	-7.13	32.70	-7.39	1.44
S_{52}	-8.87	122.93	-7.75	90.95
S_{62}	-8.76	-56.28	-7.78	-90.35

a feature of the measurement procedure, then a calibration curve can be used to further increase the accuracy of the measured bearing with respect to the actual bearing.

Table 5.6: Measured phase difference between the S parameters for the quadriphase-fed crossed-dipole feed network

Frequency	**Ideal**	**2.401 GHz**	**2.486 GHz**
	Phase difference (degrees)	**Phase difference (degrees)**	**Phase difference (degrees)**
$\angle S_{31}$ - $\angle S_{41}$	±180.00	-177.94	-179.91
$\angle S_{31}$ - $\angle S_{51}$	-90.00, 270.00	-84.87	-87.40
$\angle S_{31}$ - $\angle S_{61}$	90.00, -270.00	94.41	-266.18
$\angle S_{41}$ - $\angle S_{51}$	90.00, -270.00	93.07	92.51
$\angle S_{41}$ - $\angle S_{61}$	-90.00, 270.00	272.35	-86.27
$\angle S_{51}$ - $\angle S_{61}$	±180.00	179.28	-178.78
$\angle S_{32}$ - $\angle S_{42}$	±180.00	-177.44	-179.04
$\angle S_{32}$ - $\angle S_{52}$	90.00, -270.00	-267.67	-268.55
$\angle S_{32}$ - $\angle S_{62}$	-90.00, 270.00	-88.46	-87.25
$\angle S_{42}$ - $\angle S_{52}$	-90.00, 270.00	-90.23	-89.51
$\angle S_{42}$ - $\angle S_{62}$	90.00, -270.00	88.98	91.79
$\angle S_{52}$ - $\angle S_{62}$	±180.00	179.21	181.30

Initial Test Results

The same experiment that was carried out for the balun-fed crossed-dipole was again conducted. The only hardware change was the newly constructed quadriphase-fed crossed-dipole antenna and its accompanying feed network. One measurement change that was implemented for this experiment was to measure the S_{21} phase at 2.40 GHz rather than 2.33 GHz. This was due to the feed network showing that at 2.40 GHz had the biggest phase deviation. This would then result in the worse case scenario for radar system as 2.40 GHz is within the operating bandwidth of both antenna and feed network. Hence, conducting the experiment at this frequency.

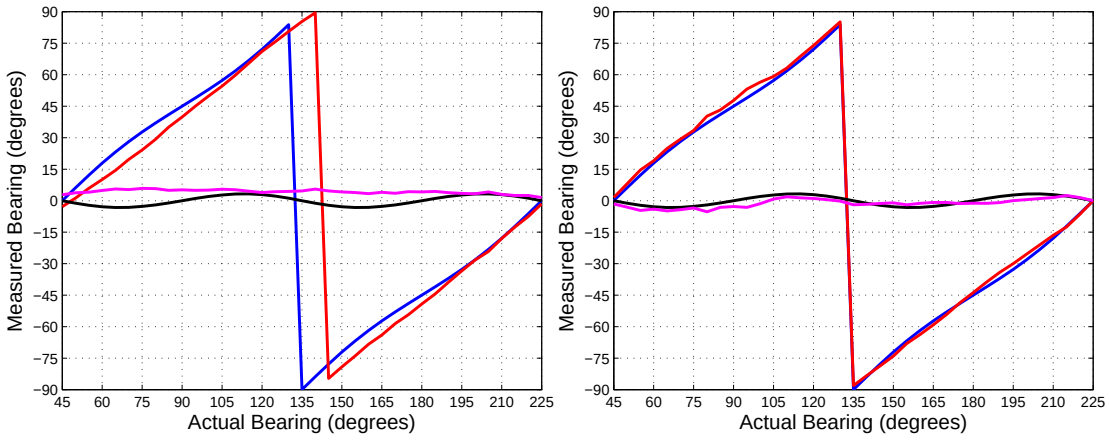

(a) (b)

Figure 5.19: Ideal quadriphase-fed crossed-dipole bearing response (blue), measured bearing response from the prototype (red), difference between linear variation and ideal crossed-dipole bearing (black) and difference between linear variation and measured crossed-dipole bearing (magenta) (a) test rig 1 (b) test rig 2

Table 5.7: Significant results from the experimental results in Figures 5.19a and 5.19b (*note that this is slightly lower than 2.30°, as the ideal crossed-dipole response is determined every 5° rather than the simulated 1° precision)

	Mean Bearing Error (degrees)	**RMS Bearing Deviation (degrees)**
Linear - Ideal	0.00	2.27*
Linear - Measured, test rig 1	4.24	4.35
Linear - Measured, test rig 2	-1.21	2.34

The initial test results with this antenna and feed network, are shown in Figure 5.19, which reveals that they were both working. However, the performance was not as good as the balun-fed crossed-dipole. The mean bearing error and the RMS deviation for both the quadriphase-fed are both increased from the balun-fed. There was some consistency between the two results where they both have the same 10° offset in the mid point of the measurement (135-145°). It was suggested that this offset could be caused by the antenna testing rig, designed and built for these experiments, with particular concern with the asymmetry in the vertical upright antenna mounts. A method to determine if asymmetry was the contributing factor, a new mount was created for the quadriphase-fed crossed-dipole antenna. With the new design having no parts of the rig obstructing the antenna and remaining symmetrical. This proved to be very significant to the measurement accuracy and improved the result dramatically. The new test rig results are shown in Figure 5.19b with a photo of test rig 2 is shown in Figure 5.13 and a photo of the experiential set up is shown in Figure 5.21.

The significant improvement in this measurement is entirely attributed to the new antenna testing rig as all the other parameters were kept the same. The new test rig, allowed the four coaxial cables to be tied together, ensuring that any cable movements were kept constant for all cables. Finally, this rig allowed the cables to protrude in the centre of the crossed-dipole, on its underside, hence, removing all obstructions in the plane of the antenna. The quadriphase-fed crossed-dipole with the new test rig has improved RMS bearing deviation, for both the quadriphase-fed and balun-fed crossed-dipole antennas with test rig 1, by more than 2° and 1.5° respectively. The expected error in the ideal crossed-dipole can be seen in Figure 5.19b (black curve) and the error in the measured result (magenta curve), shows very similar characteristics, which suggests that the antenna and four-phase feed network agree very well with the theory. The mount for the quadriphase-fed crossed-dipole was replicated as part of the radar system, which is discussed later.

In summary, the receive antenna and four-phase feed network were working very well together. Measured test results had shown that the prototype and ideal simulations were quite

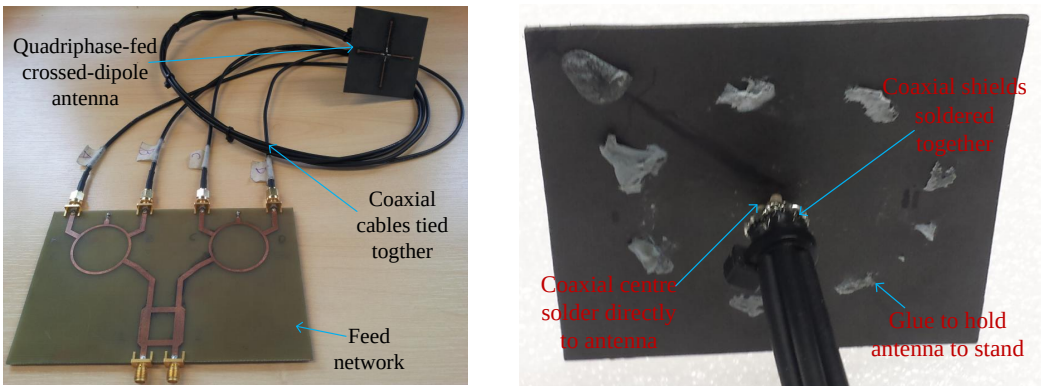

(a) (b)

Figure 5.20: (a) Photo showing the four-phase feed network and quadriphase-fed crossed-dipole antenna (b) Photo of the underside of the antenna

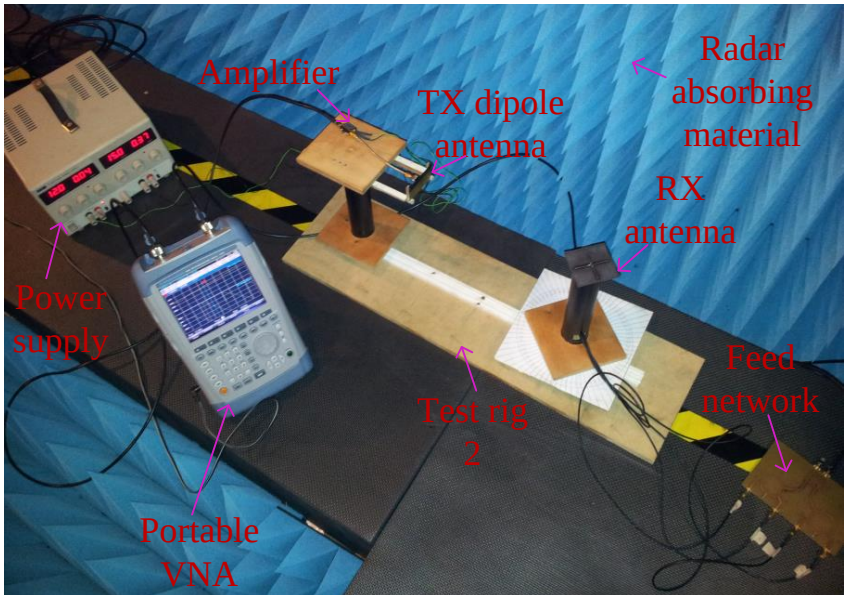

Figure 5.21: Photo of the test rig 2 used to produce the results in Figure 5.19b

close, with a mean error of -1.21° and the RMS bearing deviation is only 0.07 degrees greater than the ideal. After development of the antenna, the focus of the research moved onto radar hardware development, this is where the thesis now progresses.

5.1.3 Transmit Antenna

In previous experiments, a version of the crossed-dipole was modified into a simple printed dipole antenna. It was discussed that in order for the transmitter to also have an omnidirectional radiation pattern, symmetry was essential. The balun PCB orthogonal to the antennas main lobe in certain directions would be fairly omnidirectional, in other directions the vertical PCB could cause the pattern to alter. Hence, requiring a different antenna being developed for the transmitter, which is discussed in this section. Also discussed is the isolation between the transmit and

receive antennas, which suggests that vertical separation between antennas in conjunction with orthogonal polarisations would increase the isolation. With this in mind, the transmit antenna was designed.

Small Ground Plane Monopole Antenna

A simple monopole would be an ideal transmitting antenna, basically half of a dipole antenna with a similar radiation pattern. It is usually a rod shaped conductor mounted orthogonally to conductive metallic ground plane. Where a resonant dipole antenna would be $\lambda/2$ in length, a resonant monopole antenna conductor is $\lambda/4$, the same length as one arm of the dipole antenna. By only radiating above the ground plane, the gain of this antenna is twice (3 dB) higher than an equivalent dipole antenna, with half the radiation resistance i.e. Z=36.5+j21.25 Ω, at resonance this value is slightly lower at Z=35+j0Ω. However, this with the proviso that the ground plane is infinitely large. When designing a monopole antenna, an infinite ground plane is practically impossible, care must be taken in the size of the ground plane, as it plays a role in both the gain and radiation pattern. For relativity small ground planes, in the order of a few wavelengths, the impedance is largely unaffected. However, the main lobe radiation pattern becomes more directive along the ground plane, but this peak main lobe gain is lower than if this antenna had a larger ground plane. Its directivity along the ground plane could be considered as an advantage of the smaller ground plane. The angle of the radiation pattern is particularly vital for short range measurements with an active target. This is in order to keep the main lobes of both transmit and receive antennas in approximately the same plane as the active target antennas main lobes.

The antenna was designed in CST MWS and an example was constructed, which is shown in Figure 5.22b. The ground plane was made from sheet copper of approximately 0.40 mm thick with a radius of 62.5 mm ($\lambda/2$). The copper rod of length 31.25 mm and a diameter of approximately 3 mm was simulated. However, when it was constructed, it was made slightly longer by 2 mm to 32-33 mm, such that it could be filed down in length to fine tune the antenna and ensure a correct resonant frequency.

Figure 5.22a shows that the simulated -9.7 dB S_{11} bandwidth of the measured monopole is over 200 MHz with a centre frequency 2.41 GHz. This would be fairly sufficient for the prototype radar system. The simulated elevation -3 dB beamwidth is 102° and the azimuth is omnidirectional with the phase centre along the ground plane, with the main lobe realised gain of approximately 1 dB.

This was one of the first antenna that was constructed once the active target was designed. However, its low gain and location of the main lobe made lab based measurements hard to

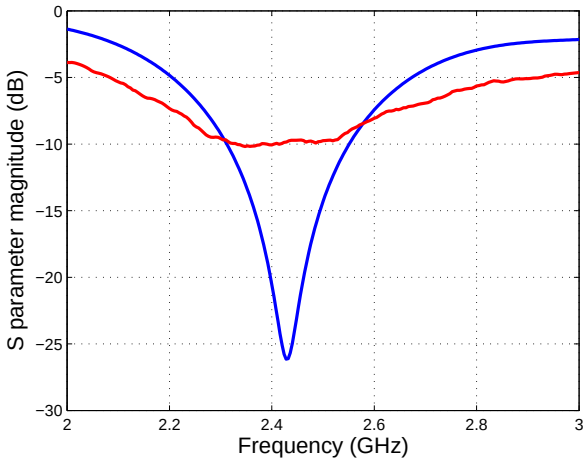

(a)

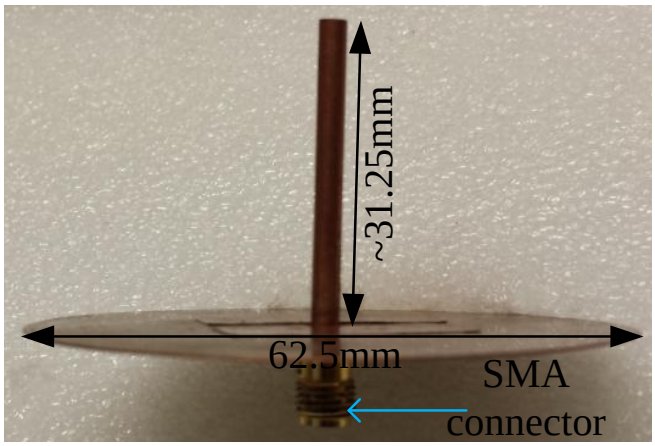

(b)

Figure 5.22: Simulated (blue) measured (red) S_{11} magnitude (dB) of the antenna, shown in 5.22b (b) Photo and dimensions of small ground plane monopole antenna

acquire. It was therefore quickly abandoned and focus shifted to an improved design made specially for this project, a conical ground plane monopole antenna.

Conical Ground Plane Monopole Antenna

To ensure that short range measurements could be obtained by avoiding strong direct coupling between the transmit and receive antennas. It was suggested that shaping the ground plane into a cone could allow these measurements. The cone shaped ground plane has the effect of deflecting the main lobe downward. However, still retaining the null pointing directly below. This antenna has many similar characteristics of a large ground plane monopole. However, where the monopole has its main lobe above the ground plane, this antenna is almost equal but in the opposite direction i.e. below the ground plane. The antennas' physical shape could be considered a merger of a bi-cone and a monopole antenna (see Figure 5.24b).

This antenna was simulated using CST MWS, the monopole rod was again simulated with

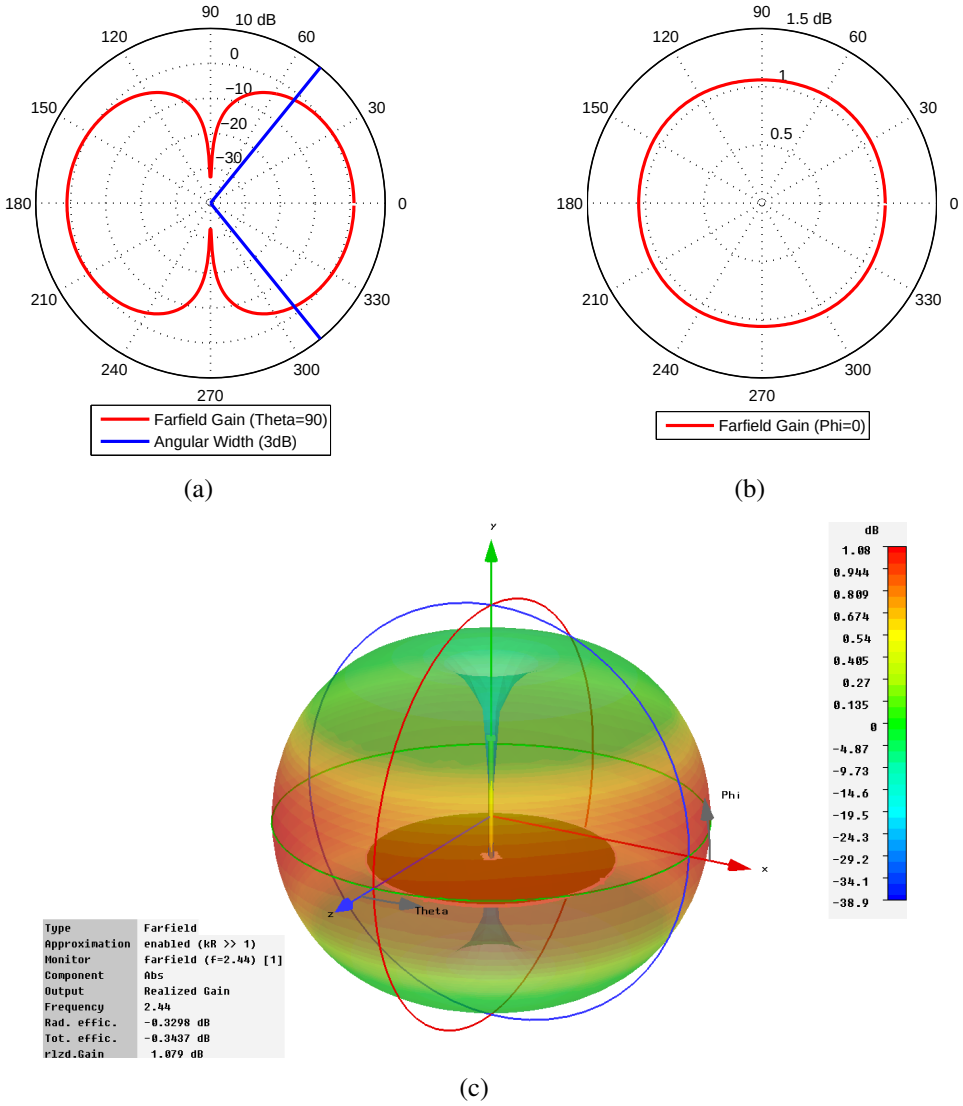

Figure 5.23: Simulated (a) 2D elevation ($\theta = 90°$) (b) 2D azimuth ($\phi = 0°$) (c) 3D far field radiation pattern of the small ground plane monopole antenna, of the antenna shown in Figure 5.22b

a diameter of 3 mm and length of 31.25 mm. It was again constructed slightly longer and then fine tuned. The ground plane was made from a 0.25 mm thick copper sheet, the top of the cone is flat and 40 mm in diameter, the cone is 50 mm vertical high and has a 100 mm bottom diameter. The cones net was designed on Diptrace PCB software as a simple shape and cut out of a piece of sheet copper using a milling machine, which required the use of a thinner copper sheet. The top flat piece was machined in the same process, but has four solder tags to connect the two pieces of the ground plane together. The practical design of the conical ground plane was unable to maintain perfect symmetry due to the soldering of the flat copper sheet to the 3-d cone, this could be part of the reason for the S_{11} being slightly asymmetric.

The size and flare angle of the ground plane was simulated with different values and the

sizes mentioned above produced the best results, in terms of far field radiation pattern and main lobe location. Figure 5.24a shows a simulated -10 dB bandwidth of 112 MHz, but the measured bandwidth is considerably higher at 460 MHz. The far field simulation in Figure 5.25a shows that the main lobe is indeed below the ground plane. It has a 3 dB angular width of 86°, 15 degrees lower than the small ground plane monopole antenna. Its mainlobe is centred at 206°, 26 degrees below the top of the ground plane. The realised gain is approximately 2 dB, 1 dB greater than the small ground plane monopole.

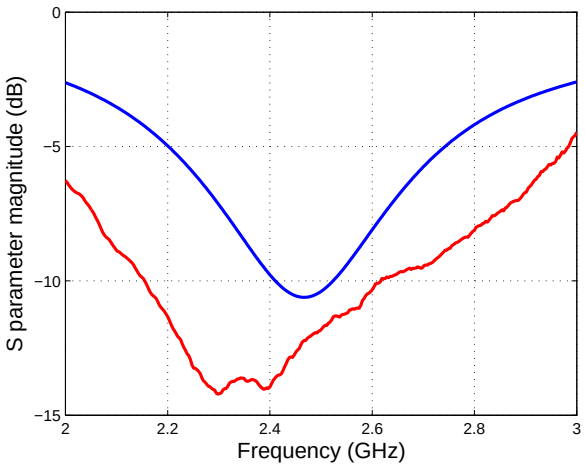

(a)

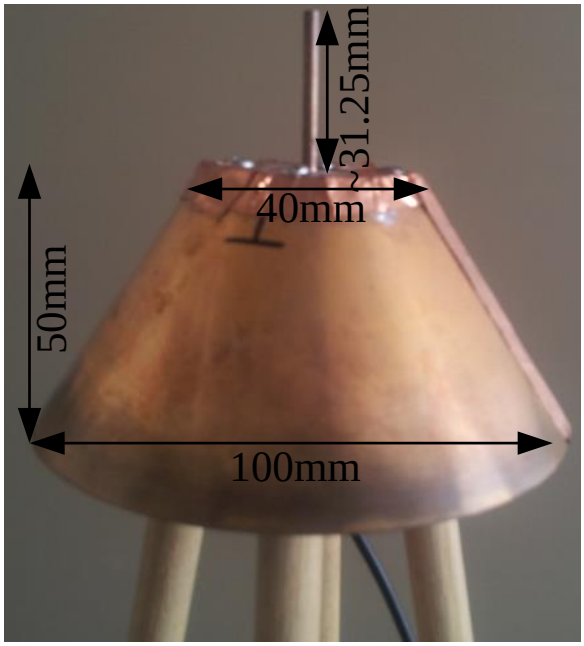

(b)

Figure 5.24: (a) Simulated (blue) measured (red) S_{11} magnitude (dB) of the antenna, shown in Figure 5.24b (b) Photo and dimensions of conical ground plane monopole antenna

As the simulated far field and real S_{11} showed that this antenna was working within the

correct band, it was used for all subsequent tests and trials carried out with the radar system.

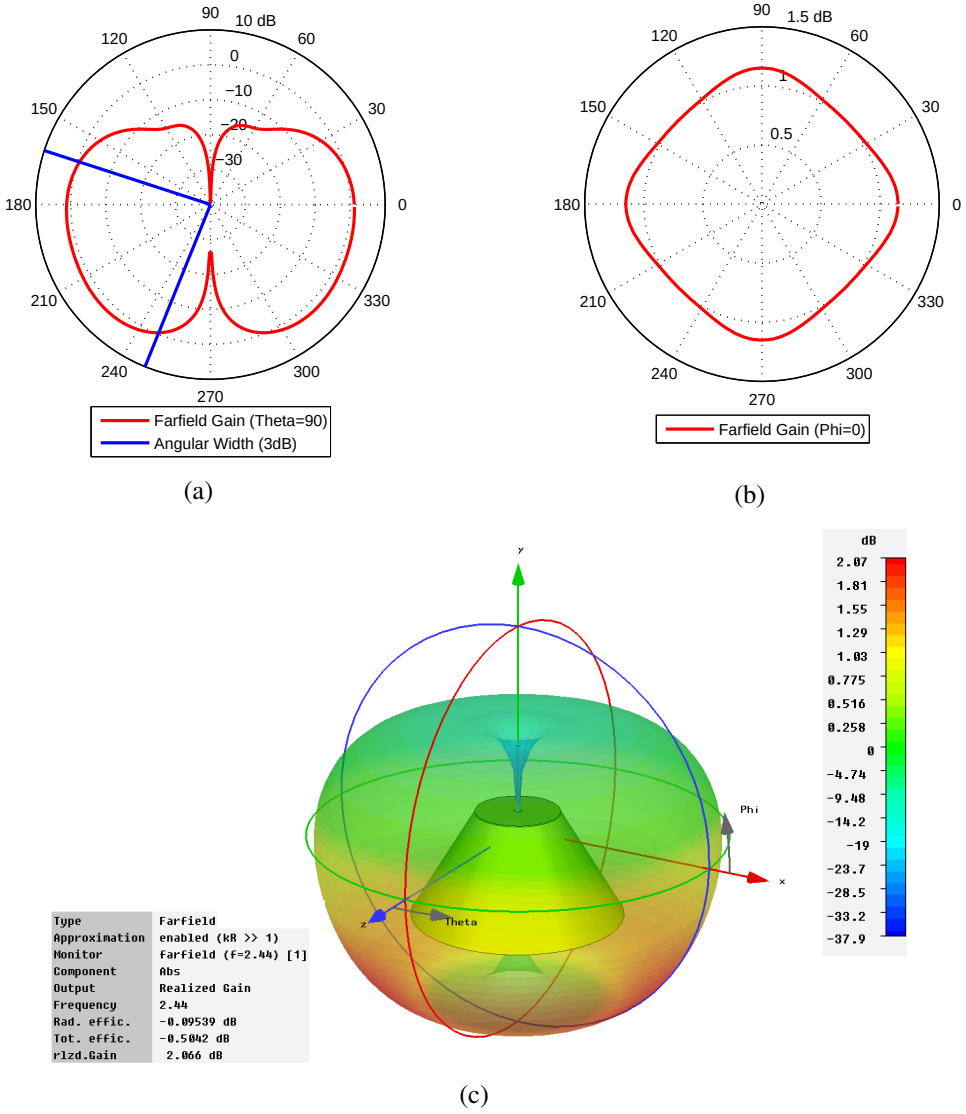

Figure 5.25: Simulated (a) 2D elevation ($\theta = 90°$) (b) 2D azimuth ($\phi = 0°$) (c) 3D far field radiation pattern of the conical ground plane monopole antenna, of the antenna shown in Figure 5.24b

5.2 Radar Hardware Development

5.2.1 Transmitter Chain

At the very start of a FMCW radar system is the generation of a chirp signal. To design the chirp waveform many different methods can be implemented, some of which were previously discussed when reviewing current radar design in Section 3.3.1. There it was shown that DDSs provide a quick and inexpensive method of generating a chirp waveform. With access to an Analog Devices DDS evaluation board, it was chosen for this project. The AD9910 evaluation board has a sample rate of 1 Gsamples/s, the Nyquist criterion limits this to a maximum signal frequency of 500 MHz. However, ideally the DDS should operate at approximately 75-80 % of the maximum, hence a practical limit of 350-400 MHz.

The output of the DDS is between DC-400 MHz and can be programmed using the evaluation software to generate the chirp signal fairly easily. However, for the chirp to be used for this project it needs to be operating in the 2.4 GHz ISM band. There are a number approaches that can be implemented and two will now be considered.

The first is probably the most common which involves the use of a mixer and up-converting the output of the DDS using a highly stable Local Oscillator (LO) signal. The Single Side Band (SSB) output can then be bandpass filtered to provide the required chirp at the correct centre frequency.

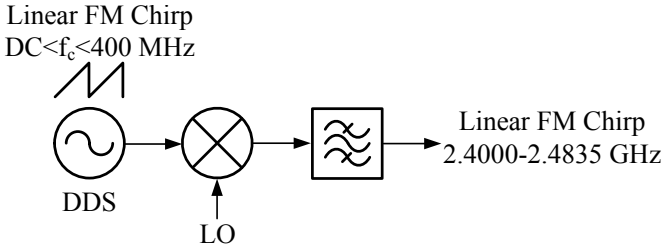

Figure 5.26: Up-converting a DDS linear FM chirp using a mixer with a stable LO signal and bandpass filtering the resultant signal

Another method is not too widely used but in this instance can be and eventually was. This is to operate the DDS in the super-Nyquist mode, which has one fundamental advantage over the up-converting method in that it does not require an additional mixer, but will still need the bandpass filter and RF amplification. Although not stated in the datasheet for this evaluation board, it can be operated in super-Nyquist mode by using the unfiltered output option provided on the evaluation board.

The possibility of using this evaluation board in super-Nyquist mode occurs because in addition to the generation of the fundamental chirp, the unfiltered output contains spectral images

of this fundamental signal. These can be in regions well beyond the maximum sampling clock of the DDS. This may seem too good to be true, however, it comes with at a price in terms of the image signals power level being considerably lower than the fundamental signal. This is due to the *sinc* frequency response of the digital-to-analogue conversion within the DAC [96] and is now briefly described [97].

Consider an analogue continuous time signal that is generated by a sequence of sampled values using delta functions:

$$x(t) = T \sum_{n=-\infty}^{\infty} x[n] \cdot \delta(t - nT) \tag{5.5}$$

the scaling factor, T, is due to the time scaling of the delta function, the DAC does not have an ideal brick wall low pass filter, hence the use of a zero-order hold filter. It takes the value of the current sample, $x[n]$, and holds it for the duration of the sampling interval, T, resulting in a continuous time signal, $x_{zoh}(t)$, with a staircase characteristic:

$$x_{zoh}(t) = \sum_{n=-\infty}^{\infty} x[n] \cdot \text{rect}\left(\frac{t - nT}{T} - \frac{1}{2}\right) \tag{5.6}$$

which results in an impulse response, shown visually in Figure 5.27:

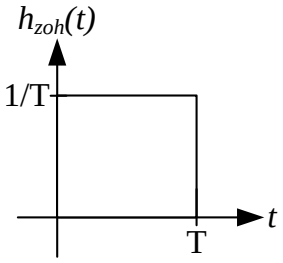

Figure 5.27: The impulse response of $h_{zoh}(t)$, the area under the curve is 1

$$h_{zoh}(t) = \frac{1}{T}\text{rect}\left(\frac{t}{T} - \frac{1}{2}\right) = \begin{cases} \frac{1}{T}, & \text{if } 0 \leq t < T \\ 0, & \text{otherwise} \end{cases} \tag{5.7}$$

hence, the frequency response is the continuous Fourier transform of the impulse response:

$$H_{zoh}(f) = \mathcal{F}\{h_{zoh}(t)\} = \frac{1 - e^{-j2\pi fT}}{j2\pi fT} = e^{-j\pi fT}\text{sinc}(fT) \tag{5.8}$$

the phase shift, $e^{-j\pi fT}$, is due to the rectangular function not being centred at zero. Usually, the images generated due to the sample and hold are low pass filtered and removed. However,

by using a bandpass filter on the unfiltered output the wanted image can be selected and the other unwanted and fundamental signals can be rejected. Table 5.8 shows the generated image frequencies based on the Nyquist zone they occupy and is depicted visually in Figure 5.28.

Table 5.8: The image frequency as a function of the clock frequency and the fundamental frequency

Nyquist zone	Image Frequency
1	$f_{fundamental}$
2	f_{clk} - $f_{fundamental}$
3	f_{clk} + $f_{fundamental}$
4	2*f_{clk} - $f_{fundamental}$
5	2*f_{clk} + $f_{fundamental}$
6	3*f_{clk} - $f_{fundamental}$

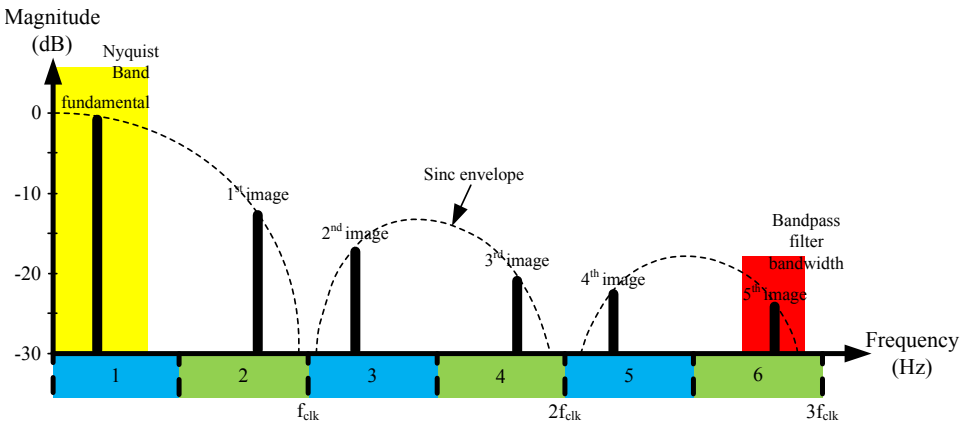

Figure 5.28: Images frequencies produced and the Nyquist zones they lay within [96]

Ideally, the fundamental/image signal should not interfere with adjacent image signals, but can do so if they are spectrally too close. If they are very close, then the bandpass filter would be unable to fully filter out the unwanted signal. To avoid this situation, the chirp bandwidth should be close to the centre of each Nyquist band, with the width of the Nyquist band much larger than the chirp bandwidth. In doing so, the bandpass filter can be fairly simple and easily bought off the shelf. Also, with a wide Nyquist band the image frequency could be in a lower Nyquist zone, hence requiring less amplification to obtain the correct signal amplitude.

Using the two main restrictions of the super-Nyquist mode described previously, the clock frequency can be determined. As stated above, ideally the centre frequency should be approximately in the centre of the Nyquist band. The first five bands will produce clock frequencies above the maximum 1 GSamples/s, hence the lowest band that can be used is the sixth band

(the fifth image). The clock frequency can be calculated by the following equation:

$$\begin{aligned} 2.75 * f_{clk} &= 2.44175 \text{ GHz} \\ f_{clk} &= \frac{2.44175}{2.75} = 887.91 \text{ MHz} \end{aligned} \tag{5.9}$$

The closest integer is 888 MHz, hence was the chosen clock frequency, which meant that the fundamental chirp had a bandwidth (83.5 MHz) from 180.25 to 263.75 MHz (this was calculated by determining $0.25*f_{clk}$ = 222 MHz as the centre frequency of the fundamental signal). The on board 25 MHz crystal oscillator which could be used to generate the required clock frequency, was originally intended to be used. However, as 888 is not a multiple of 25, the option to use an external crystal oscillator was chosen. The evaluation board has a built-in frequency multiplier which can be used to multiply the clock frequency with any integer value from 1 to 120. This allows a variety of external oscillator frequencies that could be used. An 8 MHz crystal oscillator and 'x111' multiplier were chosen in the end, largely due to the availability of the part at the time of construction. One slight detail to remember when using a DDS in this configuration, is when the fundamental signal has an increasing ramp then every even integer image will too. However, every odd image will have a decreasing ramp, it could be an issue for some applications but was not for this radar.

The output from the evaluation board does not seem to match the *sinc* envelope. This could be partly due to not using the max. hold feature for a long enough time. Hence, the top of curve is not at its maximum. However, is also in part due to the non-linear fundamental signal, the odd images (1, 3, 5 etc...) will be inverted, hence, as the highest frequency of the fundamental part of the ramp has a lower amplitude than the lower frequency. Therefore, this characteristic will be replicated but inverted for the odd images, which can be seen for image '3' in Figure 5.29. Another reason could be due to integral and differential linearity errors of the D/A converter which could cause the output of the DDS unfiltered port not to follow the *sinc* roll-off response [98].

The average power from the evaluations unfiltered output port for the fifth image was -40.75 dBm, as shown in Figure 5.29. The maximum output power allowed for radiolocation in this band is 25 mW (14 dBm). This meant that approximately 55 dB of gain was required to get the correct output power level of the radar (not including any losses that may be encountered, i.e. cable or connector losses). The transmit chain used in the radar system and also to produce the output power measurement is shown in Figure 5.31. Due to this method of generating the radar signal there is high chance of intermodulation products forming. Hence, as a result of

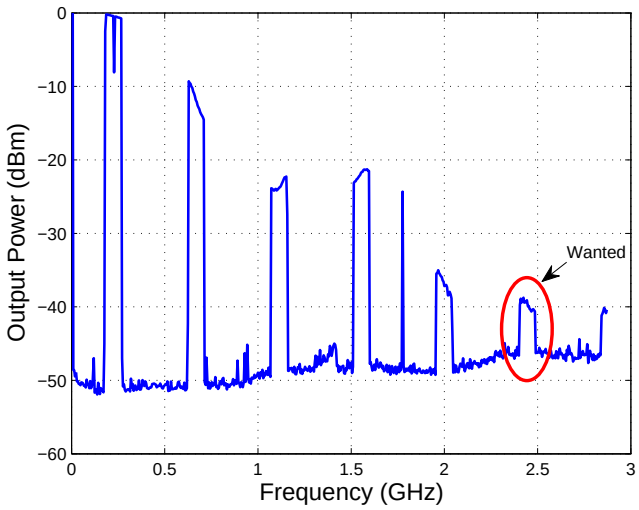

Figure 5.29: Output signal from the unfiltered output port of the AD9910 evaluation board, spectrum analyser settings were 100 kHz video and resolution bandwidth, also max. hold function used to view the bandwidth of the whole chirp

experimentation it was found that a very sharp roll off bandpass filter was required to isolate the wanted signal, whose response can be seen in Figure 5.30a. The choice of filter was an off the shelf Wainwright Instruments BPF 4-pole, 10 cavity filter [99]. Note that on Figure 5.29 the sinc envelope can just be seen.

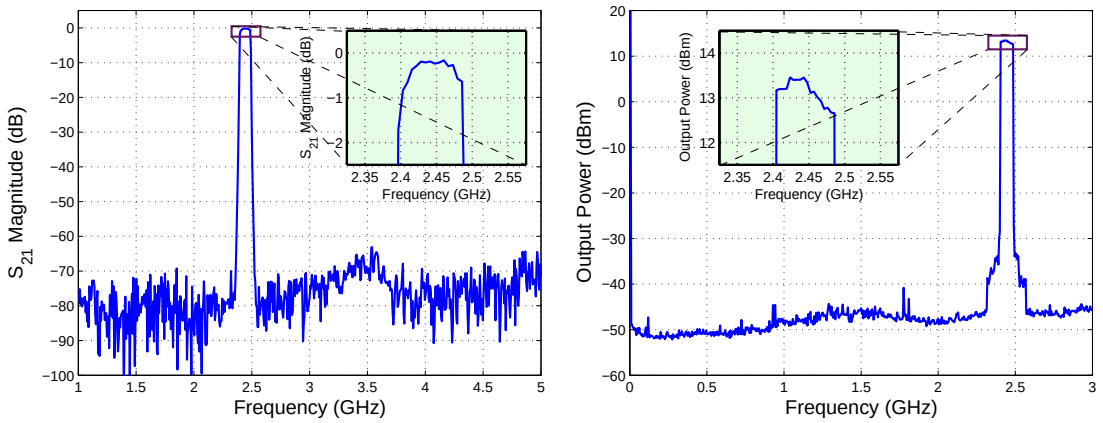

(a) (b)

Figure 5.30: Measured (a) S_{21} magnitude (dB) response of the narrowband bandpass filter (b) Transmitted signal from the radar system, VBW and RBW of 100 kHz, using the max. hold feature

The S_{21} response of the tenth order cavity bandpass filter shows that across the 2.4 - 2.4835 GHz bandwidth, with an insertion loss of approximately 0.6 dB. The bandpass response is not quite flat with a ripple from mid to end of the band, shown in Figure 5.30a, which is slightly higher than at the start of the band. This in contrast to the DDS output, which could potentially flatten the response at the output. The roll off of the filter is very high the 10 dB bandwidth

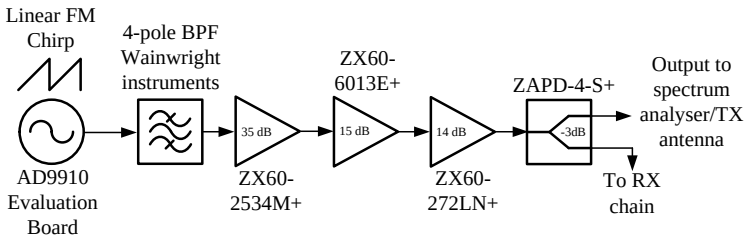

Figure 5.31: The radar transmit chain, with the individual components labelled

is 100 MHz, with a centre frequency of 2.445 GHz. The transmitted signal is shown in Figure 5.30b, shows the output power is approximately 13 dBm, 1 dB lower than the maximum allowed for this application. However, as this figure was obtained using the max. hold feature, parts of the response may not be entirely accurate. Also from this figure, the signal to noise power spectral density ratio can be determined ($13-(-47-10\log_{10}(100\text{ kHz})$=110 dB/Hz), which is quite high for super-Nyquist. The general *sinc* envelope can still be seen in the transmitted signal, so the filter response has not fully flattened the output signal as initially hoped. Note that the transmitted signal strength was determined with the use of 1 m long coaxial cable that is currently used in the radar which connects the transmitter port to the transmit antenna.

5.2.2 Receiver Chain

The receiver chain begins with the receive antenna followed by the feed network. The two outputs of the quadriphase feed network are individually bandpass filtered, to remove any out of band signals, which may have been picked up by the receive antenna within the environment. The signal is then amplified using a low noise amplifier (LNA) to ensure that the received RF signal is at least the minimum level that can be detected by the mixer. The LNA as one of the first components of the receiver chain and has a significant impact on the receiver Noise Figure. It has the effect of increasing the sensitivity of the receiver but can reduce the receivers dynamic range. Ideally, the LNA should have a low Noise Figure so it does not contribute too much noise itself. As any additional noise added in the early part of the receiver chain, will be amplified by amplifiers later in the chain. The usual gain of an LNA is approximately 13-25 dB and Noise Figure as low as 0.5 dB. The next component is the mixer to downconvert the RF signal to baseband with the use of a LO signal that is obtained with the use of connectorised 0° 3 dB power splitter from the transmitted signal. The IF signal is then fed into an anti-aliasing filter, which is combined with a high-pass filter to compensate the lower powered, high frequency signal obtained at long ranges. This would not be required if the dynamic range of ADC was such that it accommodates both the low frequency, high power signal and the lower powered, higher frequency signal. The receive chain block diagram is shown in Figure 5.32.

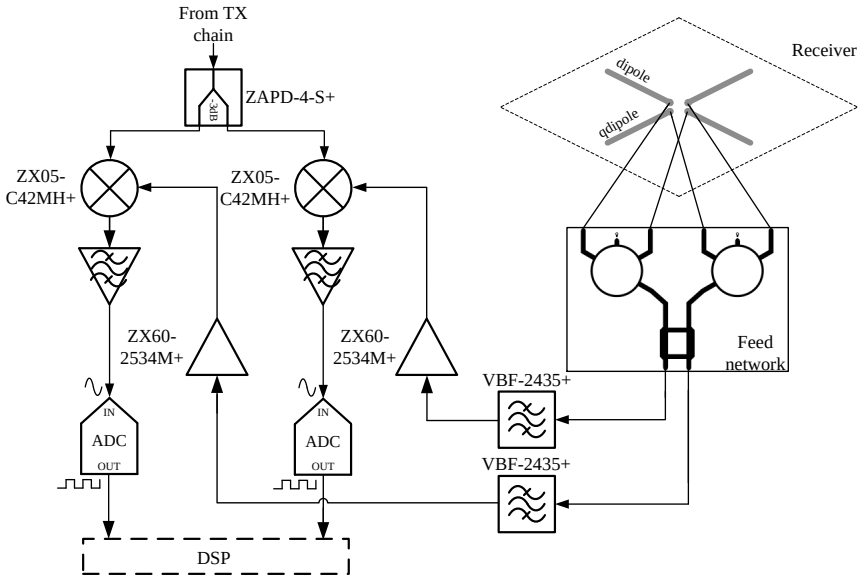

Figure 5.32: The radar receive chain, with the individual components labelled

The overall receiver has been discussed and now the individual components that make up the receiver chain will be chosen, based on the power budget and the availability of parts. The output power is limited by regulation to 14 dBm, the highest received power signal would result from the mutual coupling between the transmit and receive antennas. The worst-case coupling between the antenna can be determined by recalling equation (2.6), putting in the known values, the minimum separation between the antennas can be determined, hence the maximum received power. The transmitter gain considering a conical monopole with a 2 dBi gain, the receive antenna and feed network at best would have a combined gain of -1 dB. Inserting these parameters, the maximum power can be calculated with increasing yet reasonable separations, as discussed in Table 5.9.

Table 5.9: Received power due to direct coupling

Separation (λ)	**Separation (m)**	**P_r (dBm)**
2	0.246	-13.005
3	0.367	-16.527
4	0.492	-19.025
5	0.613	-20.964
6	0.737	-22.547

The coupling can be improved further by having orthogonal polarisation between the transmit and receive antenna. Also, separation between the antenna vertically would offer increased isolation, especially if both antenna have nulls in the vertical plane. Finally, placing some type of absorber between the antenna will absorb some of the transmitted signal and reduce its coupling into the receiver. Most materials will act as some type of absorber, but using specialised

materials tailored for certain frequencies could be placed to reduce the coupling.

Using some of the techniques described above the direct signal power can be given a conservative estimate of -30 dBm (-34 dB due to a separation of 4λ between antennas and an additional 10 dB from using orthogonal polarisation, hence totalling 44 dB). This maximum expected signal will be at a low frequency and can be used in the selection process for the ADC.

The signal bandwidth has been stated previously and is 83.5 MHz. Hence, the thermal self noise power in this bandwidth is -94.76 dBm. By considering a realistic receiver Noise Figure of 9 dB, the sensitivity level is approximately -86 dBm at the receiver input. To achieve the maximum sensitivity, the dynamic range of the receiver would need to be at least 56 dB. This sets one of the criteria the ADC must fulfil.

As the ADC samples an analogue signal and digitises it, the ADC dynamic range can be calculated using the equation $20\log_{10} 2^b$, where 2^b is the number of quantisation levels of a ADC with b bits. The ADC chosen for this project was a creative 1090 soundblaster USB sound card as it operated within the maximum expected IF signal and was available for use immediately. It has a maximum sampling frequency of 96 kHz with 24-bit resolution, using the line-in input port, it gives the ability to sample 2 analogue channels simultaneously [100]. The aim to use MATLAB to acquire the audio signal, however it is limited to 16-bit resolution, albeit with a maximum sampling rate, f_s, of 96 kHz. The quoted number of bits can be slightly misleading as it assumes that the ADC is perfect with no jitter. Ideally, the Effective Number Of Bits (ENOB) would be a better approximation, which is usually one less than the quoted number of bits. However, the main purpose of a sound card is for audio and the datasheet does not provide the ENOB. Also, as the MATLAB software limits the number of bits to 16, a reasonable assumption would be that the ADC has a ENOB of 15, hence, a dynamic range of 90.31 dB. The ADC noise floor limits the minimum signal that can be detected, which is determined by first calculating the noise voltage for the ENOB using the following relationship:

$$v_{ADC,noise} = \frac{v_{fs}}{2^{b_{ENOB}}} \tag{5.10}$$

where, v_{fs}, is the full scale voltage and for this ADC is 2 $V_{pk\text{-}pk}$ and b_{ENOB} is 15. Hence, the minimum detectable signal into a 50 Ω load can be calculated by:

$$P_{min,ADC} = 10\log_{10} \frac{v^2_{ADC,noise}}{\left(2\sqrt{2}\right)^2 \cdot 50} \tag{5.11}$$

Which when equated for this ADC is -80.31 dBm. With a maximum signal before clipping of 10 dBm which was determined by evaluated the following:

$$P_{max,ADC} = 10\log_{10}\frac{v_{fs}^2}{\left(2\sqrt{2}\right)^2 \cdot 50} \tag{5.12}$$

To fully utilise the dynamic range of the ADC, the thermal noise of the receiver in addition to the Noise Figure should equal the minimum signal detectable by the ADC. This calculation reveals that an additional gain of 5.45 dB is required by the receiver ($-80.31 - (-94.76 + 9) = 5.45$). Using the ADC parameters above, its Noise Figure can be determined using the following expression [101]:

$$F_{n,ADC}(\text{dB}) = P_{max,ADC} - 10\log_{10} kT - SNR_{ADC} - 10\log_{10}\left(\frac{f_s}{2}\right) \tag{5.13}$$

where, SNR_{ADC} is given by the expression [102]:

$$SNR_{ADC}(\text{dB}) = 6.02(b_{ENOB}) + 1.76 \tag{5.14}$$

thus, the ADC SNR is 92.06 dB, and its Noise Figure is 45 dB. The Noise Figure is very high, but as it is the last component in the receiver chain it will have the least contribution to the overall system Noise Figure.

Finally, before any other values can be attributed to system the chirp waveform, receiver Noise Figure and link budget for radar must be discussed.

Waveform Considerations

As discussed in Section 2.3.1 a linear FM waveform was chosen for this project. This was due to the expected velocity of the ship which would distinguish whether a target is moving or stationary. If the equation (2.19) in Section 2.2.1 is taken further to show how the instantaneous frequency, f_o varies by, B, the sweep bandwidth, the Doppler shift caused by a moving target during the pulse can be determined by:

$$\Delta f_D = \frac{2v_r B}{c} \tag{5.15}$$

In terms of processing the IF signal, if the Doppler shift variation approaches the FFT resolution, $1/T$ (1/ the sweep duration) the radar then nears its Doppler resolution limit. Hence, the maximum target velocity the radar can tolerate and still consider the target stationary is given

by:

$$\frac{2v_r B}{c} < \frac{1}{T}$$

$\therefore$

$$v_r < \frac{c}{2BT} \tag{5.16}$$

By considering a constant accelerating target with acceleration, a, over the course of a single chirp. The amount the received echo frequency linearly changes due to the acceleration can be determined by evaluating the differential of equation (2.18).

$$\Delta f = \frac{\Delta\omega}{2\pi} = \frac{T}{2\pi}\frac{\mathrm{d}\omega_D}{\mathrm{d}t} = \frac{2aTf_o}{c} \tag{5.17}$$

where,

$$\frac{\mathrm{d}\omega_D}{\mathrm{d}t} = \frac{4\pi f_o}{c}\frac{\mathrm{d}^2 r}{\mathrm{d}t^2} \quad and \quad \frac{\mathrm{d}^2 r}{\mathrm{d}t^2} = a \tag{5.18}$$

If this frequency variation approaches the FFT resolution, $1/T$, then the radar is approaching the limit of its tolerance to target acceleration. Hence, the maximum target acceleration can be determined by:

$$\frac{2aTf_o}{c} < \frac{1}{T}$$

$\therefore$

$$a < \frac{c}{2T^2 f_o} \tag{5.19}$$

The two maxima for the velocity and acceleration must both be satisfied when the target is simultaneously travelling at a significant velocity whilst accelerating. By substituting some sensible values (e.g 50 ms) for the pulse length, the maximum tolerable target velocity and acceleration is 35.93 ms^{-1} and 24.57 ms^{-2}. However, considering a ship coming close to an oil rig or to the harbour, then its velocity or acceleration of the target should not be this high. Hence, the choice of a relatively long transmitted pulse.

Minimum SNR

To determine the minimum SNR, it is heavily dependent on the system requirements. What is particularly crucial for this radar system is the bearing accuracy, which is highly dependant on the SNR. It is shown how significant by the relationship between phase jitter and the SNR which can be determined, per channel, by the following [103], however is only really valid for phase jitters up to 15° [104]:

$$\Delta\phi_{rms} = \frac{1}{\sqrt{2SNR}} \tag{5.20}$$

The SNR of the relative phase jitter produced by the complex conjugate product of the 1st and -1st order modes will be reduced by 6 dB due to the 'signal x noise' cross-product generation common to any square law type device. Hence, the system phase jitter is $1/\sqrt{SNR}$. Finally, the bearing deviation which is half the system phase jitter and equals $1/2\sqrt{SNR}$. For a bearing deviation of 1°, requires a minimum SNR of 29.38 dB, which shown in Section 5.2.2 occurs at a range of 290 m, hence setting 290 m as the maximum range.

Receiver Noise Figure

The Noise Figure,F_n, features in determining how much gain is required to bring the thermal noise to the minimum signal the ADC can detect. The cascaded noise factor can be obtained by considering the Friis formula for the noise factor [105]:

$$F_{nf} = F_1 + \frac{F_2 - 1}{G_1} + \frac{F_3 - 1}{G_1 G_2} + ... + \frac{F_N - 1}{G_1 G_2 ... G_{N-1}} \tag{5.21}$$

The Noise Figure is obtained converting the noise factor from a ratio to decibels, (e.g $F_n = 10\log_{10}(F_{nf})$).

Table 5.10: Receiver chain parts list

Receiver chain position	Part	F_n (dB)	Gain (dB)
1	Bandpass Filter (VBF-2435+)	1.61	-1.61
2	Amplifier (ZX60-2534M-S+)	3.20	35.00
3	0.5 m coaxial cable (rg-174)	1.00	-1.00
4	Mixer (ZX05-C42MH+)	7.00	-7.00
5	Active baseband filter	25.00	65.00
6	ADC (SB1090)	45.00	N/A

From the data shown in Table 5.10 the cascaded Noise Figure is 5.96 dB, per channel. However, as the two IF channels combine together at the signal processing stage to produce the phase difference, the Noise Figure increases by 3 dB. Hence, the whole system Noise Figure

is 8.96 dB. Also, as the IF signal is expected to begin at DC to a few kilohertz, the signal will experience high levels of flicker noise which will inevitably cause the Noise Figure to be considerably higher than value obtained by the cascade analysis. Also, at low IF frequencies it is very difficult to measure baseband filters Noise Figure. Being based on OP-AMPs it is expected to have a fairly high Noise Figure, hence the choice of a conservative value of 25 dB. However, as it is further down the chain it has a lower influence on the receiver Noise Figure. A reduction in its Noise Figure by 10 dB causes the system Noise Figure to decrease by 1 dB and an increase in its Noise Figure of 10 dB results in a system increase of 5 dB.

Link Budget

The link budget for this project is largely based on equation (2.39). There are enough system parameters known for most of them to be substituted for real values and the remainder can be justified. The minimum power received will occur at the furthest distance the target is from the radar. Hence, the link budget will be assuming the maximum range based on the minimum tolerable SNR.

Table 5.11: Radar system link budget

Radar Parameters		**Units**
P_t = Transmit power	13.5	dBm
G_t = Transmit antenna gain	2	dBi
G_r = Receive antenna + feed network gain	-1	dB
G_{tar} = Active target antenna gain	3	dBi
G_{amp} = Active target amplifier gain	35.8	dB
R_t = Target distance (Max Range)	290	m
F_n = Receiver noise figure	9	dB
λ_o = Wavelength at f_o	0.123	m
f_o = Output frequency	2.44	GHz
B = Sweep bandwidth	83.50	MHz
T = Pulse length	50.00	ms
f_d = Deramped frequency	11.13	Hz/m
ΔR = Range resolution	1.80	m
ADC sampling rate	18.00 (N) 96.00 (used)	ksamples/s
$P_n = kT_0(1/T)F_n$	-151.97	dBm
$P_{r,min} = P_tG_tG_r{G_{tar}}^2G_{amp}\ (\lambda_o/(4\pi R_t))^4$	-122.59	dBm
$SNR_{min} = P_{r,min}/P_n$	29.38	dB
$\Delta\phi_{rms} = 1/(\sqrt{2SNR})$ (Per channel)	1.37	degrees
$\sqrt{2}\Delta\phi_{rms}$(Whole system)	1.94	degrees
Bearing deviation = $\sqrt{2}\Delta\phi_{rms}/2$	0.97	degrees

A pulse length of 50 ms (PRF = 20 Hz), will be sufficient to assume a stationary target. The noise power discussed previously assumed a bandwidth equal to the sweep bandwidth (83.5 MHz) of the radar signal, which would be -86 dBm (with a receiver noise figure of 9

dB). The minimum power (-122.59 dBm) at the maximum range therefore seems to indicate a negative SNR. This is overcome because the signal bandwidth becomes the same as the PRF, hence, the noise bandwidth is also 20 Hz. This therefore provides a processing gain equal to the time-bandwidth product, which was one of the advantages of using FMCW discussed in Section 2.3.2. Hence, the thermal noise power in 20 Hz is -151.97 dBm (with a noise figure of 9 dB). Finally, this gives a SNR at 290 m of 29.38 dB. The added processing gain also improves the systems sensitivity level, which is the minimum signal that can be detected by the ADC. Hence, the minimum gain that must be applied to detect the lowest powered signal is $(-80.31 - (-122.59) = 42.28$ dB).

Previously the isolation between the transmit and receive antennas was discussed. It was shown that a separation of 0.5 m and the use of orthogonal polarisations would result in a maximum expected received power would be approximately -30 dBm. If the minimum gain ($\approx$42.3 dB) required to detect the furthest signal is applied, this would saturate the ADC (max. power of 10 dBm). However, the bandpass filter insertion loss, mixer conversion loss, cables and connectors losses will have a combined loss of approximately 10 to 12 dB. This loss must be added to the minimum gain to be able to truly detect the lowest powered signal, hence, a minimum gain of $\approx$55 dB.

Also, by utilising frequency gain control the level of receiver gain can be increased even further still without saturating the ADC and for this project, was achieved using OP-AMP active filters. However, as discussed in the Section 5.2.3 the active target plays a significant role in the baseband filters response. Therefore, the baseband filter will be discussed separately in greater detail in Section 5.2.4 .

Before connecting the antennas to the radar, a loop test was carried out using the radar hardware. It involved connecting a coaxial cable of a known length from the radars transmitter output to the receivers input and observing the deramped output signal. The cable loss should also be determined by measuring its S_{21} response. Finally, the cables dielectric constant/velocity factor must be known, to determine its electrical length, the measured deramped frequency will correspond to a point target at half the distance of cables' electrical length. As there are four receiver channels only a single channel could be connected from the transmitter to the receiver, with the experimental set-up shown in Figure 5.33. For a 20 m physical length the loss was 8 dB, with a dielectric constant of approximately 1.5, this resulted in an electrical length of 24.5 m, hence simulating a point target at 12.25 m. This corresponds to a IF signal at approximately 136 Hz ($12.25 * 11.13 = 136$). Additional in-line attenuators (30, 40 and 50 dB) were used to ensure that RF input to the mixer was well below its saturation point. Three

separate measurements were carried out each with the varying attenuations to ensure that the measurement was consistent, with the 30 and 50 dB attenuator measurement results shown. This experiment was carried out without the use of a baseband filter and the IF signal was measured directly out of the mixers IF port. Figure 5.34a shows a 145 Hz signal at 1.01 $V_{pk\text{-}pk}$ in to high impedance load, hence the 50 Ω power level of -1.95 dBm with a 30 dB attenuator (-11.16 dBm, -21.06 dBm with 40, 50 dB attenuators respectively), the power into the receiver port is -24.5 dBm ($13.5 - 8 - 30 = -24.5$ dBm). Corresponding to a receiver gain of 22.55 dB before the additional gain of the baseband filter.

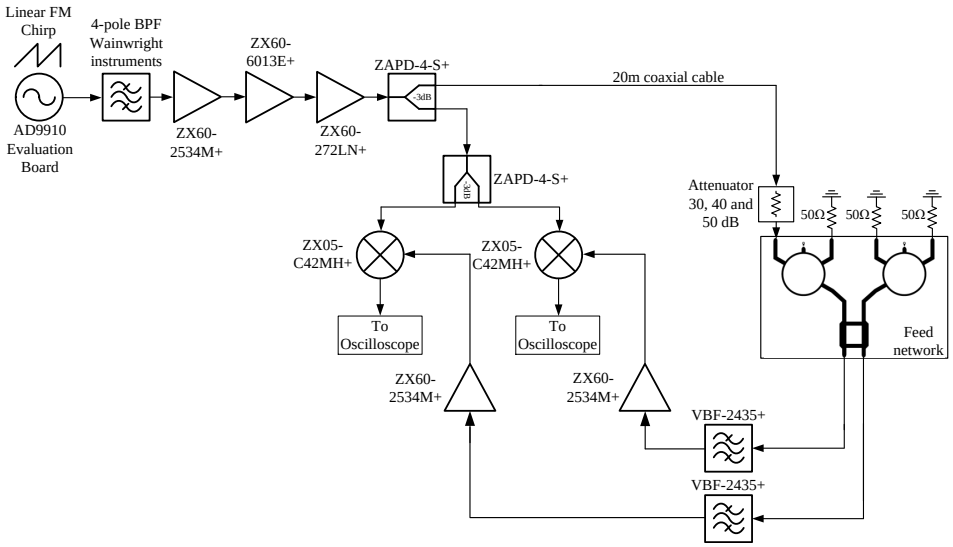

Figure 5.33: Loop test experimental set-up

Figure 5.34b does show that chirp repetition frequency is breaking through (yellow line). Hence, seeming as if the IF signal is modulated with a 20 Hz signal. In the same figure the blue curve shows the response on the other channel, but with a series 1 μF capacitor removing the low frequency PRF signal. This result shows that at the input of the baseband filter the first component should be a series capacitor.

As the radar seems to be performing adequately, attention shifted to the development of the active target, which is where this thesis continues.

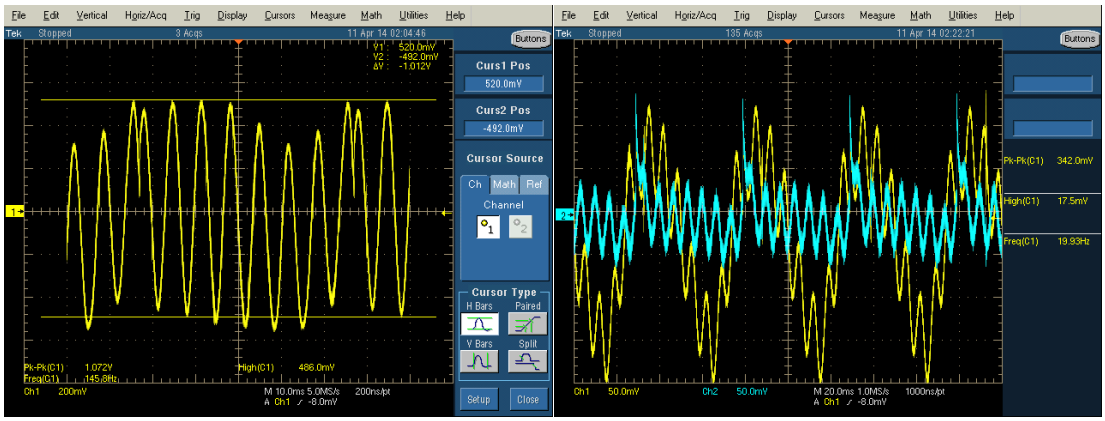

(a) (b)

Figure 5.34: Loop test results with (a) 30 (b) 50 dB attenuator, the deramped frequency in both figures is 145 Hz, also note the 20 Hz PRF in (b)

5.2.3 Active Target

The project revolves around the use of an active target as part of the radar system. The initial idea was to use a simple active target one that consists of two antennas (one transmit and one receive) with amplifiers in between, shown previously in Figure 3.2. The antenna initially chosen for the target were single edge fed patch antenna with two (YSF-272, available from www.minicircuits.com) surface mount amplifiers, each with 20 dB of gain and a bandwidth of 400 MHz (2300 - 2700 MHz). With a total gain of 40 dB this then sets the amount of isolation required between the antennas. As the transmit and receive are orthogonally polarised, the isolation due to physical separation can be slightly lower, hence, a smaller sized target. Also, in between the amplifiers there were pads milled such that a 'T' attenuator could be made with resistors, this was a precautionary measure to lower the gain if it was later found to be too high. The physical separation between the antennas phase centres was approximately 1.8λ. The Friis transmission equation (2.6) shows that the target has an isolation of 27 dB, this could lead to the possibility of self oscillation. This occurs when the transmitted signal is directly intercepted by the receive antenna. The self oscillation can continue indefinitely and cause the amplifier to overload or amplify out of bounds signals reducing the expected gain.

Another issue with only using a single patch antenna is its -10 dB bandwidth. It can vary from as little as 1 to 5% of the centre frequency. Its bandwidth is dependant on the dielectric thickness, a general rule of thumb is that the lower the separation the lower the bandwidth. With these percentages, the expected bandwidth of the patch is anywhere from 25 MHz to 120 MHz. The required bandwidth is 83.5 MHz to ensure that the antennas bandwidth is as high as possible, two single copper clad 1.6 mm thick FR-4 PCBs were epoxied (substrate side) together due to the unavailability of a 3.2 mm substrate. For a single board active target long striplines

were required to maintain the separation between the two antenna. This introduced very lossy antenna with simulations showing that these antennas only had a gain of approximately 4 dBi.

Smaller samples were made to determine the S_{11} response consisting of sample patch antennas with a shortened microstrip line. The antennas had slightly different patch dimensions and inset widths to determine the optimum patch antenna size for the correct resonant frequency and S_{11} bandwidth. Sample antennas were made with two thicknesses, the original 1.6 mm and thicker 3.2 mm substrate. Also made with differing ground plane sizes, as the single board active target would be significantly larger than the test samples. The size of the ground plane in relation to the S_{11} bandwidth had to be determined.

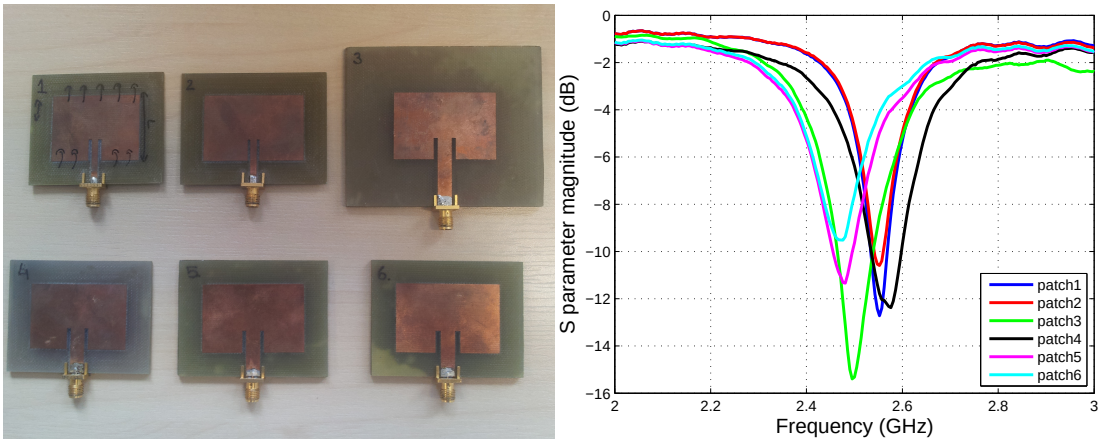

(a) (b)

Figure 5.35: (a) Photo of the sample patches antenna (b) measured S_{11} of the patches in (a)

In Figure 5.35 patches 1 and 2 were made on 1.6 mm substrates, hence the narrower microstripline, with the remaining (Patches 3-6) all constructed on 3.2 mm substrate. Patches 3 and 4 are of the same dimensions but have differing ground plane sizes. Patches 5 and 6 were made after patches 3 and 4 were tested to fine tune the antennas resonant frequency. The samples indeed agree with the theory, a doubling of the substrate thickness has doubled the bandwidth from 35 MHz to 70 MHz and the increased ground plane size results in a better impedance match. As it would be difficult to test just the antenna on the active target. Hence, the targets antenna were designed with dimensions between the patches 3 and 5, as the increased ground plane decreased the centre frequency (differences between patches 3 and 4) and patches 5 and 6 where made slightly larger than 3 and 4 for a lower resonant frequency. The measured S_{11} for all the patches shown in Figure 5.35b were carried out in an open lab as it would be similar to the intended operational environment.

Once the PCB was designed and the maximum separation that could be achieved with the PCB milling machine were established, it was constructed. The target was tested using two

patch antenna attached to a vector network analyser with the set-up shown in Figure 5.36a. The S_{21} measurement was made with the active target both on and off, as shown in Figure 5.37.

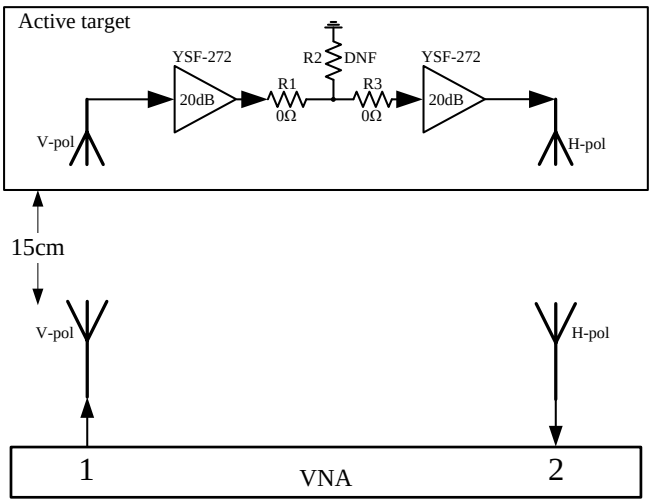

(a)

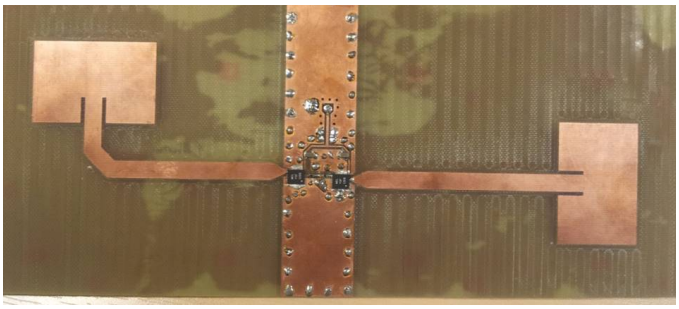

(b)

Figure 5.36: (a) Experimental set-up to measure the active target S_{21} and the targets circuit diagram (*note V-pol and H-pol antenna connected to the VNA are patches 5 and 6 respectively, orientated to provide the correct polarisation) (b) Photo of the constructed active target

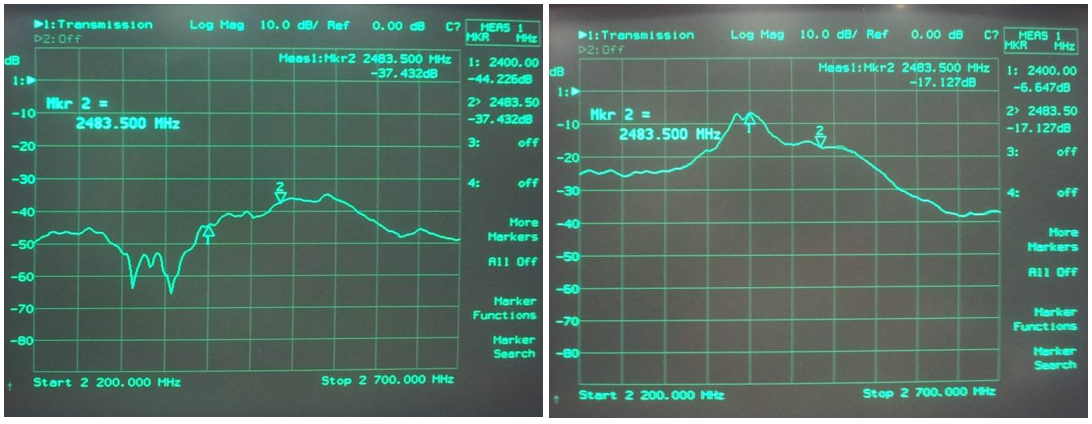

(a) (b)

Figure 5.37: Measured S_{21} using the active target and VNA, when the target is (a) off (b) on

The results in Figure 5.37 were obtained with the above described method, the distance

between the antennas on the VNA and the active target was 15 cm. The expected gain between the target on and off should be approximately 25 dB, taking into account the path loss between the antenna and the target, the targets amplifier gain and the four antenna gains. A gain of approximately 25 dB can be seen in Figures 5.37a and 5.37b.

Figure 5.39 shows the two states of the target with the transmit and receive antennas, which were used in the original tests that produced the results shown in Figure 5.19. The experimental set-up for the results in Figure 5.39 is shown in Figure 5.38 and is as follows: The transmit and receive radar antennas were horizontally separated by 1.5 m, the transmitter was connected to the radar via a 10 m coaxial cable (12.25 m electrical length). The crossed-dipole was connected to 0.97 m long coaxial cables (1.47 m electrically), with the target approximately 1 m away from the radar the expected return should be at around 14-15 m, which can just about be seen. The target was however very difficult to detect using the radar in the lab at more than 1 m, which was later determined to be a result of the clutter within the room. During initial tests clutter subtraction was required just to be able to detect the active target between 1 and 3 m. The clutter subtraction was achieved by taking a background measurement with the active target off, this data is then stored. When the active target is turned on, the background measurement was subtracted from the current measurements, leaving a result that shows the changes in environment since the background measurement. One approach would be to subtract all the frequency components, but this would have the effect of increasing the noise. Therefore, experiments were carried out to determine up to the maximum subtracted frequency and it was found that removing the frequencies components from DC-200 Hz was more than sufficient, for the indoor room measurements. A frequency of 200 Hz corresponded to approximately 18 m range, much greater than the size of the room.

The background measurement was stored as a time domain signal of a single chirp, its FFT is taken and all frequencies above 200 Hz were nullified. The low frequency components remaining were converted back into the time domain. With every subsequent chirp and with the target turned on this background low frequency time domain signal was subtracted (see Appendix C for a worked example). Using this approach, the target could now be seen in the environment, however the background measurement was only valid if nothing in the background changed and if the radar is completely stationary, This would be virtually impossible as the ship is expected to ebb up and down even whilst stationary and it would be impractical to take a background measurement with every change in the scene. Hence, it was decided to determine how the clutter affected the target response.

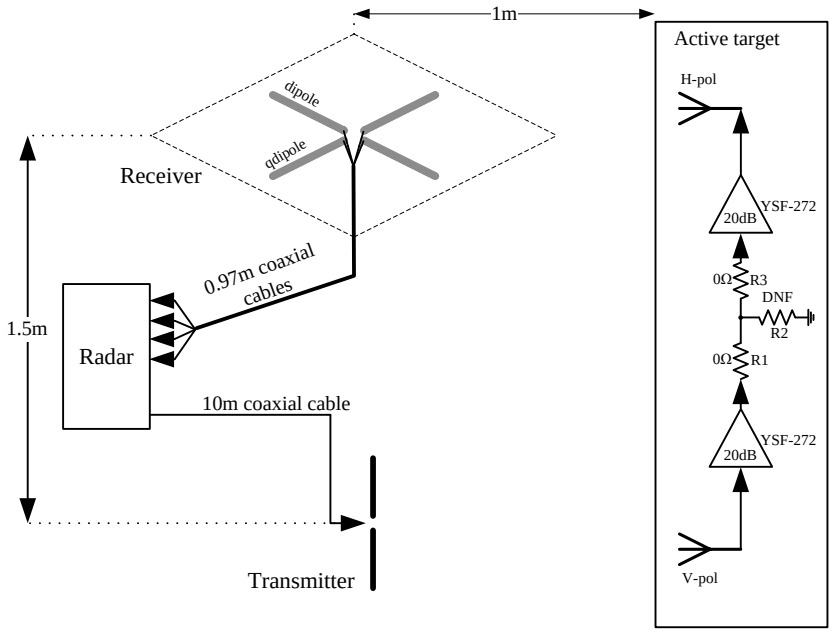

Figure 5.38: Experimental set-up with active target placed 1 m from the radar, within a lab setting

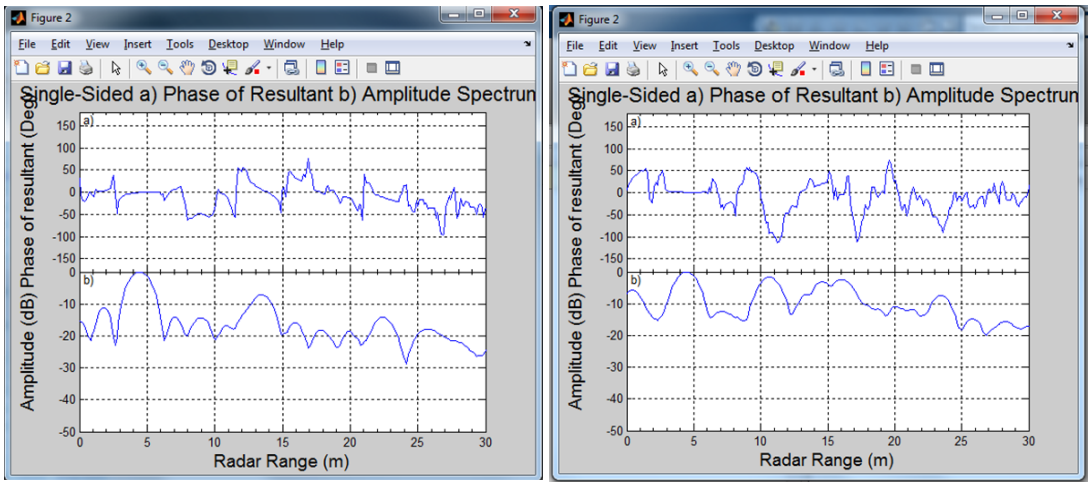

(a) (b)

Figure 5.39: Initial lab tests with the active target (a) off (b) on, with the experimental set-up as shown in Figure 5.38

Clutter Analysis

As a result of the above it was discussed that without subtracting the background measurement the target was unable to be detected. Partly due to the configuration of the room as it had many metal filing cabinets, hence, large corner reflectors. However, when determining how the clutter power varied with range, it was revealed that for an omnidirectional radar system the clutter is the annular ring whose width is the radar range resolution and the clutter coherently added up over this area. For a usual mechanically steered antenna, its narrow beamwidth and relativity

short dwell time limit the clutter affecting the received signal. Therefore resulting in a clutter area, A, which is a sector of the omnidirectional antennas clutter region. In the real system the antenna would be mounted on a mast on the ship well above sea level with the sea clutter on the sea surface at an angle, α, to the receive antenna. The clutter area can be determined by considering a typical radar system with a narrow beam antenna its azimuth beamwidth in equation (5.22) is an angle β and is shown in Figure 5.40. The area A is given by the equation:

$$\begin{aligned} A &= \frac{2\pi R\Delta R}{\cos\alpha}.\frac{\beta}{2\pi} \\ &= \frac{\beta R\Delta R}{\cos\alpha} \end{aligned} \tag{5.22}$$

where R in this equation is the range to the target. Hence, the total RCS over this region is given by the equation:

$$\begin{aligned} RCS &= A\sigma^{\circ}\cos\alpha \\ &= \beta R\Delta R\sigma^{\circ} \end{aligned} \tag{5.23}$$

where, A is substituted with (5.22), $\sigma^{\circ}\cos\alpha$, is the assumed backscatter coefficient. The intercepted power, P_{inc}, by the clutter from the radar is given by the equation (5.24), which can be determined by considering the Friis transmission equation [7]:

$$\begin{aligned} P_{inc} &= \frac{P_t G_t(RCS)}{4\pi R^2} \\ &= \frac{P_t G_t \beta R\Delta R\sigma^{\circ}}{4\pi R^2} \end{aligned} \tag{5.24}$$

hence, the power received by the radar from the clutter is:

$$\begin{aligned} P_{r,clutter} &= P_{inc}\left(\frac{\lambda_o}{4\pi R}\right)^2 \\ &= \frac{P_t G_t G_r \Delta R\beta\lambda_o^2\sigma^{\circ}}{(4\pi R)^3} \end{aligned} \tag{5.25}$$

Equation (5.25) is very similar to the standard radar equation [5], with respect to how the power varies with range ($1/R^3$). The active target radar equation (2.39) shows that the power varies with range with a ($1/R^4$) dependency. Equation (5.25) can be rewritten for the omnidirectional antenna by replacing β with 2π:

$$P_{r,clutter} = \frac{P_t G_t G_r \Delta R\lambda_o^2\sigma^{\circ}}{2(4\pi)^2 R^3} \tag{5.26}$$

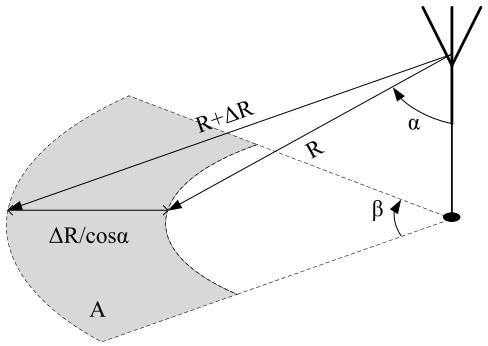

Figure 5.40: Geometry of receive antenna and the clutter region

By plotting how the clutter and target power both vary with range (see Figure 5.41), revealed exactly why the active target only worked for approximately 1 m in the lab. By setting the backscatter coefficient $\sigma^{\circ}\cos\alpha$ to fixed value of 0.1 the clutter power would be greater than the power received by the target at range of 15 m, if the backscatter coefficient is increased, to say, 1, the maximum detectable range by the radar reduces further to approximately 1.5 m. It should be noted that these values are completely arbitrary, but it does highlight the fact with this current active target the radar will be severely clutter limited. However, shifting the RF signal at the target by a relatively low frequency can remove this clutter limitation, which is now considered.

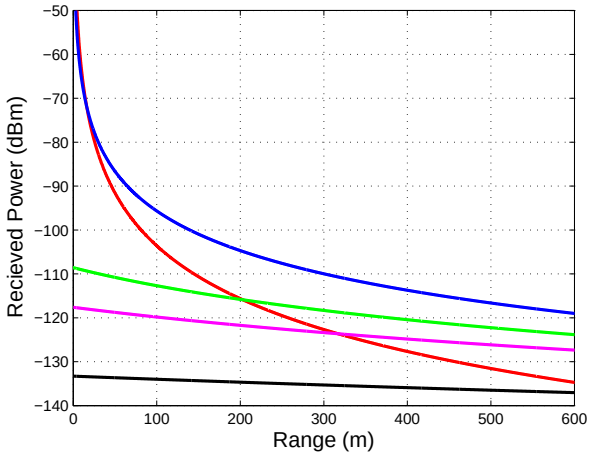

Figure 5.41: Simulated received target power (red) and clutter power with 0 Hz (blue), 3 kHz (green), 6 kHz (magenta) and 20 kHz (black) frequency shifts

Frequency Shifted Active Target

To avoid the clutter issue a small frequency offset in the order of a few kilohertz could be modulated to the RF signal, within the active target, before it was transmitted back to the radar.

Figure 5.41 shows that this will reduce the clutter power competing with the wanted target signal. In terms of the RF frequency it would be hardly noticeable. However, for the IF signal, this would move it from occupying DC-3 kHz to whatever the offset frequency + 3 kHz, where 3 kHz corresponds to an approximate maximum range of 270 m. With a higher frequency shift, the IF signal moves further away from the flicker noise region, hopefully resulting in lower system noise. However, the frequency shift cannot be indefinitely increased as it would require a higher ADC sampling rate.

Also, something that was mentioned previously with respect to the $1/R^4$ baseband filter in that it becomes increasingly complex. What was previously a DC-3 kHz IF signal, the reduction in the IF signal strength with range, requires compensation. The IF signal reduces by 12 dB for every doubling of range. Hence, an active highpass filter with approximately 40 dB/decade gain would be required to maximise the dynamic range of the ADC. When the IF signal has a frequency offset applied to it, this filter requirement remains. However, the difference between the minimum and maximum IF is no longer in the order of decades, hence, results in a very complex active filter design. The active baseband filter will be discussed later with two different filters designed for the unmodulated and modulated target.

The first idea was to design a SSB modulated target all on a single PCB with a similar design as the unmodulated target, depicted in Figure 5.42. Additional circuitry, was required for the generation of the 3 kHz signal and to SSB modulate output RF signal. When testing the unmodulated target it was difficult to determine how well the amplifiers were performing. Hence, the inclusion of directional couplers, to allow the injection of signal without altering the antenna were also included.

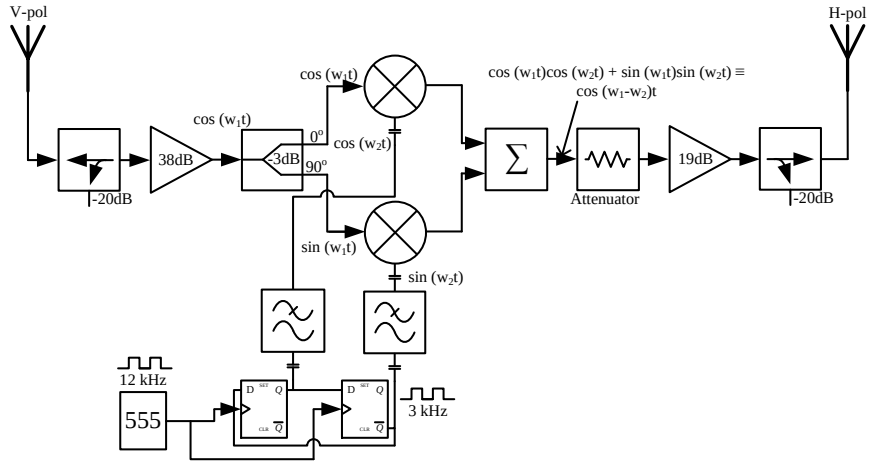

Figure 5.42: A SSB modulated active target

This approach had some difficulties with RF power levels, which were much lower than

expected and when debugging these errors, the RF line became damaged. Hence, a simpler approach that is almost as effective, is to use double-sideband modulation, and this indeed was implemented, using connectorised components, in order to prove the concept.

The unmodulated target antennas had shown -10 dB S_{11} bandwidth slightly lower than the radars sweep bandwidth, in order to maximise the antenna bandwidth and minimise losses the patch antennas were redesigned. Before the patch was matched with a 50 Ω transmission line, due to the width of this microstripline, simulation showed it to be quite lossy. Hence, the implementation of 100 Ω patches with 100 Ω microstrip lines were simulated and samples constructed. The 100 Ω microstrip line would be transformed via a quarter wave transformer to 50 Ω to match the impedance of the targets subsequent components in the RF chain.

Also, to increase the bandwidth along the length of the patch antenna, serrations were added, with the assumption that the shortest length of the patch antenna corresponding the resonant length of the highest RF frequency, 1 mm extensions were added to both sides. Therefore, at its longest, the patches total length was 2 mm greater. Hence, the patches average length was slightly below required resonant frequency. These comb structures could also be removed in pairs to increase the antennas resonant frequency. Two samples were made initially for the single board modulated target, but as single board target was unsuccessful they were both recycled for use with the connectorised modulated target. The receive antenna is vertically polarised, same as the polarisation of the radar transmit antenna, likewise the targets transmit and the radar receive antenna are both horizontally polarised. The measured results shown in Figure 5.43b are after removal of 1 and 2 pairs of combs for the transmit and receive patch antennas respectively to achieve the correct resonant frequency. The comb extensions had the added benefit of not only giving the ability to tune the antenna but also had the effect of increasing the patches bandwidth from 70 MHz as shown in Figure 5.35b to 100 and 120 MHz for the receive and transmit antenna respectively. This is probably due the extensions introducing a range of resonant frequencies close to one another, hence broadening the return loss bandwidth.

Table 5.12: Comb extension removal S_{11} -10 dB bandwidth

	Pairs of extensions removed	**-10 dB bandwidth (GHz)**
Receive antenna	0	2.33-2.42
	1	2.35-2.45
	2	2.39-2.49
Transmit antenna	0	2.37-2.46
	1	2.40-2.52

The S_{21} is a important measurement as discussed previously, before just considering the separation between antenna determined an isolation of 27 dB. As the antenna are now connec-

torised, the separation was able to be increased to 430 mm, the measured S_{21} across the band was -45 dB. Hence, approximately setting 45 dB to the maximum value of G_{tar}.

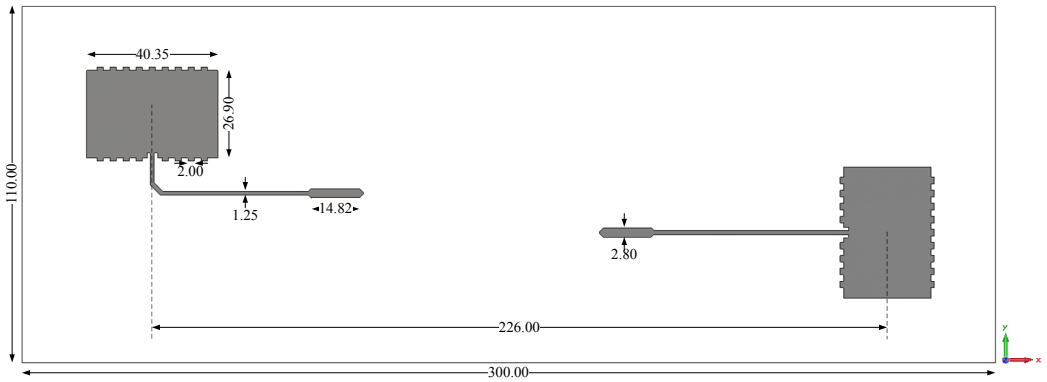

(a)

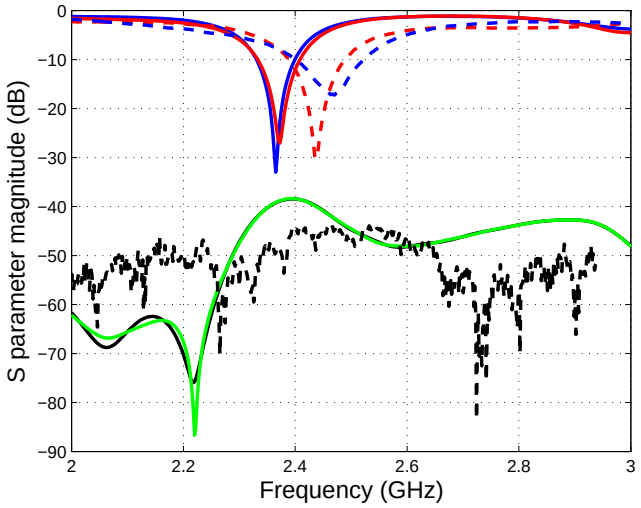

(b)

Figure 5.43: (a) Active target antenna dimensions (receiver left, transmitter right) used to generate the simulated results (b) Simulated (solid line) S-parameter magnitude (dB) S_{11} (blue), S_{21} (black), S_{12} (green) and S_{22} (red), measured (dashed line) S_{11} (blue), S_{21} (black) and S_{22} (red) (S_{11} and S_{22} correspond to the transmit and receive antenna return losses respectively)

It was noted through experiments that although the low frequency signal generation worked adequately, it was observed that after some time the frequency would drift slightly. This would cause the offset frequency to vary between measurements. Hence, using a '555' timer to generate the offset signal was not implemented for the final version of the target. Instead a combination of crystal oscillator and a frequency divider were used to generate a more stable offset frequency. A 2nd order low pass filter makes the square wave sinusoidal and D-type flip flop used to ensure a 50% duty cycle square wave, used in the original designed remained. Another aspect which was altered regarded the use of SSB modulation. The final prototype, as shown in Figure 5.47, has both sidebands present in the final IF signal, this was for simplicity

and to reduce the chance of RF errors. The low frequency circuits were designed and simulated in Multisim software, their designs and simulated responses are shown in Figure 5.44. An additional low pass filter was added on both circuits which allowed the signal amplitude to be controlled, by varying the RC combination. Finally, a series capacitor was placed just before the final filter to remove any DC biases present in the signal.

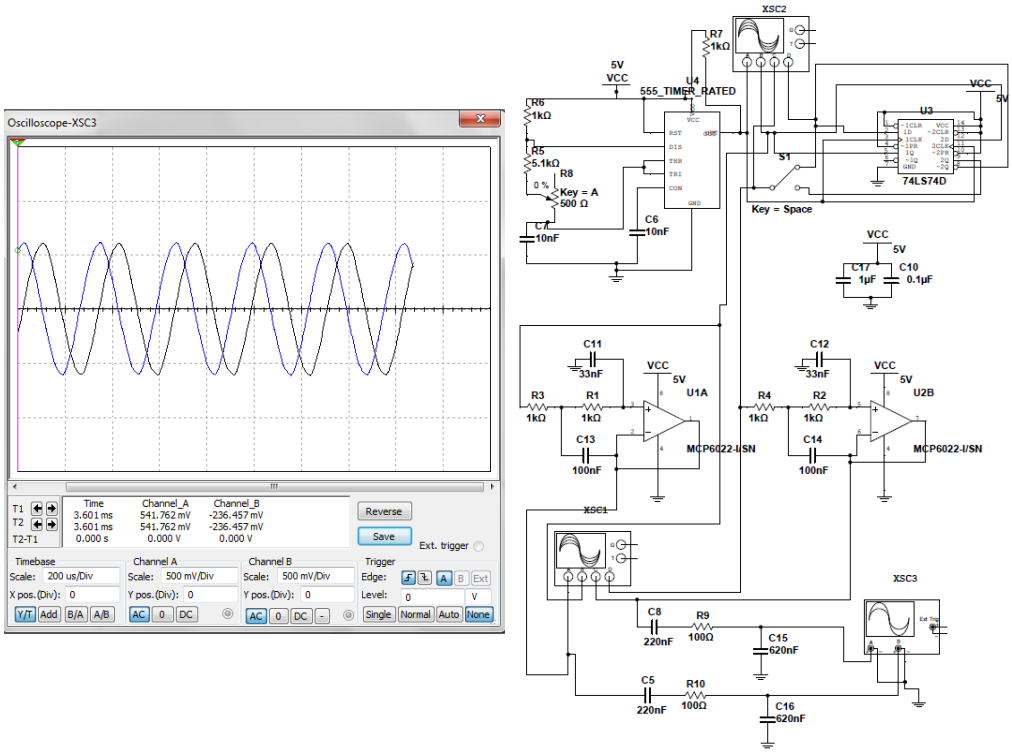

(a)

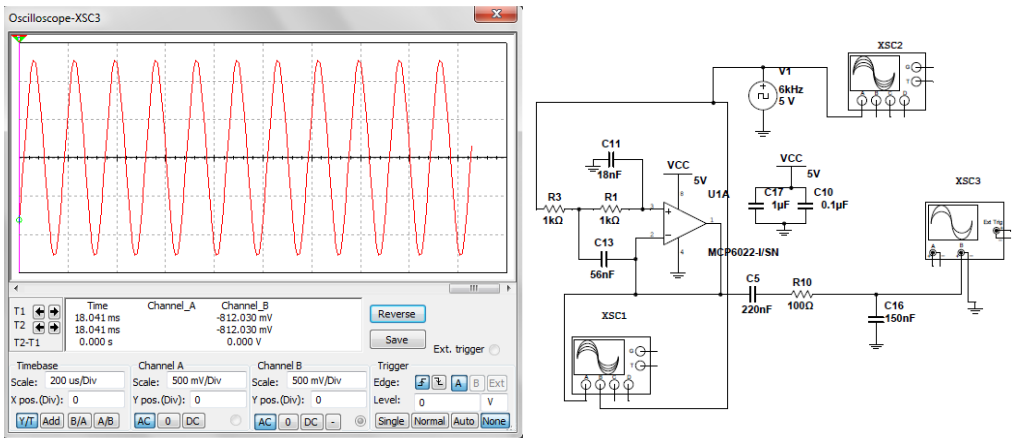

(b)

Figure 5.44: Design and simulated response of the offset frequency generation using (a) 555 timer and (b) 6 kHz square wave

Initially, an offset frequency of 3 kHz was chosen, as it equated to a signal at maximum range. However, after the clutter analysis, 6 kHz was chosen as it provided a longer range

for which the SNR would be above 29 dB, hence, allowing further range where the bearing accuracy was 1°. If the 3 kHz offset was implemented in the final prototype, the upper sideband of the next harmonic could also interfere with the wanted signal, which is shown in Figure 5.46. This was another reason for selecting an offset frequency twice that of the deramped frequency at maximum range. The choice for 6 kHz seemed a good compromise with the SNR level and the complexities involved with the active baseband filter.

The offset frequency is mixed with the RF signal using the same level 13 mixer used in the radar (part number ZX05-C42MH+, available from www.minicircuits.com). Its RF frequency range is 1000 to 4200 MHz, well within the operating range of the radar and the target. More importantly its IF frequency range is DC-1500 MHz, which was ideal as other mixers found had an IF port frequency range that started at 10s of kilohertz. However, the targets mixer is being used in a slightly unconventional manner, where the LO port is used as the input for the RF signal, its IF port is the input for the frequency offset signal and the RF port outputs the mixed signal. This approach has led to an increased conversion loss within the mixer, from the quoted 7 dB to approximately 13 dB. This could be due to the LO port being used as the input. Hence, much lower than the 13 dBm expected at this port to achieve the quoted conversion loss. The increased conversion loss needs to accounted for when determining the value for G_{tar}.

The target gain was measured at 35.8 dB, determined with the use of a signal generator at 2.44 GHz and a spectrum analyser, between the output of the receive antenna and the input of the transmit antenna. This simple measurement involved a source set to -20 dBm and an additional 50 dB attenuator was added to the output of the source. The RF signal at the end of the RF chain was measured at -38.4 dBm. The -20 dBm source signal through the 50 dB attenuator was measured at -73.8 dBm, hence resulting in the 35.8 dB target gain ($-38.4 - (-73.8) = 35.8$ dBm).

Figure 5.46 shows the initial measurements that were made with both the 3 and 6 kHz targets. These results were obtained by measuring IF signal at the mixers IF port, with the experimental set-up shown in Figure 5.45. The measurement was made at this point to verify there were no other issues that would require changes to the baseband filters profile. It reveals that the upper sideband of the wanted signal and the lower sideband of the harmonic, have a difference of 13-14 dB, for both the frequency shifts (see labels). It is clear that the 3 kHz shift, as shown in Figure 5.46a, could cause problems as it would be difficult to separate the upper sideband and lower sideband of the harmonic. This difficulty occurs when $f_{shift} \geq 4BR/Tc$ and can be proved by rearranging equations (5.27) and (5.28), which show the de-ramped frequencies for the lower and upper sidebands respectively. These equations show the requirement for

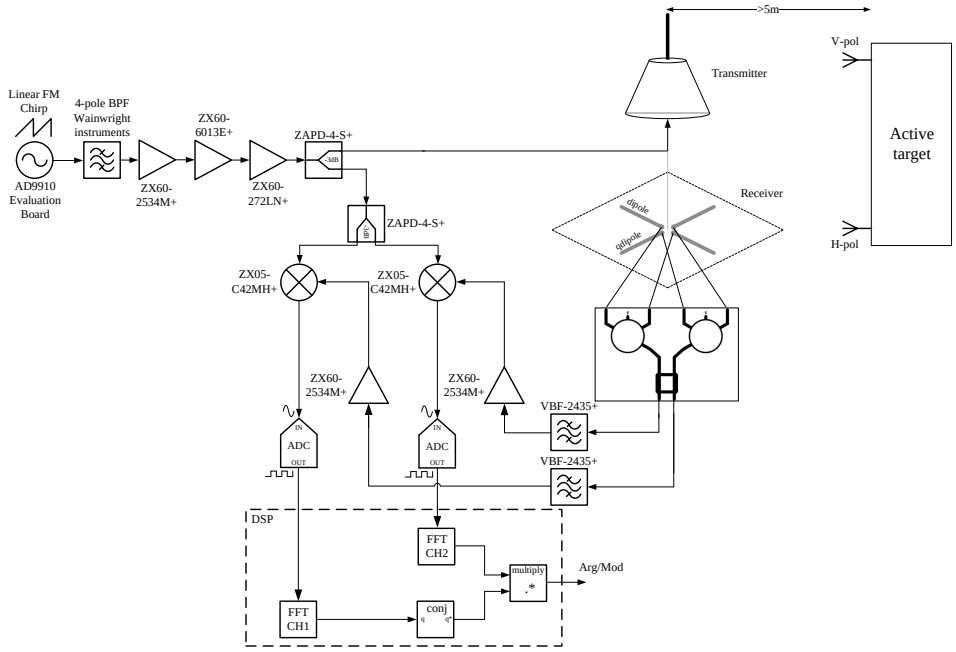

Figure 5.45: Experimental set-up used to measure the IF signal from the mixers IF port, when the active target is placed within 5 m of the radar in an office setting

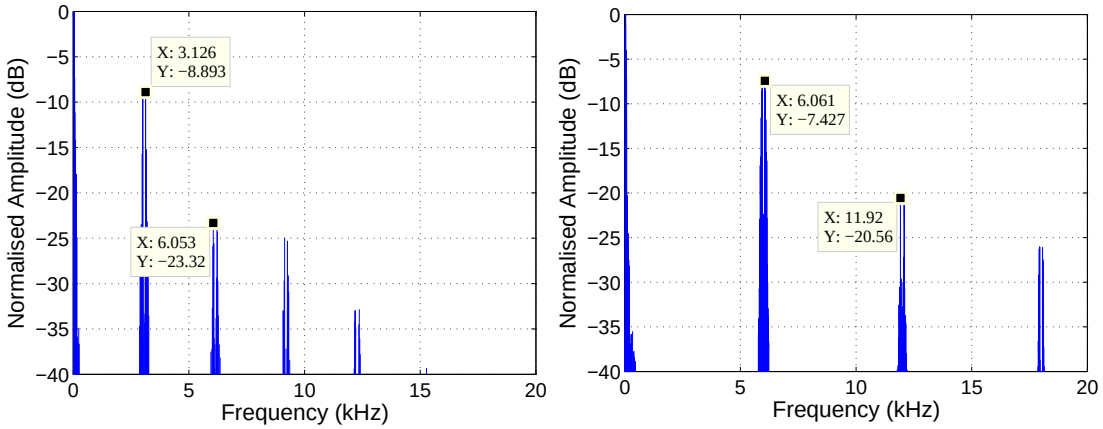

(a) (b)

Figure 5.46: Measured IF signal with (a) 3 kHz (b) 6 kHz frequency shift

a stable shift frequency as its stability is vital in accurately determine the range. Hence, the use of a crystal oscillator rather than a 555 timer based oscillator.

$$f_{d,LSB} = f_{shift} - \frac{2BR}{Tc} \tag{5.27}$$

$$f_{d,USB} = f_{shift} + \frac{2BR}{Tc} \tag{5.28}$$

The power supply for the active target consisted of five rechargeable AA batteries, each with an approximate voltage (when fully charged) of 1.5 V. All the components within the target where chosen to operate at 5 V. A Low Drop Out (LDO) 5 V regulator was used to provide a

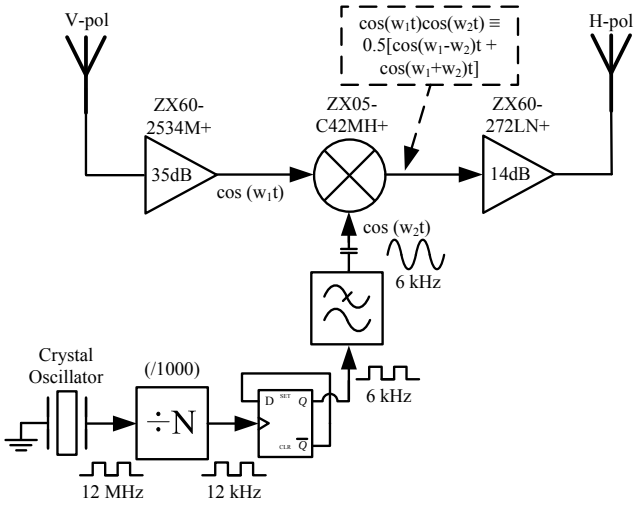

Figure 5.47: Block diagram of the 6 kHz frequency shifted active target

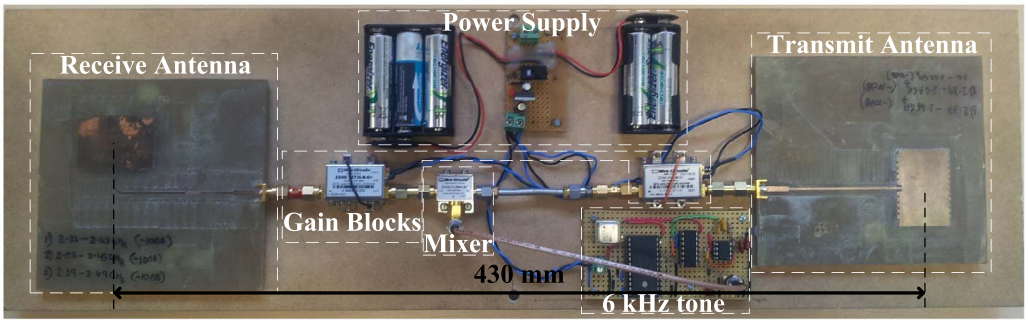

Figure 5.48: Photo of the 6 kHz frequency shifted active target

regulated power for the components. The use of a LDO was essential, as it can operate with a minimum input voltage of 5.2 V to supply the correct 5 V output. A simple SPST switch was used to turn the target on and off. Additionally, a low current LED was used to indicate when the target was on.

5.2.4 Active Baseband Filter

The baseband filter profile drastically alters with the introduction of an offset frequency within the target. The choice of a 6 kHz offset will limit the maximum range to approximately 75-80 m where SNR is above 29 dB, which can be interpreted from Figure 5.41. It was suggested that this was due to the complexities of the baseband filter. Hence, 6 kHz was a good compromising frequency for the prototype, the filter design is now discussed.

Where previously, before considering how the clutter would affect the signal, the baseband filter was designed to operate from 50 Hz to 5 kHz, with the maximum range initially thought to be approximately 500 m. The received power rolls off against range, with a $1/R^4$ relationship. Hence, the filter would have to compensate at 40 dB/decade to maximise the ADC dynamic

range. Hence, at 5 kHz the gain would have to be 80 dB higher than at 50 Hz, which is fairly feasible for this frequency range. An initial design was courtesy of Dr. Lai-Bun Lok, who had designed a filter that was almost this exact specification, it also had an anti-aliasing aspect, vital for filter that would be before the ADC. His design was recreated using Multisim and the simulated filter response is shown in Figure 5.49b. This clearly shows a 80 dB gain at approximately 5 kHz. This was designed as a two stage filter with each active stage, a 2^{nd} low pass filter with 40 dB of gain and -3 dB point at 14 kHz. It is preceded by a high pass filter, which has unity gain at 10 kHz and -40 dB gain at 10 Hz. The two filters combined response results in a bandpass filter characteristic, with 40 dB gain at 5 kHz. The second stage has the same response as the first, which gives the desired final characteristic. This filter although not used with the modulated target was used in initial loop tests and some preliminary tests with unmodulated target. The loop test in Figure 5.50 clearly shows a point target at 121 m, this result was obtained using the original 44 kHz sampling card with the cable connected to one of the receiver ports. The phase difference between the ports can be seen to stabilise where the signal is at its highest and was measured at 87.62°.

The baseband filter was ideal for the unmodulated target, but was completely impractical for the frequency shifted target. Once it was decided that 6 kHz would be the shift frequency, the RC components values were altered, to produce the same response over a different frequency region. The simple definition of a filters 'q' factor [106] suggests that with the frequency offset the required q factor would have to be extremely high. Therefore, other filter types were considered to achieve the desired response. The most promising in simulation was the Multiple Feedback Bandpass Filter (MFBP) [106]. It allows the gain and q factor to be independently varied. The final design involved four OP-AMP stages, each with slightly differing centre frequencies and gains. The first two stages had about 20 dBs of gain each and final two a combined gain of 25 dB, as shown in Figure 5.51.

$$q_{factor} = \frac{f_c}{\Delta f_{-3dB}} \tag{5.29}$$

where, f_c, is the centre frequency and Δf_{-3dB}, is the -3 dB bandwidth of the filter.

Ideally, the same characteristic of the original filter was desired. However, when testing the filter it was quite unstable and the gain was scaled back from 80 dB peak to around 65 dB. Between each stage, decoupling capacitors were used to ensure there was not DC bias that could damage the hardware. At the start of the filter the decoupling capacitor was vital as shown in Figure 5.34 to remove the chirp PRF. Finally, there is a series capacitor, again for decoupling

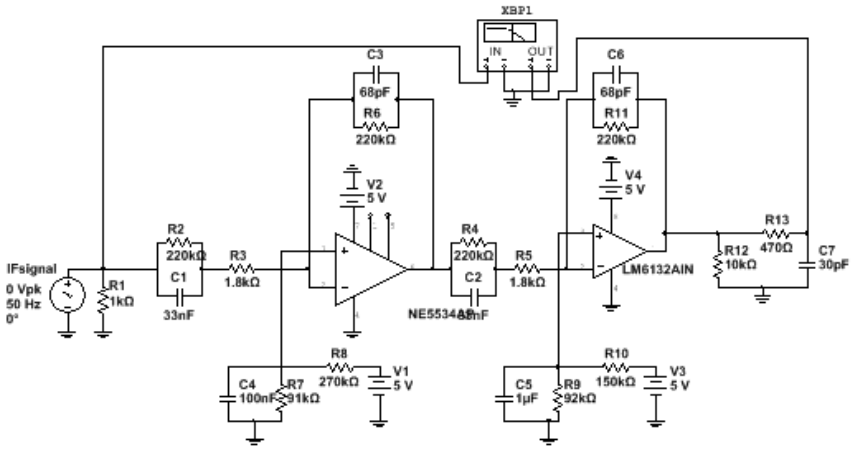

(a)

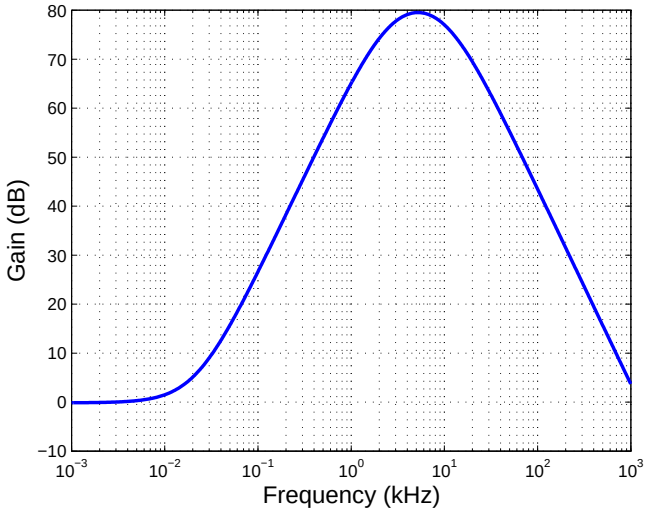

(b)

Figure 5.49: Baseband filter with 40 dB/decade gain (a) design (b) simulated response

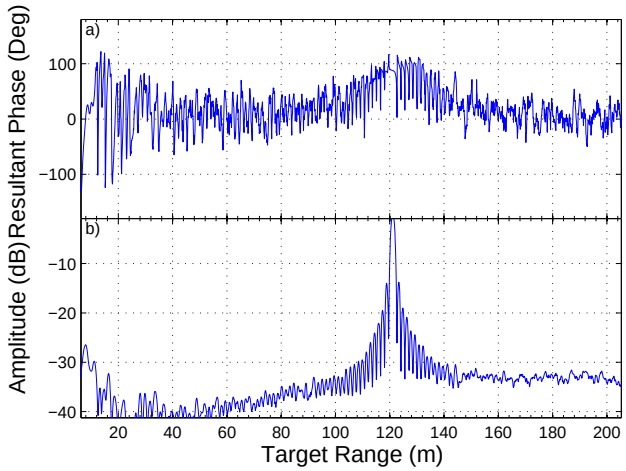

Figure 5.50: Loop test with baseband filter and a coaxial cable of 240 m physical length

and a series resistor for impedance matching.

The first test was to design the circuit on breadboard, to see if the resistors and capacitors

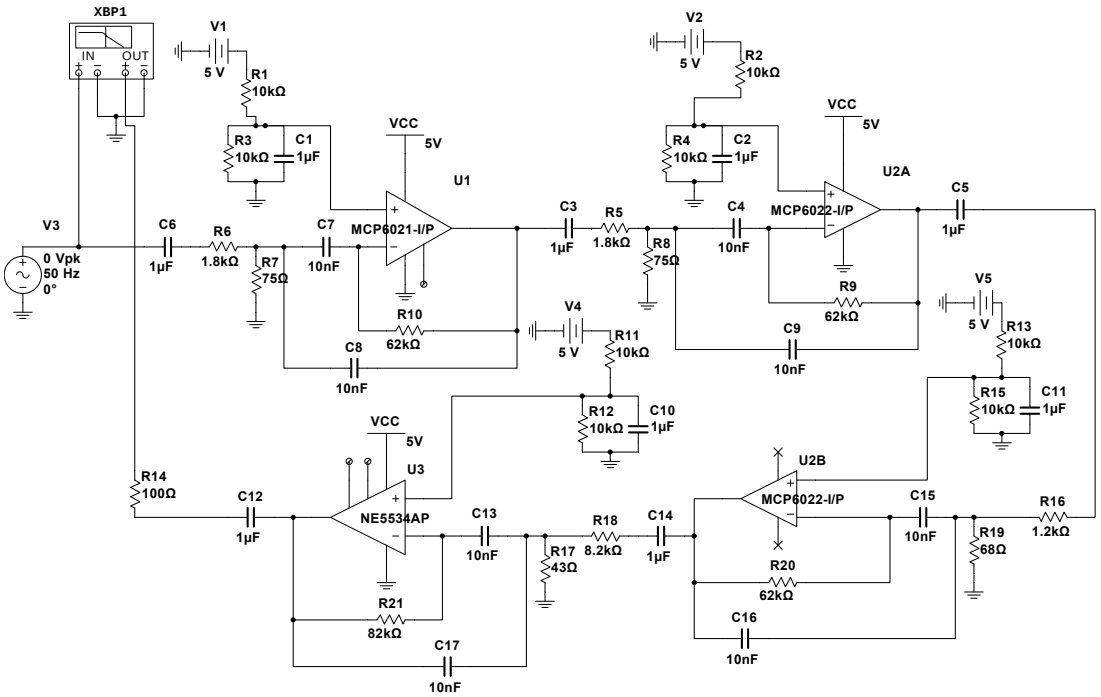

Figure 5.51: Four stage MFBP baseband filter

required any modification. Once it was determined to be fairly stable and producing the correct response, a PCB was designed using a piece of software called Diptrace. The PCB was manufactured in house and the components were hand soldered, it was tested by feeding in a low frequency signal from a signal generator and viewing the output on an oscilloscope. As the frequency increased, the input signals voltage was lowered to ensure that the output signal was not clipping.

The final filter design consists of four op-amps, in three DIL-8 packages, with 20 resistors and 17 capacitors per channel. It connects to the IF port of the mixer via a SMA connector. Each channels' filter output is via a two pin motherboard connectors, through a twisted pair cable to panel mount phono connectors. An off the shelf x2 phono to a 3.5 mm barrel jack cable, take the IF signal to the line-in port of the sound card.

The constructed filter has a slightly different response between each channel and from the simulated filter. The difference between the channels will most probably be due the tolerance of the components, as the capacitors can vary as much as 20%. Also, the op-amps will have a slight internal difference, which could also be part of the reason for the differences. The lowest peak gain of the PCB filter is 65 dB at 8 kHz with a 3.5 dB peak gain difference between channels. As the filter does not ideally negate the reduction in received signal strength with range, the expected SNR will have a slight ripple and will not have the ideal flat SNR response

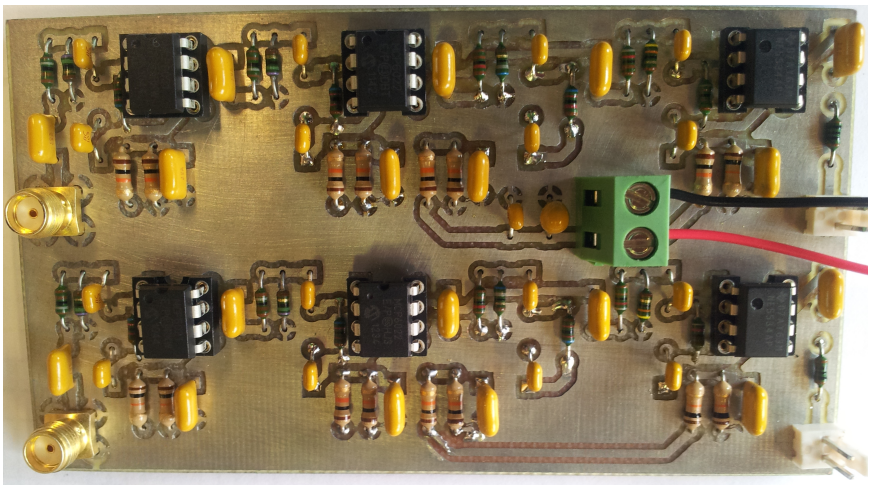

(a)

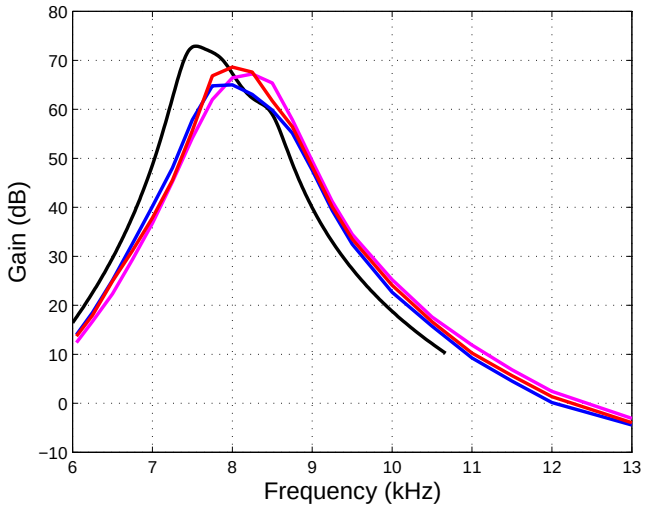

(b)

Figure 5.52: (a) Photo of the constructed baseband filter (b) baseband filter response simulated (black), breadboard test version (magenta), PCB CH1 (red) and PCB CH2 (blue)

with range and not maximise the ADC dynamic range.

This measurement allows the calculation of the maximum receiver gain 22.55+65 = 87.55 dB, this maximum gain does not occur at the furthest range, but at 8 kHz. Corresponding to a range of 180 m, where the received signal would have a power of -114.3 dBm, therefore $(-114.3 + 87.55) - (-80.31) = 53.56$, hence the signal will be around 53.5 dB above the ADC quantisation noise. However, the target power at the theoretical maximum range is -122.6 dBm, CH2 has a lower active filter gain and at this frequency is 47.6 dB. Hence, the IF signal will be 27.8 dB above the ADC quantisation noise.

The gain measurement can then be used to determine how well the Noise Figure was estimated, by measuring the noise using the ADC per channel. The four receiver inputs were terminated with 50 Ω matched loads and a measurement is taken with the radar. Using the

equation in [105] for the receiver noise power the Noise Figure can be calculated with respect to frequency.

$$P_n = G_{rec} k T_0 (1/T) F_n \tag{5.30}$$

where, G_{rec}, is the receiver chain total gain i.e the RF gain to the IF port of the mixer and the frequency dependant gain of the baseband amplifier. The receiver gain has been measured and the other factors are known. Hence, equation (5.30) can be rearranged to calculate the Noise Figure. This can be shown graphically by taking the difference between the noise signal measured by the ADC and the calculated $G_{rec} k T_0 (1/T)$ term, i.e. the difference between the red and blue curve in Figure 5.53.

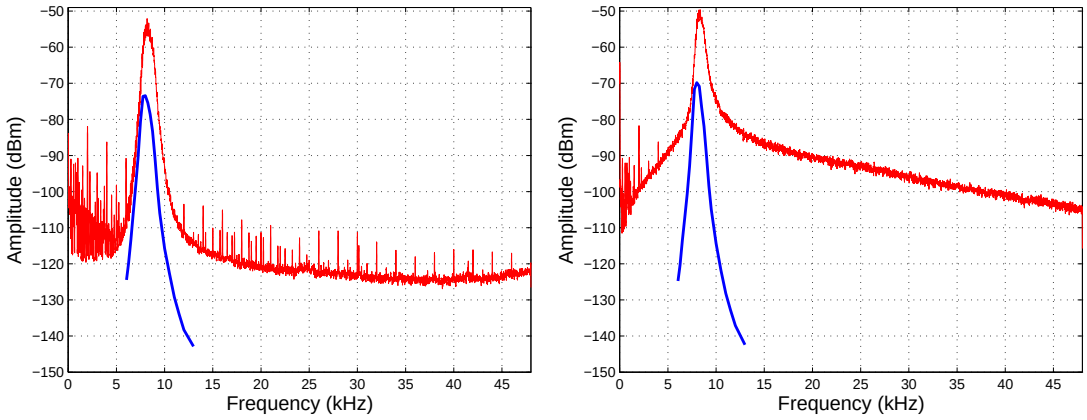

(a) (b)

Figure 5.53: Measured noise power (red), total measured gain without Noise Figure (blue) for (a) CH1 (b) CH2

The measured noise seems to be very different between the two channels and this is reflected in the Noise Figure between channels. This can only really occur due the baseband filter behaving differently on each channel, as the outputs where switched at the input of the sound card, the noise floor on each channel remained the same. This suggests that the line-in port of the ADC has different filters on each channel, which is quite probable as most soundcard ADCs focus on a single channel having a better response as most microphones used with soundcards are single channel. This could explain why the noise response of each channel is quite different.

The Noise Figure can be seen approaching a minimum value of 9 dB, for both CH1 and CH2, as shown in Figure 5.54a. However, the quoted 9 dB in Section 5.2.2 assumes this value when the two channels are combined in the processing. Therefore, the minimum measured Noise Figure is 3 dB higher than the estimated. However, for both ends for the radar range the Noise Figure is significantly higher than estimated. The real Noise Figure measurement can be

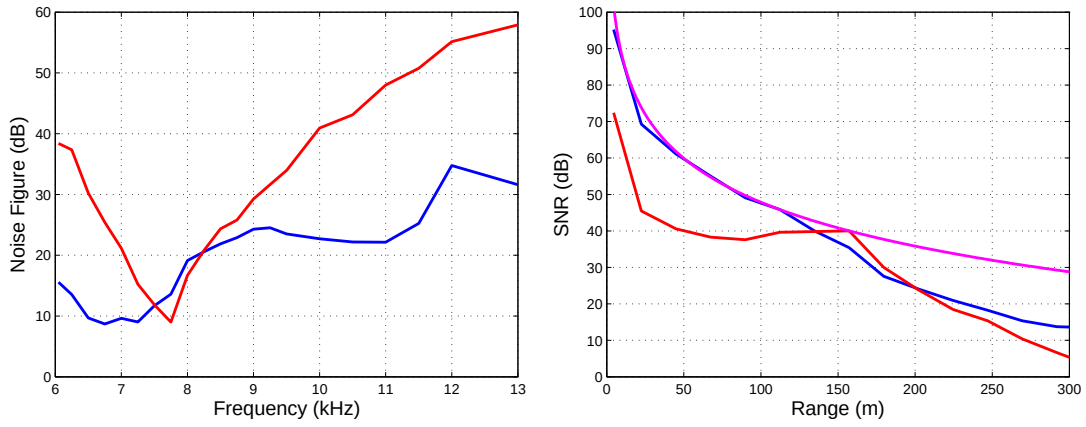

(a) (b)

Figure 5.54: (a) Measured Noise Figure for CH1 (blue) and CH2 (red) (b) SNR for CH1 (blue), CH2 (red) and with a fixed ideal Noise Figure=9 dB (magenta)

used in the SNR equation to determine the true SNR for this radar system and is shown in Figure 5.54b. The filter response can clearly be seen in Figure 5.53a in the radar's noise measurement, as the baseband filter profile is shown amplifying the system noise by a peak gain of 65 dB at 8 kHz.

The SNR is above 29 dB on each channel up to 175 m. However, as the system SNR will be 3 dB worse off due the combination of the two channels, the maximum range reduces to 165 m. This result highlights the fact that the baseband filter is less than optimum and the increased Noise Figure at the higher ranges reduces the maximum range of the radar. Improving the baseband filter and Noise Figure should significantly improve the radar range. The SNR variation is 65 and 40 dB for CH1 and CH2 respectively, a slight reduction from the ideal by approximately 6 dB. However, the SNR is nowhere near to being flat, due to such a high variation in the Noise Figure over the frequency range. This is definitely one improvement that could be made for subsequent systems.

5.2.5 Other Hardware

All the radar hardware discussed mainly concerns the RF and IF components, the antennas and their feed networks. Now in brief, the power supply within the radar and connections to the outside of the radar 19" rack unit are discussed.

The AD9910 Evaluation Board requires a 1.8 V and a 3.3 V supply, many of the miniciruit amplifiers used in the radar operate at 5 V. As does the op-amps in the baseband filter and the 8 MHz crystal oscillator and its buffer which are used to generate the external clock for the DDS. There is also a single RF amplifier operating at 12 V, used in the transmitter chain. As the total current of the radar was expected to be approximately 1 A. Therefore, 1.5 A regulators (LM317)

were used to provide all the correct voltages. The LM317 is a variable voltage regulator for output voltages from 1.2 V to 37 V. Using potentiometers the output voltage could be finely tuned. The voltage drop across the regulator is about 1.7 V, which meant that the DC power supply required had to be able to supply at least 13.7 V at around 1.2-1.5 A.

The voltage drop from 13.7 V to 1.8 V generated considerable heat, hence as the regulators were in TO220 packaging, there are a wide choice of off the shelf heatsinks. However, as the regulator has not ground tab, each voltage rail required separate heatsinks. In addition to the heatsinks, four high current 1N4001 diodes were used in series to drop further voltage (≈3.2 V) after the 12 V supply. As there were many 5 V components and to ensure that a single regulator was not supplying both the RF components and the others, two 5 V supplies were used. The heatsinks and diodes were not enough to stop the 1.8 and 3.3 V from getting very hot. Therefore, a small 80 cm PC case fan operating at 12 V was used above the lower voltage supplies to reduce their temperatures further. To connect the external power supply to the radar, two panel mount 3.5 mm connectors were wired to the input of the internal voltage regulators.

On the back panel of the radar there is a 3 A SPST switch, with two 3.5 mm connectors for the power supply. A panel mount USB A connector to allow the evaluation board to be programmed and the two panel mount phono connectors for the IF signals. The front panel has five SMA connectors (one for the transmit signal and four for the receive) and two LEDs, red and green for indicating power on and PLL lock respectively.

A final part of the radar hardware which was required, only after initial loop tests showed glitches occurring when the four phase feed network was exposed. Hence, a 2 mm thick aluminium plate was machined to cover the entire feed network. This was partly due to internal reflections from stray signals produced by the evaluation board coupling in the exposed RF lines of the feed network. Although it removed some of the glitches they are still present, however, less frequent and lower in amplitude.

5.3 Summary

This chapter has discussed the wide range of hardware developed as part of this project. Results are shown with real measurements and are compared to simulated responses to determine how well they coincide. From the antennas that were constructed for both the radar transmitter and receiver to the radar hardware itself that was developed and tested both in sections and as a whole system. Ideally, there are improvements that can be made, as with most systems. The Noise Figure is one part of the radar that could be improved to increase the operational range of the radar, by improving the SNR. An maximum gain of 45 dB could be applied to the active

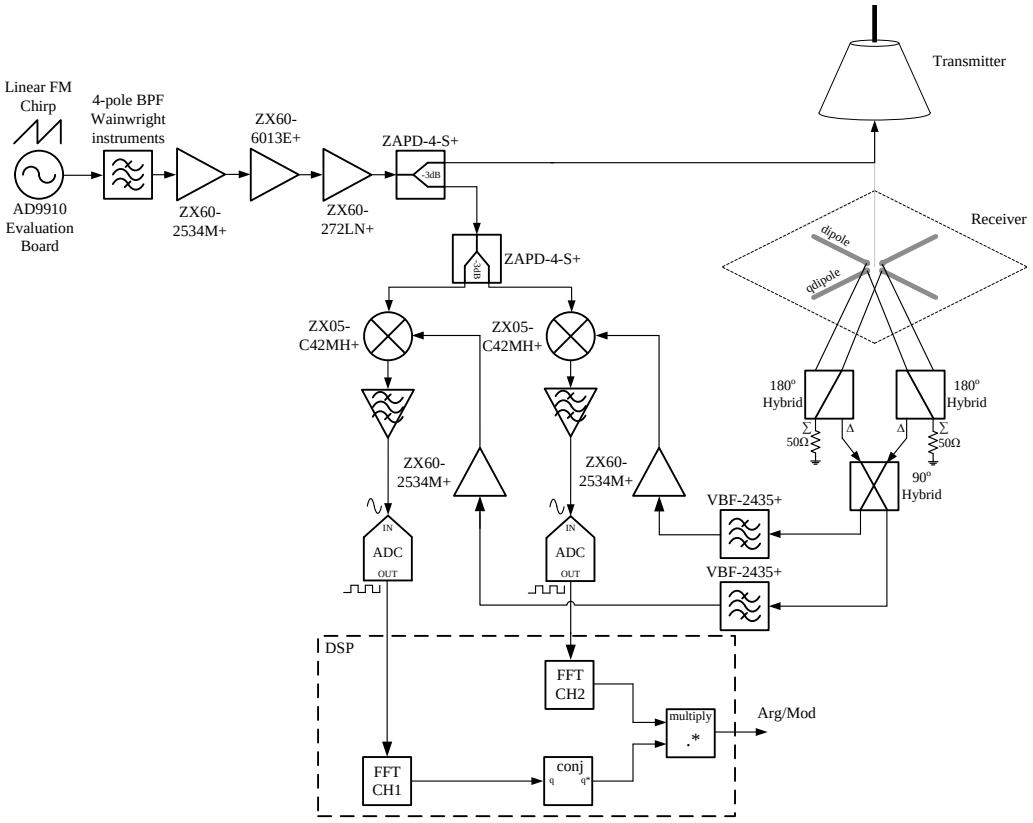

Figure 5.55: Full radar system block diagram with part numbers

target, currently has been reduced to 35.8 dB, to prevent self oscillation, as it was noticed on a few occasions with the single board target. Modulating the active target with a relatively small frequency offset with respect to the RF frequency has been shown to be ideal where an active target FMCW radar system is required, albeit it will be for quite a niche market. The frequency offset has the effect of making the active target compete with clutter from much greater ranges. All the simulating and designing has led to testing the radar with a reduced maximum range in an open field, which now follows, in addition the signal processing that was implemented as part of the radar system is also discussed.

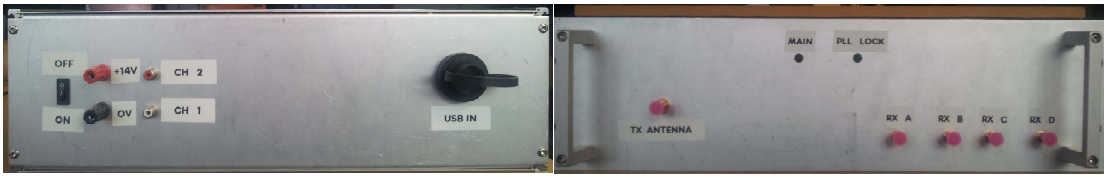

(a) (b)

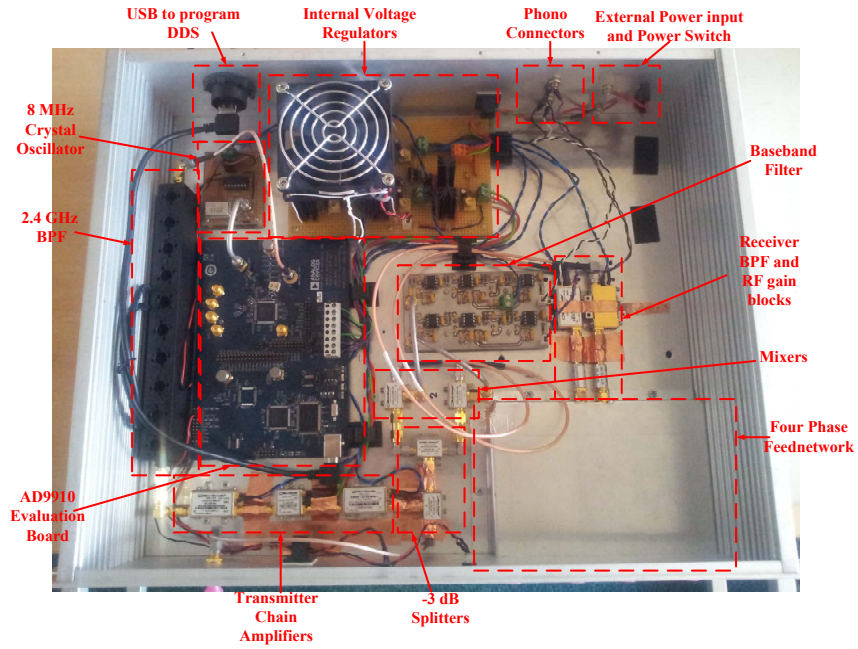

(c)

Figure 5.56: Photo of the radars (a) back plate (b) front plate (c) internal layout

Chapter 6

Measurement Campaign and Data Analysis

The radar hardware was discussed in the previous chapter, now it is shown to be working together as a whole system, producing results. This chapter begins with a discussion of how MATLAB was used to acquire the baseband signal and some Windows operating system settings, which needed consideration. It then progresses to illustrate the pre-processing techniques carried out in MATLAB and other signal processing applied, such as determining the radars Field Of View (FOV), which is dependant on the crossed-dipole antennas orientation. It goes on to discuss the results obtained on three measurement campaigns which took place in two main locations of Guidance Microwave Ltd. This is one of their external offices in Hitchin and a UCL owned sports ground in Watford, with observations and analysis based on the gathered results.

6.1 Signal Processing

This first section discusses the signal acquisition. In the first instance using an audio software called 'Audacity', it saved audio files for subsequent post-processing. For the measurement campaign real-time acquisition and signal processing were implemented using MATLAB.

6.1.1 Signal Acquisition

The first approach to acquire the audio signal was to save the raw IF time domain signal using the integrated laptop sound card in .wav format. This was achieved with the aid of an open source software called Audacity. The saved format allowed the file to be imported into MATLAB for processing. The images for the loop test results, shown in Figure 5.50, were generated in this manner. It was fairly simple to read the .wav file utilising the aptly named function 'wavread'. This very well documented function [107] extracts the sampled data, sampling frequency and number of bits. In terms of acquisition the next step was to remove the need to store the audio file and directly have MATLAB acquire and process the audio signal. Again, using a different built-in MATLAB function within the data acquisition toolbox, called 'analoginput'

[108] it was quite straight forward. It is specifically designed to access any sound cards attached to the computer and use them as an analogue input device. This function allows selecting which device to access, setting the sampling rate, up to a maximum of 96 kHz, the number of bits (16 bits maximum) and the duration of acquisition.

When moving on from the built-in sound cards to the external USB Soundblaster SB1090 required calibration. This is due to the ability of the operating system to change the recoding volume and also amplify it, from a scale of 0 to 100 (0=mute, 100=maximum). Hence, the requirement for calibration, which involved using a signal generator and generating a low frequency signal similar to the radar IF frequencies and noting the signal generator's output on a bench oscilloscope. Then, comparing this value to the signal amplitude outputted with no processing using MATLAB, effectively turning the sound card, computer and MATLAB combination into a oscilloscope. The calibration involved testing to determine which value on the sliding scale corresponded to exactly that measured by the oscilloscope. Using the SB 1090 and a Toshiba laptop used in all trials, the 1:1 relationship between the output of MATLAB and oscilloscope was found be close to identical (±0.005 V) when the volume level was set to 78.

6.1.2 Pre-Processing

Once the IF signal was acquired by MATLAB it required pre-processing, the first step was to enable it to run in real-time or as close to as possible. Once the MATLAB was successfully used to acquire the signal, the real-time implementation was achieved by continually looping the script. The MATLAB script included the processing, acquisition and also a short buffer time (approximately 0.25*acquisition time) between acquisition and processing to temporarily store the IF signal. Also, the lack of trigger signal, usually used to signify the start of the chirp was non-existent, hence, requiring some pre-processing to determine the chirp beginning, knowing when the chirp starts is vital for coherent averaging and windowing. When deciphering the content of the time domain signal acquired in MATLAB, it was noticed that there were large voltage spikes that repeated every 50 ms, indicating the beginning of the chirp, which is shown in Figure 6.1a. By differentiating one of the audio channels and setting a threshold of 50% of the maximum, the start of the chirp in the time domain was automatically detected. An example of the differentiated time domain signal is shown in Figure 6.1b.

These voltage spikes were due to the use of a sawtooth waveform. This waveform requires the chirp signal to fly back from the highest to the lowest transmitting frequency, instantly, which is practically impossible. To ensure the fly back was reduced to the minimum, its time duration was set to 0.1 μs (the minimum time allowed by the evaluation software for the AD9910). In this time the instantaneous RF signal would go from 2.4835 to 2.4 GHz, this

rapid change in frequency caused the voltage spikes. For a sampling frequency of 96 kHz for a 50 ms chirp generates 4800 samples, when pre-processing the signal the first and last 200 samples were removed with the middle 4400 containing the desired IF signal. The time domain reduction was to remove the effect of f_{b1}, which was previously shown in Figure 2.5.

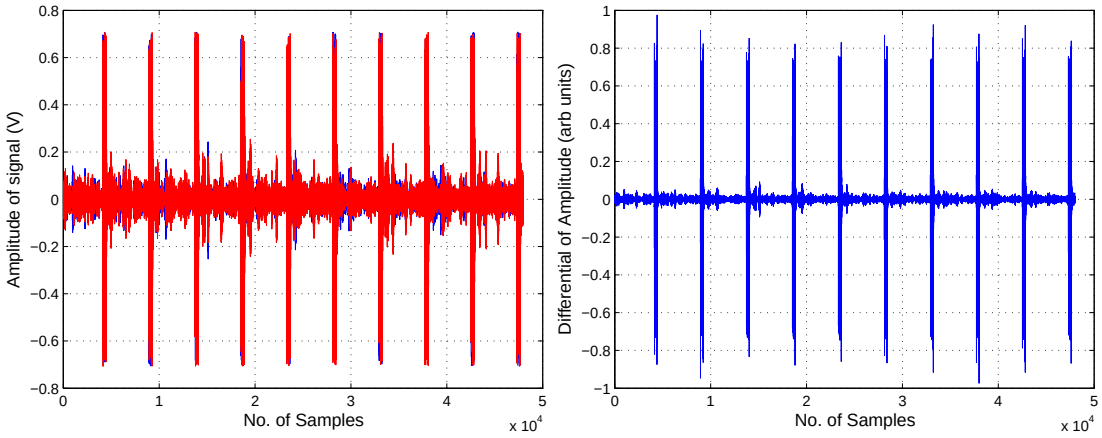

(a) (b)

Figure 6.1: (a) Time domain IF signal from the active target (b) CH1 time domain signal differentiated

Once the signal was split into individual chirps, an example of which is shown in Figure 6.2a, the next step was to window the time domain signal. Windowing can only be applied to individual chirps in the time domain. The Hanning window was chosen, as shown in Figure 6.2b, after applying different windows to the loop test data, as it offered a good compromise between sidelobe level reduction and peak broadening. An example of the Hanning window multiplied by the single chirp is shown in Figure 6.2c. It was noticed that broader peak could cause the phase to alter, hence affecting the target bearing by a few degrees. The phase change was noticed when applying a Blackman window to the loop test results, which generated Figure 5.50. Figure 6.3 shows how the application of the Blackman window to Figure 5.50 altered the frequency domain result. With/without the window, the phase difference was 87.5° and 85.7° respectively. However, the radar range remained unchanged at 121.1 m for both responses. Figure 6.3 clearly shows a reduction in the sidelobe level by 20 dB, however, the main lobe has a broader peak as energy must be conserved.

A slight deviation from pre- to post-processing, the two phase values discussed above were obtained using a weighted average. The averaging is based on the previous three and next three amplitude values around the maximum, shown pictorially in Figure 6.3 (seven red dots). This method allowed the phase difference to be defined based on a range of amplitudes around the maximum rather than a single value. It was shown previously with increasing range, the phase

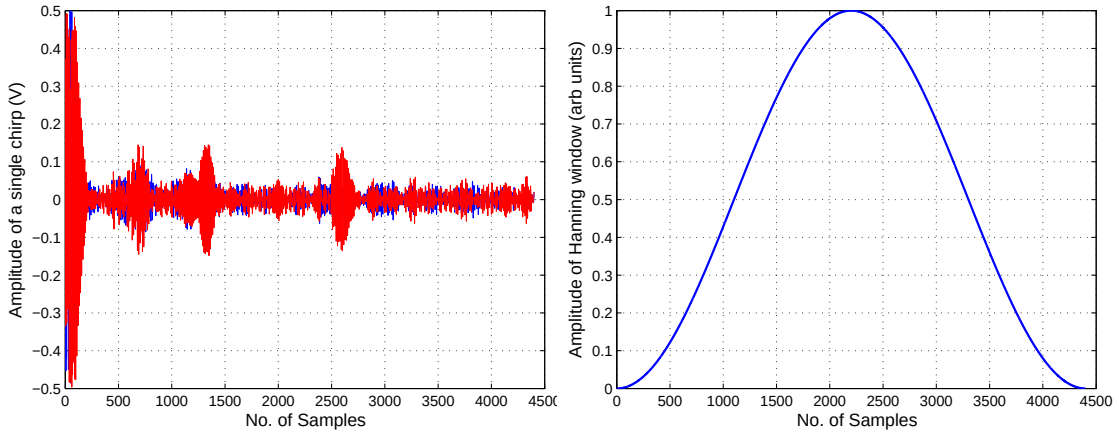

(a) (b)

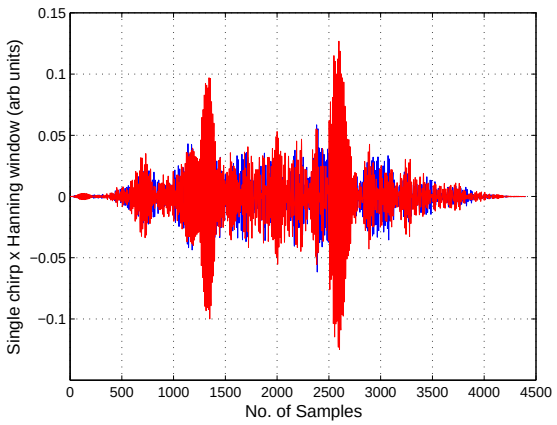

(c)

Figure 6.2: (a) Segmented time domain signal showing only a single chirp (b) the Hanning window which is multiplied with the single chirp (c) the result of the single chirp multiplied by the Hanning window

difference can vary greatly, due to the reduction in SNR. By using weighted averaged phase differences, the target bearing will be less erratic. The phase difference weighting method has been explained qualitatively and is expressed mathematically by the following:

$$weighted\ phase\ diff = \sum_{n=-3}^{3} phase\ diff(n) \frac{amp(n)}{\sum_{n=-3}^{3} amp(n)} \tag{6.1}$$

6.1.3 Antenna Position Calibration

Previously discussed in this thesis was the presence of a 180° ambiguity, due to the use of the 1st and -1st order phase modes. Therefore, only allowing the radar, to unambiguously determine the target bearing in a semi-circular region. To ensure that Cartesian coordinate system accurately reflects the orientation of the antenna and radar relative to the target required cali-

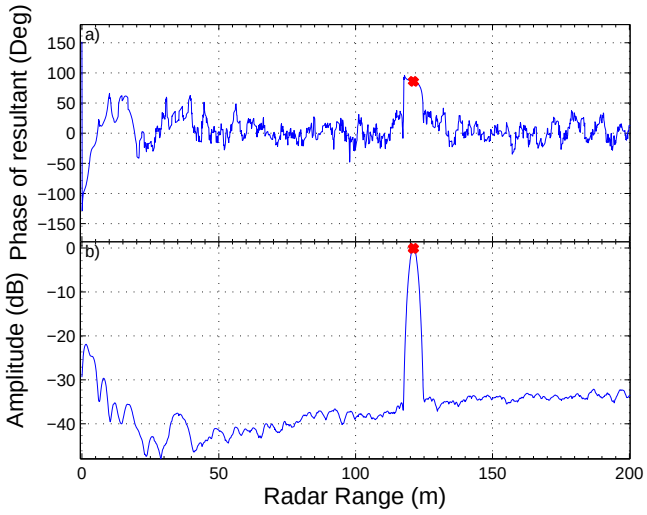

Figure 6.3: Blackman windowed loop test result with a coaxial cable a physical length of 240 m

bration, which is made up of two parts. Firstly, in Figure 5.19 it was shown that there is an inherent offset between the actual bearing and the measured bearing. As this is a fixed offset of 45°, it can be easily incorporated to the phase difference to bearing conversion, such that the measured and actual bearing are directly proportional. Secondly, the ideal orientation of the antenna relative to the FOV is shown in Figure 6.4a, to allow the simplest phase difference, (ϕ), to bearing, (θ), relationship, where $\theta = \phi/2 + 90°$. This is for a special case scenario, occurring when the antenna is correctly orientated, a more general solution, which allows the FOV to be in the positive 'y' axis, for a given antenna orientation offset, $\Delta\theta$, is given by equation (6.2) and is illustrated in Figure 6.4b when $\Delta\theta = 30°$. The simple case can be obtained by experimentally orientating the antenna for which one corner has a zero degree bearing. If rotating the antenna in a clockwise direction causes a negative bearing increase, the equation to calculate the bearing i.e. FFT(CH1).*conj(FFT(CH2)) the order of the multiplication can be reversed i.e. FFT(CH2).*conj(FFT(CH1)). Therefore, ensuring the target always occupies the correct half of the coordinate system.

$$\theta = \begin{cases} \frac{\phi}{2} + 90° - \Delta\theta, & \text{if } \phi \geq 2\Delta\theta - 180° \\ \frac{\phi}{2} + 270° - \Delta\theta, & \text{otherwise} \end{cases} \tag{6.2}$$

Mapping to Cartesian coordinates, then becomes trivial, where '$x = r\cos\theta$', '$y = r\sin\theta$' and 'r' is target range determined by the FFT of the time domain voltage signal of either audio channel. By calculating the bearing based on equation (6.2) the target will always appear to be in front of the radar. This may not seem too important, but when testing in the lab and initial longer

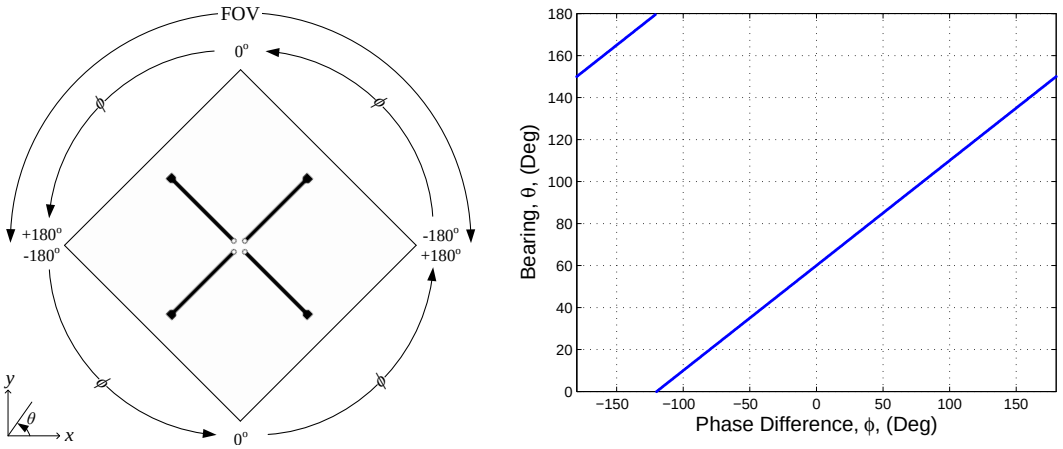

(a) (b)

Figure 6.4: (a) FOV relative to the antenna orientation (b) bearing (degrees) vs. phase difference (degrees) when $\Delta\theta = 30°$

distance tests, the target position would sometimes fluctuate between the true bearing and the ambiguous 180° image, rendering the averaging between successive chirps incorrect. Hence, by forcing the bearing into the positive half of the 'y' axis, allowed for increased averaging.

6.2 Shenley Trials 10/07/2013

Initial tests within the lab showed that the radar was working, however, due to the size of the room and clutter made it difficult to gauge how well the radar was performing at longer ranges. Therefore, the radar system was taken to Shenley sports ground in Watford, for increased range testing. With field size over 20,000 sq. metres it was an ideal location to test the radar, in the presence of very little clutter within 200 m. There the radar and target bearing accuracy degradation at longer ranges could be established, a chance to test the signal processing at typical target ranges and determine the ideal experimental procedure to plot the measured target bearing against actual bearing. The original plan was to use a surveying unit to accurately measure both the targets range and bearing, placing the target at discrete measured angles around a semi-circular region, however to accurately place the target at these angles become virtually impossible even at short ranges (≈15 m). With the site only available for a day, once the radar had been set up, the majority of the time was unsuccessfully spent trying to accurately place the target at different angles. It was decided to use the remaining time to keep the target angle fixed at a bearing of 90° to the radar and take measurements at different ranges (5 m, 48.47 m and 97.95 m), these results are shown in Figure 6.5.

The radars measured response shows that target range and bearing agreed well with the surveying tools measurement. Figure 6.5a shows that the radar measured a range of 5.69 m

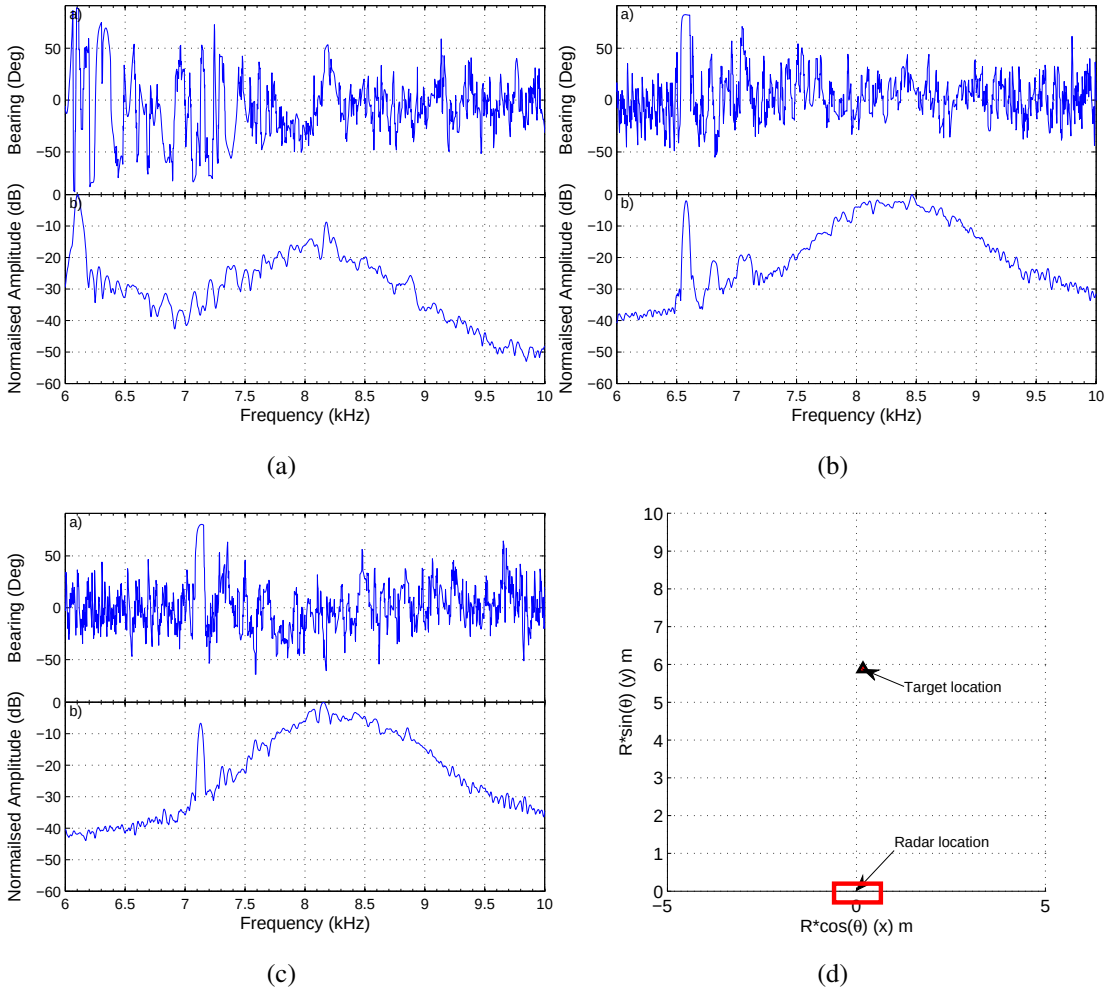

Figure 6.5: Measured response by the radar with the target at a range of (a) 5 m, (b) 48.47 m and (c) 97.95 m (d) an example of the Cartesian plot for image in (a) where the radar is located at (0,0)

and a bearing of 88.26° and also in a Cartesian coordinates system in Figure 6.5d. Figures 6.5b and 6.5c respectively have measured ranges of 48.6 m and 98.0 m with bearings of 82.12° and 80.19° respectively. Although, it became difficult to accurately measure the bearing using the surveying tool at the longer ranges, small deviations in cross range will result in very little bearing differences. Hence, the measured bearing should be quite close to 90°, at longer ranges. However, at 98 m, the bearing is approximately 10° off. This would correspond to a cross range movement of 125 m, which is highly unlikely. This bearing error was expected, as SNR decreases with increasing range, the bearing accuracy would also decrease. However, the SNR at approximately 100 m is far below the expected value, which was later determined to be a consequence of high transmitter noise coupling into the receiver.

Using the AD9910 in super-Nyquist mode, as discussed previously, required a gain of 55 dB to maximise the transmitter power, recalling that the 5^{th} image in the 6^{th} Nyquist zone was

used. The image power is usually 8-10 dB lower than the previous, this is one of the major drawbacks of using a high order image, for lower order images this method would be perfect or for low transmit power systems. The considerable gain had the added effect of amplifying the transmitter noise by 55 dB. However, the isolation between the transmitter and receiver is approximately 44 dB, which results in a discrepancy of 11 dB, which resulted in increasing the receiver noise floor. Hence, decreasing the SNR and the range at which the bearing will have a 1° accuracy is now significantly lower. This explains partly why the measured bearing at ~50 m and ~100 m is very different to the surveying tool angle estimation. Also, note that in these two measured results the noise floor is higher than the signal response, hence requiring additional signal processing to automatically locate the target.

Due to the radars increased noise floor, the target response is below the system noise floor. The noise floor also varies with frequency due to the response of the active baseband filter. Therefore, a simple gain flattening technique was implemented to allow the target to be accurately detected. Initially, the noise threshold was to be set by using a Constant False Alarm Rate (CFAR) [109] algorithm. However, the increased noise around the region of interest was due to the filter characteristic and constant between measurements. A simpler approach than CFAR was implemented, by just evaluating two linear line equations, the first for the increasing part of the filter response and the second for the decreasing. Once these equations were calculated, it became trivial to remove them from the current data and was implemented in real time for the subsequent radar trials. Figure 6.6 shows the off-line processing when the noise floor has been flattened using the line equations, the target is now detected automatically and the averaging applied correctly.

To determine the extent of the transmitter noise coupling into the receiver, lab based measurements were taken with the radar in the absence of the active target. The first measurement was with the transmit and receive antenna both connected to the radar. For the second, the receiver remained connected and the transmitter terminated with a matched load. Due to the frequency shift within the target and the IF signal is offset by 6 kHz, the influence of clutter should not play a role in disparity between the two measurements in the 6 to 9 kHz frequency region, with any differences due to the transmitter coupling. Figure 6.7 shows the difference between the measurements, if there was sufficient isolation or lower transmitter noise these two curves should almost perfectly overlap. The difference between them is due to transmitter noise coupling into the receiver, which is between 4-8 dB at peak receiver gain for CH2 and CH1 respectively. Ideally, to solve this issue rather than using super-Nyquist, upconverting the low frequency signal will reduce the number of amplifiers in the transmitter chain, hence lowering

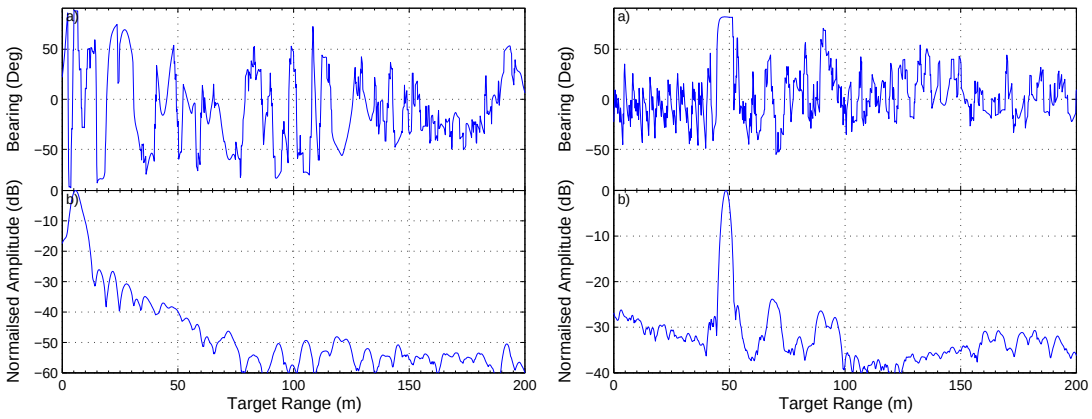

(a) (b)

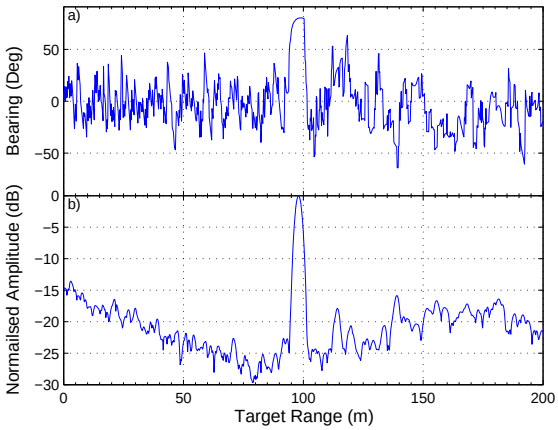

(c)

Figure 6.6: Noise floor flattening applied to the results obtained in Figure 6.5

the transmitter noise and making it no longer contribute to the system noise. Also, the antennas could be placed further apart, but this will result in a bigger structure, if size were not an issue this too could be implemented in conjunction with the upconversion to completely eliminate the transmitter noise coupling.

To summarise this trial, the data showed that the radar was working up to a range of 100 m, however the bearing was not as precise as suggested by the link budget. Subsequent measurements indicating that the transmitter noise was coupling into the receiver, a partial cause for the increased receiver noise floor. Assuming that the SNR degraded by the average of the noise floor increase for both channels (6 dB), the maximum range which was 290 m is now reduced to 210 m. This trial also revealed the difficulty of precisely measuring both the target range and bearing, this was eventually overcome with a fairly simple test rig and will be discussed in the next section. Finally, this trial revealed that the signal processing could be improved for future trials with the use of gain flattening and saving the raw time domain signal for 5 seconds worth of data per range and bearing, rather than a single chirp. This increased

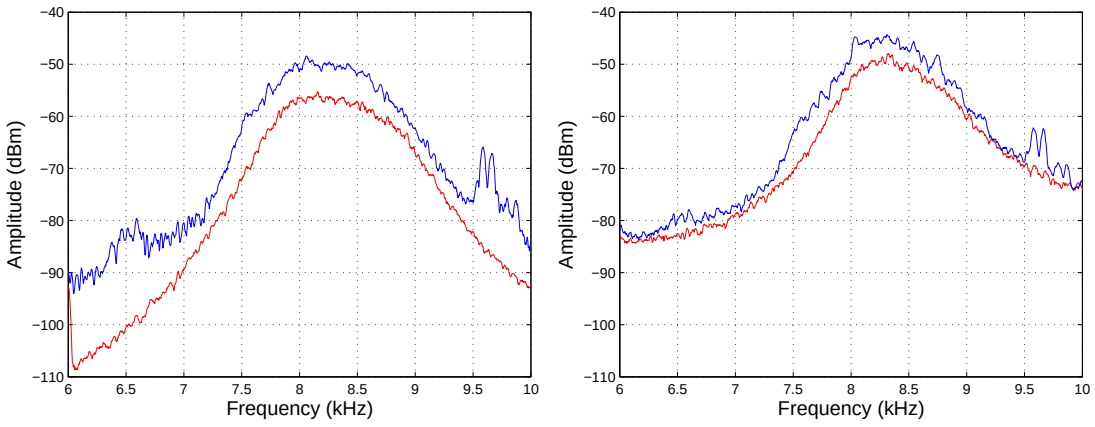

(a) (b)

Figure 6.7: Difference between transmitter connected (blue) unconnected (red) for (a) CH1 and (b) CH2

averaging and by saving the data, it gave the ability for additional post-processing revealing more information about the targets bearing accuracy. Figure 6.8a shows how the antennas are mounted on to the radar and how the gap between the antenna is maintained and Figure 6.8b show the active target mounted to a tripod used in the experimental set-up which incidentally is shown in Figure 6.9.

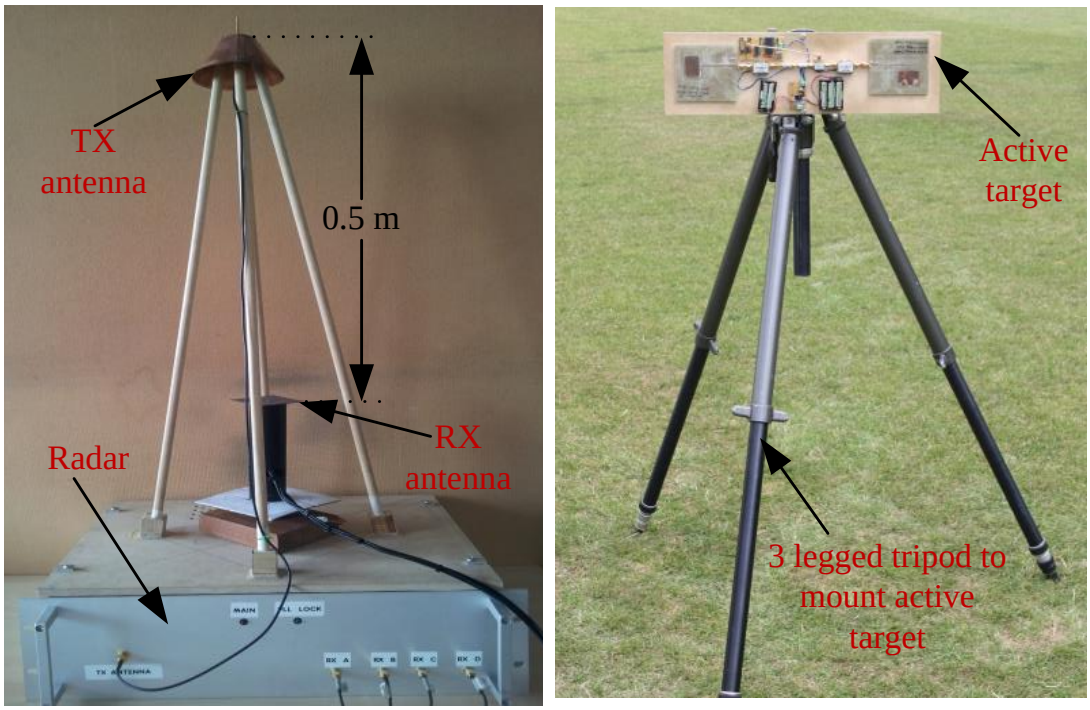

(a) (b)

Figure 6.8: (a) Photo of RX and TX antennas mounted on top of the radar (b) photo of active target mounted to the tripod used for all trials

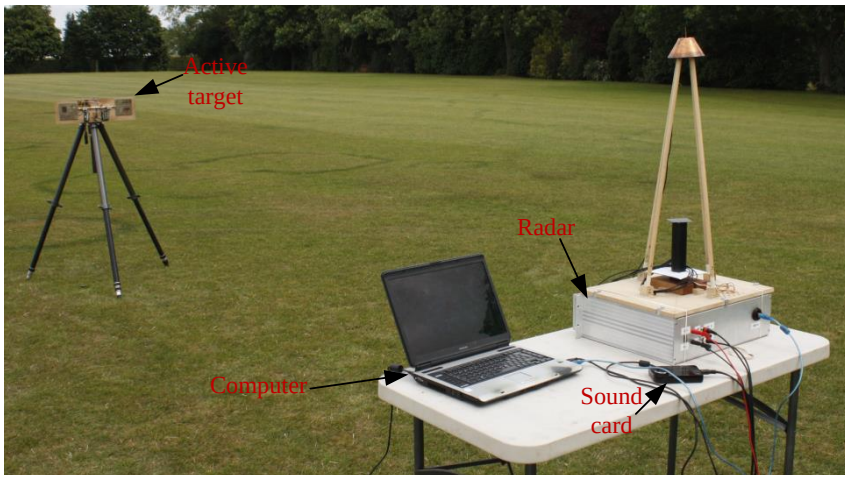

Figure 6.9: Photo of the experimental set up in Shenley

6.3 Hitchin Trials 23/07/2013-06/08/2013

The challenges of the first trial were solved in time for the next set of trials. The signal processing included the ability to save a longer dataset and gain flattening. However, the biggest improvement was with how the bearing of the target would be determined, eventually based on the same method used to obtain the experimental antenna measurements of Section 5.1.2. By rotating the whole radar and keeping the target perpendicular to it was the solution, simple yet very effective. The manually rotating structure had an accuracy of 2°, measurements were made every 10° with the target at a bearing of 0° to 170°, the raw time domain signal was timestamped for post processing. Over this two week period, the trial lasted for four separate days, measuring the target bearing for different ranges and elevations.

Hitchin is an external site for Guidance Microwave Ltd. They kindly allowed the use of their garage and parking area for some extended range testing, however it was limited to 30 m. The location gave the ability to test the radar with parked cars acting as sources of clutter and the garage area had all the necessary power connections for the radar and laptop. These were vital for a full days testing, the previous trial in Shenley the power was limited, only external car batteries and inverters were available for the necessary AC voltage to run the radar and laptop.

Figure 6.10 show the layout of the experiment, the target is mounted on a tripod at a height of 137 cm, such that the targets antenna mainlobes were in the same plane as the midpoint between the radar antennas. Note that in this figure the rotating structure that allowed the rotation of the whole radar system can just be seen on the bottom left. It was constructed from recycling an old rotating tripod and with some minor modifications became an ideal platform for the radar system. Also, shown is how the vertical gap between the radar antennas is maintained, the conical monopole is screwed into four wooden dowels with a slant angle of 80° from the

horizontal plane. The vertical separation between the antennas is 50 cm (4λ), with the receive antenna mounted on a 20 cm tube for better cable management. The antenna mounts are simply placed on top of the radar box and the radar itself screwed into the stand, allowing repeatable measurements and short set-up times. The radar and antenna mounts are placed on the rotating structure which itself is clamped to flat surface allowing the radar and antenna to rotate, but keeping the base fixed and secure.

Figure 6.10: Photo of the experimental set up in Hitchin

The first test carried out with the radar was with the target placed at 7.65 m, here the surveying tool was unavailable and the range was measured using a laser measuring tool (Fluke 419D). The bearing and range were both measured in 10° intervals for target at this range, as previously discussed. The targets actual bearing was measured using notches in the rotating part of the radar mount and aligned to a printed protractor mounted to the stationary part of the mount. This experiment was repeated for a range of 30.64 m and both results are shown in Figure 6.11.

Figure 6.11 shows the measured bearing of the target relative to the ideal response of a crossed-dipole antenna, the bearing ripple is evident between both the ideal and measured. The mean bearing error for a target range of 7.65 m and 30.64 m results are -0.08° and 0.47°, with a standard deviation of 2.15° and 2.64° respectively. The ideal crossed-dipole would have a mean bearing error of 0° and standard deviation of 2.30°. These results showed that the method employed for this experiment was valid, with the added advantage of quick and repeatable measurements. Both bearing results show good linearity and monotonicity, vital for estimating the target bearing. The radar range measurements for the shorter range measurement, as with the

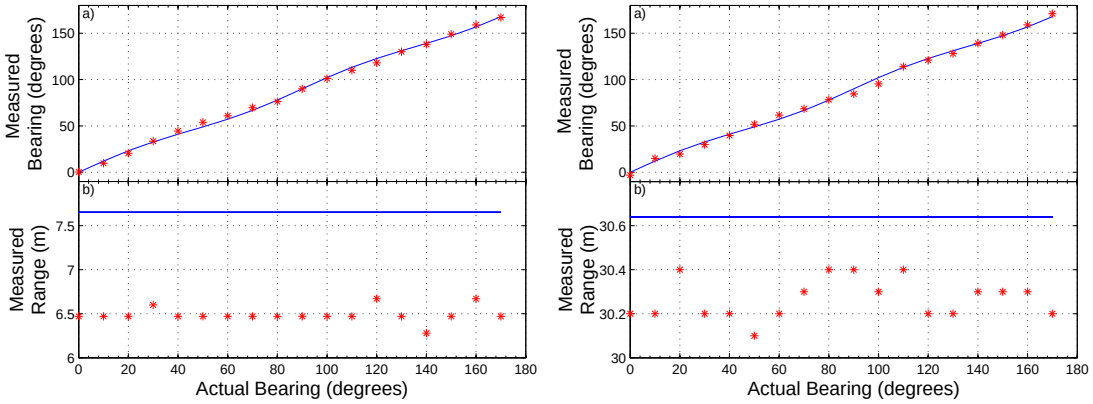

(a) (b)

Figure 6.11: Measured bearing (red*) and ideal crossed-dipole bearing (blue) (top) and radar range (red*) laser measured (blue) (bottom) for (a) 7.65 m (b) 30.64 m

result in Figure 6.5a, shows the radar range is over 1 m off the laser measured range. This is most likely due to the multipath effects due ground reflections being comparable to the direct signal. The radar range is determined using equation (2.29) from the measured baseband frequency. Also in this calculation is the consideration of the electrical length of the coaxial cables in the system which carry any RF signals. The total electrical length was determined to be approximately 3.4 m corresponding to a frequency of 37.85 Hz. This value was taken off the measured frequency, as well as the offset frequency (6 kHz) to determine the targets true range.

Using the measured results above and response of an ideal crossed-dipole, fitting a calibration curve to remove the systematic error due to the crossed-dipole in bearing was attempted. Figure 6.12 shows the error in the measured bearing when compared to the error of an ideal crossed-dipole. By subtracting the ideal response from the measured should result in a perfect linear relationship between measured and actual bearing. Provided the bearing error was only due to the systematic ideal crossed-dipole error. The general trend between the ideal and measured can just be seen for both ranges, but with an offset of approximately 20°, other than environmental influences it is unclear how else this type of error could occur. The peak to peak error is fairly constant between these two measurements at approximately ±5°, where the ideal crossed-dipole would have an error of ±3.26°.

Over the time spent in Hitchin, other measurements were made mainly to determine how the use of absorber between the radar antennas affected the range and bearing, in particular when the target was elevated. At first, the measurement was made at a short range of 7.96 m, with a small elevation of 2.5° without any absorber. These results with the absorber were not ideal due to the unavailability of absorber rated to operate at 2.4 GHz, hence, all the elevation

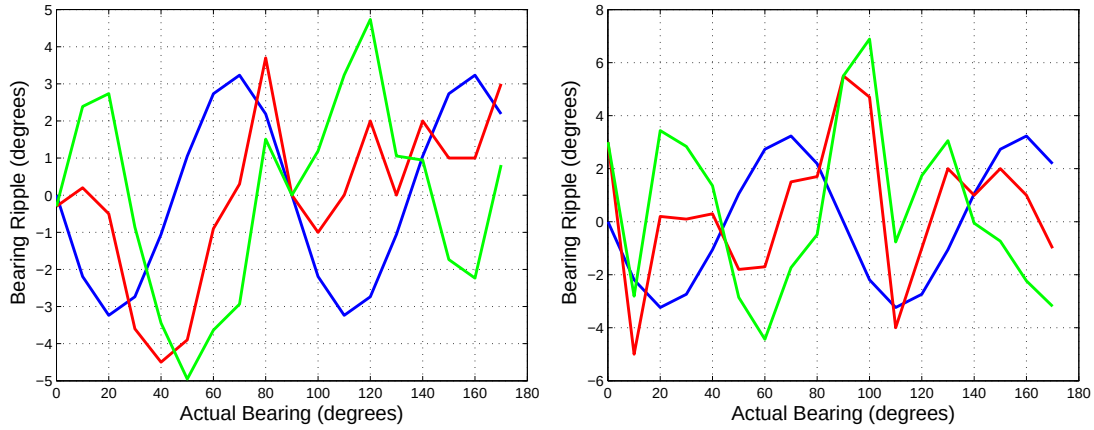

(a) (b)

Figure 6.12: Bearing error calibration for the ideal crossed-dipole (blue), measured bearing error (red) and difference between the measured and ideal (green) for (a) 7.65 m (b) 30.64 m

and absorber measurements are shown in Appendix D.

Figure 6.13 shows the layout of the parking area where the radar system was tested in Hitchin, this aerial view shows the general location of the cars and shows the limitations of this area to be used as a radar testing site beyond 30 m.

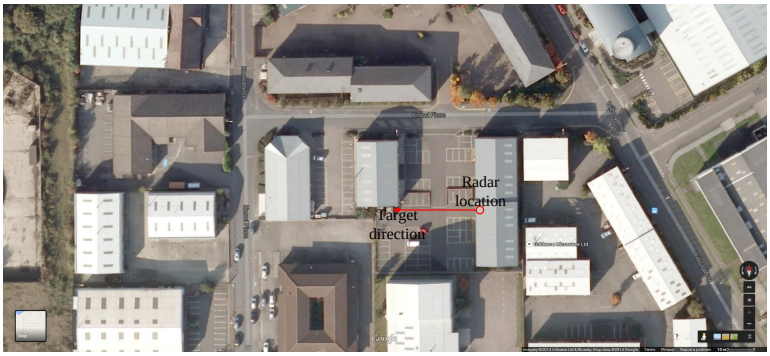

Figure 6.13: Google Maps satellite image for the Hitchin radar trial site

To summarise the results obtained in Hitchin, the improvements made to data collection with respect to the rotating radar mount were validated and with recoding more data post-processing techniques could be applied for better data presentation and more analysis. At both ranges, the measured bearing was monotonic, with very low systematic error and close to ideal bearing standard deviation. Trying to calibrate the ideal crossed-dipole error did not yield the desired response, suggesting there may well be another source of error other than the crossed-dipole systematic error, possibly environmental.

6.4 Shenley Trials 14/08/2013-15/08/2013

With good results obtained in Hitchin, another trial was organised to take place in Shenley, mainly in response to the limited testing range at Hitchin. Over this two day trial the aim was to carry out the same experiment which produced the Hitchin results in the previous section, but at increased range. From the original Shenley trial it was clear that the increasing range severely effected the SNR, hence, was likely to cause higher mean bearing errors. However, until the radar was tested at these ranges, it remained unclear the extent of the errors. For this reason the target bearing and range were measured at five longer ranges (45.22 m, 65.30 m, 84.02 m, 102.66 m and 125 m).

Table 6.1: Significant outcomes from the experimental results in Figures 6.14 and 6.15

	45.22 m	**65.30 m**	**84.02 m**	**102.66 m**	**125 m**
Mean (actual -radar) Bearing (degrees)	-2.30	-2.25	-6.08	-3.46	2.04
Mean (radar) Range (m)	45.41	65.28	84.33	102.80	125.53
STD (actual -radar) Bearing (degrees)	4.29	4.76	4.18	10.61	26.08
STD (radar) Range (m)	0.14	0.09	0.08	0.03	1.23

*It should be noted that ranges 45.22 m and 84.02 m, Figures 6.14a and 6.14c respectively, were measured on the second day with rest measured on the first. The main outcomes from the results presented in Figures 6.14 and 6.15 are summarised in Table 6.1.

From these results it would appear that the radar does work fairly well as a range radar up to 125 m, however the bearing becomes increasingly inaccurate as the SNR decreases. In Figures 6.14e and 6.14d, there seems to be some interference in the received signal between the bearings 130° and 150°. During the experiment it was unclear what could be causing this interference, but at this distance, within the vicinity of the radar there was a small house which may well have been the source of the interference, possibly wi-fi. This interference eventually affects both the range and bearing quite drastically and causes large mean errors and a high standard deviation (STD) for the bearing results, with less impact on errors in range. This is due to less stringent requirements on the SNR level to determine the range, compared to the SNR level required to accurately establish the target bearing. Note also there is no sign of this error in Figure 6.14c, suggesting that it was a error was due to the location and day of testing rather than another systematic error.

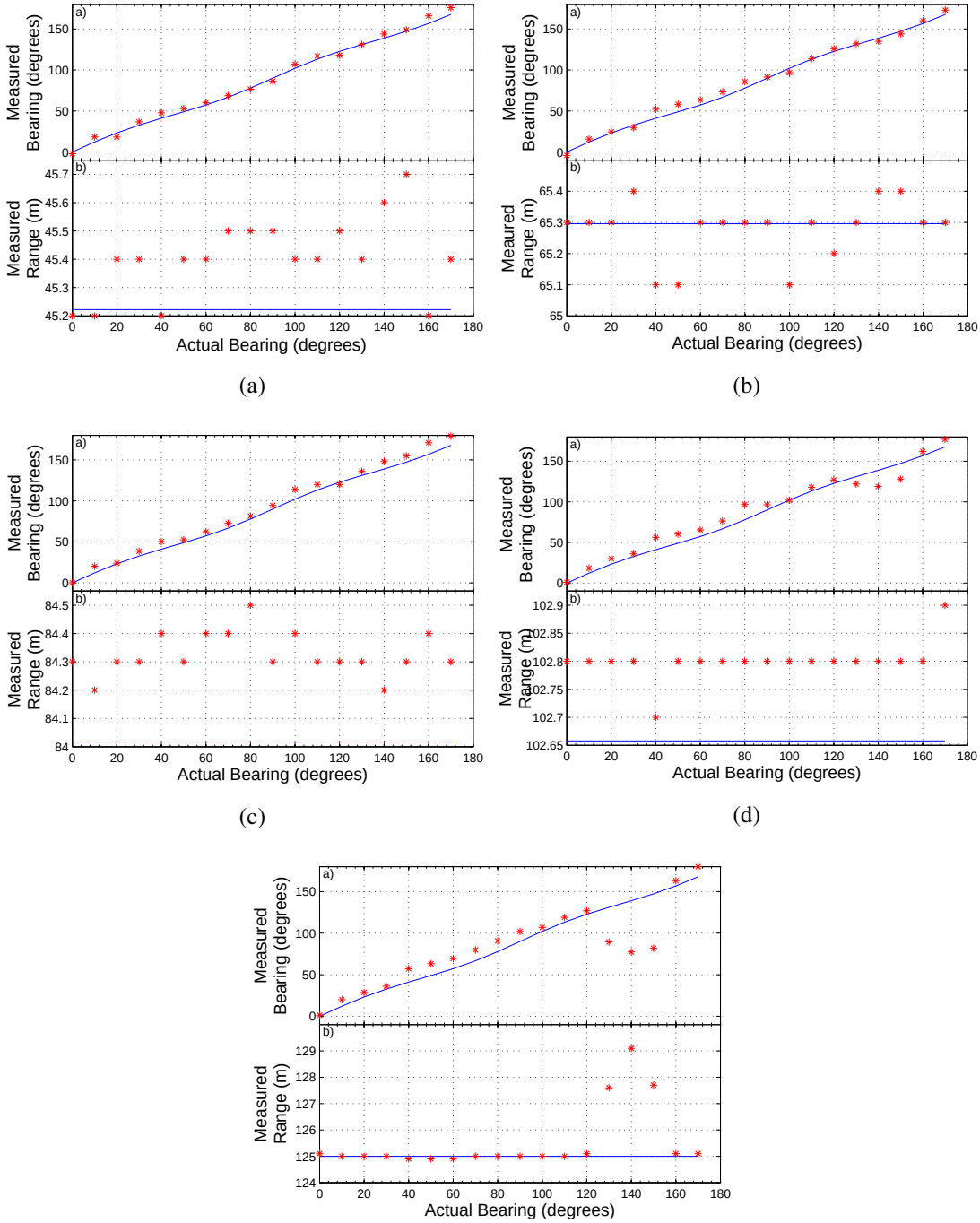

Figure 6.14: Measured bearing (red*) and ideal crossed-dipole bearing (blue) (top) and radar range (red*) surveying tool measured (blue) (bottom) for (a) 45.22 m, (b) 65.30 m, (c) 84.02 m, (d) 102.66 m and (e) 125 m

If these individual results are removed, there is a general increase in the mean error, the STD stays quite constant between the different ranges at approximately 4.5° between the ranges of 45 m and 85 m. The mean error seems to be negative across all measurements in Shenley, this suggests that there could be an alignment error with the target. With increasing range the

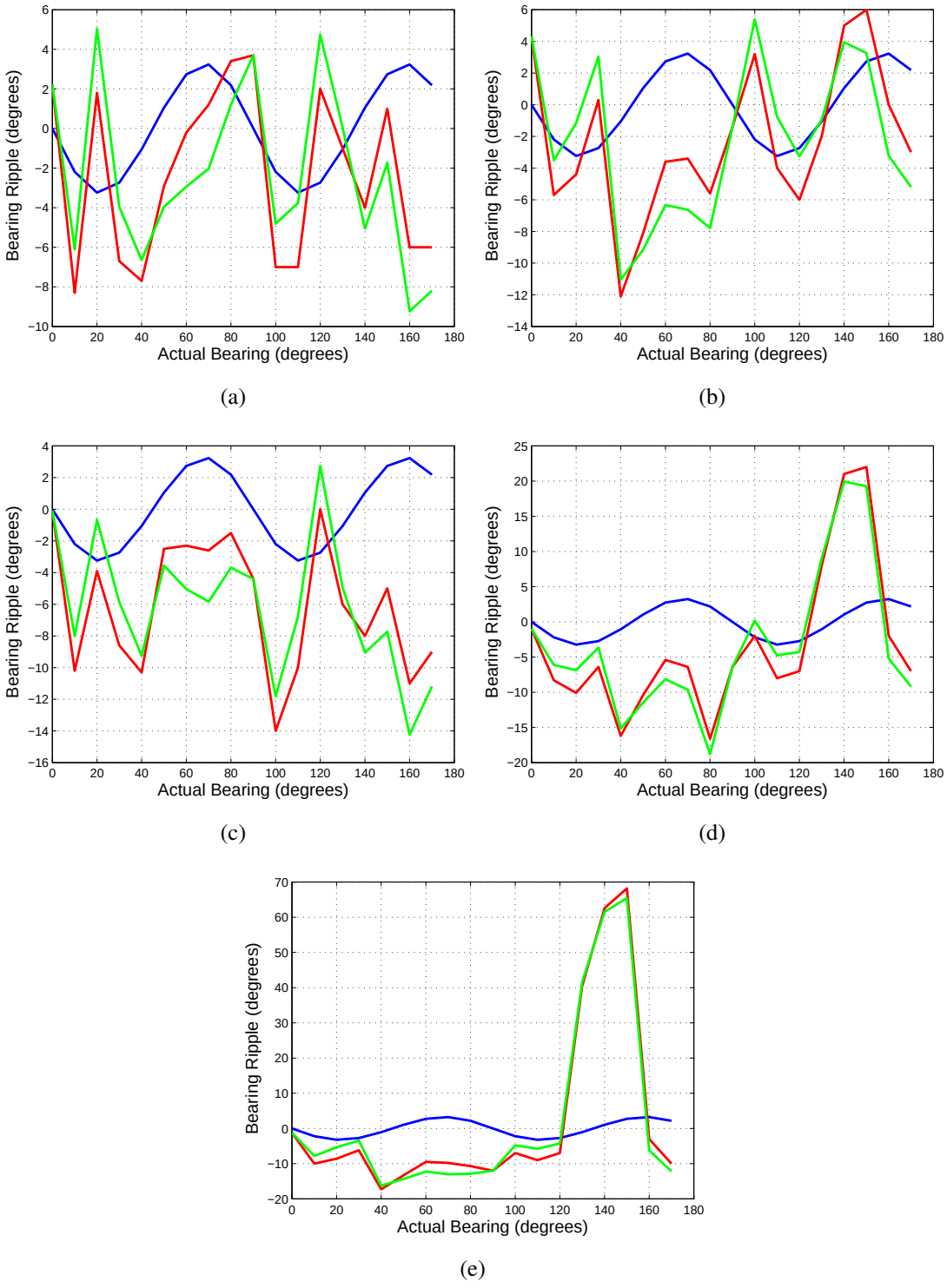

Figure 6.15: Bearing error calibration for the ideal crossed-dipole (blue), measured bearing error (red) and difference between the measured and ideal (green) for (a) 45.22 m, (b) 65.30 m, (c) 84.02 m, (d) 102.66 m and (e) 125 m

lower SNR has also affected the monotonicity of the results which will impact the accuracy in determining the targets bearing. For a non-monotonic result there could be more than one measured bearing corresponding to a real bearing. All the actual ranges were again measured with

the surveying tool, except for the measurement at 125 m, which was estimated using a measuring tape from the 102.66 m measurement, hence its real range measurement is rounded to the closest metre. All range measurements are well within the radars range resolution, suggesting that the 10-15 dB SNR level is more than adequate for range measurements. The radar range is compared to the actual range when the target was perpendicular to the radar and is shown in Figure 6.16 with measured and actual range almost identical.

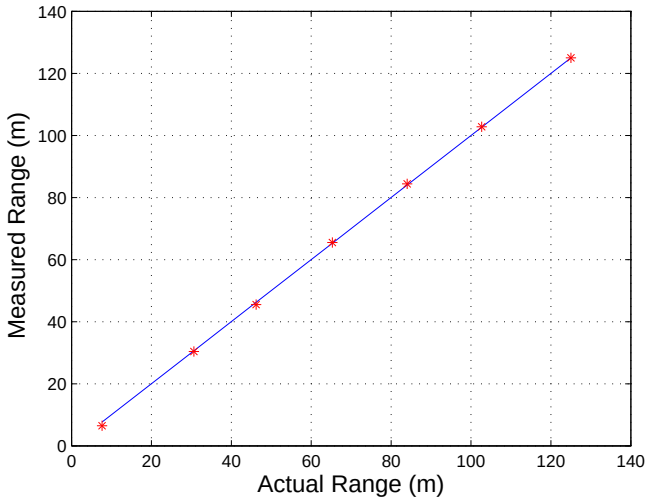

Figure 6.16: Measured range (red*) actual range (blue) for all ranges measured in both Hitchin and Shenley

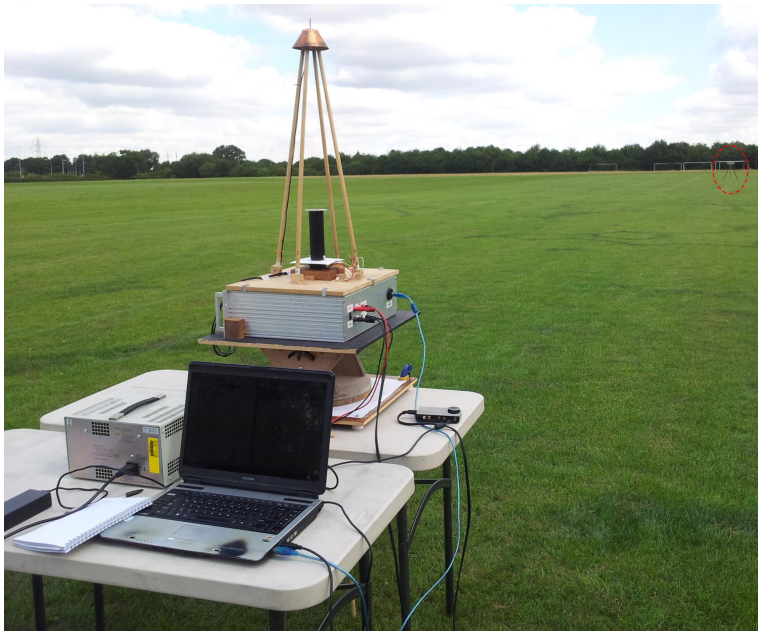

Figure 6.17: Photo of the experimental set up in Shenley, the target is circled in red, at approximately 65 m

The experimental set up is shown in Figure 6.17. The house that was approximately 120

m is just out of shot to the right of the photo. The goal posts at the end of the photo are approximately 220 m away from the radar. Beyond the tree line in the background is the M25 and to the left are a few houses and behind are the football ground facilities. A better view of the surrounding area to the field are shown in the satellite image in Figure 6.18.

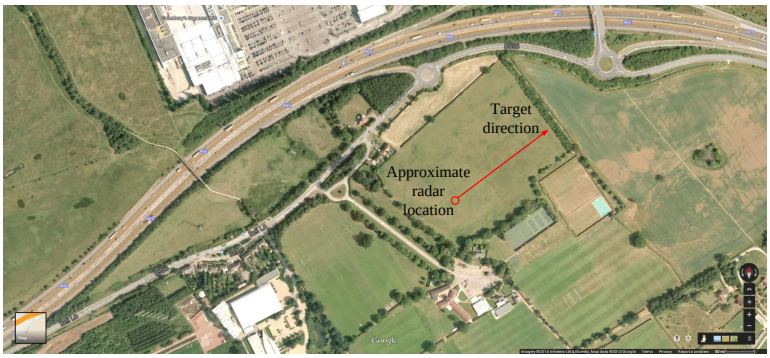

Figure 6.18: Google Maps satellite image for the Shenley radar trial site

To summarise this radar trial, the results showed that the radar operated fairly well over the extended range and as expected the bearing accuracy decreased with range. The radars range accuracy remained fairly constant with the lower SNR and well within the systems range resolution. However, this was expected as a lower SNR can still adequately measure the target range, whereas the bearing accuracy requires higher SNR. The origin of the unexpected interference at approximately 100-125 m still remains unclear, suspicion is with the house that is approximately at this distance. This interference could also be seen in the raw FFT result, at all bearings, but with more impact on the bearing between 130° and 150° at these two ranges. On the second day of testing, the interference was not present at all in the 84 m result, suggesting could have been a specific interference on that day. Attempts to calibrate out the systematic error, due to the phase ripple present in the crossed-dipole did not produce intended response, suggesting there could be an additional alignment error. This may also be true for the negative mean error. At longer ranges, the monotonicity of the bearing degrades, which could cause an incorrect target bearing estimation, with slight improvements to the system, such as SNR, these problems could be negligible at these distances and improve the maximum operating range of the radar.

6.5 Summary

This chapter has shown that the radar system developed throughout this thesis worked as described. However, with less accurate bearing response than expected. The radar was tested with the active target in two locations, an urban type environment (office parking area) in Hitchin and an open grass field in Watford. Both areas have shown good results for bearing accuracy with a

mean error of -6.08° with a standard deviation of 4.18°, at a range of 84.02 m. An unidentified source of interference affected the bearing accuracy beyond this range. The range accuracy was however much better, well within the radars range resolution with a mean error of 20 cm and standard deviation of 8 cm, at a range of 84.02 m.

The first trial revealed that the signal processing could be improved, by flattening the noise floor, this helped identify the target. It also made averaging and further processing more robust and accurate. With the use of windowing the target sidelobe were substantially reduced, with minimal affect on the target range and bearing. Differentiating the time domain signal allowed the start of the chirp to be identified and a 0.5 second time domain signal to be separated into individual chirps and windowed. The resulting nine or ten full chirps were then averaged using weighted amplitudes, in the later trials this was increased to a 5 second time domain signal. It also revealed that to be able to properly present the final result the raw time domain signal required storing, which was realised in the first trial and implemented in subsequent code iterations and on the next two trials. Initially, the aim was to keep the radar fixed and move the active target into the correct bearing position and take a measurement. The difficulty with this was quickly realised and an alternative method was implemented, where the target position was fixed and the radar was rotated instead, the simple rotating structures design allowed for quick and repeatable measurements. This however has the effect of the active target being in the same clutter area.

Access to the testing sites presented some logistical challenges, hence, limiting the number of radar trials, with sea trials the obvious next testing site. The increased noise floor due to noise from the transmitter coupling into the receiver revealed some limitations of using super-Nyquist mode as the radars signal source. If the output power required was significantly lower or the isolation between the antenna improved, maybe with the use of absorbers, the system noise floor could be improved. Alternatively, upconversion could be used in generating the chirp at the desired frequency. Upconverting would require less signal amplification to achieve the desired signal output power, having the added effect of less transmitter noise amplification.

Chapter 7

Conclusions and Future Work

7.1 Conclusions

This thesis has shown that an FMCW radar teamed with a circular array antenna can detect an active target, such a system that could be used in niche applications. For example, ships navigating around harbours, oil rigs or off-shore wind turbines. Systems described in Section 3.1 are mainly radars with mechanical or electrically steered antennas, the prototype system which was built as part of this PhD had neither of these steering methods. The development of a crossed-dipole antenna, approximating a circular array, allowed the application of established phase mode theory, which is usually associated with circular arrays. Finally, leading to a radar system with no moving parts locating an active target in both range and bearing.

A prototype FMCW radar was developed as part of this project, operating in the 2.4 GHz ISM band, which is part of the S band, a band commonly used for marine navigation radar systems. The additional advantage of operating in this band is the wide choice of components which can be bought off the shelf. The operating bandwidth was 83.5 MHz, which resulted in a range resolution of 1.80 m. The advantage of no moving parts is the use of long chirps (50 ms). The increased chirp length provides a 17 dB improvement over a mechanical system (assuming a scan rate of 1 rev/s and a pulse duration of 1 ms). The reduced receiver gain for the crossed-dipole antenna (approximately -1 dB including feed network losses) has less of an impact on the operational range of the radar due the longer chirps.

The method of generating the FMCW sawtooth waveform presented choices. It was concluded that use of the AD9910 evaluation board, based on a DDS, was the most convenient method of generating a highly linear chirp, which was shown to have only a 1 dB ripple. The conventional approach is to upconvert the lower frequency signal, by mixing the low frequency chirp with a high frequency local oscillator signal to generate the chirp in the desired frequency band. For this project the AD9910 was operated in super-Nyquist mode, utilising an image

present in the unfiltered output. The fifth image in the sixth Nyquist zone gave the correct S band operating frequency, but to have the signal at the correct output power level, amplifiers with a total gain of 55 dB were required after the bandpass filtered signal. The high levels of gain was later attributed to the increase in transmitter noise, which raised the system noise floor on average for both channels by 6 dB, see Figure 6.7, therefore reducing the SNR. If rather than using super-Nyquist an upconversion signal generation method is used the SNR should improve by at least 6 dB. This then led to a decreased maximum range and reduced bearing accuracy. If operated as a range radar or where the bearing is not required to be as accurate, this system was shown to work up to 125 m. When the bearing is important, in its current state, this prototype radar system at a range of 84 m had a mean error of -6.08° with a standard deviation of 4.18° over a semi-circular sector. The target placed at this distance had a mean error in range of 20 cm with a standard deviation of 8 cm.

Many antennas were developed for this project, namely the transmit conical monopole antenna, the active target patch antennas and various iterations of the crossed-dipole antenna. They were all designed and simulated in CST which outputted their S-parameter responses and far field radiation patterns. This software was also used to develop the various feed networks, including the rat-race, branchline coupler combination used for the final single sided crossed-dipole antenna. It was also used to design the ultimately unused power splitter feed network for the 9.25 GHz circular array.

One part of this radar system that stood out was the use of frequency shifting within the active target. In the first instance it was not clear how the clutter would affect the target response. When testing the first prototype active target, it became clear that the clutter in the lab was affecting the received signal from the target. What followed was understanding that clutter power, for an omnidirectional receive antenna had a $1/R^3$ roll off, whereas the target return power roll off with range has a $1/R^4$ relationship. For this radar system, these relationships indicated that the clutter power would be greater than the target return at a range of 15 m. The proposed frequency shifting solution involved using the fundamental property of FMCW radar systems, where the beat frequency is proportional to range. By modulating the RF signal within the target with a frequency equivalent to twice the maximum operating range of radar (6 kHz), the target now competed with clutter almost 550 m away. Thus, allowing the project to continue and produce the results shown in Chapter 6.

Processing the beat frequency requires signal acquisition, for this radar system that came courtesy of a Creative SB1090 sound card, with its 16 bit resolution, 96 kHz sampling rate and more importantly dual analogue inputs, making it ideal for sampling both outputted baseband

signals (one per phase mode). The use of the sound card and the signal acquisition toolbox in MATLAB allowed for the signal to be processed in real-time, with code written to both acquire and process the signal. Processing involved providing a trigger point, such that the signal of a certain duration could be split into individual chirps, windowed and averaged. The target bearing was determined by taking the difference in phase between the two analogue channels, in the frequency domain. The amplitude of the FFT of either channel indicated target range, simply by searching for the maximum within the frequency band of interest (6 - 9 kHz) it revealed the range. This amplitude was also used to weight the phase difference values, improving the bearing averaging and increasing bearing accuracy. The response of the baseband filter made it difficult to automatically detect the target return, this was simply solved with the use of gain flattening, by approximating two line equations that represented the filter characteristics.

In summary, this work produced a working prototype active target location radar system, along with its novel crossed-dipole receive antenna fed with a quadriphase microstripline feed network.

7.2 Future Work

It has been mentioned a few times throughout this thesis that although the super-Nyquist operation of the AD9910 provided a chirp with the correct characteristics. The fact that it was the fifth image, meant that 55 dB of gain and a 4 pole cavity filter was required to remove the fundamental and other image signals. In hindsight, it seems that using the DDS and a local oscillator to upconvert the fundamental chirp would have been a better solution and any subsequent developments of this prototype would definitely have this upgrade.

It was previously shown in Section 5.2.3 that the clutter power was greater than the target power without frequency shifting within 15 m. Figure 5.41 revealed that increasing the frequency shift would reduce the clutter power further still, currently the 6 kHz shift allows a 29 dB signal-to-clutter ratio (SCR) at a range of 41.4 m, provided a backscatter coefficient, σ°, is -10 dB. The SCR for given frequency shifts and backscatter coefficients are shown in Table 7.1. If it were possible to introduce a 80 kHz shift the radar would become noise rather than clutter limited, for the current maximum range of 270 m. This could go a long way in explaining the shortcomings with respect to the radars maximum range.

The 80 kHz shift would be ideal for high clutter environments, it was discussed that increasing the shift frequency will make the baseband filter virtually impossible to construct. Also, if the shift frequency was this high, a different DAQ would also be required. One way to overcome this problem could be to introduce the same frequency shift in both the target and

Table 7.1: Ranges (m) at which SCR = 29 dB, at different shift frequencies and backscatter coefficients

$\mathbf{f_{shift}}$ (kHz)	σ° (dB)			
	0	**-10**	**-20**	**-30**
0	<0.1	<0.1	0.2	1.5
6	23.1	41.4	77	148.7
80	156.1	281.3	511.7	948.5
1000	1030	1845	3320	6032

radar. This would allow the baseband frequency to occupy the original 0-3 kHz band or any 3 kHz band of the users choice, the frequency shift could be introduced into the radar along with an image reject filter. This filter would also be present in the target with the same LO frequency modulating the RF signal within the target with SSB modulation. The revised system block diagram with the additional image reject filter and upconversion to generate the chirp is shown in Figure 7.1. This method would allow the frequency shift to be well beyond 80 kHz with no effect on the baseband frequency band, it would also allow the use of the current DAQ. The LO for both the signal generation and the filter would need to be synchronised with one another to ensure there is no offset in baseband frequency.

Another way of achieving the same goal would be to use two DDSs, one to generate the transmitted chirp and the other with a slight offset corresponding to the required frequency shift, being used as the reference signal for the received signal. Again both DDSs would need to be synchronised, the frequency offset within the target could also be generated using the same DDS. This approach would result in a simpler radar, but more complex and potentially more expensive depending on the number of targets, which leads on to the next suggested improvement.

For this radar system to be viable in the harbour environment, multiple targets and/or radars may be in operation at any given time. These targets therefore require some sort of identification. One method would to be asynchronously code the target, using a single bit per pulse. Hence, over a duration of 1 second, a 20 bit word could be encoded onto the RF signal. With asynchronous coding the signal processing becomes more complex. This is due to the potential mis-synchronisation between the start of the ID and the chirp, shown pictorially in Figure 7.2. Also shown in this figure is how the FFT amplitude varies for a given ‘shift’ (shift in this context means the length of time the chirp start is mis-synchronised from the data bit start). If the signal was unsynchronised by the amount as shown in the figure, the FFT amplitude would be close to zero, by resynchronising the code with the start of the chirp, the FFT amplitude can be closer to maximum, therefore detecting the target. The resynchronisation

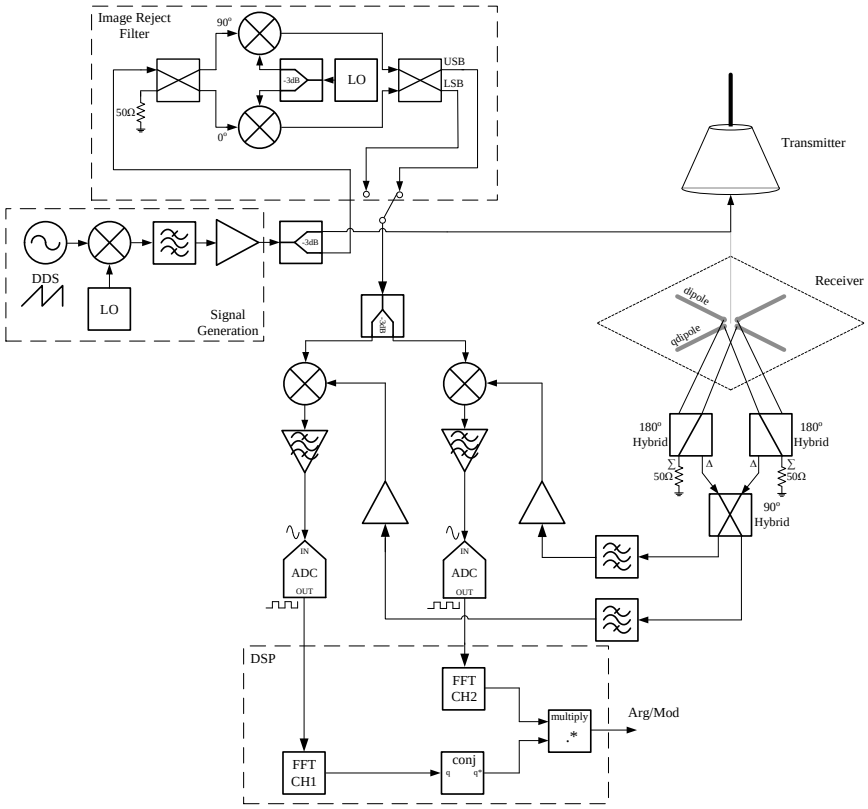

Figure 7.1: Radar system block diagram with the image reject filter and upconversion chirp generation

method could be removed if different chirp lengths were used. This is due to higher probability that one of the chirp lengths would be closer to optimum FFT amplitude. The 20 bit ID would continually repeat where a '0' would multiply the signal with a -1 and a '1' by +1. Finally, this type of coding would increase the number of components in the target by three: A component where the ID is stored, probably some sort of microcontoller, followed by some sort of FIFO clocking in the ID bit for the length of one chirp and an additional mixer for mixing ID with the frequency shifted RF signal. A block diagram of the active target with the asynchronous coding is shown in Figure 7.3.

This radar system thus far has only been testing in an open field and an office parking area, it is yet to be tested on a ship or in a harbour setting. If this project were to be carried forward and the changes discussed above implemented, then taking the system to this location would need to be part of its future plan.

Moving the current operating frequency from S band to X band would present some challenges as discussed in Section 5.1.1 with the size of the antenna each arm would go from the current ∼31 mm to ∼8 mm. The mounting of a system would be problematic. However, it has the benefit of using the current active targets installed by Guidance Microwave present in

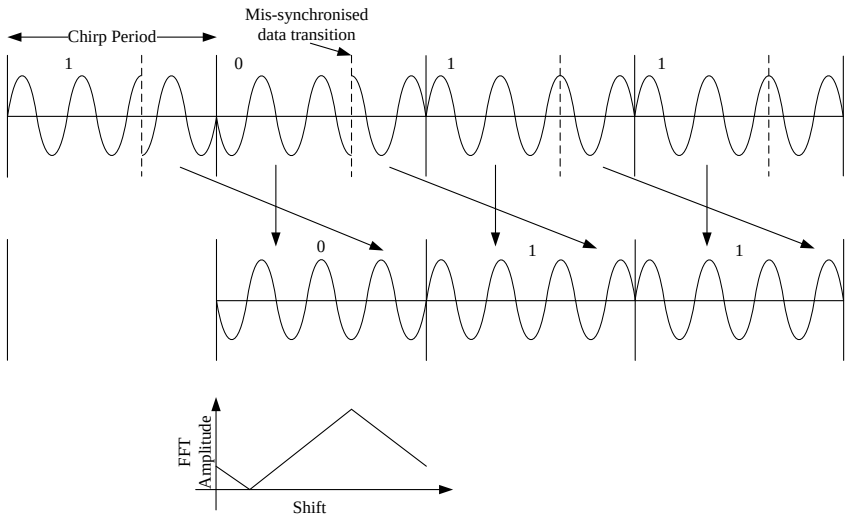

Figure 7.2: Deramped frequency re-alignment

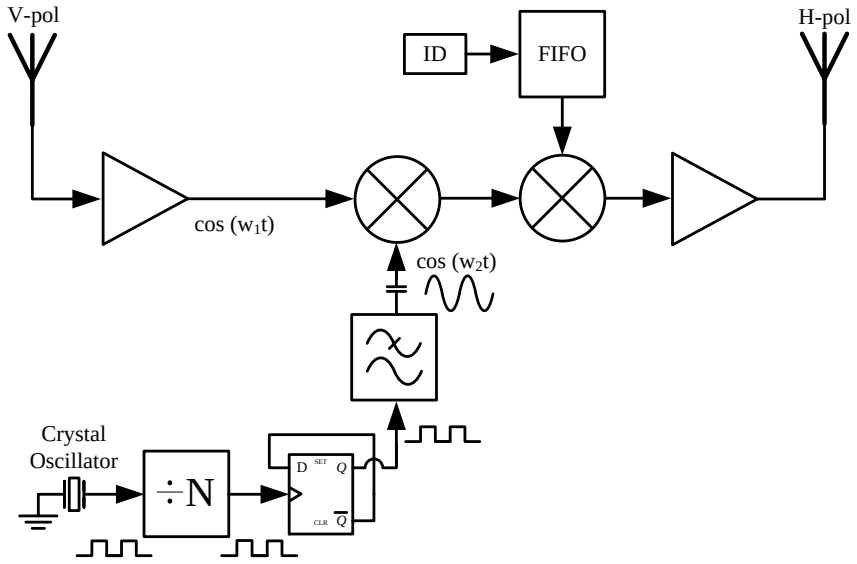

Figure 7.3: Active target with ID block diagram

harbours across the United Kingdom. Therefore presenting an opportunity for this prototype radar to work alongside the current RadaScan system. Where this prototype would be used with smaller pleasure boat type vessels, due to its comparability smaller size.

There is also the opportunity for the abandoned system, discussed in Section 4.1 to be revived with a more sophisticated feed network. The advantage has previously been discussed and is repeated again now, by using the 0^{th} and 1^{st} order phase modes, the ability of monitor and detect targets in 360° unambiguously would be achieved. If the prototype design was to be taken forward from where it stopped, then the antenna and feed network would be extremely small (~150 x 37 mm). If then coupled with a single PCB radar system, the whole system could

be on the scale of an A5 piece of paper (148 x 210 mm).

In summary, if these improvements were made to the radar system, then there is potential for it to operate well beyond its current maximum operating range with the same accuracy or at the current range with higher accuracy.

Appendix A

Far Field for Continual Circular Array

Proof for the far field radiation (2.59) in the azimuth plane in terms of the m^{th} pattern function, the far-field radiation is given by the equation:

$$E(\phi) = \frac{1}{2\pi} \int_{-\pi}^{\pi} V(\varphi) EL(\phi - \varphi) e^{j\beta R \cos(\phi - \varphi)} \mathrm{d}\varphi \tag{A.1}$$

The excitation function is periodic and can be expanded using a Fourier series, using the complex Fourier series with the definition [110]:

$$f(t) = \sum_{m=-\infty}^{\infty} X\left(\frac{m}{T}\right) e^{2\pi j m \frac{t}{T}} \tag{A.2}$$

$$X\left(\frac{m}{T}\right) = X_m = \frac{1}{T} \int_{-\frac{T}{2}}^{\frac{T}{2}} f(t) e^{-2\pi j m \frac{t}{T}} \mathrm{d}t \tag{A.3}$$

For the circular array with the excitation $V(\varphi)$ over a time period $T = 2\pi$ complex Fourier series is:

$$V(\varphi) = \sum_{-\infty}^{\infty} C_m e^{jm\varphi} \tag{A.4}$$

$$C_m = \frac{1}{2\pi} \int_{-\pi}^{\pi} V(\varphi) e^{jm\varphi} \mathrm{d}\varphi \tag{A.5}$$

where each co-efficient C_m is a phase mode. With the $m = 0$ the first phase mode for which all the signals are added in phase, with no phase variation between the elements of the circular array. The m^{th} mode has $m.2\pi$ phase variation, with m being able to be both positive and negative.

Considering all omnidirectional elements, the array factor now becomes:

$$E(\phi) = \frac{1}{2\pi}\int_{-\pi}^{\pi} V(\varphi)e^{j\beta R\cos(\phi-\varphi)}\mathrm{d}\varphi \tag{A.6}$$

Using equations (A.5) and (A.6) and reversing the order of the summation and the integration:

$$E(\phi) = \sum_{-\infty}^{\infty}\frac{1}{2\pi}\int_{-\pi}^{\pi} e^{jm\varphi}e^{j\beta R\cos(\phi-\varphi)}\mathrm{d}\varphi \tag{A.7}$$

As the radiated far field is also periodic over 2π, it can be expressed as in a Fourier series:

$$E(\phi) = \sum_{-\infty}^{\infty} A_m e^{jm\phi} \tag{A.8}$$

where A_m, is the far field phase mode amplitude, which relates to C_m the excitation phase mode amplitude by the expression:

$$A_m = C_m\frac{1}{2\pi}\int_{-\pi}^{\pi} e^{jm(\varphi-\phi)}e^{j\beta R\cos(\varphi-\phi)}\mathrm{d}\varphi \tag{A.9}$$

this is the Bessel function of the first kind in its integral form:

$$J_n(z) = \frac{1}{2\pi j^n}\int_{-\pi}^{\pi} e^{jm\theta}e^{jz\cos\theta}\mathrm{d}\theta \tag{A.10}$$

$\therefore$

$$A_m = j^m C_m J_m(\beta R) \tag{A.11}$$

The pattern function from the m^{th} excitation mode is as equation (2.60):

$$E_m(\phi) = j^m C_m J_m(\beta R)e^{jm\phi} \tag{A.12}$$

Appendix B

9.25 GHz Circular Array - Feed Network Individual PCBs

To reduce the time taken for simulation, the feed network was broken up into its simplest components and individually simulated. This also gave rise to minor modifications, as can be seen in Figure B.1. The centre coax pin is connected to four orthogonal transmission lines, then bend at an angle go to where the feed point of the antenna is located. The reason behind the initial orthogonal transmission lines is to accommodate the 1st order feed that will have to pass through this board. This can be seen more clearly in Figure 4.9. Note that the port located on the transmission line that connects to the receive antenna array is output port and where these transmission lines connect is the input port.

The S-parameters for the horizontal board are not ideal, the expectation was a lower return loss for the S_{11}, ensuring that more power is delivered to ports 2-5. One of the reasons that this simulation may not be entirely accurate is due to the port impedance; the input port (port 1) has an impedance of 25 Ω. The output ports impedances are 100 Ω (ports 2-5), the four-way equal power spilt from 25 Ω to 100 Ω, should have a loss of approximately 6 dB. This simulation shows that the magnitude and phase S-parameters (S_{21} to S_{51}) are all equal and approximately -7.2 dB, hence good symmetry, however, at a lower power level, due to higher reflection than the desired at the input port.

For the PCB shown in Figure B.2a the input port is located at the centre, and is a 50 Ω port connected to a 50 Ω transmission line, splitting equally into two 100 Ω transmission lines. Then using a quarter wave transformer the impedance decreases to 25 Ω at ports 2 and 3, which in Figure B.1 is labelled as port 1. The two 100 Ω transmission lines are not completely orthogonal and are at an angle, to improve the S_{11} as shown in Figure B.2b. The quarter wave transformer has chamfered corners as does the patch antenna for the bends in the transmission line, as seen in Figure 4.4, usually implemented to minimise the transmission line discontinuities. These

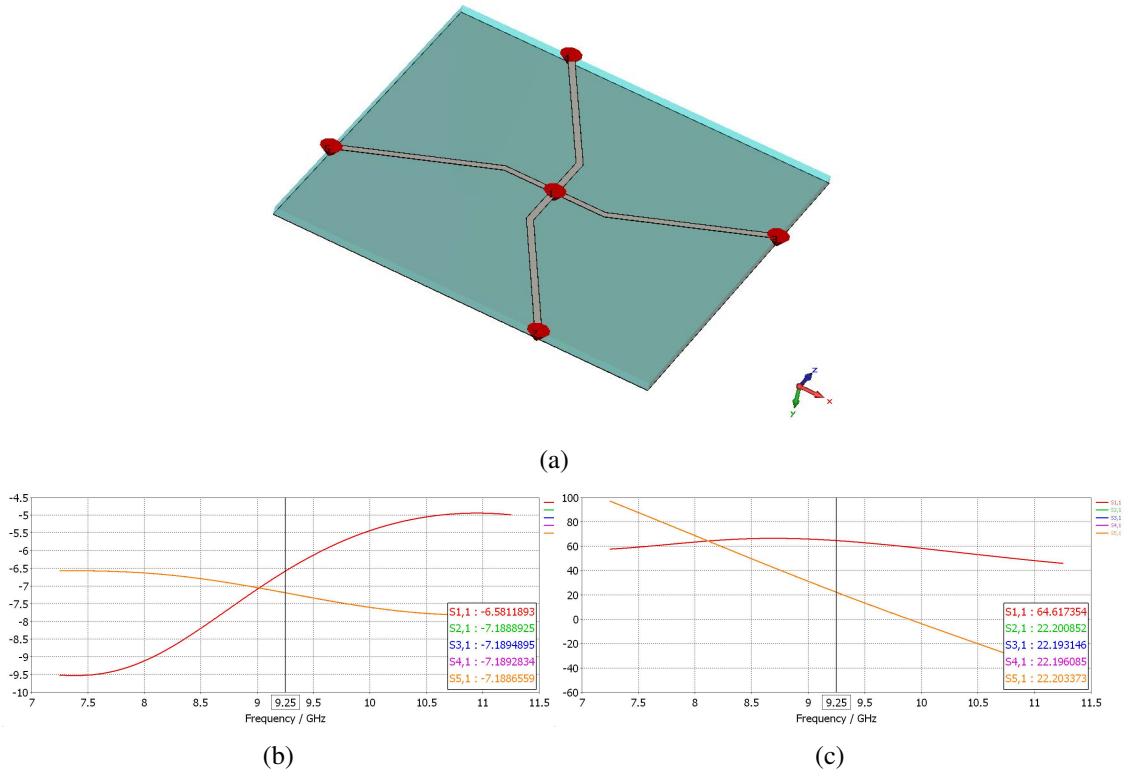

Figure B.1: (a) Horizontal 0^{th} order feed network PCB. S-parameter (b) magnitude (dB) and (c) phase (degrees) for the horizontal 0^{th} order feed network PCB

occur due to the inside of the bend having an electric current density higher than outside, thus causing the transmission line to radiate. For this project where two strip lines of differing widths meet, the wider line is chamfered at an angle of 45° until it meets the thinner line, the required length of the quarter-wave transformer begins and ends at the centre point of the chamfered line.

The return loss for this board is much lower than the horizontal 0^{th} order PCB, this may be due to the fact that the one of the ports (port 1) in this simulation is at 50 Ω, which is the default port impedance for simulations using CST MWS (2010-2011), with different value ports the simulations have some discrepancies. This has been a problem that has occurred for many simulations during the project, for this PCB the S_{11} seems to be adequate. The -10 dB bandwidth covers the bandwidth which is allocated for the purposes of this radar. The power (-3.36 dB) and phase split is equal for ports 2 and 3. To reiterate, the 0^{th} order requires the individual antenna to have both equal amplitude and phase.

The 1^{st} order horizontal PCB has its coaxial feed point slightly off the centre point. This was done so that the 0^{th} and 1^{st} order feed points would not overlap and render the construction impossible. The location of the 25 Ω feed point was established such that the three of the four 100 Ω transmission lines would be straight and the longest has bends to increase the transmis-

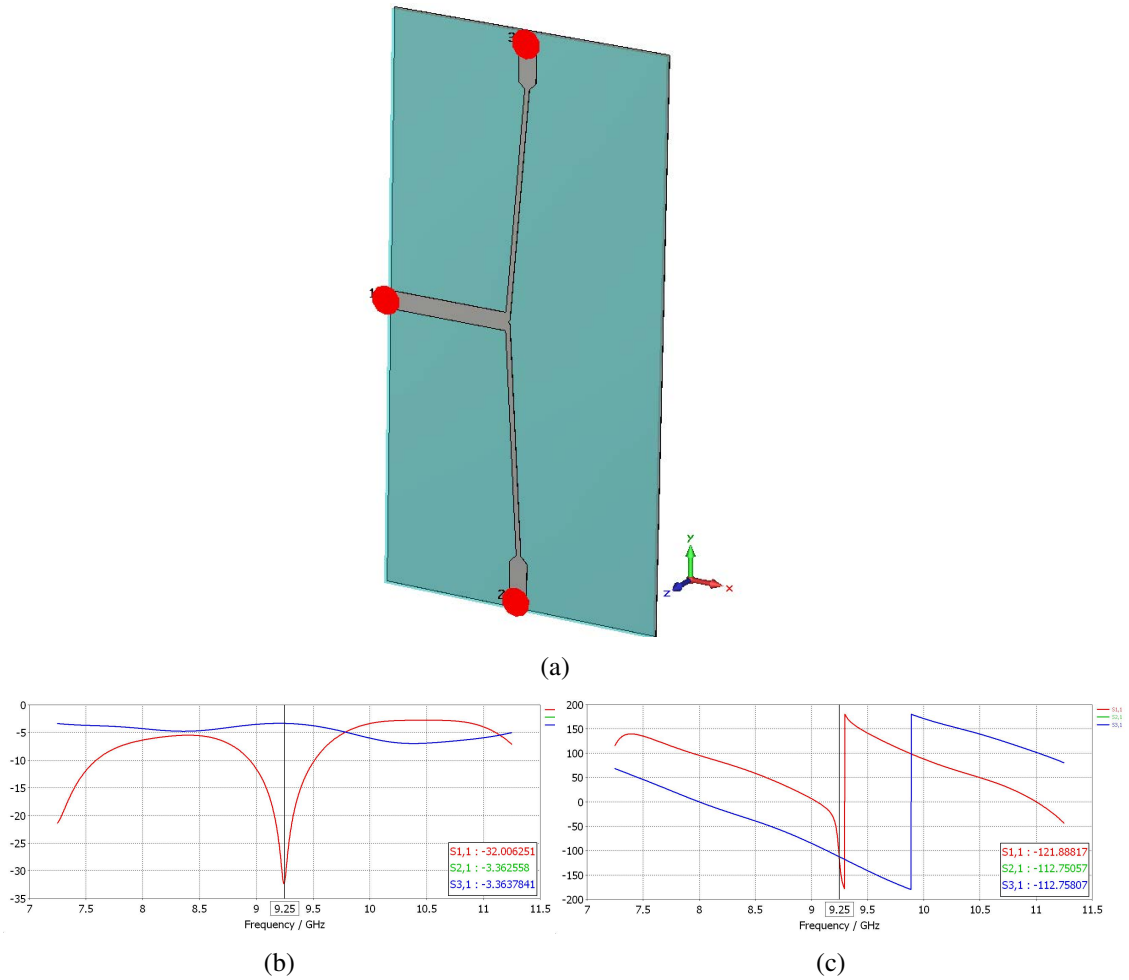

Figure B.2: (a) Vertical 0^{th} order feed network PCB. S-parameter (b) magnitude (dB) and (c) phase (degrees) for the vertical 0^{th} order feed network PCB

sion line length to achieve the correct phase difference between the output ports. A small script was written to determine the location of the input port (port 1), as the coordinates of ports 2-5 were known, by centring a circle at ports 2-5, whose radius increased adjacently in length by a quarter wavelength (90° increase), i.e. The centre point of a circle at port 2 has a radius 'r', port 3 a radius 'r + $\lambda/4$', port 4 'r + $2\lambda/4$' and finally port 5 'r + $3\lambda/4$', simple geometry shows that there will be at least one point where ports 2-4 circles intersect. Port 5 transmission line length can then be increased by introducing a bend in the line to get the required phase difference. The value of 'r' was determined to be 14.63 mm.

The method of finding the location of the 25 Ω coaxial feed point indeed shows that there is a point where port 2-4 intersect, the coordinates of this singular point are accurate to 2 d.p. It was therefore decided that location would be the midpoint of where the transmission lines intersect (2.765 mm, 4.775 mm). This script was used to design the PCB as seen in Figure B.4a.

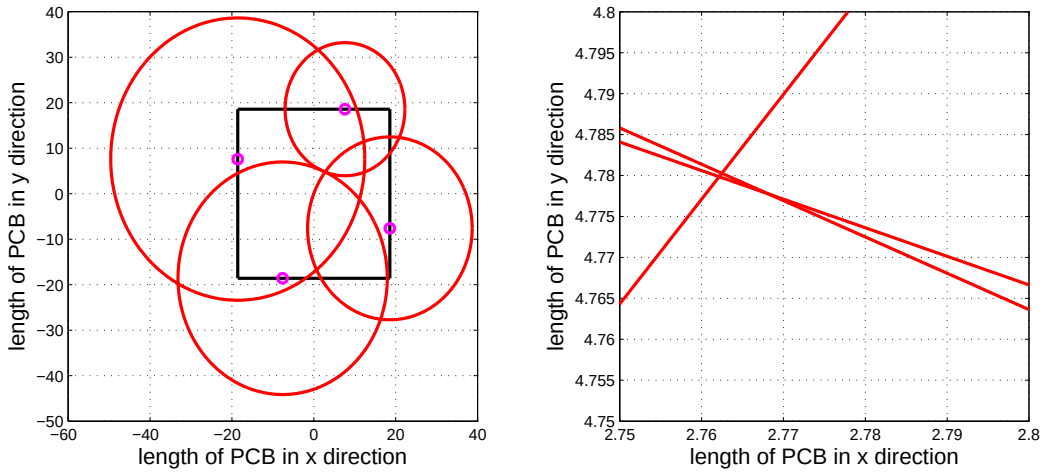

(a) (b)

Figure B.3: (a) Determining the location of the 25 Ω coaxial feed point for the 1st order horizontal PCB, the magenta '∘' show the location of the antenna feed points and solid black line indicates the perimeter of the PCB (b) magnified to show the intersection location of the three circles, all dimensions are in mm

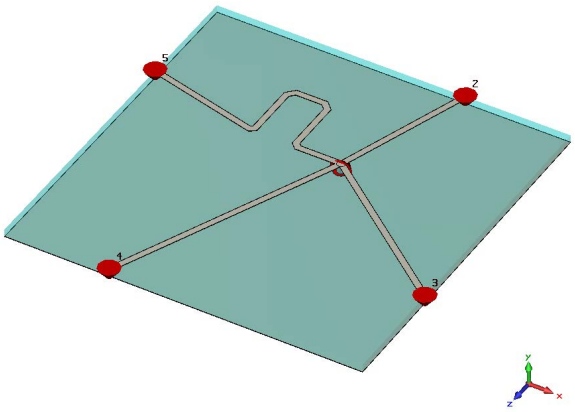

(a)

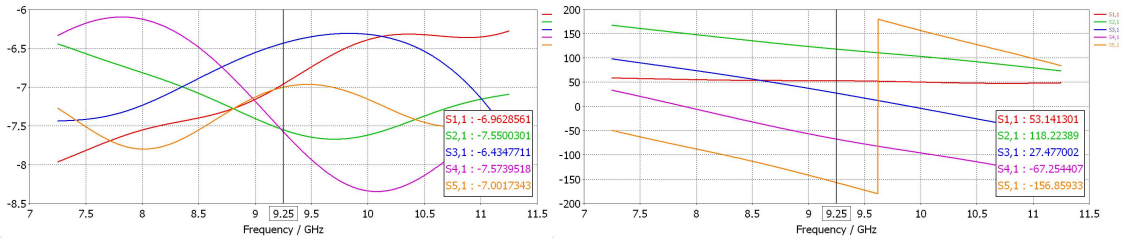

(b) (c)

Figure B.4: (a) Horizontal 1st order feed network PCB. S-parameter (b) magnitude (dB) and (c) phase (degrees) for the horizontal 1st order feed network PCB

As shown in Figure B.1b, Figure B.4b again has a high return loss and the power available to the output ports was not as expected, as the power split is unequal. Again this may be due the method of defining the ports, the return loss is as high as the power delivered. Hence, there

will be as much power reflected back as is transmitted. Figure B.4c, does however show that the phase between the output ports is approximately 90° apart. Once again this result may not be entirely accurate due non optimal magnitude S-parameters.

The PCB shown in Figure B.5a has the same characteristics as the 0^{th} order vertical PCB (Figure B.2a). However, the port located at the top of this PCB (port 3) has a longer 100 Ω transmission line, an increase of $\lambda/8$, introducing the required 45° phase shift between the two output ports (ports 2 and 3). The input port is located in the centre of the PCB, same as the 0^{th} order.

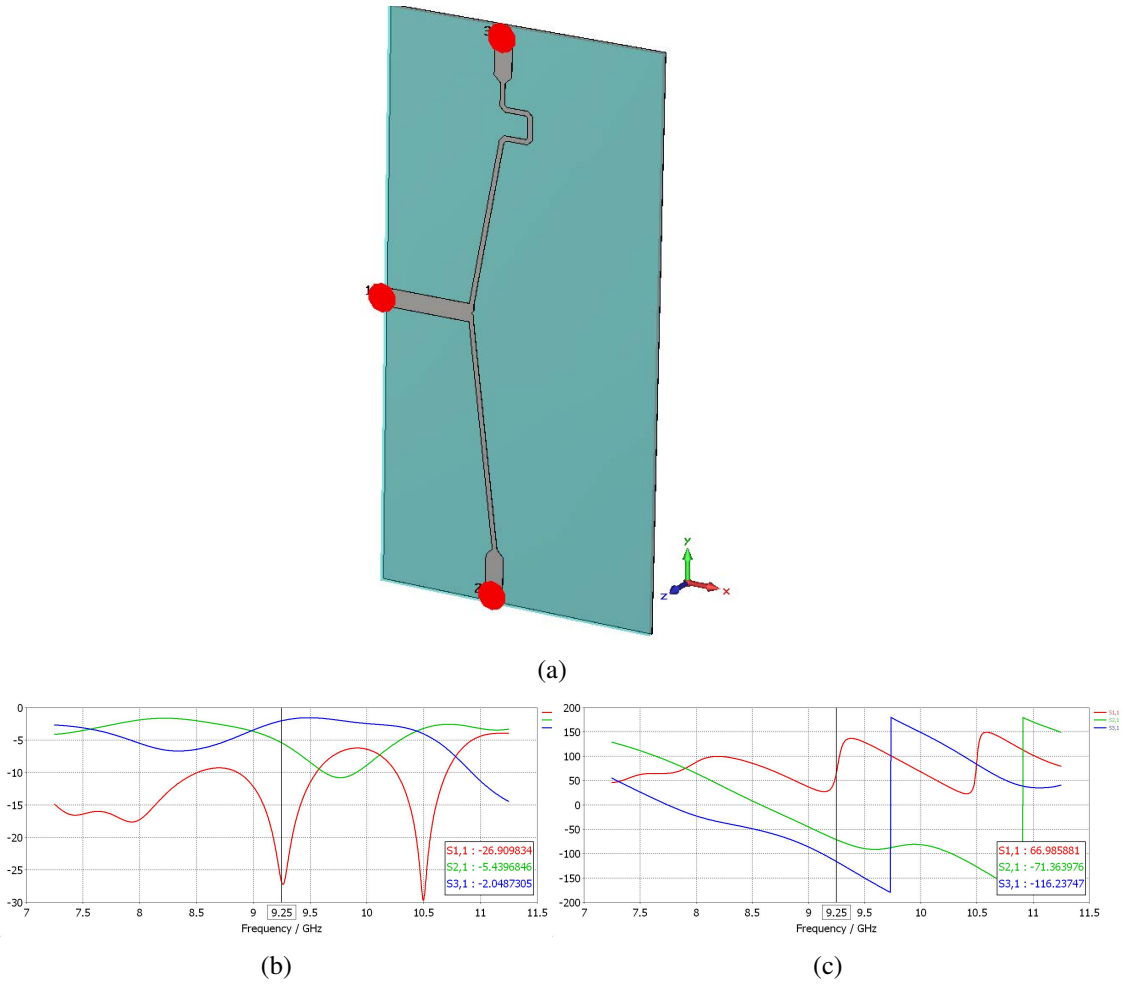

(a)

(b)

(c)

Figure B.5: (a) Vertical 1^{st} order feed network PCB. S-parameter (b) magnitude (dB) and (c) phase (degrees) for the vertical 1^{st} order feed network PCB

The vertical 1^{st} order board has a better S_{11} return loss than the horizontal 1^{st} order PCB, but the magnitude is not split equally as expected. The phase S-parameter as shown in Figure B.5c, does show that the port 3 has a 45° lag compared to port 2, which is maintained over the required bandwidth.

Appendix C

Low Frequency Removal - Unmodulated Active Target

It was discussed that without removing the background clutter the unmodulated target was unable to be detected with ranges above 1 to 2 m. It was suggested that a simple time domain subtraction would enable measurements within the lab to take place without any hardware modifications.

The first step was to keep the target turned off and run the MATLAB code and store a single chirps data. This was the measurement of the background including all the environmental contributions to the received signal. For the left and right audio channels, this calibration had to be carried out separately as the orientation of the receiver would have different effects on the ADC, hence, the raw data for the chirp on each channel was stored and any received signal was calibrated on a per channel basis.

Figure C.1 shows the time domain signal when the target is off, i.e. the background measurement, whilst the target was off, more measurements were taken to determine how well the background clutter signal was subtracted.

As was discussed previously, the conclusion was reached by determining how much of the frequency spectrum was considered to be low frequency and thus removed from the signal. This was mainly set by the size of the room and location of large scatters. Removing the first 20 frequency components was found to remove most of the clutter and was used for initial testing. Figure C.2 show the FFT of the time domain signal before any low frequency removal, the target was expected at around 50 Hz. However, even when the target was turned off, there remains a large return at 50 Hz, which was found to be to ground loops. Slightly beyond 50 Hz the large returns were due to the cabinets in the room.

By removing the first 20 frequency components, the high returns between 40 - 100 Hz in Figure C.2 have been removed by a minimum of 10 dB. As was intended, the target was then

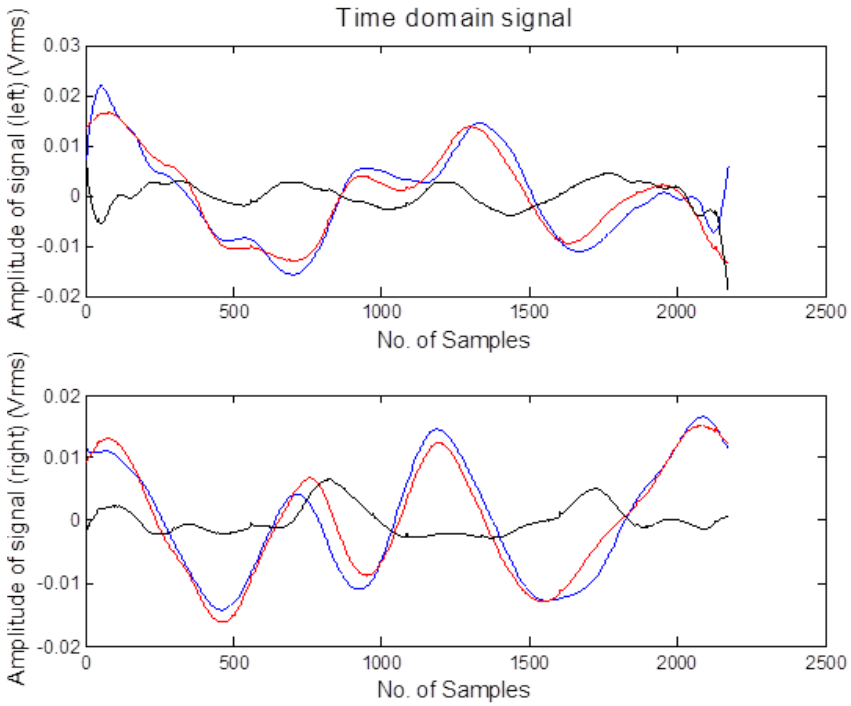

Figure C.1: Time domain signal for a single chirp when the target is off (top: left audio channel) (bottom: right audio channel) background measured signal (blue), received signal under test (red) and background signal minus current signal (black)

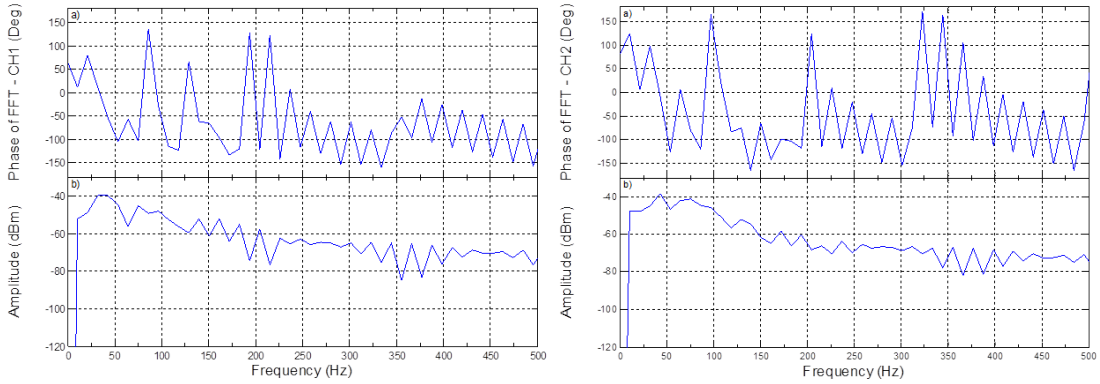

(a) (b)

Figure C.2: FFT of (a) CH1 (b) CH2 before low frequency removal, the FFT of the red curves in Figure C.1

switched on and produced the following results.

Figure C.6 shows a return from the target at approximately 50 Hz at a similar signal strength to that when the target was off. This highlights the fact that the target would be undetectable without removing the lower frequency components. Initially, it was thought that this would only be required for when the target was close to the radar in a high clutter environment. However, once the clutter analysis was carried out it was obvious that without modulating the

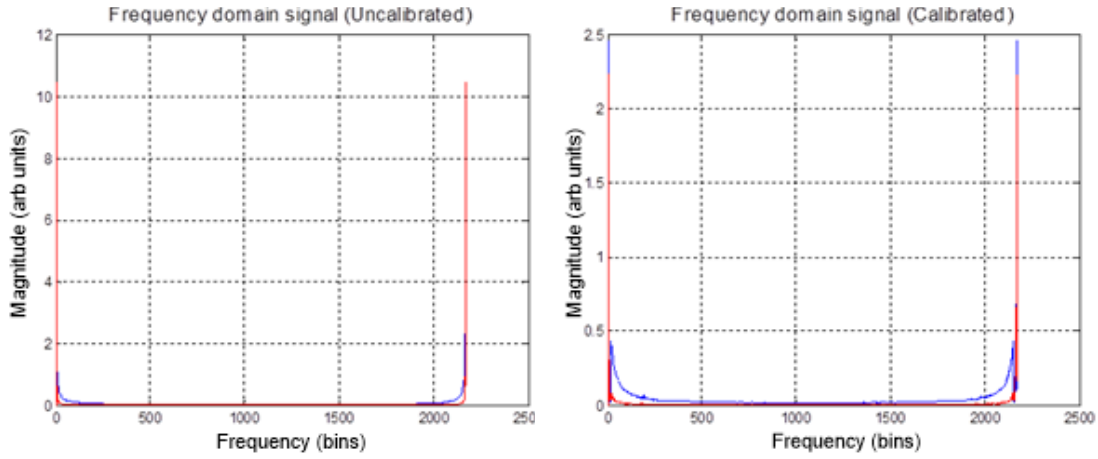

(a) (b)

Figure C.3: (a) FFT of red curves in Figure C.1 i.e no frequency removal (b) first 20 frequency components of red curves subtracted from corresponding channels blue curves of Figure C.1

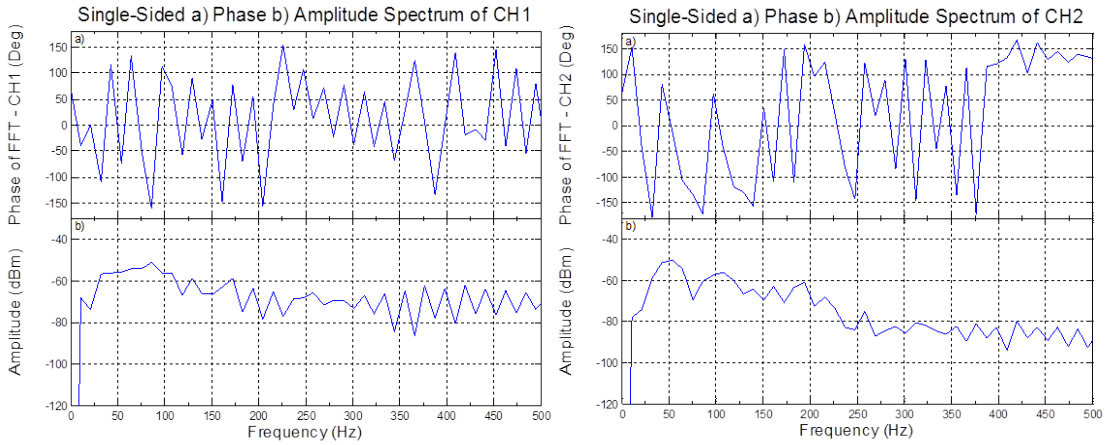

(a) (b)

Figure C.4: FFT of time domain signal (a) CH1 (b) CH2 of black curves in Figure C.1

target this radar system would probably not function at all.

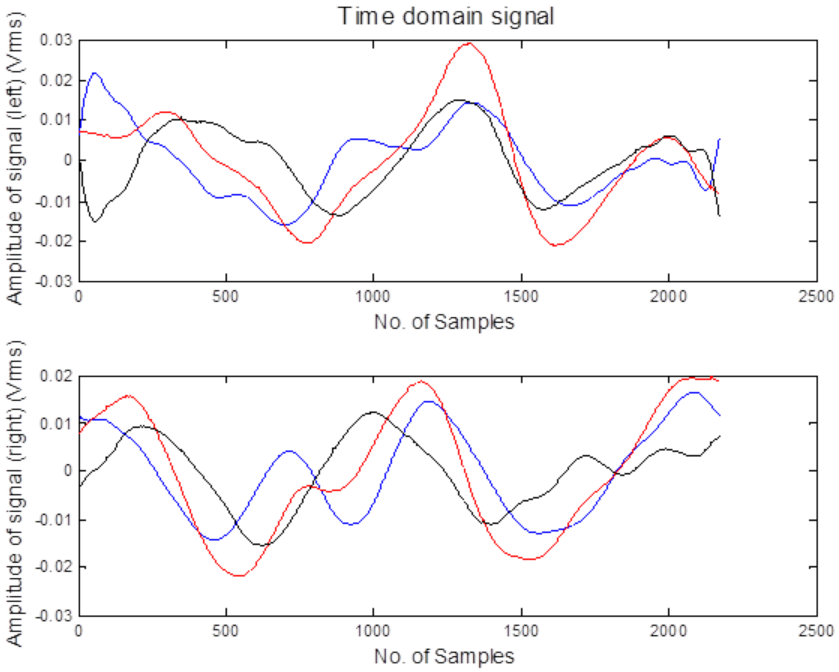

Figure C.5: Time domain signal for a single chirp when the target is on (top: left audio channel) (bottom: right audio channel) background measured signal (blue), received signal under test (red) and background signal minus current signal (black)

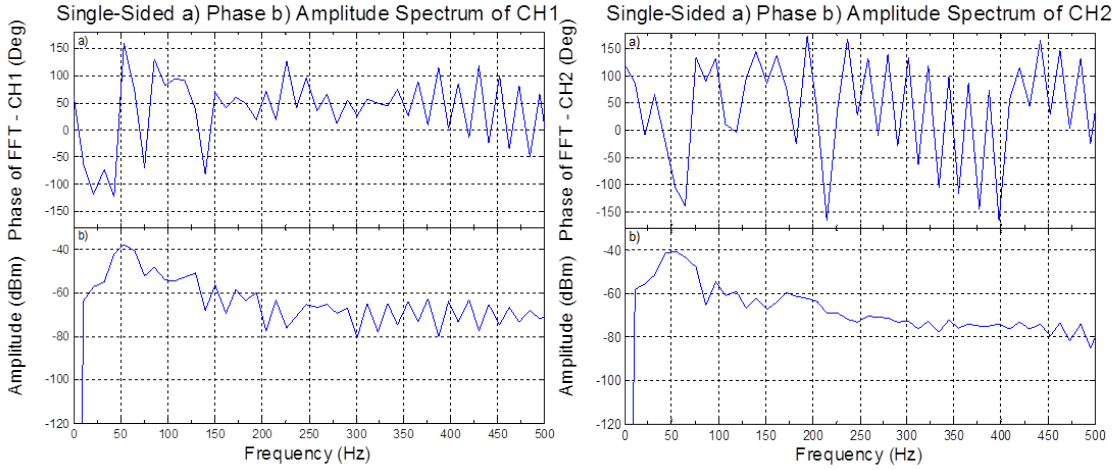

(a) (b)

Figure C.6: FFT of (a) CH1 (b) CH2 after low frequency removal i.e. FFT of black curves in Figure C.5, target is on

Appendix D

Elevated Target With/Without Absorber Results

During the Hitchin trials in an attempt to increase the isolations between the transmit and receive radar antennas foil backed Eccosorb AN 73 was placed between the antenna. This was the only absorber available at the time, it is however optimised for higher frequency applications and offers 3-4 dB of reflectivity at 2.4 GHz [111]. Various configurations were attempted, such as with a single absorber sheet placed between the antenna. Also, with the absorber placed in front of the receiver to minimise ground reflections and with no absorber. Therefore, allowing a direct comparison between measurements with respect to the bearing accuracy at range of 8.29 m. However, firstly shown is the 2.5° elevation result without any absorber. Both the mean error

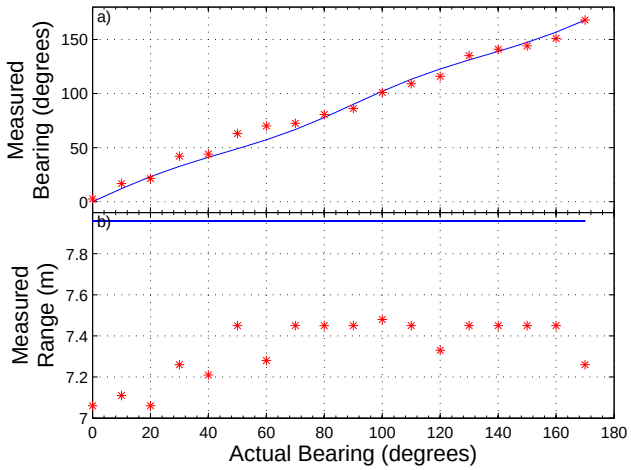

Figure D.1: Measured (red*) crossed-dipole ideal (blue) bearing (top) and measured (red*) real (blue) range (bottom) for 7.96 m with 2.5° elevation

and RMS bearing deviation have increased significantly and are -1.93° and 6.14° respectively, the error in range is between 40 and 80 cm which is similar to that of the 7.65 m result shown in Figure 6.11a. The same experiment was carried out on another day hence the slight variations

both measured range 8.29 m and target elevation of 2.4°.

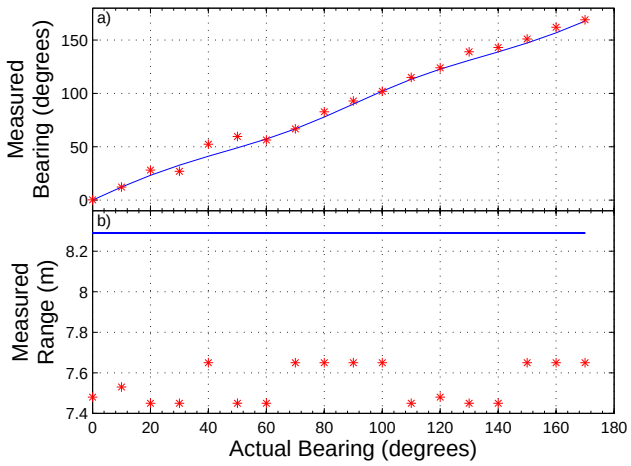

Figure D.2: Measured (red*) crossed-dipole ideal (blue) bearing (top) and measured (red*) real (blue) range (bottom) for 8.29 m with 2.4° elevation

With respect to Figure D.1 the mean error is worse at -2.95°, but with an improved RMS bearing deviation of 5.31°. The error with range is still fairly similar between 40 and 80 cm, still within the range resolution of the radar.

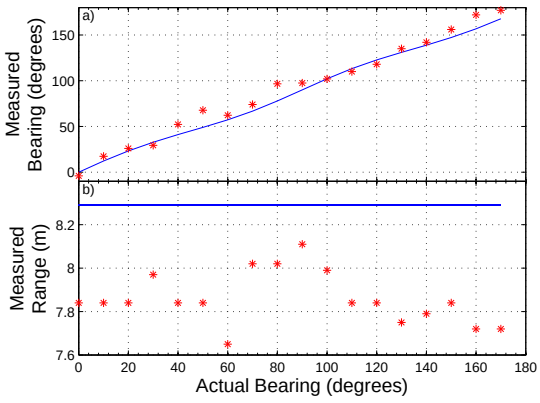

(a)

(b)

Figure D.3: (a) Measured (red*) crossed-dipole ideal (blue) bearing (top) and measured (red*) real (blue) range (bottom) for 8.29 m with 2.4° elevation (absorber in between) (b) Photo of absorber placement

With the absorber placed in between the radars transmit and receive antennas, the mean error is worse at -5.60° as is the RMS bearing deviation of 8.13°. This was quite unexpected, a slight improvement or a similar result was expected, the range estimation is slightly improved

but still at its worst is 60 cm less than the measured range. For Figure D.4 the absorber was

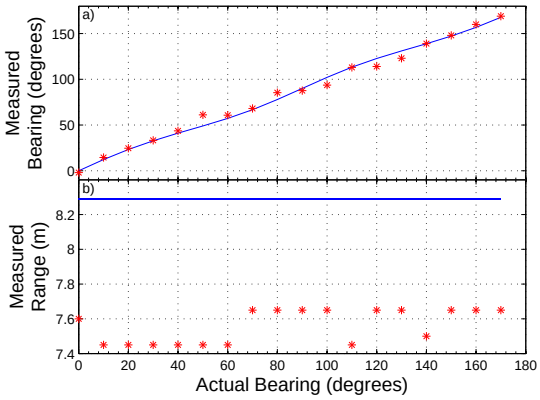

(a)

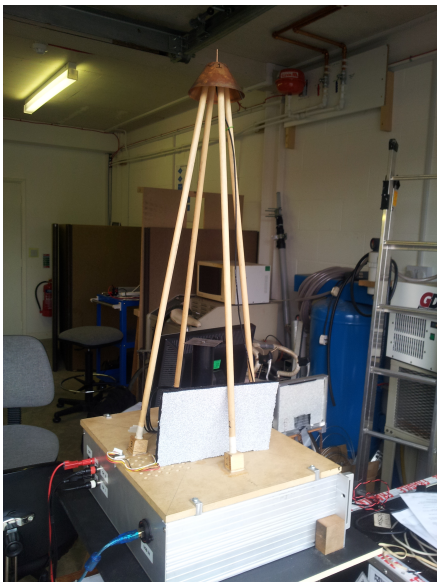

(b)

Figure D.4: (a) Measured (red*) crossed-dipole ideal (blue) bearing (top) and measured (red*) real (blue) range (bottom) for 8.29 m with 2.4° elevation (absorber in front) (b) Photo of absorber placement

placed in front of the receiver in attempt to reduce the ground reflections. This experiment was to see if the absorber could improve the range measurement and if there was any change with the bearing estimation. The mean error was greatly improved to -0.36° as did the RMS bearing deviation at 4.54°, this was quite a significant improvement over the results in Figure D.2. The expected improvement in the targets' range estimation due to the absorber is not significant with the range still between 60 and 80 cm less that the laser based value.

To summarise, the slightly elevated target results are significantly worse than when the target is in the same plane as the radar antenna. In order to draw a better conclusion, longer range measurements with greater elevations angles are definitely required. Added to that is the use of absorber with greater absorption at the desired frequency.

References

[1] P. Drouilhet, "The Development of the ATC Radar Beacon System: Past, Present, and Future," *IEEE Transactions on Communications*, vol. 21, pp. 408–421, May 1973.

[2] F. Gross, "Harbor Radar Systems," *Transactions of the IRE Professional Group on Communications Systems*, vol. 3, pp. 64–64, Mar. 1955.

[3] B. Wade, "SharpEye A New Technology marine radar," in *Radar Systems, 2007 IET International Conference on*, pp. 1–5, 2007.

[4] D. Pearce, "A high resolution FMCW X-band radar sensor for vessel underway replenishment at sea applications," *2010 IEEE Radar Conference*, pp. 647–650, 2010.

[5] M. I. Skolnik, *Introduction to Radar Systems*. Boston: McGraw-Hill Higher Education, third ed., 2002.

[6] C. A. Balanis, *Antenna Theory: Analysis and Design*. Wiley-Blackwell, 2005.

[7] T. A. Milligan, *Modern Antenna Design*. Wiley-Blackwell, 2005.

[8] L. Josefsson and P. Persson, *Conformal Array Antenna Theory and Design (IEEE Press Series on Electromagnetic Wave Theory)*. Wiley-Blackwell, 2006.

[9] ETSI, "ETSI EN 300 440-1," *Telecomunications Series*, vol. 1.6.1, pp. 1–67, 2010.

[10] NAVAL AIR SYSTEMS COMMAND, "Electronic Warfare and Radar Systems Engineering Handbook," Tech. Rep. April 1997, Avionics Department AIR-4.5 Washington, DC 20361, 1999.

[11] H. Griffiths, "New ideas in FM radar," *Electronics & Communication Engineering Journal*, vol. 2, no. 5, pp. 185–194, 1990.

[12] L. Stankovic and S. Stankovic, "An analysis of instantaneous frequency representation using time-frequency distributions-generalized Wigner distribution," *IEEE Transactions on Signal Processing*, vol. 43, no. 2, pp. 549–552, 1995.

[13] A. Stove, "Linear FMCW radar techniques," *IEE Proceedings F Radar and Signal Processing*, vol. 139, no. 5, p. 343, 1992.

[14] J.-C. Marchais, *Air and Spaceborne Radar Systems: An Introduction*. William Andrew, 2001.

[15] Y. Huang, P. Brennan, D. Patrick, I. Weller, P. Roberts, and K. Hughes, "FMCW BASED MIMO IMAGING RADAR FOR MARITIME NAVIGATION," May 2011.

[16] H. Landau, "Sampling, data transmission, and the Nyquist rate," *Proceedings of the IEEE*, vol. 55, no. 10, pp. 1701–1706, 1967.

[17] H. Urkowitz, C. Hauer, and J. Koval, "Generalized Resolution in Radar Systems," *Proceedings of the IRE*, vol. 50, pp. 2093–2105, Oct. 1962.

[18] T. S. Rappaport, *Wireless Communications: Principles and Practice (2nd Edition)*. Prentice Hall, 2002.

[19] G. Breed, "The Fundamentals of Patch Antenna Design and Performance." `http://www.highfrequencyelectronics.com/Archives/Mar09/HFE0309_Tutorial.pdf`, 2009. [Online; Accessed 28/06/2012].

[20] D. Orban and G. Moernaut, "The basics of patch antennas." `www.orbanmicrowave.com/The_Basics_Of_Patch_Antennas.pdf`. [Online; Accessed: 29/06/2012].

[21] E. O. Hammerstad, "Equations for Microstrip Circuit Design," in *1975 5th European Microwave Conference*, pp. 268–272, IEEE, Oct. 1975.

[22] R. Garg, P. Bhartia, I. Bahl, and A. Ittipiboon, *Microstrip Antenna Design Handbook (Antennas & Propagation Library)*. Boston: Artech House, 2000.

[23] S. Winder, J. Davies, and J. J. Carr, *Newnes Radio and RF Engineering Pocket Book (Newnes Pocket Books)*. Newnes (an imprint of Butterworth-Heinemann Ltd), 2002.

[24] J. D. Kraus and R. J. Marhefka, *Antennas For All Applications*. Boston: McGraw-Hill Higher Education, third ed., 2001.

[25] H. Chireix, "Antennes à Rayonnement Zénithal Réduit," *LOnde Electrique*, vol. 15, pp. 440–456, 1936.

[26] H. Knudsen, "The Field Radiated by a Ring Quasi-Array of an Infinite Number of Tangential or Radial Dipoles," *Proceedings of the IRE*, vol. 41, no. 6, pp. 781–789, 1953.

[27] T.-S. Chu, "On the use of uniform circular arrays to obtain omnidirectional patterns," *IRE Transactions on Antennas and Propagation*, vol. 7, no. 4, pp. 436–438, 1959.

[28] H. Jones, M.R.; Griffiths, "Prediction of circular array phase mode characteristics," *Electronics Letters, IEEE*, vol. 2, no. 13, pp. 23–24, 1988.

[29] A. Rudge, K. Milne, A. Olver, and P. Knight, *The Handbook of Antenna Design, Volume 2 (IEE Electromagnetic Waves)*. Institution of Engineering and Technology, 1983.

[30] D. Davies, "Circular Arrays: Their Properties and Potential Applications," *IEE Proceedings of Second International Conference on Antennas and Propagation*, vol. 53, no. 1, pp. 1–10, 1981.

[31] T. Rahim and D. Davies, "Effect of directional elements on the directional response of circular antenna arrays," *Microwaves, Optics and Antennas, IEE Proceedings H*, vol. 129, no. 1, 1982.

[32] J. H. Provencher, "A Survey of Circular Symmetric Arrays," in *Proceedings of Phased Array Symposium, Polytechnic Institute of Brooklyn*, pp. 292–300, 1970.

[33] J. Boyns, C. Gorham, A. Munger, J. Provencher, J. Reindel, and B. Small, "Step-scanned circular-array antenna," *IEEE Transactions on Antennas and Propagation*, vol. 18, pp. 590–595, Sept. 1970.

[34] J. Butler and R. Lowe, "Beamforming Matrix Simplifies Design of Electronically Scanned Antennas," *Electronic Design*, vol. 9, pp. 170–173, 1961.

[35] D. Davies, "A transformation between the phasing techniques required for linear and circular aerial arrays," *Proceedings of the Institution of Electrical Engineers*, vol. 112, no. 11, pp. 2041–2045, 1965.

[36] B. Sheleg, "A matrix-fed circular array for continuous scanning," *Proceedings of the IEEE*, vol. 56, no. 11, pp. 2016–2027, 1968.

[37] W. Nester, "The fast Fourier transform and the Butler matrix," *IEEE Transactions on Antennas and Propagation*, vol. 16, pp. 360–360, May 1968.

[38] J. Shelton, "Fast Fourier transforms and Butler matrices," *Proceedings of the IEEE*, vol. 56, no. 3, pp. 350–350, 1968.

[39] Kelvin Hughes Ltd., "NAVAL AND COAST GUARD RADAR SYSTEMS," 2008.

[40] E. Sharp and M. Diab, "Van Atta reflector array," *IRE Transactions on Antennas and Propagation*, vol. 8, pp. 436–438, July 1960.

[41] Guidance Microwave Ltd., "Radascan target specification." `http://marine.guidance.eu.com/ui/content/content.aspx?ID=377`. [Online; Accessed: 19/04/2012].

[42] A. Lestari, P. Hakkaart, J. Zijderveld, F. Zwan, M. Hajian, and L. Ligthart, "INDRA: The Indonesian Maritime Radar," in *2008 38th European Microwave Conference*, pp. 1600–1603, IEEE, Oct. 2008.

[43] C. Moller-Hundborg, A. C. K. Thomsen, O. Marqversen, K. Hansen, M. Pedersen, and M. Lokke, "Small target detection with SCANTER 5000 & 6000 radar series," 2011.

[44] J. C. Pedersen, "SCANTER 5000 and 6000 Solid State Radar: Utilisation of the SCANTER 5000 and 6000 series next generation solid state, coherent, frequency diversity and time diversity radar with software defined functionality for security applications," in *2010 International WaterSide Security Conference*, pp. 1–8, IEEE, Nov. 2010.

[45] W. Kazimierski and J. Lubczonek, "Analysis of broadband radar picture in the aspect of marine target tracking," 2011.

[46] A. Jimenez, R. Ceres, and F. Seco, "A laser range-finder scanner system for precise manoeuver and obstacle avoidance in maritime and inland navigation," in *Electronics in Marine, 2004. Proceedings Elmar 2004. 46th International Symposium*, pp. 101–106, 2004.

[47] A. Ruiz and F. Granja, "A Short-Range Ship Navigation System Based on Ladar Imaging and Target Tracking for Improved Safety and Efficiency," *IEEE Transactions on Intelligent Transportation Systems*, vol. 10, pp. 186–197, Mar. 2009.

[48] N. Kunzner, J. Kushauer, S. Katzenbeiser, and K. Wingender, "Modern electro-optical imaging system for maritime surveillance applications," in *2010 International WaterSide Security Conference*, pp. 1–4, IEEE, Nov. 2010.

[49] K. Waegel, D. Hounam, R. Bauer, H. Bloetscher, M. Zink, M. Schwerdt, and B. Mayr, "An encoding SAR-transponder for target identification," in *IEEE 1999 International Geoscience and Remote Sensing Symposium. IGARSS'99 (Cat. No.99CH36293)*, vol. 1, pp. 20–22, IEEE, 1999.

[50] J. Briggs, *Target Detection by Marine Radar (IEE Radar Series) PBRA0160*. Institution of Engineering and Technology, 2004.

[51] L. Hallman, "Considerations in the Design of a Universal Beacon System," *Proceedings of the IRE*, vol. 36, pp. 1526–1529, Dec. 1948.

[52] G. Hansen, "Naval Use of Radar and Radio Telephone in Navigation and Harbor Defense," *Transactions of the IRE Professional Group on Communications Systems*, vol. 3, pp. 59–59, Mar. 1955.

[53] A. L. P. Milwright, "A survey of harbour approach aids," *Proceedings of the IEE - Part B: Radio and Electronic Engineering*, vol. 105, no. 9, pp. 351–357, 1958.

[54] P. Planck, "Active-Scatterer Radar System," *IEEE Transactions on Aerospace and Electronic Systems*, vol. AES-5, pp. 1008–1009, Nov. 1969.

[55] D. Davies and H. Makridis, "Two-frequency secondary radar incorporating passive transponders," *Electronics Letters*, vol. 9, no. 25, p. 592, 1973.

[56] D. Davies, M. Withers, and R. Claydon, "PASSIVE CODED TRANSPONDER USING AN ACOUSTIC-SURFACE-WAVE DELAY LINE," *Electronics Letters, IEEE*, vol. 11, no. 8, pp. 163–164, 1975.

[57] C. McEwen, "Identity-transponder system using c.w. interrogation," *Electronics Letters*, vol. 11, no. 25-26, p. 642, 1975.

[58] D. Abadie, M. De Vecchis, and J. Puyhaubert, "A 3 GHz Radar Beacon ("Racon") using a Microwave Acoustic Delay Line," in *7th European Microwave Conference, 1977*, pp. 499–503, IEEE, Oct. 1977.

[59] C. Mathews, E. Isbister, and J. Fee, "Marine radar interrogator-transponder," *IEEE Journal of Oceanic Engineering*, vol. 2, pp. 179–184, Apr. 1977.

[60] J. Fee, "Optimized location for navigation transponders," in *28th IEEE Vehicular Technology Conference*, vol. 28, pp. 400–404, IEEE, 1978.

[61] J. Thornton and D. Edwards, "Modulating retro-reflector as a passive radar transponder," *Electronics Letters*, vol. 34, no. 19, p. 1880, 1998.

[62] J. Thornton and D. Edwards, "Range measurement using modulated retro-reflectors in FM radar system," *IEEE Microwave and Guided Wave Letters*, vol. 10, no. 9, pp. 380–382, 2000.

[63] F. Williamson, L. Moore, R. Brooks, J. Williamson, and M. McGee, "A coded radar reflector for remote identification of personnel and vehicles," in *The Record of the 1993 IEEE National Radar Conference*, pp. 186–191, IEEE, 1993.

[64] J. Gavan, "Transponders for the detection and identification of remote cooperative targets," in *Proceedings of IEEE National Telesystems Conference - NTC '94*, pp. 229–232, IEEE, 1994.

[65] S. Smolskiy and I. Komarov, *Fundamentals of Short-Range FM Radar (Radar Library)*. Artech House, 2003.

[66] M. Ash, P. Brennan, N. M. Vriend, J. McElwaine, and C. Keylock, "FMCW phased array radar for automatically triggered measurements of snow avalanches," in *Radar Conference (EuRAD), 2011 European*, pp. 166–169, 2011.

[67] F. Folster, H. Rohling, and U. Lubbert, "An automotive radar network based on 77GHz FMCW sensors," in *IEEE International Radar Conference, 2005.*, pp. 871–876, IEEE, 2005.

[68] P. Burke, "Ultra-linear chirp generation via VCO tuning predistortion," in *1994 IEEE MTT-S International Microwave Symposium Digest (Cat. No.94CH3389-4)*, pp. 957–960, IEEE, 1994.

[69] Y.-T. Im, J.-H. Lee, and S.-O. Park, "A DDS and PLL-based X-band FMCW radar system," in *2011 IEEE MTT-S International Microwave Workshop Series on Intelligent Radio for Future Personal Terminals*, pp. 1–2, IEEE, Aug. 2011.

[70] H. Griffiths, "The effect of phase and amplitude errors in FM radar," in *High Time-Bandwidth Product Waveforms in Radar and Sonar, IEE Colloquium on*, pp. 9/1–9/5, 1991.

[71] M. Withers, "Matched filter for frequency-modulated continuous-wave radar systems," *Proceedings of the Institution of Electrical Engineers*, vol. 113, no. 3, p. 405, 1966.

[72] W. Von Aulock, "Properties of Phased Arrays," *Proceedings of the IRE*, vol. 48, pp. 1715–1727, Oct. 1960.

[73] M. Vossiek, R. Roskosch, and P. Heide, "Precise 3-D Object Position Tracking using FMCW Radar," in *29th European Microwave Conference, 1999*, vol. 1, pp. 234–237, IEEE, Oct. 1999.

[74] W. Hausz and R. A. Zachary, "Phase-Amplitude Monopulse System," *IRE Transactions on Military Electronics*, vol. MIL-6, pp. 140–146, Apr. 1962.

[75] S. Sharenson, "Angle Estimation Accuracy with a Monopulse Radar in the Search Mode," *IRE Transactions on Aeronautical and Navigational Electronics*, vol. ANE-9, pp. 175–179, Sept. 1962.

[76] Mircowaves101.com, "Monopulse antennas." `http://www.microwaves101.com/encyclopedia/monopulseantennas.cfm`. [Online; Accessed: 07/12/2013].

[77] M. Katzin, "Back scattering from the sea surface," in *IRE International Convention Record*, vol. 3, pp. 72–77, Institute of Electrical and Electronics Engineers, 1955.

[78] S. Watts, "Radar sea clutter: Recent progress and future challenges," in *2008 International Conference on Radar*, pp. 10–16, IEEE, Sept. 2008.

[79] T. Leonard, I. Antipov, and K. Ward, "A comparison of radar sea clutter models," in *RADAR 2002*, pp. 429–433, IEE, 2002.

[80] K. D. Ward, R. J. Tough, and S. Watts, *Sea Clutter: Scattering, The K Distribution and Radar Performance (IET Radar, Sonar, Navigation and Avionics)*. The Institution of Engineering and Technology, 2006.

[81] C. Harrison, "Symmetrical Antenna Arrays," *Proceedings of the IRE*, vol. 33, pp. 892–896, Dec. 1945.

[82] C. Earp and R. Godfrey, "Radio direction-finding by the cyclical differential measurement of phase," 1947.

[83] V. Ammula, S. M. Rao, and S. M. Wentworth, "Dual excited planar circular array antenna for direction agile applications," in *2010 42nd Southeastern Symposium on System Theory (SSST 2010)*, pp. 138–142, IEEE, Mar. 2010.

[84] M. Moody, "Direction of arrival estimation using a sparse circular array and multiplicative beamforming," *IEEE Transactions on Antennas and Propagation*, vol. 31, pp. 678–682, July 1983.

[85] N. Li and R. Li, "The Application of Circular Sparse Antenna Array Synthesis Based on Differential Mind Evolutionary Algorithm," in *2010 2nd International Workshop on Database Technology and Applications*, pp. 1–4, IEEE, Nov. 2010.

[86] R. Sanudin and T. Arslan, "Semi-circular antenna array for azimuth DOA estimation," in *2012 Loughborough Antennas & Propagation Conference (LAPC)*, pp. 1–4, IEEE, Nov. 2012.

[87] J. Freese, G. Tudosie, M. Schussler, and R. Jakoby, "Semi-circular microstrip array on a planar reflector with extended beam-scanning range," in *IEEE Antennas and Propagation Society International Symposium. Digest. Held in conjunction with: USNC/CNC/URSI North American Radio Sci. Meeting (Cat. No.03CH37450)*, vol. 1, pp. 284–287, IEEE, 2003.

[88] E. J. Wilkinson, "An N-Way Hybrid Power Divider," *IEEE Transactions on Microwave Theory and Techniques*, vol. 8, pp. 116–118, Jan. 1960.

[89] L. G. Maloratsky, *Integrated Microwave Front-Ends with Avionics Applications*. Artech House, 2012.

[90] R. Smith and C. Holt Smith, "Elimination of errors from crossed-dipole direction-finding systems," *Electrical Engineers - Part IIIA: Radiolocation, Journal of the Institution of*, vol. 93, no. 1, pp. 575–587, 1946.

[91] Mini-Circuits, "Ceramic Balun RF transformer." `http://194.75.38.69/pdfs/NCS1-292+.pdf`, 2011. [Online; Accessed 09/06/2011].

[92] D. Cure, S. Melais, T. Weller, P. Herzig, and R. Roeder, "2.45 GHz end-loaded dipole backed by a high impedance surface," in *2010 IEEE Antennas and Propagation Society International Symposium*, pp. 1–4, IEEE, July 2010.

[93] K. Mohammadpour-Aghdam, H. Aliakbarian, S. Farsi, R. Faraji-Dana, G. Vandenbosch, and W. De Raedt, "Miniaturized loaded crossed dipole antenna with omnidirectional radiation pattern in the horizontal plane," 2009.

[94] J. Reed and G. Wheeler, "A Method of Analysis of Symmetrical Four-Port Networks," *IEEE Transactions on Microwave Theory and Techniques*, vol. 4, pp. 246–252, Oct. 1956.

[95] H.-x. Xu, G.-m. Wang, and K. Lu, "Microstrip Rat-Race Couplers," *IEEE Microwave Magazine*, vol. 12, pp. 117–129, June 2011.

[96] K. Gentile, "Super-Nyquist Operation of the AD9912 Yields a High RF Output Signal." http://www.analog.com/static/imported-files/application_notes/AN-939.pdf. [Online; Accessed: 22/03/2012].

[97] R. Tymerski, "Chapter 3 - zero-order hold." http://web.cecs.pdx.edu/~tymerski/ece452/Chapter3.pdf. [Online; Accessed: 10/05/2014].

[98] Analog Devices, Inc., "A Technical Tutorial on Digital Signal Synthesis." http://www.analog.com/static/imported-files/tutorials/450968421DDS_Tutorial_rev12-2-99.pdf. [Online; Accessed: 15/11/2014].

[99] Wainwright Instruments GmbH, "Datasheet - BPF 2441.75 MHz." http://tinyurl.com/wainwright-BPF-2441-75, 2012. [Online; Accessed 12/11/2014].

[100] Creative Technology Ltd., "Creative Soundblaster SB1090 Specification." http://us.store.creative.com/Sound-Blaster-XFi-Surround-5.1/M/B0017QQQAE.htm. [Online; Accessed: 20/03/2013].

[101] W. Kester, "ADC Noise Figure - An Often Misunderstood and Misinterpreted Specification." http://www.analog.com/static/imported-files/tutorials/MT-006.pdf, 2014. [Online; Accessed: 21/04/2013].

[102] W. Kester, "Taking the Mystery out of the Infamous Formula, "SNR = 6.02N + 1.76dB," and Why You Should Care." http://www.analog.com/static/imported-files/tutorials/MT-001.pdf, 2009. [Online; Accessed 21/04/2013].

[103] P. V. Brennan, *Phase-locked loops: principles and practice*. Macmillan Press, 1996.

[104] P. Brennan, K. Nicholls, L. Lok, and H. Corr, "Phase-sensitive FMCW radar system for high-precision Antarctic ice shelf profile monitoring," Feb. 2014.

[105] H. Friis, "Noise Figures of Radio Receivers," *Proceedings of the IRE*, vol. 32, pp. 419–422, July 1944.

[106] Texas Instruments, "Chapter 16 - Active Filter Design Techniques (Literature Number SLOA088)." http://www.ti.com/lit/ml/sloa088/sloa088.pdf, 2012. [Online; Accessed 12/11/2014].

[107] The MathWorks, Inc., "wavread." http://www.mathworks.co.uk/help/matlab/ref/wavread.html. [Online; Accessed: 25/07/2012].

[108] The MathWorks, Inc., "Acquiring Data with a Sound Card." `https://www.mathworks.co.uk/products/daq/code-examples.html?file=/products/demos/daq/acquiring_data/acquiring_data.html`. [Online; Accessed: 01/09/2012].

[109] H. Rohling, "Radar CFAR Thresholding in Clutter and Multiple Target Situations," *IEEE Transactions on Aerospace and Electronic Systems*, vol. AES-19, pp. 608–621, July 1983.

[110] O. Ersoy, "A comparative review of real and complex Fourier-related transforms," *Proceedings of the IEEE*, vol. 82, pp. 429–447, Mar. 1994.

[111] EMERSON & CUMING MICROWAVE PRODUCTS, INC, "ECCOSORB AN." `http://www.eccosorb.com/Collateral/Documents/English-US/AN.pdf`, 2011. [Online; Accessed 06/08/2013].